Title
Planetary magnetism : investigations of paleomagnetic properties of the Earth and Moon

Author
Lawrence, Kristin Portle

Publication Date
2008

UNIVERSITY OF CALIFORNIA, SAN DIEGO

Planetary Magnetism: Investigations of Paleomagnetic Properties of the Earth and Moon

A dissertation submitted in partial satisfaction of the
requirements for the degree Doctor of Philosophy

in

Earth Sciences

by

Kristin Portle Lawrence

Committee in charge:

Professor Catherine L. Johnson, Chair
Professor Lisa Tauxe, Co-Chair
Professor Cathy Constable
Professor David Sandwell
Professor Mark Thiemens

2008

The Dissertation of Kristin Portle Lawrence is approved, and it is acceptable in quality and form for publication on microfilm:

Co-Chair

Chair

University of California, San Diego

2008

To my Family

Magnetism is one of the Six Fundamental Forces of the Universe, with the other five being Gravity, Duct Tape, Whining, Remote Control, and The Force That Pulls Dogs Toward The Groins Of Strangers.

Dave Barry

TABLE OF CONTENTS

LIST OF FIGURES

LIST OF TABLES

ACKNOWLEDGEMENTS

I would like to acknowledge the many people who have played a role in my educational adventure. It is difficult to overstate my gratitude to my Ph.D. supervisor, Dr. Catherine Johnson. This work would not have been possible without the support and encouragement of my colleague and friend. Throughout my thesis, she has provided sound advice as well as guidance balanced by the freedom to express myself through this work. And most importantly I would like to thank her for providing a really cool project to work on! I would also like to thank my co-chair, Lisa Tauxe for providing balance and creative solutions for numerous research questions. Her enthusiasm and support made this thesis not only fun but outstanding science. Thanks to Cathy Constable for her support and many helpful scientific conversations. I thank all of my coauthors for their hard work and insightful contributions. I would also like to thank my committee for taking the time to work with me. I extend my gratitude to the members of the Antarctica Field teams (Hubert Staudigel, Lisa Tauxe, Cathy Constable, Jasper Konter, Julie Bowles and Elise Sbarbori), who all labored or froze to one extent or another in order to collect data for Chapter 3.

I cannot end without thanking my family, on whose constant encouragement and love I have relied throughout my time as a graduate student. Who knew that remote control stuffed animal doors, light-up Valentine's boxes, and "eggernaut" experiments would have lead to a geophysics dissertation. Thank you Dad, for all those crazy, creative projects. Thank you Mom for helping me to always look on the bright side of things and being the intelligent, patient, and driven role model that I strive to emulate.

And to my husband for always being there but never asking why it was taking so long ... I love you Jesse.

Chapter 2, in full, is a reprint of the material as it appears in Lawrence, K.P.; Constable, C.G.; Johnson, C.L (2006), Paleosecular variation and the average geomagnetic field at ± 20° latitude, *Geochemistry, Geophysics, Geosystems*, 7, doi:10.1029/2005GC001181. The dissertation author was the primary investigator and author of this paper.

Chapter 3, in part, has been submitted for publication of the material as it may appear in Lawrence, K. P., L. Tauxe, H. Staudigel, C. G. Constable, W. McIntosh, M. Heizer, C. L. Johnson (2008), Paleomagnetic field properties near the southern hemisphere tangent cylinder, *Geophysics, Geochemistry and Geosystems*. The dissertation author was the primary investigator and author of this paper.

Chapter 4, in full, is a reprint of the material as it appears in Lawrence, K.P.; Johnson, C.L.; Tauxe, L.; Gee, J.S. (2008), Lunar paleointensity measurements: Implications for lunar magnetic evolution, *Physics of the Earth and Planetary Interiors*. The dissertation author was the primary investigator and author of this paper.

VITA

1999	B.A., Carleton College, Northfield, MN Cum Laude with Distinction in Physics
2001	Teaching Assistant, Washington University, St. Louis, MO
2002	M.A., Washington University, St. Louis, MO in Earth & Planetary Sciences
2003-2007	Research Assistant, Scripps Institute of Oceanography, La Jolla, CA
2005	Assistant Instructor, COSMOS, La Jolla, CA
2008	Ph.D. in Earth Science, Scripps Institution of Oceanography, La Jolla, CA

PUBLICATIONS

Lawrence, K.P., L. Tauxe, H. Staudigel, C.G. Constable, W. McIntosh, A. Koppers, C.L. Johnson (2008), Paleomagnetic field properties near the southern hemisphere tangent cylinder, *Geophysics, Geochemistry and Geosystems*, submitted.

Lawrence, K.P., C.L. Johnson, L. Tauxe, J.S. Gee (2008), Lunar paleointensity measurements: Implications for lunar magnetic evolution, *Physics of the Earth and Planetary Interiors,* in press.

Lawrence, K.P., C.G. Constable, and C.L. Johnson (2006), Paleosecular variation and the average geomagnetic field at +/- 20 degrees latitude, *Geochemistry, Geophysics, Geosystems*, **7**, doi:10.1029/2005GC001181.

Lawrence, K.P., and R.J. Phillips (2003), Gravity/topography admittance inversion on Venus using niching genetic algorithms, *Geophysical Research Letters*, **30**, 1994, doi:10.1029/2003GL017515.

HONORS AND AWARDS

2004	American Geophysical Union Outstanding Student Award
2001	Nominated for Teaching Assistant of the Year
1999	McDonnell Center Graduate Fellowship (3 year award)
1999	Sigma Xi
1998	Awarded funding through Research Experience for Undergraduates
1998	Scholarship from Minnesota Space Grant Institution

ABSTRACT OF THE DISSERTATION

Planetary Magnetism: Investigations of Paleomagnetic Properties of the Earth and Moon

by

Kristin Portle Lawrence

Doctor of Philosophy in Earth Sciences

University of California, San Diego, 2008

Professor Catherine Johnson, Chair

Professor Lisa Tauxe, Co-Chair

A planetary body's ability to generate a dynamo is dependent on its thermal history and possible energy sources, particularly the convective states of the core and overriding mantle. This dissertation addresses questions regarding the characteristics of magnetic fields for both the Earth and the Moon. The temporal and spatial variations of the Earth's geomagnetic field are investigated using rock magnetic properties (direction and intensity) for the past 5 Ma. This thesis analyzes both published data at ±20° and provides new paleomagnetic measurements of direction and intensity for a high latitude site (-78°) to investigate both the longitudinal and latitudinal variations of Earth's field. Investigations of zonal statistical paleosecular variation (PSV) models reveal that recent models are incompatible with the empirical ±20° directional distributions. The ±20° latitude data suggest less PSV and smaller persistent deviations from a geocentric axial dipole field during the Brunhes. High dispersion and low intensity observed at -78° agrees with the global observation of anti-correlation between dispersion and intensity.

Comparisons with temporally-varying dipole magnitude models show that the lack of increased paleointensity at high latitude likely results from temporal sampling bias.

Previous paleointensity studies of Apollo era samples suggest strong paleointensities for ancient (>3.6 Ga) lunar rocks and little-to-no strength for younger (< 3.6 Ga) rocks. By extrapolation, these results were interpreted as the Moon having an early, short-lived dynamo. However, previous paleointensity measurements do not meet current lab protocols and substantial scatter exists in paleointensities from the putative dynamo period. I analyze published and measure new absolute (thermal and microwave) and relative paleointensities from five Apollo samples spanning from 3.3 to 4.3 Ga to re-examine the hypothesis of an early lunar dynamo. In light of the new experiments and a thorough re-evaluation of existing paleointensities, I show that although some samples with ages of 3.6 Ga to 3.9 Ga are strongly magnetized with occasional stable directions, no observations verifiably demonstrate a primary thermal remanence. In agreement with satellite measurements of crustal magnetism, current paleointensity measurements do not support the existence of a 3.9-3.6 Ga lunar dynamo.

Chapter 1

Introduction

1.1 Preface

Magnetic fields are a fundamental consequence of cooling of (terrestrial) planets with iron-rich cores. The Earth's geomagnetic field varies as a complex function of space and time, with both internal (to the solid planet) and external contributions. Nearly four centuries ago William Gilbert demonstrated that the Earth's magnetic field was dipolar in nature (like that of a bar magnet) and established the association of the global magnetic field with interior Earth processes. Surveys were originally carried out by sea-faring vessels and later by permanent observatories located around the world, providing direct measurements as early as 400 years ago. More recently near-Earth satellites such as MAGSAT, Ørsted, CHAMP, and SAC-C recorded global magnetic field variations. Both historical and satellite records indicate that the Earth's geomagnetic field changes over timescales from hours to centuries. To understand geomagnetic field behavior over much longer timescales; records which extend into the geological past are necessary. Paleomagnetism provides such records through remanent magnetization of lavas, sediments and artifacts for which independent age estimates of magnetization are reliably determined. In this Chapter, I provide a basic background for the paleomagnetic investigations in Chapters 2 through 5 and a cursory geophysical history of the Moon to provide context for Chapters 4 and 5. Due to the breadth of subject matter covered within this thesis, a final summary and conclusion chapter has been omitted in lieu of individual summary and conclusions within each chapter.

1.2 Paleomagnetic Background

Small concentrations of ferromagnetic minerals such as magnetite and hematite are present in most rocks and sediments. These minerals can attain a stable natural remanent magnetization (NRM) parallel to an ambient magnetic field through thermal remanent magnetization (TRM) or detrital remanent magnetization (DRM). This thesis focuses on TRMs measured from igneous rocks because they record ancient field properties at relevant timescales (up to 4 Ga) and they can provide absolute paleointensity estimates of the ancient field (DRMs only provide relative paleointensities). A TRM is acquired as magnetic grains of a material cool through their Curie temperatures and acquire magnetic moments. As magnetic grains cool below their Curie temperatures they stabilize and become effectively blocked to further applications of a magnetizing field. While magnetic moments may decay with time given sufficient application of energy (thermal or electromagnetic), relaxation times are typically comparable to geologic timescales. Therefore, both the direction and intensity of a magnetizing field are, in principle, measurable in a rock sample well after the field has changed or been removed. Theory [*Néel*, 1955] and experiments [e.g. *Tauxe and Yamazaki*, 2007; *Thellier and Thellier*, 1959; e.g. *Valet*, 2003] have demonstrated that the intensity of a TRM or a partial TRM (pTRM) is directly proportional to the intensity of the magnetizing field. Hence it is, in principle, possible to retrieve information about the paleointensity of the geomagnetic field by normalizing a TRM; this concept is expanded upon in Chapters 3 and 4.

A geomagnetic field vector is described by three independent components, as shown in Figure 1.1. Here I define the Cartesian coordinates with $\hat{x}$, $\hat{y}$, and $\hat{z}$ corresponding to North, East, and vertical directions. The magnetic field vector can alternatively be defined by D, I, and B components which correspond to declination, inclination, and intensity.

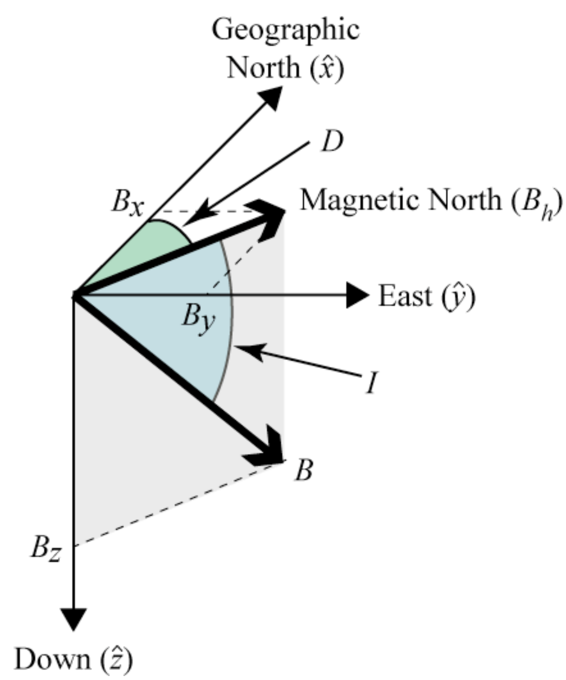

Figure 1.1: Components of the geomagnetic field vector **B** in Cartesian coordinates (B_x, B_y, B_z) and geomagnetic elements (*D, I, B*). B_h is the projection of the field vector **B** onto a plane tangent to the Earth's surface. *D* (declination) is measured clockwise from geographic North. *I* (inclination) is measured positive down from the horizontal plane.

The conversion between Cartesian components and geomagnetic elements are expressed as follows,

$$
\begin{aligned}
B &= \sqrt{B_x^2 + B_y^2 + B_z^2} \\
D &= \tan^{-1}\left(\frac{B_y}{B_x}\right) \\
I &= \sin^{-1}\left(\frac{B_z}{\left(B_x^2 + B_y^2\right)^{1/2}}\right)
\end{aligned} \quad , \tag{1.1}
$$

where B is the magnitude of the magnetic field vector.

The geomagnetic field as measured by data collected at or above Earth's surface (and assuming a source-free region) can be described by a spherical harmonic expansion in which the scalar magnetic potential due to a core field is given by

$$
\Psi(r,\theta,\phi) = a\sum_{l=1}^{\infty}\sum_{m=0}^{l}\left(\frac{a}{r}\right)^{l+1}\left(g_l^m \cos m\phi + h_l^m \sin m\phi\right)P_l^m(\cos\theta) \tag{1.2}
$$

where a is Earth's radius (6371 km), r is radius, θ is colatitude, ϕ is longitude, l and m are harmonic degree and order, P_l^m are partially normalized Schmidt functions, g_l^m and h_l^m are the Gauss coefficients. Specifically, g_1^0, g_2^0 and g_3^0 are the axial dipole, quadrupole and axial octupole terms respectively. The magnetic field vector, ***B***, is the gradient of the potential and D, I, and intensity are non-linearly related to the field components.

Observations of the magnetic field allow remote sensing of Earth's deep interior, providing indirect information about the dynamics of the liquid outer core. For this reason, we often simplify the magnetic field to describe measurable characteristics of the geodynamo. In paleomagnetism the Earth's geomagnetic field is typically approximated as a geocentric dipole aligned with Earth's rotation axis, referred to as the geocentric axial dipole (GAD) approximation. Both inclination and intensity vary with latitude (λ)

in a GAD field, following the relationships,

$$\tan I = 2\tan\lambda \tag{1.3}$$

and

$$B = \frac{B_0}{r^3}\left(1+3\sin^2\lambda\right)^{1/2}, \tag{1.4}$$

where $B_0 = g_1^0 a^3$.

Long-term temporal variations (time scales of up to ~10^6 yrs) of the geomagnetic field are identified using paleomagnetic observations from field direction and intensity recorded in archeomagnetic materials, sedimentary and igneous rocks. These time variations are known as paleosecular variation (PSV). The time-averaged field (TAF) over specific time intervals such as the current or past few polarity chrons (normal or reverse states of the geomagnetic field) is used to investigate small but persistent departures from GAD. Specifically, average inclination and declination anomalies are defined as the difference between observed direction and GAD.

Spherical harmonic formulation allows paleomagnetic observations to be interpreted in the context of global field models, where the model parameters are the spherical harmonic coefficients. The TAF can be modeled in terms of time-averaged values of g_l^m and h_l^m; PSV can be modeled in terms of the variance in the g_l^m and h_l^m. In Chapters 2 and 3, I use the spherical harmonic estimates of the TAF from paleomagnetic directions from locations at ±20°, and test existing statistical PSV models by comparing their predictions with our ±20° latitude data and with high latitude observations from

Antarctica.

Chapters 2 and 3 investigate spatial and temporal variations in the Earth's geomagnetic field by analyzing the magnetic properties (direction and intensity) of igneous samples for the past 5 Ma. Of specific interest are the longitudinal variations in the paleomagnetic field, which may reflect core-mantle interactions and their influence on the magnetic field. In Chapter 2, I compile and analyze previously published paleomagnetic properties (declination and inclination) at ±20° latitude to remove the latitudinal dependence, thereby providing a characterization of the statistical behavior of the geomagnetic field. In Chapter 3, I characterize high-latitude (-78°) paleomagnetic measurements from Antarctica in an effort to highlight possible geomagnetic differences between the high-latitude region of the outer core where gravitationally driven vortices likely dominate as compared to the low and mid latitudes where Coriolis effects dominate. Prior to this thesis, data coverage above ±60° latitude was insufficient to discern any differences with meaningful statistical relevance.

1.3 Brief Geophysical History of the Moon

The Earth is not the only planetary body in our solar system with a magnetic field. Direct measurements of planetary magnetic fields by spacecraft like Lunar Prospector, Mariner 10, Mars Global Surveyor, and Galileo have revealed magnetic fields at the Moon, Mercury, Mars, Europa, and Ganymede, respectively [for a review see *Connerney*, 2007]. These planetary fields are caused by three primary mechanisms: (1) active dynamo, (2) remanence, or (3) induction, all of which are observed in the planets and satellites of the solar system. Observations of Mercury's and Ganymede's magnetic fields suggest that there may be a mechanism by which an internally generated magnetic field can be actively sustained in relatively small planetary bodies [*Christensen*, 2006; *Stanley, et al.*, 2005]. The existence of crustal magnetic anomalies on the Moon and Mars without evidence of an active internally generated magnetic field, suggests an earlier dynamo era and indicates that physical conditions within these bodies have changed through time. Investigations into the magnetic fields and geophysical histories of other planets provide a broader context for understanding Earth's magnetic history. Chapters 4 and 5 specifically address lunar magnetic observations and their implications with respect to the evolution of the Moon.

From the mid-20th century, repeated scientific missions were dedicated to the Moon, beginning in the 1950's with a series of probes by both the United States (Ranger) and Russia (Zond and Luna). Starting in the 1960's, the Apollo missions (both manned and unmanned) provided a wealth of information about the Moon. Soil and rock samples were collected and returned from six sites, while instrument packages (ALSEP) were deployed on the surface to collect seismic, cosmic (charged particle and cosmic ray), and magnetic data at five sites. Figure 1.2 shows a shaded relief map of the moon with the Apollo landing sites labeled. Our knowledge of the Moon's magnetic field is largely derived from combined analyses of returned lunar samples and observations at or above (ALSEP and satellite) the surface of the Moon.

Scientific exploration of the Moon was rejuvenated with the orbiting Clementine and Lunar Prospector spacecrafts in the mid-nineties. Lunar Prospector mapped crustal magnetic fields via both Magnetometer and Electron Reflectometer instruments. More recently, the European Space Agency's SMART-1 spacecraft was in orbit about the Moon from 2004 to 2006 while Japan and China currently have spacecrafts in orbit (Kaguya and Chang'e 1, respectively). In the near future there will be a flurry of activity concerning lunar science. For example, NASA intends to launch Lunar Reconnaissance Orbiter (LRO) in late 2008 and India will launch Chandrayaan-1 in summer of 2008.

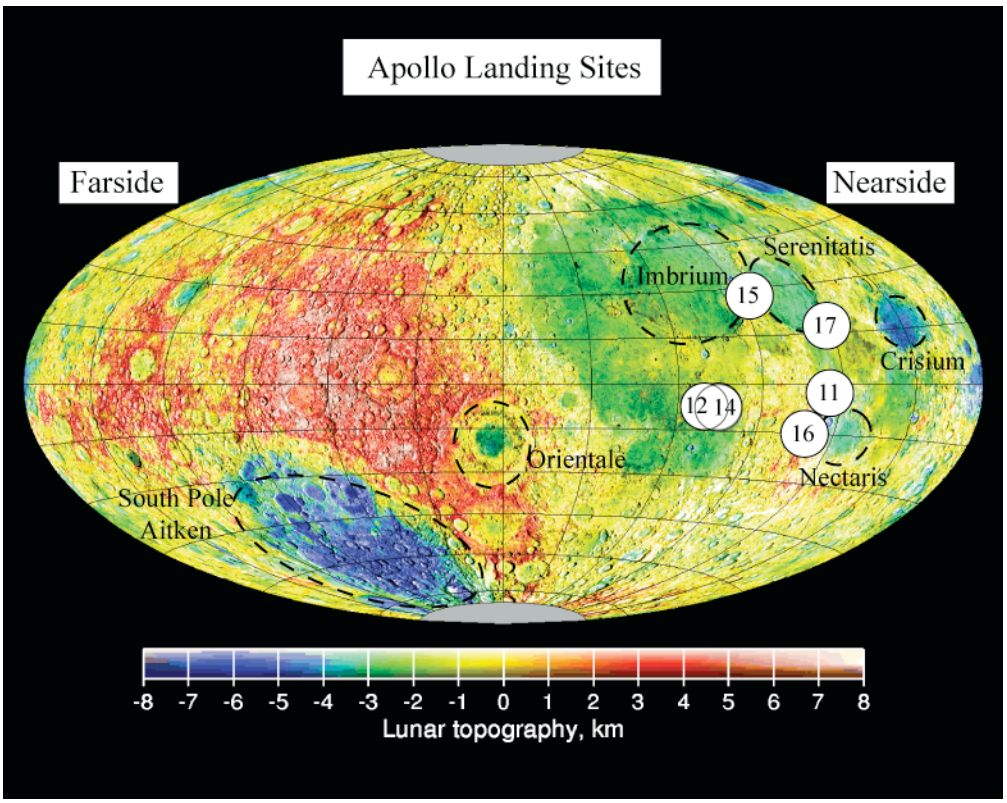

Figure 1.2: Lunar topography map (from the laser altimeter on Clementine [*Smith, et al.*, 1997]) overlain with the locations of the Apollo landing sites (white circles) and major impact basins located.

The Moon is the largest satellite among the terrestrial planets, with a radius of 1738 km and a mass of little greater than 1% of the Earth's. The Moon is a differentiated body with a crust, mantle, and a small core of its own. The bulk composition of the Moon is similar in composition to the Earth's mantle. The surface consists of two major geological terrains; the higher-albedo, older, more heavily cratered highlands and the darker, younger, less cratered maria. The highlands are composed of primordial crustal material known as anorthosite, while the maria are basaltic lava flows that have filled impact basins. The ages of most mare basalt samples range from 3.9 to 3.2 Ga [*Breuer and Moore*, 2007], however they span 4.2 [*Taylor, et al.*, 1983] to 1.3 Ga [*Hiesinger, et al.*, 2000]. The moon exhibits a hemispheric asymmetry where the farside consists primarily of highlands while the nearside is mostly mare. This dichotomy is also seen in the crustal thickness estimates for the Moon; the near side has a significantly thinner crust, resulting in a ~ 2 km offset between the center of mass and center of figure [*Kaula, et al.*, 1972]. For both hemispheres, impact cratering has been the dominant modification process for the entire lunar surface for the duration of its evolution.

Compositional and structural models of the lunar interior are generally based on Apollo seismic data, mean density estimates, and moment of inertia measurements. A slight measurable deviation of the mean normalized moment of inertia (0.3931 ± 0.0002; [*Konopliv, et al.*, 1998]) from that of a homogenous sphere (0.4) indicates that the Moon is differentiated, but if the core is predominantly iron, it cannot exceed 330 km in radius [*Wieczorek, et al.*, 2006]. A separate study of the lunar magnetic moment induced by the geomagnetic tail of the Earth constrains the radius of the lunar core to 340 ± 90 km [*Hood, et al.*, 1999]. The direct seismological evidence (PKP waves) concerning a lunar core is unconvincing as it depends on poorly-located farside moonquakes detected during the short duration of seismic recordings [*Sellers*, 1992]. Many authors have constructed one-dimensional compositional models of the Moon based on seismic velocity models that allow for a core radius of up to ~530 km [*Kuskov, et al.*, 2002]. *Khan et al.* [2004] ran a Monte Carlo optimization for the best set of four input parameters (mean density, normalized moment of inertia, tidal potential Love number, seismic quality factor) to minimize data misfit for the combined inversion of the lunar laser ranging and seismic data. The optimal solution implies a molten or partially molten iron core with radius and density of about 350 km and 7200 kg/m^3, respectively. Despite these improved estimates, the composition, size, and phase of the core are still unconstrained. For a review of geophysical methods used to investigate the potential existence and subsequent trade-off between size and composition of a lunar core see *Wieczorek et al.* [2006] and *Lognonné and Johnson* [2007].

Presently, the Moon lacks an internally generated global magnetic field [*Russell, et al.*, 1974]; however, both subsatellite and surface magnetometer measurements made during the Apollo missions revealed evidence of remanent magnetization in the lunar crust. Surface magnetometer measurements at Apollo 12, 14, 15 and 16 landing sites demonstrated surface intensities up to hundreds of nT [*Dyal and Gordon*, 1973]. Subsatellites from Apollo 15 and 16 measured numerous sites of localized anomalous crustal magnetic fields, varying in lateral scale from 7 km to ~500 km [*Hood, et al.*, 1981]. More recently, *Mitchell et al.* [2008] compiled measurements from the Lunar Prospector Electron Reflectometer instrument to produce a global map of surface magnetic field strength. Similarly, *Richmond and Hood* [2008] presented a global magnetic field vector data set compiled from measurements by the Lunar Prospector

Magnetometer instrument. Figure 1.3 (reproduced from [*Mitchell, et al.*, 2008]) shows that the Moon's crust is only weakly magnetized (< 400 nT) on measurable spatial scales (> 5 km). It is also apparent that four of the large impact basins (e.g., Orientale, Imbrium, Serenitatis, and Crisium) have some of the weakest (near zero) magnetic signatures, while their antipodes have the largest.

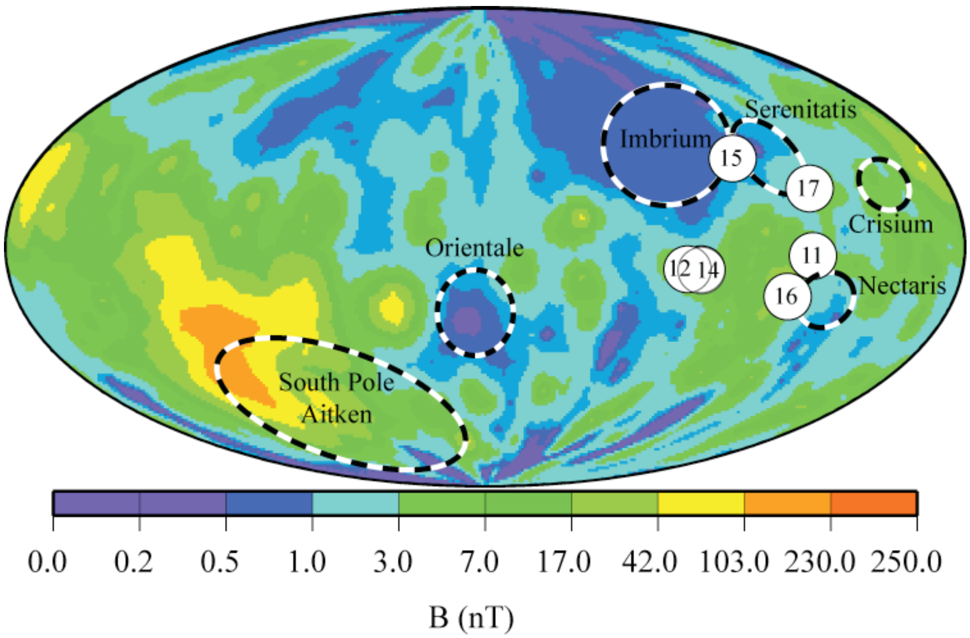

Figure 1.3: Surface crustal magnetic field intensity map of the Moon. Field intensity (B) measurements (ranging from 0 to 250 nT) were made using the Lunar Prospector Electron Reflectometer instrument. Magnetic measurements are binned into 5 x 5-degree elements and interpolated to 1 x 1-degree grid. Dashed circles represent major impact basins and solid white circles denote Apollo landing sites. Data from *Mitchell et al.* [2008].

The origin of lunar magnetic anomalies is still unconstrained. The strong magnetic crustal fields antipodal to large impact basins have motivated the hypothesis that crustal magnetization resulted from hypervelocity impacts causing plasma clouds that compress and amplify pre-existing ambient magnetic fields (whether internal dynamo or inter-planetary magnetic field in origin) near the antipode of an impact site [e.g. *Crawford and Schultz*, 1991; e.g. *Crawford and Schultz*, 1999; *Hood and Artemieva*, 2007; *Hood and Huang*, 1991; *Snkra, et al.*, 1979]. An alternative explanation for surface magnetization is impact by cometary coma [*Gold and Soter*, 1976; *Schultz and Srnka*, 1980], which is based on the correlation between areas of high magnetization and areas of unusually high albedo. It has also been inferred from previously reported strong paleointensities (~100 μT; see Chapter 4 for more detail) from ancient (>3.6 Ga) lunar rocks and little-to-no strength for younger (<3.6 Ga) rocks, that the Moon may have had an early, short-lived dynamo [*Cisowski, et al.*, 1983; *Runcorn*, 1994; *Runcorn, et al.*, 1983].

It should be noted that it is difficult -though not impossible- to predict sufficiently high core heat flux until 3.6 Ga for sustained lunar dynmo generation with thermal evolution models given the small size of the lunar core. For example, thermal evolution models incorporating 2- and 3-D convection require a highly temperature-dependent rheology which could possibly lead to the generation of an internally driven lunar dynamo from core formation to 3 Ga [*Konrad and Spohn*, 1997; *Spohn, et al.*, 2001]. Alternatively, *Stegman et al.* [2003] propose a complex model of lunar evolution to explain a putative high-field era. In this model, a dense ilmenite and pyroxene cumulate layer (result from magma ocean cooling and crystallization) sinks to the deep lunar interior after a duration of cooling. This layer encircles and insulates the lunar core, thereby preventing core convective heat loss and subsequent dynamo generation. After some duration, radioactive decay could heat the layer such that it ascends from thermal expansion, allowing the core to cool through convection, thereby possibly producing a late-onset, short-lived, thermally driven lunar dynamo.

The observation and distribution of remanent magnetization in both the return samples and surface field anomalies pose many questions about the structure, composition and ultimately the evolution of the Moon. Reconciling the inferred strength of a magnetizing field as measured in paleointensity experiments on lunar samples with the global distribution of surface anomalies will provide needed insight into the origin of the magnetizing field(s). However, there are relatively few previous paleointensity measurements, most of which do not meet current lab protocols. In addition, there is substantial scatter in paleointensity measurements during the putative dynamo period. The fact that complex lunar evolution models such as *Stegman et al.* [2003] are based on outdated data motivates the two avenues of investigation presented in Chapters 4 and 5. First, I compile and revisit previously published intensity data. Second, I attempt new intensity measurements with more sophisticated laboratory techniques adapted for lunar samples, such as the IZZI modified Thellier-Thellier experiment using both thermal (Chapter 4) and microwave (Chapter 5) energy sources.

1.4 References

Breuer, D., and W. B. Moore (2007), Dynamics and thermal history of the terrestrial planets, the Moon, and Io, in *Treatise on Geophysics, Planets and Moons Volume*, edited by T. Spohn, pp. 299-348, Elsevier.

Christensen, U. R. (2006), A deep rooted dynamo for Mercury, *Nature*, *444*, 1056.

Cisowski, S. M., et al. (1983), A review of lunar paleointensity data and implications for the origin of lunar magnetism, *J. Geophys. Res.*, *88*, A691-A704.

Connerney, J. E. P. (2007), Planetary Magnetism, in *Treatise on Geophysics, Planets and Moons Volume*, edited by T. Spohn, pp. 243-280, Elsevier.

Crawford, D. A., and P. H. Schultz (1991), Laboratory investigations of impact-generated plasma, *J. Geophys. Res.*, *96*, 18807-18817.

Crawford, D. A., and P. H. Schultz (1999), Electromagnetic properties of impact-generated plasma, vapor and debris, *International Journal of Impact Engineering*, *23*, 169-180.

Dyal, P., and D. Gordon (1973), Lunar surface magnetometers, *IEEE Transactions on Magnetics*, *9*, 226-231.

Gold, T., and S. Soter (1976), Cometary impact and the magnetization of the moon, *Planetary and Space Science*, *24*, 45-54.

Hiesinger, J., et al. (2000), Ages of mare basalts on the lunar nearside, *J. Geophys. Res.*, *105*, 29239-29275.

Hood, L. L., and N. A. Artemieva (2007), Antipodal effects of lunar basin-forming impacts: Initial 3D simulations and comparisons with observations, *Icarus*, *in press*, doi:10.1016/j.icarus.2007.1008.1023.

Hood, L. L., and Z. Huang (1991), Formation of magnetic anomalies antipodal to lunar impact basins: Two-dimensional model calculations, *J. Geophys. Res.*, *96*, 9837-9846.

Hood, L. L., et al. (1999), Initial measurements of the lunar induced magnetic dipole moment using Lunar Prospector magnetometer data, *Geophys. Res. Lett.*, *26*, doi:10.1029/1999GL900487.

Hood, L. L., et al. (1981), Contour maps of the lunar remanent magnetic fields, *J. Geophys. Res.*, *86*, 1055-1069.

Kaula, W. M., et al. (1972), Analysis and interpretation of lunar laser altimetry, *Proceedings of the Lunar Science Conference 2*, 2189.

Khan, A., et al. (2004), Does the moon possess a molten core? Probing the dep lunar interior using results from LLR and Lunar Prospector, *J. Geophys. Res.*, *109*, doi:10.1029/2004JE002294.

Konopliv, A. S., et al. (1998), Improved gravity field of the Moon from Lunar Prospector, *Science*, *281*, 1476-1480.

Konrad, W., and T. Spohn (1997), Thermal history of the Moon: Implications for an early core dynamo and post-accretional magmatism, *Advances in Space Research*, *19*, 1511-1521.

Kuskov, O. L., et al. (2002), Geochemical constraints on the seismic properties of the lunar mantle, *Phys. Earth Planet. Int.*, *134*, 175-189.

Lognonné, P., and C. L. Johnson (2007), Planetary Seismology, in *Treatise on Geophysics, Planets and Moons Volume*, edited by T. Spohn, pp. 69-122, Elsevier.

Mitchell, D. L., et al. (2008), Global mapping of lunar crustal magnetic fields by Lunar Prospector, *Icarus*, *194*, 401-409.

Néel, L. (1955), Some theoretical aspects of rock-magnetism, *Advances in Physics*, *4*, 191-243.

Richmond, N. C., and L. L. Hood (2008), A preliminary global map of the vector lunar crustal magnetic field based on Lunar Prospector magnetometer data, *J. Geophys. Res.*, *in press*, doi:10.1029/2007JE002888.

Runcorn, S. K. (1994), The early magnetic-field and primeval satellite of the Moon: Clues to planetary formation, *Philos. Trans. R. Soc. London, Ser. A*, *349*, 181-196.

Runcorn, S. K., et al. (1983), Lunar palaeomagnetism and its implications, *Advances in Space Research*, *2*, 21-29.

Russell, C. T., et al. (1974), The permanent and induced magnetic dipole moment of the moon, *Proceedings of the Fifth Lunar Science Conference*, *3*, 2747-2760.

Schultz, P. H., and L. J. Srnka (1980), Cometary collisions on the moon and mercury, *Lunar and Planetary Science XI*, 1009-1011.

Sellers, P. C. (1992), Seismic evidence for a low-velocity lunar core, *J. Geophys. Res.*, *97*, 11663-11672.

Smith, D. E., et al. (1997), Topography of the Moon from the Clementine LIDAR, *J. Geophys. Res.*, *102*, 1591-1611.

Snkra, L. J., et al. (1979), Magnetic field and shock effects and remanent magnetism in a hyper-velocity impact environment, *Earth Planet. Sci. Lett.*, *42*, 127-137.

Spohn, T., et al. (2001), The longevity of lunar volcanism: Implications of thermal evolution calculations with 2D and 3D Mantle convection models, *Icarus*, *149*, 54-65.

Stanley, S., et al. (2005), Thin shell dynamo models consistent with Mercury's weak observed magnetic field, *Earth Planet. Sci. Lett.*, *234*, 27-38.

Stegman, D. R., et al. (2003), An early lunar core dynamo driven be thermochemical mantle convection, *Nature*, *421*, 143-145.

Tauxe, L. T., and T. Yamazaki (2007), Paleointensities, in *Treatise on Geophysics, Geomagnetism Volume*, edited by M. Kono, pp. 509-563, Elsevier.

Taylor, L. A., et al. (1983), Pre 4.2-A.E. mare basalt volcanism in the lunar highlands, *Earth Planet. Sci. Lett.*, *66*, 33-47.

Thellier, E., and O. Thellier (1959), Sur l'intensité du champ magnétique terrestre dans le passé historique et géologique, *Ann. Geophys.*, *15*, 285-378.

Valet, J. P. (2003), Time variations in geomagnetic intensity, *Reviews of Geophysics*, *41*, 1004, doi:1010.1029/2001RG000104.

Wieczorek, M. A., et al. (2006), The constitution and structure of the lunar interior, in *New Views of the Moon*, edited, p. 221, Mineralogical Soc America, Chantilly.

Chapter 2

Paleosecular Variation and the Average Geomagnetic Field at ±20° Latitude

Abstract

We assembled a new paleomagnetic directional data set from lava flows and thin dikes for four regions centered on ±20° latitude: Hawaii, Mexico, the South Pacific and Reunion. We investigate geomagnetic field behavior over the past 5 Myr and address whether geographical differences are recorded by our data set. We include inclination data from other globally distributed sites with the ±20° data to determine the best fitting time-averaged field (TAF) for a two-parameter longitudinally symmetric (zonal) model. Values for our model parameters - the axial quadrupole and octupole terms – are 4% and 6% of the axial dipole, respectively. Our estimate of the quadrupole term is compatible with most previous studies of deviations from a geocentric axial dipole (GAD) field. Our estimated octupole term is larger than that from normal polarity continental and igneous rocks, and oceanic sediments, but consistent with that from reversed polarity continental and igneous rocks. The variance reduction compared with a GAD field is ~12%, and the remaining signal is attributed to paleosecular variation (PSV). We examine PSV at ±20° using virtual geomagnetic pole (VGP) dispersion and comparisons of directional distributions with simulations from two statistical models. Regionally, the Hawaii and Reunion datasets lack transitional magnetic directions and have similar inclination

anomalies and VGP dispersion. In the Pacific hemisphere, Hawaii has a large inclination anomaly and the South Pacific exhibits high PSV. The deviation of the TAF from a GAD contradicts earlier ideas of a "Pacific dipole window" and the strong regional PSV in the S. Pacific contrasts with the generally low secular variation found on short time scales. The TAF and PSV at Hawaii and Reunion are distinct from values for the South Pacific and Mexico, demonstrating the need for time-averaged and paleosecular variation models that can describe non-zonal field structures. Investigations of zonal statistical PSV models reveal that recent models are incompatible with the empirical ±20° directional distributions and cannot fit the data by simply adjusting relative variance contributions to the PSV. The ±20° latitude data set also suggests less PSV and smaller persistent deviations from a geocentric axial dipole field during the Brunhes.

2.1 Introduction

Observations of the magnetic field allow remote sensing of activity in Earth's deep interior, providing indirect information about the dynamics of the liquid outer core over timescales of centuries to millions of years. Paleomagnetic studies can be used to identify long term temporal variations of the geomagnetic field on local, regional, and global scales. These time variations are known as paleosecular variation (PSV). The time-averaged field (TAF) over specific time intervals such as the current or past few polarity chrons is also of interest. The TAF may indicate long-term departures from the geocentric axial dipole (GAD) - the most basic field model used throughout paleomagnetism. Both paleomagnetic field strength and direction are used to study TAF and PSV; here we only consider directional data because of their greater abundance and reliability.

Paleodirections used in PSV studies can be obtained from both sedimentary and igneous rocks, but in this work we focus exclusively on the latter. Data from igneous rocks, specifically lava flows or thin dikes that cool rapidly during emplacement provide a record of the paleofield at a single time and place that, from a geological perspective, can be considered instantaneous. Given adequate temporal and spatial sampling such flows could provide a global record of the field spanning millions of years. However, sampling is limited by the geographical distribution of volcanic sources and the irregular occurrence of eruptions. Statistical methods are used to characterize the TAF and PSV since poorly known age relationships among lava flows prohibit the construction of an accurate sequence of field measurements through time.

PSV is often described in terms of angular dispersion in local field directions or in virtual geomagnetic pole (VGP) position about GAD. As Earth's field is predominantly dipolar, early studies of PSV attempted to distinguish contributions to angular dispersion from the dipole and non-dipole parts of the field. Contributions from dipole variations were further separated into temporal variations in the dipole moment, and those from variations in dipole orientation (dipole wobble) with respect to the Earth's rotation axis. Over the past 40 years, many models have been proposed to explain the observed latitudinal variation in angular dispersion: these have been comprehensively reviewed by *Merrill et al.* [1996]. Most modern PSV models are based on a general approach developed by *Constable and Parker* [1988] that provides a complete statistical description of the geomagnetic field. In these models the measurable part of the global geomagnetic field generated in Earth's outer core is represented by the spherical harmonic expansion of a Laplacian potential. The statistics of the temporal variations in the field are described in terms of statistical distributions of the coefficients of the individual spherical harmonic terms. In the *Constable and Parker* [1988] model, the spherical harmonic coefficients are considered to be samples drawn from a Gaussian statistical process with mean and variance specified according to spherical harmonic degree and order. Many variations to this model have since been proposed [e.g. *Constable and Johnson*, 1999; *Hatakeyama and Kono*, 2002; *Hulot and Gallet*, 1996; *Kono and Hiroi*, 1996; *Quidelleur and Courtillot*, 1996; *Tauxe and Kent*, 2004], none of which are completely satisfactory since no model explains all aspects of existing PSV data. Nevertheless, recent work by *Hulot and Bouligand* [2005] shows that this approach can be useful in discriminating among various symmetry properties of the paleofield.

The nature of non-GAD persistent contributions to the TAF is also debated, and there are numerous TAF models for the time period 0-5 Ma [*Carlut and Courtillot*, 1998; *Constable and Parker*, 1988; *Gubbins and Kelly*, 1993; *Hatakeyama and Kono*, 2002; *Johnson and Constable*, 1995, 1997; *Kelly and Gubbins*, 1997; *McElhinny, et al.*, 1996b; *Quidelleur, et al.*, 1994; *Schneider and Kent*, 1990]. Almost the only common feature in these TAF models is a small axial quadrupole contribution whose size ranges from 2.5 to 8% of the axial dipole term [*McElhinny*, 2004]. The axial quadrupole is the simplest parameterization (in spherical harmonic models for the field) that explains observations of low-latitude negative inclination anomalies (observed inclination minus that predicted for a GAD) in the paleofield. Although several authors propose that all further departures from GAD arise from inadequacies in quality and spatio-temporal data distributions

[*Carlut and Courtillot*, 1998; *McElhinny, et al.*, 1996b], others are of the opinion that these departures reflect real field structure [*Gubbins and Kelly*, 1993; *Hatakeyama and Kono*, 2002; *Johnson and Constable*, 1995, 1997; *Kelly and Gubbins*, 1997], including persistent asymmetries between the Pacific and Atlantic hemispheres.

In this study, we compile and examine previously published paleodirections derived from lava flows emplaced over the past 5 million years at latitudes close to ±20°. We conduct a comprehensive analysis of the average field and secular variation recorded from 4 regions centered on Hawaii, Mexico, Reunion, and in the Southern Pacific Ocean. We discuss how data quality and transitional field directions affect PSV and TAF estimates, and we investigate the possibility of equatorial and longitudinal asymmetries in both PSV and the TAF. Low PSV in the Pacific (sometimes misleadingly termed the "Pacific dipole window") has been the topic of ongoing debate [*Johnson and Constable*, 1997, 1998; *McElhinny, et al.*, 1996a; *McWilliams, et al.*, 1982; *Miki, et al.*, 1998; *Shibuya, et al.*, 1995], since it was first proposed by *Doell and Cox* [1971] using Hawaiian data. We revisit this issue, comparing the statistical properties of the paleofield at these mid and circum-Pacific and Indian Ocean locales, and assess how well our new data compilation is described by current [*Constable and Johnson*, 1999; *Tauxe and Kent*, 2004] PSV models.

2.2 The Data Set

We have compiled paleomagnetic directional data from published volcanic flow studies from Hawaii, Mexico, Fiji, Cook, Society, Reunion, and Mauritius Islands. We group data from the Fiji, Cook, and Society Islands (our "South Pacific"), and merge the

Mauritius data with those from Reunion giving four distinct regions (Figure 2.1). Sampling latitudes lie within 5° of ±20°. Our compilations for Hawaii and Reunion include and extend directional data used by *Love and Constable* [2003], and our compilation for Mexico is very similar to that of *Mejia et al.* [2005]. We limit our analyses to data spanning the past 5 Myr for two reasons: first, the number of data available diminishes rapidly with increasing age; second, for ages less than 5 Myr the plate motion corrections needed to obtain accurate paleo-site locations are small and reasonably well known. A summary of the data that we examined is given in Table 2.1. The total number of paleodirections is 1125 for Hawaii, 567 for Mexico, 267 for Reunion, and 690 for the South Pacific.

We assigned numerical ages to all the paleomagnetic sites, so that we could restrict our analyses to the period 0-5 Ma and assess the temporal distribution within our compilation. Where possible we use site ages determined by radiometric methods and reported in the original reference. When the flow or the region was dated radiometrically, but at a different location from the paleomagnetic site, we assign the reported flow or region date to the site in question. When only the geological epoch was reported (e.g., Pliocene or Miocene) the midpoint of the epoch age range was used. For epochs spanning the Brunhes-Matuyama transition, sites with reverse polarity were assigned ages greater than 0.78 Ma.

The age distributions for each geographical region are shown in Figure 2.2. The temporal distribution for each region is non-uniform. Data sets from Reunion, Hawaii, and Mexico are heavily biased to Quaternary age flows. The ~0.5 Ma peak in the Hawaiian data distribution reflects extensive sampling of young flows on (the big Island of) Hawaii. The peak around 3-3.5 Ma corresponds to flows on Oahu, Kauai, and Nihoa Islands [*Doell*, 1972a; 1972b; *Herrero-Bervera and Coe*, 1999; *Laj, et al.*, 1999]. The

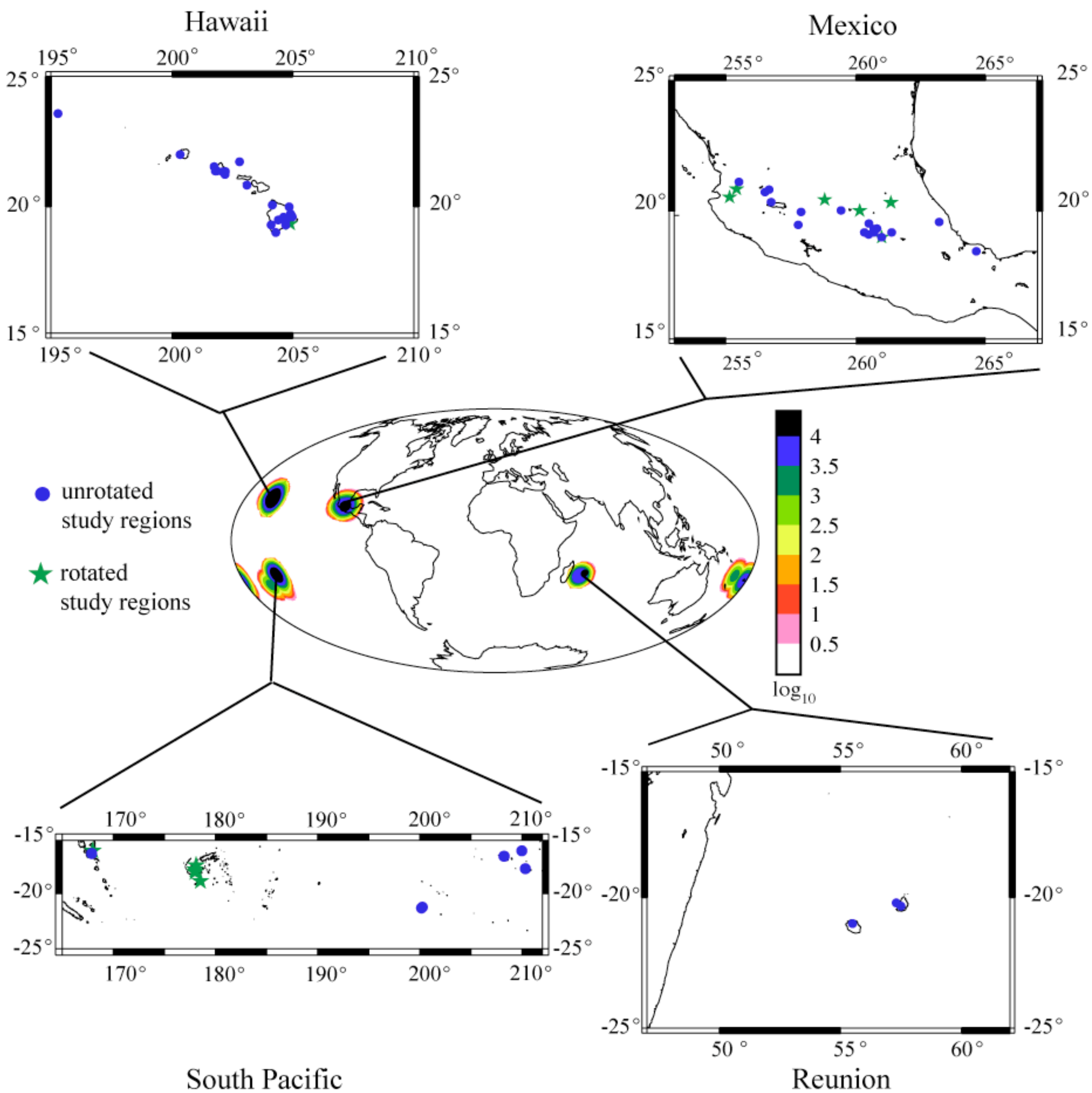

Figure 2.1: Empirically derived data density for study regions; Color scale is logarithmic. Boxes show the study locations; blue circles represent studies without tectonic rotation reported, green stars are those reporting post-emplacement tectonic rotation. More information on the data from each site is in Table 2.1

Table 2.1 List of Data References

Mexico (27 studies)	**Latitude (°N)**		**Longitude (°E)**								**Polarity**		**mean (N)**		**mean (R)**	
Reference	**max**	**min**	**max**	**min**	**Nt**	**r**	**a**	**No κ**	**n**	**Nu**	**N**	**R**	**ΔD**	**ΔI**	**ΔD**	**ΔI**
Alor and Uribe, 1986	20.32	19.62	258.58	257.61	13	0	0	0	0	13	9	4	-23.8	-5.7	-6.6	-27.1
Alva-Valdivia et al., 2001	18.60	18.23	265.31	264.65	12	0	1	0	0	11	4	7	-10.0	-1.7	1.6	-2.9
Böhnel et al., 1997	19.33	19.33	260.82	260.82	1	0	0	0	0	1	1	0	-12.7	2.3	--	--
Böhnel et al., 1990	19.00	19.00	261.00	261.00	1	1	0	0	0	0	--	--	--	--	--	--
Böhnel and Negendank, 1981	19.93	18.15	263.60	262.38	55	0	18	0	0	37	34	3	-1.7	-5.6	8.4	-30.5
Böhnel and Molina-Garza, 2002	21.14	19.05	263.10	255.50	6	0	0	0	0	6	6	0	-2.0	-5.0	--	--
Delgado-Granados et al., 1995	20.50	19.04	258.45	256.35	36	0	11	0	0	25	17	8	1.1	-0.5	10.1	0.2
Gonzalez et al., 1997	19.82	19.10	260.83	257.78	13	0	0	0	0	13	13	0	4.9	5.9	--	--
Herrero-Bervera et al., 1986	19.00	19.00	261.00	261.00	10	0	0	0	0	10	10	0	-8.4	-9.4	--	--
Maillol and Bandy, 1997	20.82	20.42	255.28	255.03	16	16	0	0	0	0	--	--	--	--	--	--
Mejia et al., 2005	22.84	18.98	260.75	258.09	16	0	1	2	0	13	2	11	28.7	-6.3	0.9	2.5
Mooser et al., 1974	19.73	19.04	261.40	260.02	187	0	119	0	0	68	52	16	2.9	-7.4	-8.5	-11.5
Mora-Alvarez, et al., 1991	19.37	19.20	260.76	260.66	5	0	0	0	1	4	2	2	35.0	-36.9	-46.0	-25.5
Morales, et al., 2001	19.32	19.04	260.75	260.38	7	0	0	0	0	7	7	0	-0.4	-7.8	--	--
Nieto-Obergon, et al., 1992	20.97	20.15	255.58	254.97	13	13	0	0	0	0	--	--	--	--	--	--
Osete, et al., 2000	19.58	19.30	260.68	260.40	30	0	0	3	0	27	18	9	-9.8	-0.3	-15.0	-6.0
Petronille et al., 2005	21.21	21.03	255.64	255.05	17	0	0	1	0	16	14	2	-1.8	-2.0	-10.1	0.8
Rosas-Elguera and Urrutia-Fucugauchi, 1992	20.25	20.02	259.66	259.40	14	0	2	0	0	12	7	5	-14.8	-8.3	-30.3	-5.1
Ruiz-Martinez, et al., 2000	20.66	19.06	263.58	261.19	25	8	0	0	0	17	14	3	-0.4	-9.3	-1.1	-31.8
Soler-Arechalde and Urrutia-Fucugauchi, 2000	20.03	19.84	260.19	259.40	9	9	0	0	0	0	--	--	--	--	--	--

continued

Table 2.1 (continued)

Mexico (27 studies)	**Latitude (°N)**		**Longitude (°E)**								**Polarity**		**mean (N)**		**mean (R)**	
Reference	**max**	**min**	**max**	**min**	**Nt**	**r**	**a**	**No κ**	**n**	**Nu**	**N**	**R**	**ΔD**	**ΔI**	**ΔD**	**ΔI**
Steele, 1971, 1985	19.22	19.10	260.37	260.34	35	0	0	0	0	35	34	1	-0.8	-1.4	-52.6	-24.8
Uribe-Cifuentes and Urrutia-Fucugauchi, 1999	20.46	20.13	258.96	258.75	13	13	0	0	0	0	--	--	--	--	--	--
Urrutia-Fucugauchi, 1996	19.34	19.18	260.83	260.78	13	0	0	0	0	13	13	0	-2.0	-2.2	--	--
Urrutia-Fucugauchi, et al., 2000	20.78	20.75	256.66	256.50	6	0	0	0	0	6	5	1	-1.7	-9.0	0.0	-2.0
Urrutia-Fucugauchi, et al., 1988	20.78	20.75	256.66	256.50	6	0	0	0	0	6	5	1	0.7	-13.9	91.1	-15.6
Vlag, et al., 2000	19.10	19.10	260.50	260.50	1	0	0	0	0	1	1	0	-21.5	15.6	--	--
Watkins, et al., 1971	20.85	20.76	256.66	256.65	7	0	5	0	0	2	2	0	-14.3	-8.5	--	--
Mexico Totals	22.84	18.15	265.31	254.97	567	60	157	6	1	343	270	73				
After Flow average					548	60	157	5	1	325						

Hawaii (23 studies)	**Latitude (°N)**		**Longitude (°E)**								**Polarity**		**mean (N)**		**mean (R)**	
Reference	**max**	**min**	**max**	**min**	**Nt**	**r**	**a**	**No κ**	**n**	**Nu**	**N**	**R**	**ΔD**	**ΔI**	**ΔD**	**ΔI**
Brassart, et al., 1997	20.21	20.07	204.43	204.10	10	0	0	0	0	10	10	0	-6.4	-4.5	--	--
Bogue and Coe, 1984	22.16	22.06	200.67	200.26	84	0	0	0	0	84	32	53	15.4	4.4	-13.4	-5.6
Bogue, 2001	22.10	22.07	200.26	200.24	50	0	0	0	0	50	28	22	-11.3	-10.7	-11.9	-6.8
Castro and Brown, 1987	19.30	19.30	204.80	204.10	2	0	0	0	0	2	2	0	12.3	-3.0	--	--
Coe, et al., 1978	19.83	19.05	205.16	204.12	16	0	0	1	0	15	15	0	10.1	-2.3	--	--
Doell, 1969	19.49	19.49	204.40	204.40	54	0	0	0	0	54	54	0	-5.2	-11.2	--	--
Doell, 1972a	22.23	21.90	200.68	200.27	119	0	0	27	0	92	48	44	-3.3	-11.6	1.6	-8.4
Doell, 1972b	23.60	21.78	199.95	195.30	39	0	7	0	0	32	25	7	-2.0	-7.8	10.1	-1.8
Doell, 1972c	21.46	21.26	202.34	202.15	26	0	0	0	0	26	26	0	-1.3	-4.9	--	--
Doell and Cox, 1965	20.13	18.90	204.95	204.42	148	0	0	36	1	111	111	0	5.7	-4.8	--	--

continued

Table 2.1 (continued)

Hawaii (23 studies)	**Latitude (°N)**		**Longitude (°E)**								**Polarity**		**mean (N)**		**mean (R)**	
Reference	**max**	**min**	**max**	**min**	**Nt**	**r**	**a**	**No κ**	**n**	**Nu**	**N**	**R**	**ΔD**	**ΔI**	**ΔD**	**ΔI**
Doell and Dalrymple, 1973	21.75	21.34	202.80	201.74	99	0	1	0	0	98	33	65	0.7	-3.9	-1.3	-14.1
Herrero-Bervera and Coe, 1999	21.45	21.40	201.87	201.80	65	0	2	0	10	53	27	26	3.3	-25.6	-12.2	-8.0
Herrero-Bervera, et al., 2000	20.87	20.70	203.11	202.12	8	0	0	0	0	8	0	8	--	--	-9.1	4.2
Herrero-Bervera and Valet, 2002	21.42	21.26	202.37	202.13	17	0	0	0	0	17	17	0	-1.4	-3.4	--	--
Herrero-Bervera and Valet, 2003	21.38	21.28	202.35	202.05	10	0	0	0	0	10	0	10	--	--	-3.5	-20.5
Herrero-Bervera and Valet, 2005	21.55	21.55	201.77	201.77	45	0	0	0	0	45	11	34	3.9	-18.1	13.8	-18.9
Holcomb, et al., 1986	19.71	19.06	205.17	204.16	135	0	5	0	0	130	130	0	2.1	0.0	--	--
Jurado-Chichay, et al., 1996	19.00	19.00	204.00	204.30	3	0	0	0	0	3	3	0	3.9	-16.1	--	--
Laj, et al., 1999	21.40	21.40	20.80	201.80	105	0	0	0	0	105	105	0	3.0	-14.8	--	--
Mankinen and Champion, 1993	19.71	18.97	204.96	204.38	24	0	0	0	0	24	24	0	2.4	-3.6	--	--
Riley, et al., 1999	19.34	19.29	204.70	204.70	51	30	0	0	0	21	21	0	18.0	-13.2	--	--
Tanaka and Kono, 1991	19.34	19.34	205.16	204.51	7	0	0	0	0	7	7	0	11.3	-0.3	--	--
Valet, et al., 1998	19.73	19.20	204.91	204.40	8	0	0	0	0	8	8	0	-11.2	-0.2	--	--
Hawaiian Totals	23.60	18.90	205.17	195.30	1125	30	15	64	11	1005	737	269				
After Flows are averaged					1015	30	15	64	11	895						

Reunion (6 studies)	**Latitude (°N)**		**Longitude (°E)**								**Polarity**		**mean (N)**		**mean (R)**	
Reference	**max**	**min**	**max**	**min**	**Nt**	**r**	**a**	**No κ**	**n**	**Nu**	**N**	**R**	**ΔD**	**ΔI**	**ΔD**	**ΔI**
Chaumalaun, 1968	-21.0	-21.0	55.5	55.5	97	0	0	21	53	23	12	11	4.2	-7.4	172.6	1.7
Chauvin, et al., 1991	-21.0	-21.0	55.5	55.5	30	0	0	2	0	28	28	0	356.1	-9.7	--	--
McDougall and Chamalaun, 1969	-20.3	-20.3	57.5	57.5	35	0	18	2	8	7	5	2	355.3	-19.2	187.5	-12.3
Rais, et al., 1996	-21.0	-21.0	55.5	55.5	70	0	0	5	0	65	65	0	356.4	-3.3	--	--

continued

Table 2.1 (continued)

Hawaii (23 studies)	**Latitude (°N)**		**Longitude (°E)**								**Polarity**		**mean (N)**		**mean (R)**	
Senanayake, et al., 1982	-20.2	-21.0	57.3	55.5	14	0	7	7	0	0	--	--	--	--	--	--
Watkins, 1973	-21.0	-21.0	55.5	55.5	21	0	0	0	0	21	19	2	0.6	-2.8	223	79.3
Reunion Totals	-20.2	-21.0	57.5	55.5	267	0	25	37	61	144	129	15				

South Pacific (13 studies)	**Latitude (°N)**		**Longitude (°E)**								**Polarity**		**mean (N)**		**mean (R)**	
Reference	**max**	**min**	**max**	**min**	**Nt**	**r**	**a**	**No κ**	**n**	**Nu**	**N**	**R**	**ΔD**	**ΔI**	**ΔD**	**ΔI**
Chauvin, et al., 1990	-17.67	-17.67	210.33	210.33	123	0	0	0	0	123	59	64	188.2	0.3	3.7	30.8
Duncan, 1975	-16.50	-17.67	210.58	208.27	60	0	0	1	0	59	40	19	185.6	0.0	359.7	7.6
Falvey, 1978	-16.00	-16.00	168.00	168.00	14	14	0	0	0	0	--	--	--	--	--	--
Inokuchi, et al., 1992	-17.75	-17.75	178.00	178.00	40	40	0	0	0	0	--	--	--	--	--	--
James and Falvey, 1978	-18.00	-18.00	178.00	178.00	16	16	0	0	0	0	--	--	--	--	--	--
Malahoff, et al., 1982	-17.37	-18.06	178.46	177.08	38	38	0	0	0	0	--	--	--	--	--	--
Morinaga, et al., 1991	-21.25	-22.50	208.67	200.25	18	0	5	1	0	12	1	11	190.3	3.2	319.1	105.4
Roperch and Duncan, 1990	-16.00	-16.00	210.00	210.00	132	0	0	3	0	129	83	46	219.5	39.4	351.9	7.6
Tarling, 1967c	-21.33	-21.39	200.19	200.16	14	0	0	9	0	5	1	4	178.6	-8.7	286	75.2
Tarling, 1967a	-18.00	-18.00	178.00	178.00	23	23	0	0	0	0	--	--	--	--	--	--
Tarling, 1967b	-15.35	-17.50	168.57	167.63	19	0	8	2	1	8	8	0	--	--	0.4	12.4
Taylor, et al., 2000	-16.87	-19.08	178.60	177.42	44	44	0	0	0	0	--	--	--	--	--	--
Yamamoto, et al., 2002	-16.44	-17.65	210.62	207.74	149	0	0	3	0	146	92	54	177.9	-6.1	2.4	1.6
South Pacific Totals	-15.35	-22.50	210.62	167.63	690	175	13	19	1	482	284	198				

Nt, total number of paleodirections from unique sites reported; **r**, sites reported to be effected by tectonic rotation; **a**, sites older than 5 Myr; **No κ**, no value of kappa reported for site; **n**, number of sites with less than 3 samples used for statistics; **Nu**, number of sites used in the this analysis; **Polarity N**, number of normal polarity sites used in this analysis; **Polarity R**, number of reverse polarity used; **mean ΔD, ΔI**, the mean declination and inclination anomalies of the data used for both normal **(N)** and reversed **(R)** polarity data

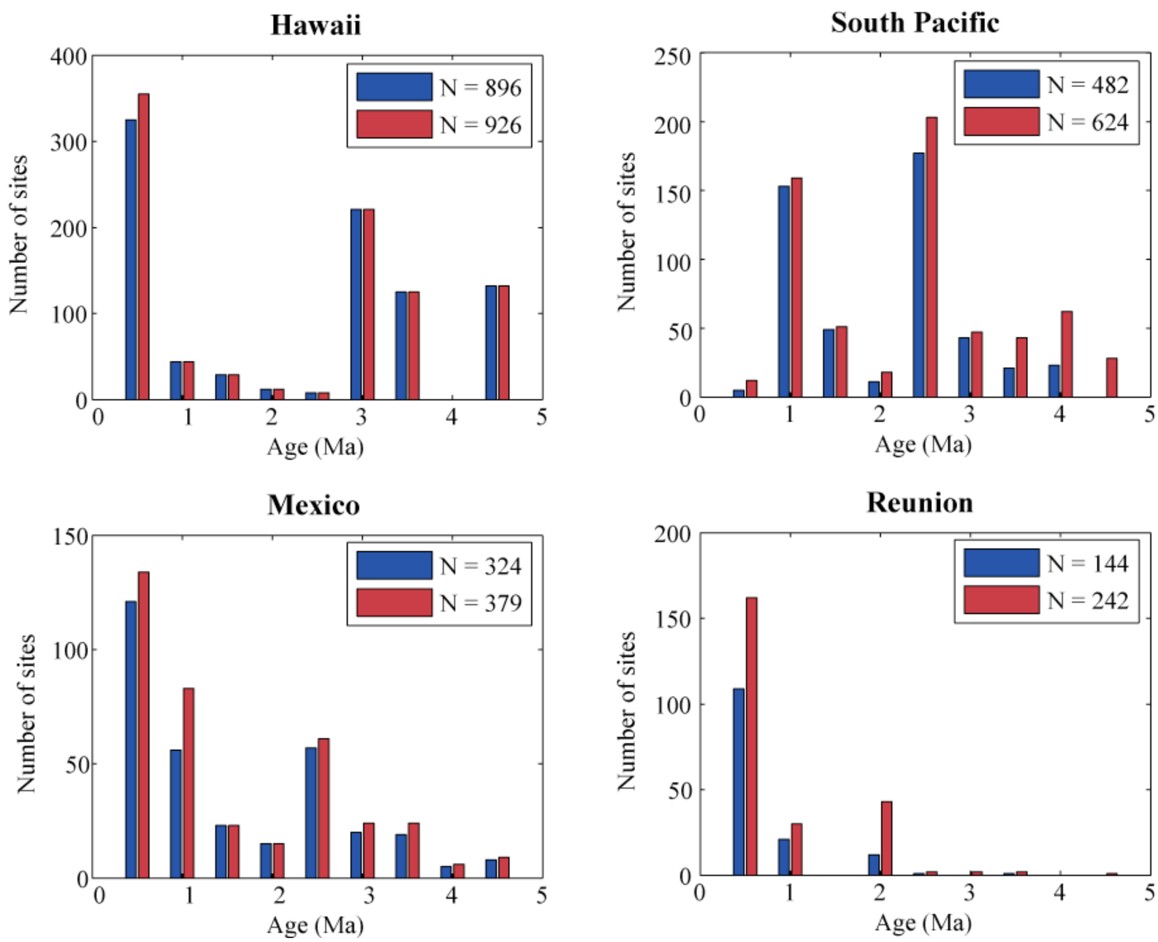

Figure 2.2: Age distribution of sites in each geographical region. Bin size is 0.5 Myr. Red represents all sites younger than 5 Ma including tectonically rotated sites. Blue represents sites not contaminated by tectonic movement, and with more than two samples.

South Pacific age distribution is strongly influenced by studies focused around the Matuyama/Gauss transition [*Duncan*, 1975; *Yamamoto, et al.*, 2002], in the Late Pliocene (~2.5 Ma) and the Brunhes/Matuyama transition at ~0.8 Ma [*Chauvin, et al.*, 1990]. Reunion and Mauritius sites are younger than 3.5 Ma and primarily of Brunhes age.

We present our complete data collection in Figure 2.3. The left column shows an equal area display of local field direction, D and I, the center column shows the equivalent VGP positions and the right column shows the D' and I' directions [*Hoffman*, 1984]. D' and I' correspond to local field directions that have been rotated so that the center of the projection is the direction from the predicted GAD field at that site. The use of D', I' coordinates helps to remove the effect of latitudinal differences among sites. PSV and TAF studies require paleomagnetic directions from sites that either have not been subject to post-emplacement tectonic rotation or can be corrected back to their original position and orientation. Sites with uncorrected tectonic rotations are likely to exhibit increased scatter and/or bias in paleomagnetic directions. A significant percentage of paleodirections from two of the four regions investigated here are affected by post-emplacement tectonic rotation (Figure 2.3, green symbols). Multiple studies note regional tectonic rotation over the past 5Myr in Mexico [*Maillol, et al.*, 1997; *Mejia, et al.*, 2005; *Nieto-Obergon, et al.*, 1992; *Uribe-Cifuentes and Urrutia-Fucugauchi*, 1999] and in the South Pacific [*Falvey*, 1978; *Inokuchi, et al.*, 1992; *James and Falvey*, 1978; *Malahoff, et al.*, 1982; *Tarling*, 1967; *Taylor, et al.*, 2000] and one study notes local tilt in Hawaii [*Riley, et al.*, 1999]. Two studies of Mexican volcanics indicate regional counterclockwise rotation [*Ruiz-Martinez, et al.*, 2000; *Soler-Arechalde and Urrutia-Fucugauchi*, 2000], while a third supports tilting due to listric faulting [*Nieto-Obergon, et al.*, 1992]. There is no obvious pattern of overall bias from rotation visible in the paleomagnetic directions or VGP latitudes for the Mexican data. The majority of tectonically rotated sites in the South Pacific sub-region result from counterclockwise rotation of the Fiji platform. This is apparent in the nearly 20° westerly rotation in

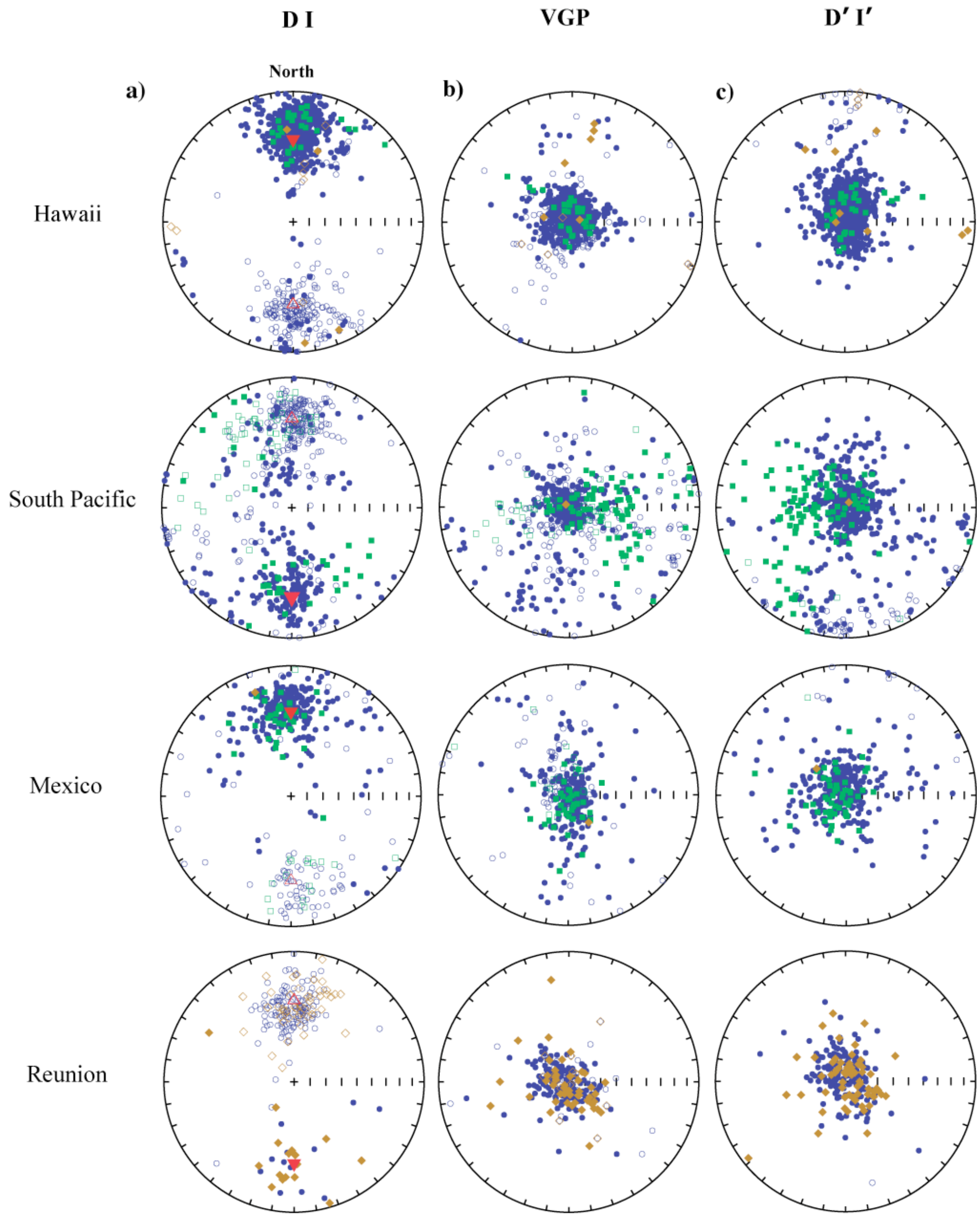

Figure 2.3: Equal area plots of (a) declination (D) and inclination (I), (b) virtual geomagnetic pole (VGP), and (c) D' I'. North is 0° declination. In (c) the paleomagnetic directions are rotated such that the expected direction from a geocentric axial dipole (GAD) field is at the center of the projection and reversed polarity sites are mapped into their antipodal directions [*Hoffman*, 1984]. Solid (open) blue circles represent sites with no tectonic rotation and projected onto upper (lower) hemisphere, solid (open) green squares are upper (lower) hemisphere sites affected by tectonic rotation. Solid (open) brown diamonds are sites with n < 3. The GAD direction is represented by the red triangle.

magnetic directions from GAD, and in the corresponding longitudinal bias in VGPs. For the South Pacific compilation we examined studies from a wide longitudinal range to maximize the temporal distribution of the data. However, all but two sites west of 200°E are excluded because of post-emplacement rotations, so that the South Pacific region sampling is centered at 205°E ± 5°E and is heavily biased towards pre-Brunhes age sites. Few Hawaiian data and no Reunion data are considered tectonically rotated. We exclude from further analysis all sites with uncorrected tectonic rotation; see Table 2.1 for details.

Declination and inclination data from Hawaii cluster around the GAD prediction (red triangle). A negative mean inclination anomaly is present in both the normal and reverse polarity data and appears as a northward elongation of the data distribution in D', I' coordinates. Few transitional directions are recorded, as evidenced by the small percentage of low VGP latitudes. The South Pacific has a highly scattered distribution, a result that could be attributed to preferential sampling of transitional data in French Polynesia. The scatter appears greater to the South in both VGP and D', I'. The Mexican sites suggest a negative mean inclination anomaly, perhaps of smaller amplitude than at Hawaii. The VGP distribution appears elongate in the North-South direction, in contrast to the more circular VGP distribution in the Hawaiian data. The corresponding D', I' plot shows increased scatter to the North compared to the South. Reunion and Mauritius Islands have an approximately 15° NW trend in the VGP distribution and 5° NNW trend in the D', I' distribution.

In PSV studies it is common to select data a priori based on various choices about the number of data, their quality, and the temporal or spatial distribution. Our strategy is more inclusive than most. We discarded sites that are older than 5 Ma, tectonically rotated (green symbols in Figure 2.3), and for which one or more of the following are not reported: declination, inclination, or a measure of within-site dispersion. When multiple results are reported from a single lava flow we average them (Table 2.2). Sites with fewer than 3 samples (brown symbols in Figure 2.3) are eliminated to reduce the effect of orientation error. Apart from these criteria we include all available data in our initial analyses (including transitional directions), and investigate how further data selection criteria affect the results. Table 2.1 reports all studies consulted for the data compilation, along with the numbers of sites from each that are excluded for the reasons listed above. The final number of normal and reverse polarity data used and the mean declination and inclination are given in Table 2.1. Note that we do not distinguish transitional data as a distinct state of the field. Instead all data with positive (negative) VGP latitudes are considered normal (reversed). We retain 80% of the original directions from Hawaii, 57% from Mexico, 70% from the South Pacific and 54% from Reunion.

2.3 Estimates of TAF and PSV

We use our data set to investigate the TAF and PSV at ±20° latitude. We correct each site for plate motion using the model NUVEL 1-A [*DeMets, et al.*, 1994] and our estimate of site age. We convert reverse polarity directions to their normal antipode. This provides sufficient data for statistical analyses, but carries the implicit assumption of symmetry in normal and reverse polarity fields. We then calculate summary statistics for the combined ±20° data set and for each region, to assess whether either the TAF or PSV is anomalous in the Pacific, specifically at Hawaii.

Table 2.2 Averaged or Duplicated Flows Between Studies

	Reference	# of Sites	Site Names	Exclusion & Inclusion Rationale
Mexico	**Xitle Flow**			
	Morales et al., 2001	1	JM	Average all these values.
	Böhnel et al., 1997	1	Xitle	
	Gonzalez et al., 1997	1	S-9	
	Mooser et al., 1974	2	SdC14, SdC15	
	Urrutia-Fucugauchi, 1996	13	All	
	Pelado Flow			
	Morales et al., 2001	1	JB	Use *M et al.*, 2001 because κ of JB > κ of S-10
	Gonzalez et al., 1997	1	S-10	
	Tres Cruces			
	Vlag et al., 2000	1	Mean	Use *V et al.,* 2000 because it has greater *n* than *G et al.*, 1997
	Gonzalez et al., 1997	1	S-6	
Hawaii	**1960AD**			
	Tanaka and Kono, 1991	1	1960AD	Use *C et al.*, 1978 because *T&K*, 1991 don't report κ
	Coe et al., 1978	1	1960AD	
	1950AD			
	Castro and Brown, 1987	1	1950AD	Use *C&B, 1987* because more through demagnetization techniques employed
	Coe et al., 1978	1	1950AD	
	Honolulu Volcanic Series			
	Herrero-Bervera and Valet, 2002	17	All	Use data from *H-B&V, 2002* because it duplicates *D*, *1972c* with modern measurement techniques.
	Doell, 1972c	26	All	
	Napali Formation (Kauai)			
	Bogue, 2001	50	All	Use the sequence of independent flows (Table 2, *B, 2001*) consisting of grouped sites from the studies by *B, 2001* and *B&C, 1984*. *B&P, 1993* is presented in more detail in *B, 2001.*
	Bogue and Paul, 1993	16	All	
	Bogue and Coe, 1984	44	KT1-32 P1-13	
	Koolau Series (Oahu)			
	Doell and Dalrymple, 1973	33	A-G	Use *H-B&V*, 2003 because they have more consistent results than *D&D, 1973.*
	Herrero-Bervera and Valet, 2003	10	All	
	Waianae Series (Oahu)			
	Herrero-Bervera and Coe, 1999	65	All	According to *H-B&V*, 2003 there is no overlap with the Waianae series reported in *L et al.,* 1999. *H-B&V*, 2005 is the only published data from the Upper Mammoth portion of the Waianae series. There could be overlap with *D&D*, 1973 with many of these studies. However, it is very difficult to determine decisively, and to avoid missing data we include all of *D&D*, 1973.
	Herrero-Bervera and Valet, 2003	10	All	
	Laj et al., 1999	105	All	
	Herrero-Bervera and Valet, 2005	45	All	
	Doell and Dalrymple, 1973	46	P-Z	

continued

Table 2.2 (continued)

	Summary	n	ΔD	ΔI	k_u
Mexico	Pelado Flow	13	-8	1	269
	Tres Cruces	9	-21.5	15.3	195.6
	Xitle: Average flow	18	-2.3	-0.6	146.2
Hawaii	1960AD	8	9.1	-1.2	342
	1950AD	127	12.9	-1.6	277
	Honolulu Volcanic Series	17	-1.4	-3.4	116.5
	Napali Formation	45	N/A, multiple flows define series		
	Waianae Series	271	N/A, multiple flows define series		
	Koolau Series	10	N/A, multiple flows define series		

The summary statistic used to characterize the TAF is the inclination anomaly (ΔI), while for PSV we estimate VGP dispersion (S_B). The inclination anomaly (ΔI) and the declination anomaly (ΔD) are defined as follows:

$$\Delta I = I_{obs} - I_{GAD} \tag{2.1}$$

$$\Delta D = D_{obs} - D_{GAD} \qquad (2.2),$$

where I_{obs} and D_{obs} are the observed site inclination and declination, and I_{GAD} and D_{GAD} are the predictions of the geocentric axial dipole field. Inclination anomaly as defined by equation 1 is appropriate for a single site, however we want ΔI for the average direction of multiple sites ($\overline{\Delta I}$), which is not simply the average of multiple measurements of ΔI. First, paleomagnetic directions are rotated to D' and I' to account for dipolar latitudinal variations, then the vector average is calculated and rotated back to inclination which is used to compute the average inclination anomaly of a group of measurements, $\overline{\Delta I}$.

A property often used to analyze the PSV is angular dispersion of VGPs, *S,* defined by,

$$S = \sqrt{\sum_{i=1}^{N} \frac{\Delta_i^2}{N-1}} \quad (2.3),$$

where each i represents a site, Δ_i is the angle between the i^{th} VGP latitude and the spin axis and N is the total number of sites. The total angular dispersion, *S,* is a combination of between-site dispersion (S_B), attributable to PSV, and within-site dispersion (S_W) arising from uncertainty in the paleomagnetic direction for the site. Since these are independent we can write $S^2 = S_W^2 + S_B^2$. We are interested in the between-site dispersion given by

$$S_B = \sqrt{\frac{1}{N-1} \sum_{i=1}^{N} \left(\Delta_i^2 - \frac{S_{w_i}^2}{\bar{N}_{S_i}} \right)} \quad (2.4).$$

$\bar{N}_S$ is the average number of samples per site. The within-site VGP dispersion is approximated by

$$S_w \approx \frac{81°}{\sqrt{\kappa}} \quad (2.5).$$

Most published studies include k, an estimate of κ, and the 95% confidence (α_{95}) circle for all sites. Where only α_{95} is reported we calculate k using

$$\alpha_{95} \approx \frac{140°}{\sqrt{kN}} \quad (2.6),$$

where N is the number of samples per site. Although this approximation fails when $k \leq 25$ [*Tauxe, et al.*, 1991] such sites have poorly defined directions. We will see later that they would normally be rejected from our analyses. Confidence intervals on S_B and $\overline{\Delta I}$ can be calculated using a bootstrap method [*Tauxe*, 1998] .

Before we can make a sensible assessment of PSV and the TAF, two issues need to be addressed; what are the effects of data quality and of transitional sites on estimates of the statistics defined above? Transitional data are typically excluded on the grounds that reversals and excursions are not part of normal PSV. However, this choice clearly affects the resulting PSV [e.g. *Vandamme*, 1994] and TAF estimates. It is also known that data quality affect estimates of TAF and PSV. For example, selection criteria based on κ or α_{95} have been used in compiling PSV data sets [*Johnson and Constable*, 1995; *Lee*, 1983; *McElhinny, et al.*, 1996b; *Quidelleur, et al.*, 1994]. More recently, *Tauxe et al.* [2003] concluded that data quality had a significant effect on estimates of dispersion. Here we examine how transitional sites and data quality influence estimates of the TAF and PSV.

2.3.1 Influence of Data Quality

We use the within-site estimate for Fisherian kappa as a measure of data quality. There are two distinct estimates of kappa that we will employ in the rest of our analyses. To investigate the effect of data quality on estimates of PSV we wish to study how an unbiased estimate of S_B varies as a function of κ. The statistic,

$$k_u = \frac{N-2}{N-R} \tag{2.7}$$

is an unbiased estimate for κ [*McFadden*, 1980]. From equation (2.4) it is apparent that to obtain an unbiased estimate of S_B one needs an unbiased estimate of S_W. Since S_W^2 varies as $1/\kappa$ (equation (2.5)) we need an unbiased estimate for $1/\kappa$. We use the estimator $1/k_f$, where *McFadden* [1980] defines k_f as

$$k_f = \frac{N-1}{N-R} \tag{2.8}$$

k_f is the estimate of κ typically used in paleomagnetic literature. In cases where sample numbers are large, the difference between equations (7) and (8) is minimal. Many of the sites we use in our study only have three samples, which could have significant impact on the κ cut-off criterion used for analyzing the effects of data quality. Therefore, when investigating how S_B and $\overline{\Delta I}$ vary as a function of κ, we will use k_u, the unbiased best estimate for κ.

The effect of data quality on estimates of S_B (PSV) and $\overline{\Delta I}$ (TAF) is shown in Figure 2.4. For a specific value of k_u, denoted by $k_u^{cut-off}$ (data quality) we exclude sites with k_u less than $k_u^{cut-off}$ and calculate S_B and $\overline{\Delta I}$ for the remaining sites. Larger values of $k_u^{cut-off}$ correspond to increasingly stringent data quality requirements. A clear choice concerning data quality would correspond to a value of $k_u^{cut-off}$ above which estimates of S_B and $\overline{\Delta I}$ are stable, yet both S_B and $\overline{\Delta I}$ are fairly smooth functions of $k_u^{cut-off}$ (Figure 2.4). S_B has an average value that decreases from 24° to 18° as $k_u^{cut-off}$ increases from 0 to 500, and $\overline{\Delta I}$ has an average value increasing from -5.1° to -2.5°. The absence of a stable estimate for S_B and $\overline{\Delta I}$ at the largest values of $k_u^{cut-off}$ is a consequence of insufficient data. As has been noted in many previous studies, at the lowest values of k_u (less than ~ 40) estimates of S_B are unreliable.

For $k_u^{cut-off}$ values between 0 and 200 there is a range in VGP dispersion of only 4° and a change in $\overline{\Delta I}$ of ~ ½°. For simplicity, we choose to exclude rather than downweight low quality data. Based on Figure 2.4 we select a value of 100 for $k_u^{cut-off}$, meaning that we exclude all sites with k_u less than 100 from further analyses. This retains a balance between number and quality of data and is consistent with previous studies such as *Tauxe et al.* [2003].

2.3.2 Influence of Transitional Data

One of the major problems that plagues paleomagnetic field analyses is how to define and treat transitional data. Typically, transitional data are defined as measurements with absolute value of VGP latitude less than 45°, and are excluded from estimates of PSV and the TAF. The arbitrariness of this criterion is highlighted by several studies [*Clement*, 2000; *Coe, et al.*, 2000] showing that by this definition the apparent length of a reversal varies substantially with location. *Vandamme* [1994] proposed a technique that iteratively identifies a critical VGP latitude for transitional data, to produce an estimate for S_B, but this method assumes that there is a clearly identifiable distinction between normal and transitional data. We analyze S_B and $\overline{\Delta I}$ as functions of VGP latitude (λ_{VGP}) cut-off, using the data quality criterion discussed above (Figure 2.5). S_B

changes gradually as a function of λ_{VGP}, and there is no clear distinction between stable polarity and transitional data. S_B has a maximum value of 24° when all sites are included, a value of 15° when λ_{VGP} equals 45° and drops off rapidly for λ_{VGP} greater than 70°. Estimates of S_B (and ΔI) for λ_{VGP} greater than 70° are unreliable, since they will exclude a significant fraction of sites exhibiting typical field variability during a stable polarity chron. As with VGP dispersion, inclination anomaly is most stable for λ_{VGP} between 20° and 65° and has an average value of -4°. Similar analyses and conclusions were presented by *Shibuya et al.* [1995] and *Tauxe et al.* [2003].

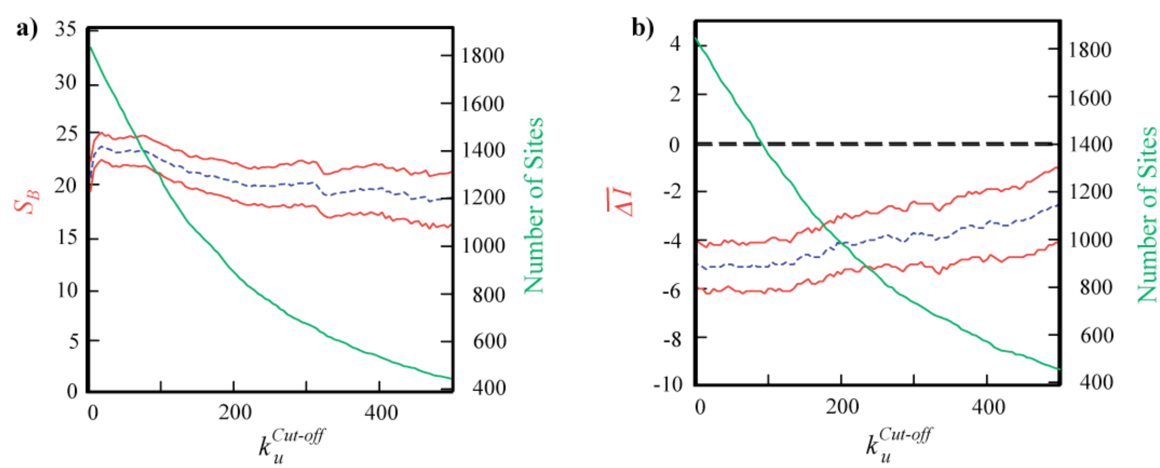

Figure 2.4: Combined data set: a) VGP dispersion (S_B), b) mean inclination anomaly ($\overline{\Delta I}$) as functions of $k_u^{cut-off}$ (see text for a discussion of k_u versus κ). Blue dashed line is the average value, the solid red lines represent the 95% confidence interval and the solid green line is the number of sites as a function of $k_u^{cut-off}$.

The results shown in Figure 2.5 show no clear delineation between transitional and non-transitional data. Consequently, truncating the data by arbitrarily defining some directions as "transitional" is ill advised. It may be particularly problematic when considering smaller spatial or temporal subsets of the data, which fail to sample the field adequately. If transitional data are to be incorporated in analyses then the number of transitional sites included must represent the equivalent duration of time the field spent in transition. In this study there are 97 data sites with an absolute value of λ_{VGP} less than 45° which is ~8% of the entire data set (with k_u > 100). Over the past 5 Myr the field has reversed 10 times [*Cande and Kent*, 1995] with an average reversal duration of 6 kyr [*Constable*, 2003]; one would infer that the field spends about 1% of the time in transition. At face value this suggests that we have a sampling bias towards transitional data in our data set, but the situation is more complex. Excursions during the Brunhes are becoming increasingly well documented, and there are probably between 10 and 20 of these [*Langereis, et al.*, 1997; *Lund, et al.*, 1998; *Lund, et al.*, 2001]. By their very nature excursions correspond to VGP directions that lie far from the geographic axis. If we estimate the average excursion length at half that for a reversal (i.e., 3 kyr) and suppose that 10 excursions and one transition occurred since 800 kyr, then the expected percentage of directions with $\lambda_{VGP} < 45°$ rises to 4.5%. Longer duration excursions or more of them could plausibly raise the expected percentage of data with $\lambda_{VGP} < 45°$ as high as that found in our data set. Nevertheless, it is clear that temporal sampling is non-uniform among the various regions. In particular the prevalence of data from the Matuyama-Brunhes and Gauss-Matuyama transitions (totaling 20% transitional sites) in the South Pacific dataset indicate that those transitions are over-represented, while other time intervals that might be expected to contain excursions are under-represented.

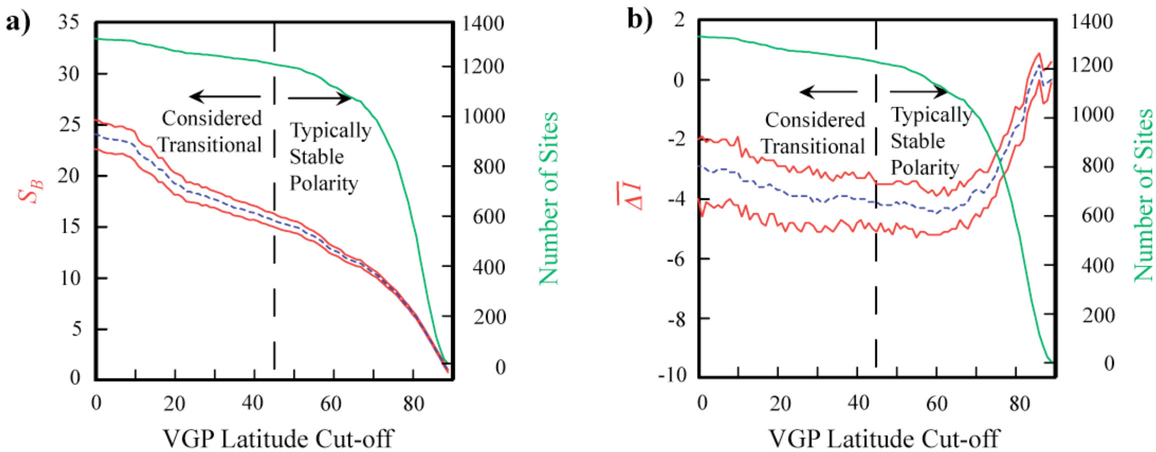

Figure 2.5: Combined data set: a) VGP dispersion (S_B) and b) mean inclination anomaly ($\overline{\Delta I}$) as functions of VGP latitude cut-off (λ_{VGP}). Blue dashed line is the average value, the solid red lines represent the 95% confidence interval and the solid green line is the number of sites as a function of cut-off. The sites used in calculating S_B and $\overline{\Delta I}$ for λ_{VGP} have values of $k_u > 100$.

With a more comprehensive and accurately dated data set, it might be possible to explore the influence of temporal sampling, and what happens with the appropriate representative sampling of transitions. This is not possible with the current data. However, we can compare the Brunhes data with those from earlier epochs, namely the Matuyama, Gilbert and Gauss chrons (here designated non-Brunhes). The merging of the non-Brunhes data is necessary to provide large enough data groups. The dispersions in the Brunhes are consistently smaller than for non-Brunhes data, except for Mexico, where they are indistinguishable (Figure 2.6). The 95% confidence intervals at Reunion overlap for the two time periods, but Hawaii and the combined data set are significantly different. The mean inclination anomalies are also smaller during the Brunhes than during non-Brunhes periods. Again, Mexico has equivalent mean values and the 95% confidence intervals for Reunion overlap. These results indicate that the TAF is closer to GAD and that there is less SV during the Brunhes than during the polarity intervals prior to the Brunhes. Most importantly, these results seem robust even when considering possible bias from the South Pacific. Although there are no data for the Brunhes in our South Pacific group, data from Easter Island (at 27°S) offer some support for the observation of lower dispersion during the Brunhes [*Brown*, 2002; *Miki, et al.*, 1998].

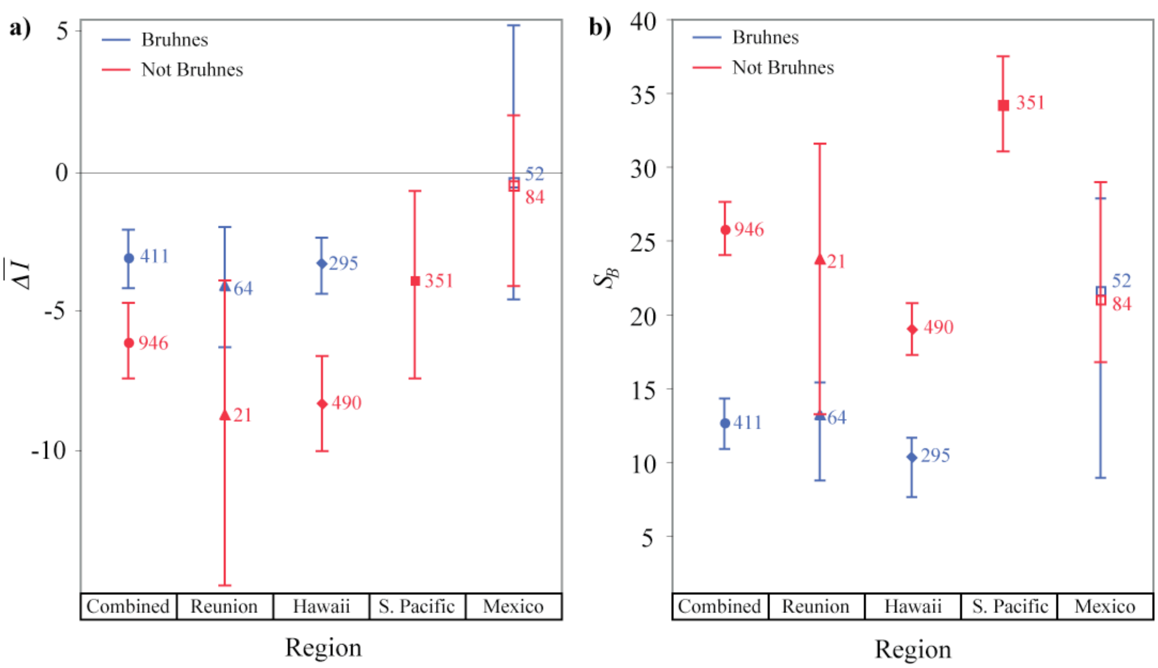

Figure 2.6: Brunhes (0-0.78 Ma) (blue) versus older (0.78 – 5.0 Ma) (red) a) inclination anomaly ($\overline{\Delta I}$) and b) dispersion (S_B) estimates for the combined data set (dot), Hawaii (diamond), Mexico (open square), Reunion (triangle), and the South Pacific (solid square). Data having a kappa < 100 are excluded. The error bars represent 95% confidence intervals. Each point is labeled with the number of data points used to calculate that value.

2.3.3 Regional Variations in Field Behavior

We are now in a position to assess the time-averaged field and paleosecular variation on a regional level. We use ΔI as a measure of departure of the TAF from GAD and S_B as a measure of PSV, and present regional and combined data results in Table 2.3. Non-zero time-averaged declination anomalies have been used to argue for persistent longitudinal structure in the TAF [*Gubbins and Kelly*, 1993; *Johnson and Constable*, 1995, 1997; *Kelly and Gubbins*, 1997; *Love and Constable*, 2003] , we focus here on the time-averaged inclination anomaly. In contrast to some previous studies [e.g. *Johnson and Constable*, 1995], time-averaged declination anomalies for the four regions studied here are small (typically less than 1°). In addition, inclination information is available for sediment cores; the same is not true of absolute declination information. Although we do not consider such data sets in detail here, our results will be useful for future comparisons of lava flow and sediment data sets. Our null hypothesis is that both PSV and any departures from GAD in the TAF are axisymmetric and only exhibit latitudinal signatures. Following the results of Sections 2.3.1 and 2.3.2 we reject all data with k_u < 100, and calculate statistics, first for all remaining data, and then excluding those with $|\lambda_{VGP}| < 45°$ which we label as transitional. Reunion and Hawaii have angular dispersions (16.4°) that are smaller than other regions, but the uncertainties overlap with those from the estimates of dispersion for Mexico. The South Pacific has the largest angular dispersion (34.4 ± 3.0°), and is significantly different from other study localities. Hawaii has the largest average inclination anomaly (-6.3 ± 1.0°), distinctly larger than that at Mexico (-0.4 ± 2.9°). However, within uncertainties, $\overline{\Delta I}$ for Hawaii does not differ from Reunion or the South Pacific. The combined ±20° data set has an average inclination anomaly of -5.1° and an angular dispersion of 22.7°.

We note here that plate motion corrections contribute only a 0.1° change in estimates of inclination anomaly for the combined 20° data set and less than 0.5° change to VGP dispersion estimates. Approximately 25% of our data set is from studies published before 1980, and might not have received adequate laboratory cleaning by modern standards. If we were to perform the same analysis using data only published after 1980 the results are unchanged within the confidence intervals, except for S_B, the dispersion for Hawaii and the combined data set. This is a result of different temporal sampling in the post-1980 data, which sample 70% less of the Matuyama polarity chron than the entire collection. This results in a decreased dispersion for Hawaii and therefore the combined data set.

When transitional data are excluded, there are only small changes in $\overline{\Delta I}$ except for the South Pacific region, which shows a slightly positive average inclination anomaly (0.6 ± 2.2°). All dispersion estimates decrease as one would expect, and the confidence

Table 2.3 Regional Property Results For Sites With $k_u > 100$

	Hawaii	Mexico	Reunion	South Pacific	Combined
N	785	136	85	351	1357
$\overline{\Delta I}$	-6.3 ± 1.0°	-0.4 ± 2.9°	-5.2 ± 2.4°	-3.7 ± 3.4°	-5.1 ± 1.0°
S_B	16.4 ± 1.3°	21.1 ± 4.4°	16.4 ± 3.9°	34.4 ± 3.0°	22.7 ± 1.4°
$N_{\|VGP\| > 45}$	766	132	84	280	1262
$\overline{\Delta I}_{\|VGP\| > 45}$	-6.5 ± 1.2°	-2.9 ± 2.1°	-4.9 ± 2.3°	0.6 ± 2.2°	-4.4 ± 0.8°
$S_{B\ \|VGP\| > 45}$	14.6 ± 0.7°	16.2 ± 2.0°	14.4 ± 2.0°	17.7 ± 1.5°	15.6 ± 0.6°

$\overline{\Delta I}$ is average inclination anomaly, S_B is angular dispersion. |VGP| > 45 indicates statistic was calculated using only sites with $|\lambda_{VGP}| > 45°$.

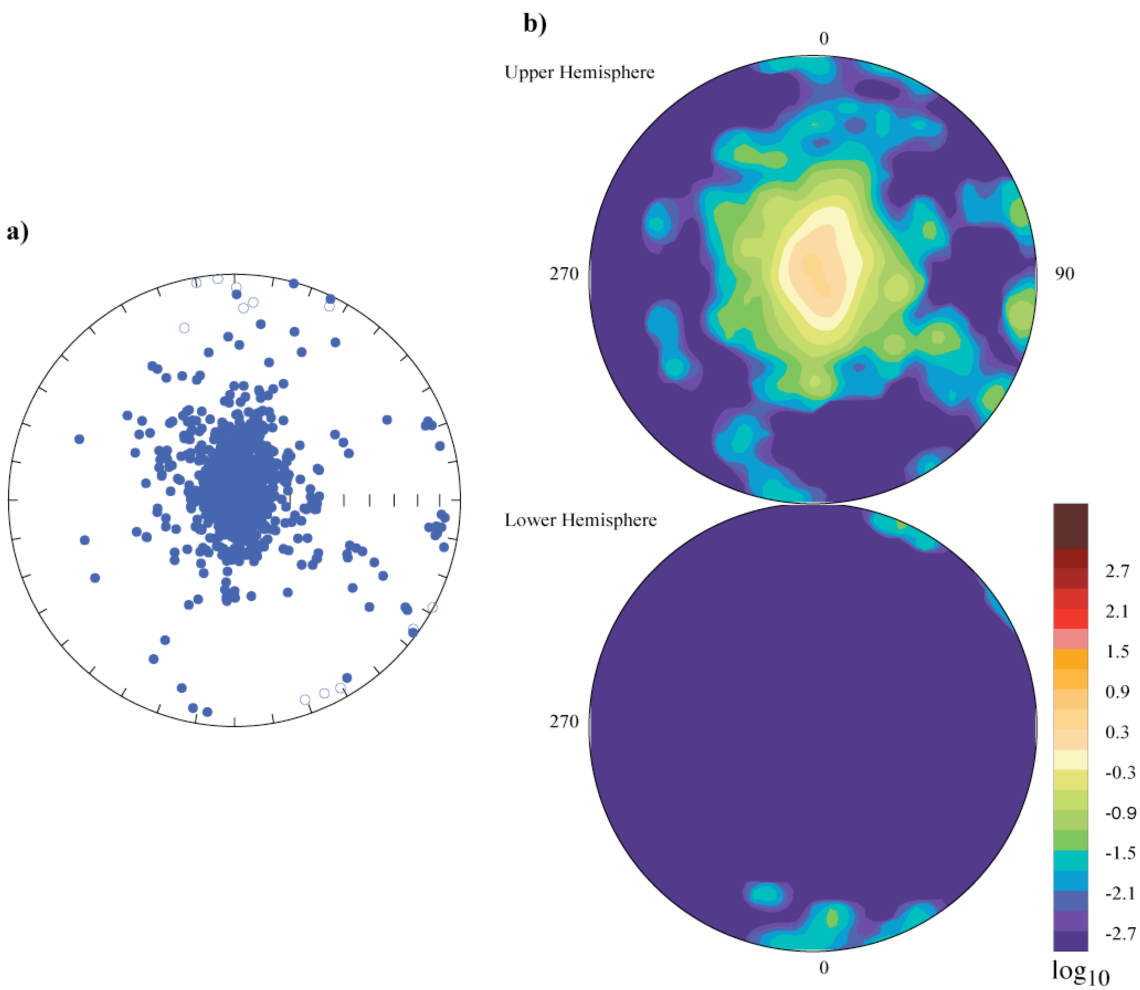

Figure 2.7: a) Equal area projection of D', I' for the combined data set corrected for plate motions and selected using the following criteria: age < 5 Ma, n > 2, k_u > 100 and no tectonic rotation post-emplacement. **b)** 2-D empirical PDF of the data shown in a). Color scale is logarithmic.

limits tighten accordingly. Hawaii still has the smallest mean dispersion, and it becomes measurably different from that at both Mexico and the South Pacific, but not Reunion. The South Pacific and the combined data sets have much reduced dispersion. This is due to large number of transitional directions from the South Pacific: they make up 20% of that region's data. The angular dispersion for the combined ±20° data set is 15.6 ± 0.6° when transitional data are excluded. This is comparable with estimates made by *McElhinny and McFadden* [1997] for globally distributed data at this latitude.

2.4 Time Averaged Field and Paleosecular Variation Models

We turn now to a more detailed evaluation of the statistical distributions of our observations and comparisons with distributions predicted from two current paleosecular variation models. The observed D' and I' for the combined ±20° directions are shown in Figure 2.7a, however the large number of data conceals details of field behavior. An empirical probability density plot (Figure 2.7b) exposes more structure in the distribution, which is elongated in the North-South direction, and shows considerable scatter. Structure in Figure 2.7 reflects both the time-averaged field and paleosecular variation.

The density distribution in Figure 2.7b gives a clear idea of the shape of the data distribution, but it is not suitable for testing whether the data are compatible with predictions from a particular statistical model for PSV, or detecting small differences among such models. We use one-dimensional distributions of declination and inclination data and the 2-sample Kolmogorov-Smirnov (K-S) test [*Press, et al.*, 1992] to assess whether the observations are compatible with the distributions of simulations of D and I from specific models. We apply the K-S test directly to D and I, since we can use our statistical models to predict directions at the same latitudes and longitudes as our data. The D and I directional distributions of our data are shown in Figure 2.8 as both 2-D (2.8a) and 1-D (2.8b) probability density functions. Figure 2.8a provides the visual link between the 2-D PDF for D' and I' (Figure 2.7b) and the 1-D PDFs for D and I (Figure 2.8b and 2.8c). The 1-D PDF of declination has a single peak at 0°. Inclination shows two peaks, at approximately ±40°, representing the normal polarity inclination of Northern and Southern hemisphere sites, respectively. In Figure 2.8a these peaks occur in the upper and lower hemispheres, respectively. Recall that reverse polarity sites have been mapped to their antipodal directions.

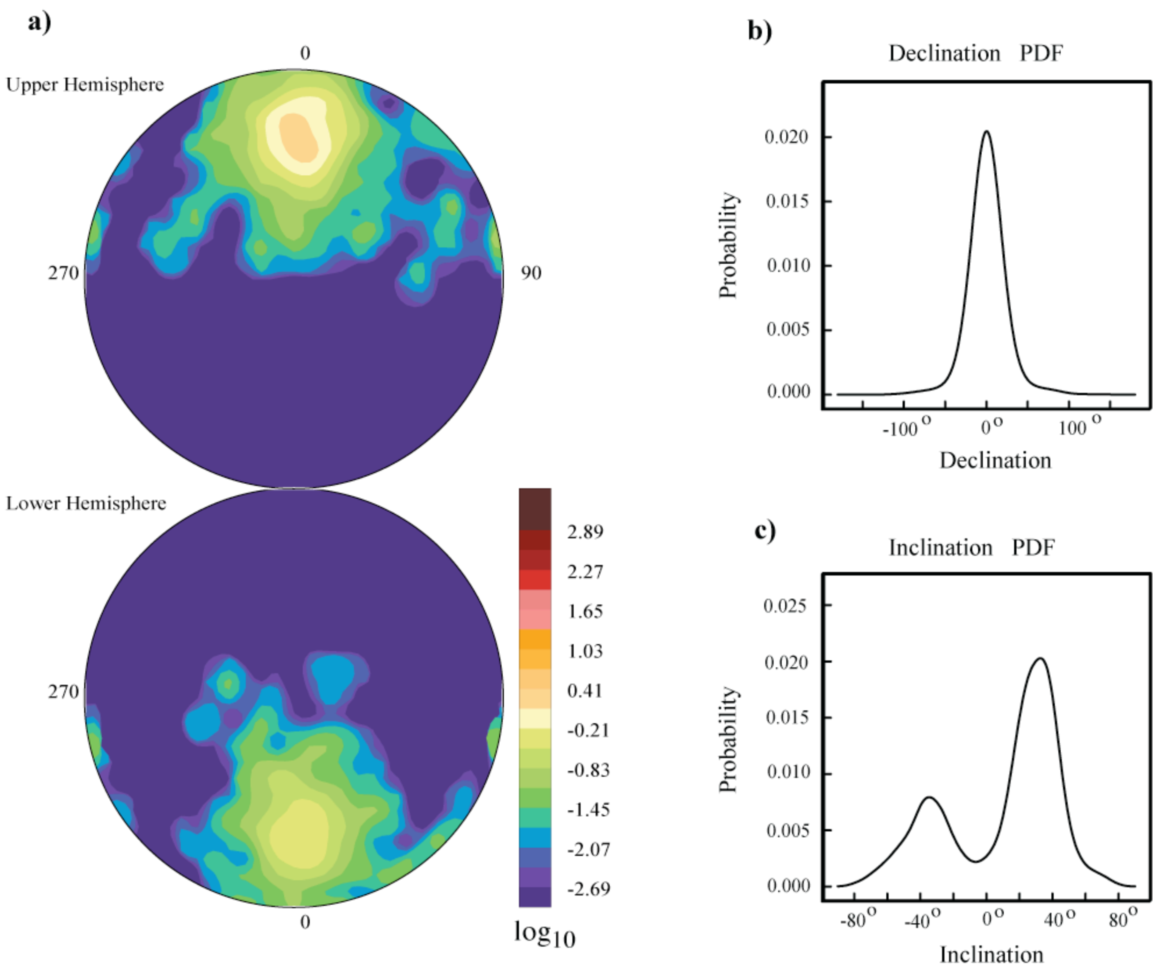

Figure 2.8: a) 2-D empirical PDF of D, I for the ±20° data set shown in Figure 2.6. Color scale is logarithmic. **b)** 1-D empirical PDF of D and **c)** I for the same data set. All reverse polarities have been flipped to their antipodes using VGP latitude as a determinant of polarity.

2.4.1 PSV Model Formulation

We compare observed paleomagnetic directions with simulations from PSV models proposed by *Constable and Johnson* [1999], CJ98, and *Tauxe and Kent* [2004], TK03. These models are based on a statistical approach to paleosecular variation initiated by *Constable and Parker* [1988] who produced a PSV model, that we label CP88. The geomagnetic field is described by a spherical harmonic expansion in which the scalar magnetic potential due to an internal field generated at the core is given by

$$\Psi\left(r,\theta,\phi\right)=a\sum_{l=1}^{\infty}\sum_{m=0}^{l}\left(\frac{a}{r}\right)^{l+1}\left(g_l^m\cos m\phi+h_l^m\sin m\phi\right)P_l^m\left(\cos\theta\right) \qquad (2.9),$$

where a is Earth's radius, r is radius, θ is colatitude, ϕ is longitude, l and m are harmonic degree and order, P_l^m are partially normalized Schmidt functions, g_l^m and h_l^m are the Gauss coefficients representing the field model. Specifically, g_1^0 is the axial dipole term, while g_2^0 and g_3^0 are the axial quadrupole and axial octupole terms, respectively. *Constable and Parker* [1988] proposed that a giant Gaussian process can represent PSV. The spherical harmonic coefficients g_l^m and h_l^m are assumed to be temporally independent random variables with Gaussian distributions having means (μ) and variances (σ) described by,

$$\mathcal{G}_l^m \sim N\left(\mu_{g_l^m},\sigma_{g_l^m}\right) \qquad (2.10)$$

and

$$\mathcal{H}_l^m \sim N\left(\mu_{h_l^m}, \sigma_{h_l^m}\right). \tag{2.11}$$

In general, the means and variances can vary with both spherical harmonic degree and order. Although the specific model parameters used for CP88 are now considered inappropriate to describe the 0-5 Ma PSV, the basic formalism has been widely used. CJ98 and TK03 are both zonal models, modifications of CP88 proposed to explain latitudinal variation of S_B, but using distinctly different philosophies. CJ98 satisfies S_B variations by imposing increased variance in the l=2, $m=1$ terms putting excess energy into PSV at degree 2. TK03 preserves part of Constable and Parker's original conceptual model in the form of a white spatial power spectrum at the core-mantle boundary, by assigning different variances to the dipole (*l-m* odd) and non-dipole (*l-m* even) terms. This effectively identifies a different behavior for equatorially symmetric and anti-symmetric contributions to the field [for more on this see *Hulot and Bouligand*, 2005]. Two further characteristics differentiate TK03 and CJ98: TK03 has a lower mean for g_1^0 than CJ98 and thus fits recent estimates of the observed mean field strength [*Selkin and Tauxe*, 2000]; CJ98 has a small average axial quadrupole term, whereas in TK03 all the Gauss coefficients except g_1^0 have zero mean.

2.4.2 Time Averaged Field

As noted above the statistical PSV models require estimates of the time averaged-field ($\mu_{gl}^{\ m}$ and $\mu_{hl}^{\ m}$). Previous PSV models have either used GAD [*Tauxe and Kent*, 2004] or GAD plus an axial quadrupole contribution [*Constable and Johnson*, 1999;

Constable and Parker, 1988]. The average field plays an important role when comparing data with PSV models. Here we investigate a range of TAF models that are compatible with our observations. We restrict ourselves to zonal models to avoid unnecessary complications, noting that average declination anomalies within each region are less than a degree, while keeping in mind that the differences in inclination anomalies may yet demand non-zonal structure in the TAF. If we attribute our average inclination anomaly for the combined data set to a dipole plus quadrupole field the g_2^0 term required is approximately 10% of the g_1^0 term. This is a larger quadrupole contribution to the paleomagnetic field than previously suggested [see *McElhinny*, 2004 for a review] and is mainly controlled by the sizeable negative inclination anomaly at Hawaii. To ensure that our estimate of the TAF is compatible with other high quality data sets we compile additional data that allow us to model the time averaged latitudinal variation in inclination (Figure 2.9). We then investigate the misfit of models that include g_1^0, g_2^0, and g_3^0 terms to these data.

The variation of inclination anomaly with latitude for our data compilation is shown in Figure 2.9. We supplement our ±20° data set with the highest quality data present in the global database of *McElhinny and McFadden* [1997] (Demag level 4). We also include data collected as part of the Time-Averaged Field Investigations (TAFI) project [*Johnson, et al.*, 2005]. TAFI data are from sites in: the Aleutians [*Stone and Layer*, 2005], British Columbia [*Mejia, et al.*, 2002], the Snake River Plain [*Tauxe, et al.*, 2004b], San Francisco Volcanics [*Tauxe, et al.*, 2003], Costa Rica (in preparation), Chile ([*Brown, et al.*, 2004b] and Brown (personal communication, 2005)), Argentina [*Brown,* *et al.*, 2004a; *Mejia, et al.*, 2004], Ecuador [*Opdyke, et al.*, 2006], Australia [*Opdyke and Musgrave*, 2004], Antarctica [*Tauxe, et al.*, 2004a], the Azores [*Johnson, et al.*, 1998], and the Canaries [*Tauxe, et al.*, 2000]. Data from the ±20° data set, and the TAFI sites supercede and replace those from *McElhinny and McFadden* [1997] in our compilation. For consistency with the data compiled by *McElhinny and McFadden* [1997] we exclude all data with VGP latitudes less than 45°. While this is not a complete global data set, it provides a reasonable latitudinal data distribution with which to investigate zonal TAF field models.

We investigate the misfit of TAF models to our data for varying contributions from g_2^0 and g_3^0, relative to g_1^0. For given values of G2 = (g_2^0/g_1^0) and G3 = (g_3^0/g_1^0) terms we calculate the corresponding inclination anomalies at our data locations. We compute the root mean-square (RMS) misfit of the predicted to observed inclinations using

$$RMS = \sqrt{\frac{1}{N}\sum_{i=1}^{N}\left(I_{obs} - I_i\right)^2} \;. \tag{2.12}$$

Figure 2.10 shows contours of RMS misfit for TAF field models where g_1^0 is set to -1.0 and the g_2^0 and g_3^0 contributions vary from 0 to ± 0.5. The best-fit model has G2 = 0.04 and G3 = 0.06 (black dot in Figure 2.10) and an RMS misfit of 13.8°. The RMS misfit of GAD (black star in Figure 2.10) is 14.7°. Predicted inclination anomalies for various TAF models are also shown in Figure 2.9. It is clear that the latitudinal distribution of data affects estimates of G2 and G3, for example improved sampling at low latitudes would better constrain the bounds on G2.

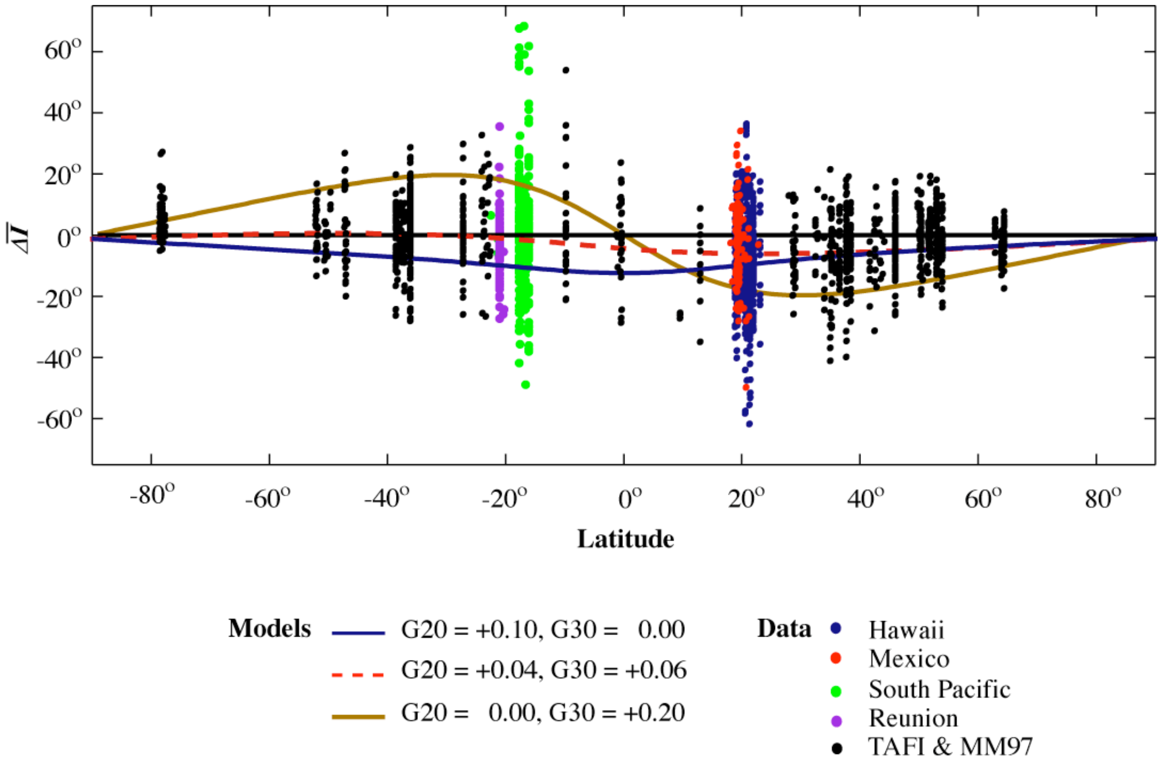

Figure 2.9: Inclination anomaly ($\overline{\Delta I}$) as a function of latitude for data from each region of this study, Hawaii (blue), Mexico (red), South Pacific (green), Reunion (purple), and *McElhinny et al.* [1997] and TAFI data sites [*Johnson, et al.*, 2005] that passed data selection criterion (black). Models of the TAF for illustrative combinations of g_2^0 and g_3^0 are also shown. Specifically, the best-fit model for all data sites is shown in dashed red.

2.4.3 Tests of PSV Models

We now examine whether existing zonal PSV models can be made to fit our new ±20° data set with an appropriate TAF. We use statistical models CJ98 and TK03 and prescribe two distinct TAFs, either GAD or G2 = 0.04 and G3= 0.06 as derived in the previous section. We generate data at the same locations as our paleomagnetic sites. We simulate one sample per site and assign within-site κ equivalent to that reported at each site in the observed data set. We compare our models with the data using 1-D empirical PDFs and the corresponding cumulative distribution functions (CDFs) for declination and inclination. We assess the model fit using the 2-sample K-S test for inclination and a slightly modified K-S test for declination, which exploits the Kuiper statistic, a more robust test of data that are circularly distributed [*Press, et al.*, 1992].

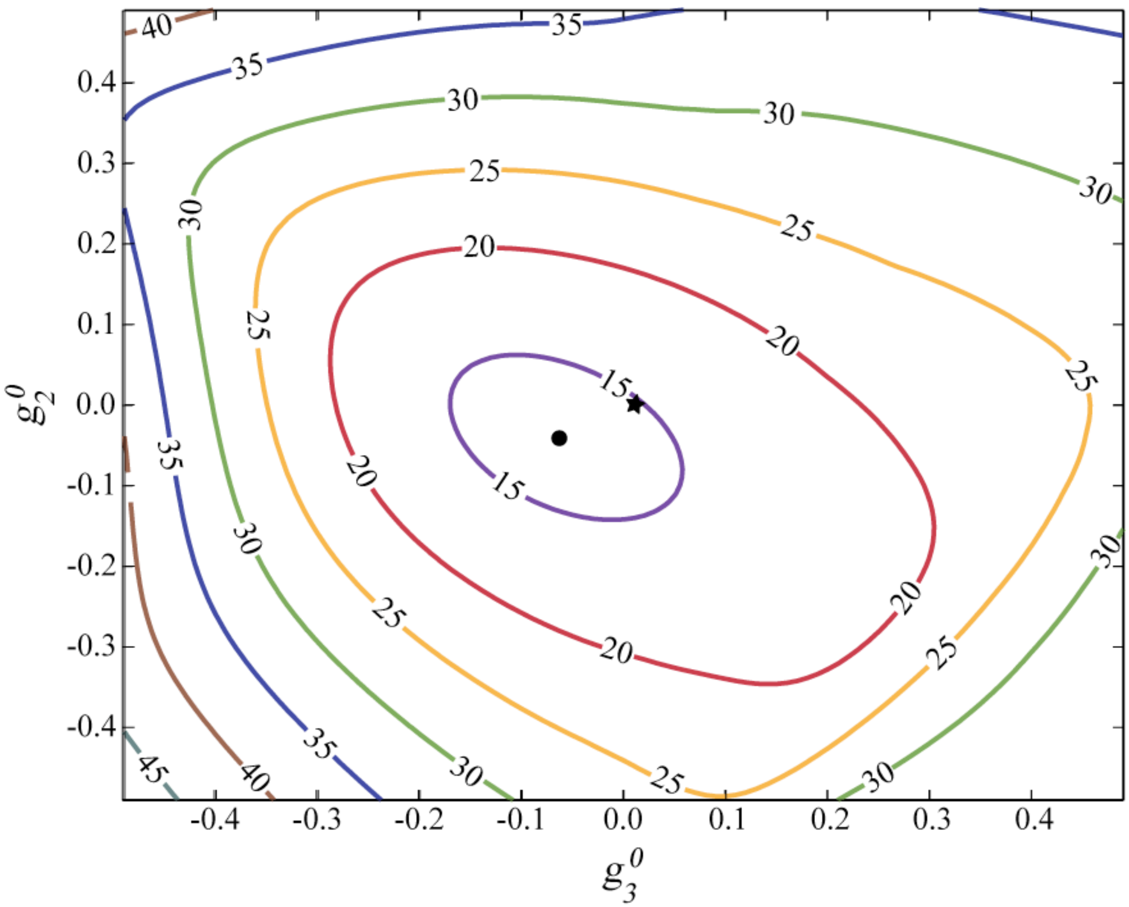

Figure 2.10: Contour plot of RMS misfit of inclination anomaly using data compiled from our ±20° data set, the TAFI data set [*Johnson, et al.*, 2005] and the McElhinny database [*McElhinny and McFadden*, 1997], see text for complete references and data descriptions. Axes are values of gauss coefficients, g_2^0 and g_3^0. g_1^0 has been set to -1.0. The dot represents the best-fit model of g_2^0 = -0.04 and g_3^0 = -0.06 and the star is GAD.

Comparisons of PSV models with our ±20° data are shown in Figure 2.11. For all models and data (black line) the declination PDF is unimodal while the inclination PDF is bimodal since we have both Northern and Southern hemisphere sites. Differences between the observed and predicted inclination distributions are seen in both the CDF and PDF whereas declination differences are seen more easily in the CDF. CJ98 (blue line) appears to predict the mean declination and inclination well, as we might expect, given that we are using our best-fit TAF model. But the model fails when it comes to fitting the shape of the distributions. We quantify this in Table 2.4 using the K-S test. In the K-S test the measure of difference between two distributions is characterized by the statistic d, that measures the maximum distance between sample distribution functions for two data sets. Small values of d correspond to samples from similar distributions.

Associated with the d-statistic is a probability (significance level) that describes the likelihood of getting a d value this large or greater if the underlying distributions are the same. The significance level varies monotonically from 0 to 1, where 1 is a 100% probability. The results of K-S are given for a number of different models in Table 2.4. Neither of the recent CJ98 nor TK03 models is adequate to model the data, although the nature of the mismatch is somewhat different, when our preferred TAF model is used. Declination performs worst for CJ98 and inclination for TK03: for TK03, there is a probability of .00003 of getting such a large mismatch in inclination distributions if it were the correct model and .02 in declination; CJ98 also performs poorly.

One might wonder whether simple modifications to these models would improve the situation, and we did explore this possibility for TK03 by varying β, the ratio of standard deviations in the equatorially symmetric to antisymmetric families of Gauss coefficients. *Tauxe & Kent* [2004] chose this parameter to be 3.8 to satisfy latitudinal variations in VGP dispersion, but another end member model is given by the earlier CP88 model (green line, with $\beta = 1.0$), which essentially exhibits no latitudinal variation. We investigated TK03 type models with β ranging from 1 to 5 in steps of 0.1 and find $\beta = 2.0$ has the best fit to our data (red line). It should be noted, however, that even this best fit has what would generally be regarded as an unacceptable low probability (p= .001) for the declination distribution, and it is unlikely to satisfy the global variations in VGP dispersion. Table 2.4 also indicates that CP88 provides an acceptable fit to inclination but not declination. As β is varied the fit to declination is improved at the expense of inclination. For example, the CP88 model has the highest inclination significance levels but compared to CJ98 and the best fitting model it has the lowest declination significance levels. The best-fit model increases the fit to the declination significantly from CP88 but does not increase the inclination fit. Although β =2.0 provides the best fit to the new 20º dataset, however, none of the models in this family can be considered adequate to represent the directional data distributions.

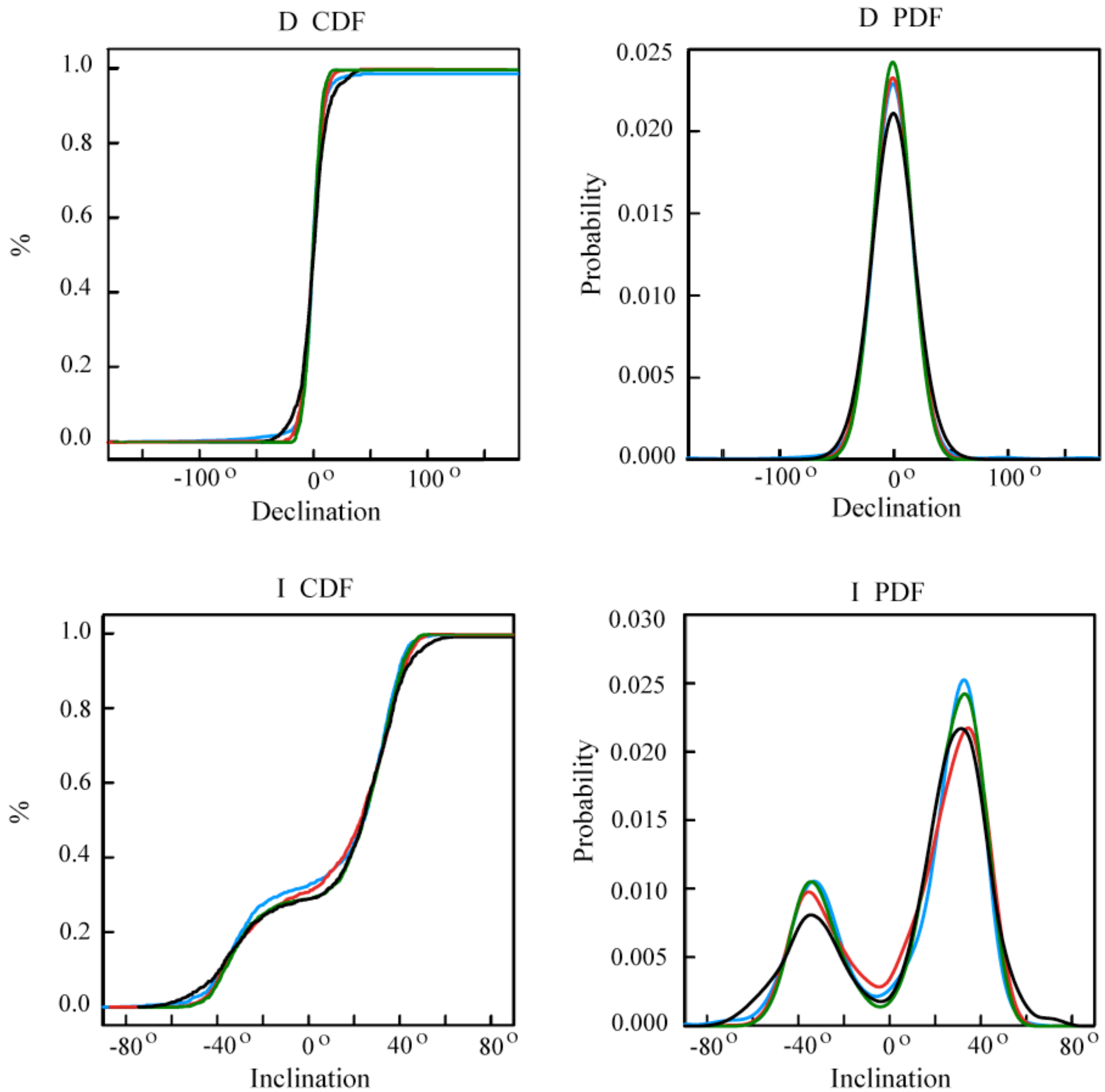

Figure 2.11: Empirical cumulative distribution functions (CDFs) and probability density functions (PDFs) of observed ±20° data (black line) and three PSV models. The CJ98 PSV model with a TAF of G2 = 4% and G3 = 6% is shown in blue. The TK03 model with variations in beta from 1.0 (green) and 2.0 (red) are also shown for the same TAF as used with CJ98.

Table 2.4 Significance Level Results of K-S Test

Significance level	**TAF Model**	**GAD**
CJ98		
Dec.	1.27E-5	5.71E-6
Inc.	0.0541	3.03E-14
CP88		
Dec.	1.71E-8	6.35E-9
Inc.	0.1755	5.86E-15
Best Fit Model		
Dec.	0.0014	0.0009
Inc.	0.1606	1.23E-12
TK03$_{\beta = 3.8}$		
Dec.	0.0217	0.0389
Inc.	2.74E-5	2.96E-14

Model: G2 = 0.04 and G3 = 0.06

2.5 Conclusions

The results presented in Table 2.3 are in agreement with previous studies. We briefly recap the results for each of the TAF and PSV and consider whether these have implications for regional variations in the overall geomagnetic field structure and the nature of its secular variation.

When data from all 4 regions are combined the average inclination anomaly for the ±20° latitude band is -5.1±1.0°, or -4.4±0.8° when transitional data are excluded. The best fitting 2-parameter zonal time-averaged magnetic field model to a global data set containing our newly compiled ±20° data set (but excluding our transitional data for compatibility with the rest of the global data set) has G2 = 0.04, and G3 = 0.06. The value for G2 is consistent with previous studies, while G3 is comparable to that found for reversed polarity continental and igneous rocks. It is, however, larger than that estimated from normal polarity continental and igneous rocks and data from oceanic sediments

[*McElhinny, et al.*, 1996b]. Creer [1983] proposed that the G3 term is overestimated by a few degrees if averages of unit vectors are used in place of the full vector field directions (including field intensity). However, the estimate of G3 we determine is too large to be attributed to this bias.

Within the new data set there are substantial regional differences in inclination anomaly. Hawaii has the largest $\overline{\Delta I}$, and it differs from that found in either the Mexico or South Pacific regions, but is very similar to that from Reunion. Thus the Hawaiian and Reunion data could be explained in terms of a TAF consisting of GAD plus an equatorially symmetric contribution like g_2^0. The distinction in $\overline{\Delta I}$ between Hawaii and Mexico is clear regardless of whether transitional data are included. However, in comparing Hawaii with the South Pacific we find that when the many transitional data from South Pacific are retained, the large angular dispersion renders the almost 3° difference in average inclination anomaly insignificant at the 95% confidence level. This brings up issues about temporal and spatial sampling, which we revisit below. If transitional data are excluded, Hawaii has a TAF, which is distinct from both the Mexico and the South Pacific data sets, raising the possibility of regional differences around the Pacific. The exclusion of transitional data for the South Pacific generates a small positive $\overline{\Delta I}$ for that region, contributing to the relatively large value of G3 in the best-fitting model.

PSV results from our ±20° data set indicate that Hawaii and Reunion exhibit the lowest VGP dispersion. This result does not depend on the inclusion or exclusion of transitional data: exclusion reduces S_B by about 2° in each case. Both Mexico and the

South Pacific have higher VGP dispersion than either Hawaii or Reunion: the 95% confidence intervals for Reunion overlap with those for Mexico and for the non-transitional South Pacific data, but Hawaii is significantly different from both Mexico and the South Pacific regardless of what transitional data are excluded.

Hawaii has long been at the center of debate about low secular variation (SV) in the Pacific region. For the modern and historical field previous discussions have emphasized hemispherical differences in SV at the core-mantle boundary [*Bloxham, et al.*, 1989; *Gubbins and Gibbons*, 2004], while for PSV [e.g. *Shibuya et al.*, 1995], Hawaii has been a representative case of low VGP dispersion for the Pacific hemisphere. Millennial scale field [*Korte and Constable*, 2005] are based on archeomagnetic and lake sediment data sets, which seem to exhibit less high frequency content in the Pacific regions. In this study, we examined three distinct regions within the Pacific hemisphere, and find different results in Hawaii compared with both Mexico (on the Eastern border of the hemisphere), and the South Pacific, which lies well within the region identified as anomalous at the core-mantle boundary in historical field models [*Jackson, et al.*, 2000; *Johnson and Constable*, 1998]. The Hawaiian results are most similar to the Reunion region, which in contrast to the Pacific has high modern SV rates [see for example, *Constable and Korte*, 2006, Figure 2.1]. If we interpret all the differences in $\overline{\Delta I}$ and S_B as being purely geomagnetic in origin this would suggest a more complicated view of geomagnetic paleosecular variation than has been considered so far.

Before we can accept a geomagnetic origin for these results we must consider the effects of sampling bias. The potential biases come from differing numbers and quality of data, and variable temporal sampling, in particular serial correlations and the effects of transitional data. The TAF results are robust with respect to data quality issues (Figure 2.4) and number of data. The inclusion or exclusion of transitional directions (and selection of λ_{VGP} cut-off, Figure 2.5, and Table 2.3) has minimal effect except for the South Pacific. The same cannot be said for S_B, the VGP dispersion due to paleosecular variation. From Table 2.3 we see that the percentages of transitional data at Hawaii, Mexico, Reunion and the South Pacific are 2.5%, 3%, 1%, and 20%, respectively. Hawaii and Reunion have astonishingly few transitional directions. The South Pacific clearly has over-representation of transitional data in some time intervals, because of the inclusion of studies specifically targeting two field transitions, but this may be balanced by a lack of data from excursional intervals during the Brunhes, for example. One further point worth noting is that a larger fraction of the transitional data are excluded by the k_u criterion than of the stable polarity observations highlighting the difficulty of obtaining reliable transitional records at all locations. The relative reduction in our dispersion estimates corresponds to the fraction of transitional data.

The large $\overline{\Delta I}$ at Hawaii is unlikely due to temporal sampling bias, because a similar value is found from three drilled cores on the big island of Hawaii, that span 0-400 ka in total [summarized in *Herrero-Bervera and Valet*, 2003; *Holt, et al.*, 1996; *Laj, et al.*, 2002; *Teanby, et al.*, 2002]. This strongly suggests that the field at Hawaii is indeed unusual over time scales of 0-5 Myr. An immediate consequence of this is that the 2-parameter zonal TAF model is too simplistic, a result that has been noted previously [*Gubbins and Kelly*, 1993; *Johnson and Constable*, 1995]. It is important to remember that a non-zonal TAF field model may be necessary even if there is no mean declination anomaly.

An exploration of statistical models for PSV [*Constable and Johnson*, 1999; *Constable and Parker*, 1988; *Tauxe and Kent*, 2004] shows that none of these are adequate to describe the ±20° data set. This is not a surprise! The prescription of allowed variance in any of these models is somewhat ad hoc and too restrictive. Even after adjusting to an appropriate zonal TAF model for our data, we were unable to simultaneously enforce the correct variance for the distributions of declination and inclination (Figure 2.11 and Table 2.4). Further efforts are clearly necessary to produce a realistic global PSV model.

This data compilation and others like it provide new opportunities for assessing TAF and PSV. Large regional data sets can be used to determine the local TAF departure from GAD, and to study geographical differences in variance of the magnetic field. The ultimate goal is to find a statistical description for PSV that correctly predicts the directional and intensity distributions at any location.

2.6 Acknowledgments

We thank Lisa Tauxe and Victoria Mejia for useful discussions. We also thank David Gubbins and Jean-Pierre Valet for thorough reviews. This work was funded by NSF grant EAR-0337712.

This chapter is a reformatted version with updated references of Lawrence, K.P.; Constable, C.G.; Johnson, C.L (2006), Paleosecular variation and the average geomagnetic field at ± 20° latitude, *Geochemistry, Geophysics, Geosystems*, 7, doi:10.1029/2005GC001181.

2.7 References

Bloxham, J., et al. (1989), Geomagnetic secular variation, *Philosophical Transactions Of The Royal Society Of London Series A-Mathematical Physical And Engineering Sciences*, *329*, 417.

Brown, L. (2002), Paleosecular variation from Easter Island revisited: Modern demagnetization of 1970s data set, *Physics of the Earth and Planetary Interiors*, *133*, 73-81.

Brown, L. L., et al. (2004a), Paleomagnetism and $^{40}Ar/^{39}Ar$ chronology of lavas from Meseta del Lago Buenos Aires, Patagonia, *Geochemistry Geophysics Geosystems*, *5*, doi:10.1029/2003GC000526.

Brown, L. L., et al. (2004b), Paleomagnetic directions and $^{40}Ar/^{39}Ar$ ages from the Tatara-San Pedro volcanic complex, Chilean Andes; lava record of a Matuyama-Brunhes precursor? *Journal of Geophysical Research*, *109*, no.B12, 17.

Cande, S. C., and D. V. Kent (1995), Revised calibration of the geomagnetic polarity timescale for the Late Cretaceous and Cenozoic, *Journal Of Geophysical Research-Solid Earth*, *100*, 6093-6095.

Carlut, J., and V. Courtillot (1998), How complex is the time-averaged geomagnetic field over the past 5 million years? *Geophysical Journal International*, *134*, 527-544.

Chauvin, A., et al. (1990), Records of Geomagnetic Reversals From Volcanic Islands of French Polynesia 2. Paleomagnetic Study of a Flow Sequence (1.2-0.6 Ma) From the Island of Tahiti and Discussion of Reversal Models, *Journal of Geophysical Research*, *95*, 2727-2752.

Clement, B. M. (2000), Assessing the fidelity of palaeomagnetic records of geomagnetic reversal, *Philosophical Transactions - Royal Society. Mathematical, Physical and Engineering Sciences*, *358*, 1049-1064.

Coe, R. S., et al. (2000), An examination of simulated geomagnetic reversals from a palaeomagnetic perspective, *Philosophical Transactions - Royal Society. Mathematical, Physical and Engineering Sciences*, *358*, 1141-1170.

Constable, C. G. (2003), Geomagnetic Reversals: Rates, Timescales, Preferred Paths, Statistical Models, and Simulations, in *Earth's Core and Lower Mantle*, edited by C. A. Jones, et al.77-99, Francis and Taylor.

Constable, C. G., and C. L. Johnson (1999), Anisotropic paleosecular variation models: Implications for geomagnetic field observables, *Physics of the Earth and Planetary Interiors*, *104*, 35-51.

Constable, C. G., and M. Korte (2006), Is the Earth's magnetic field reversing? *Earth and Planetary Science Letters*, *246*, 1-16.

Constable, C. G., and R. L. Parker (1988), Statistics of the geomagnetic secular variation for the past 5 m.y., *J. Geophys. Res.*, *93*, 11569-11581.

Creer, K. M. (1983), Computer synthesis of geomagnetic palaeosecular variations, *Nature*, *304*, 695-699.

DeMets, C., et al. (1994), Effect of recent revisions to the geomagnetic reversal time scale on estimates of current plate motions, *Geophysical Research Letters*, *21*, 2191-2194.

Doell, R. R. (1972a), Paleomagnetism of volcanic rocks from Niihau, Nihoa, and Necker Islands, Hawaii, *Journal of Geophysical Research*, *77*, 3725-3730.

Doell, R. R. (1972b), Paleosecular variation of the Honolulu Volcanic Series, Oahu, Hawaii, *Journal of Geophysical Research*, *77*, 2129-2138.

Doell, R. R., and A. Cox (1971), Pacific geomagnetic secular variation, *Science*, *171*, 248-254.

Duncan, R. A. (1975), Palaeosecular Variation at the Society Islands, French Polynesia, *Geophysical Journal of the Royal Astronomical Society*, *41*, 245-254.

Falvey, D. A. (1978), Analysis of palaeomagnetic data from the New Hebrides, *Bull. Aust. Soc. Explor. Geophys.*, *9*, 177-122.

Gubbins, D., and S. Gibbons (2004), Low Pacific Secular Variation, in *Timescales of the Paleomagnetic Field*, edited by J. E. T. Channell, et al.,145, 320, American Geophysical Union, Washington, D. C.

Gubbins, D., and P. Kelly (1993), Persistent patterns in the geomagnetic-field over the past 2.5 Myr, *Nature*, *365*, 829-832.

Hatakeyama, T., and M. Kono (2002), Geomagnetic field model for the last 5My: Time-averaged field and secular variation, *Physics of the Earth and Planetary Interiors*, *133*, 181-215.

Herrero-Bervera, E., and R. S. Coe (1999), Transitional field behavior during the Gilbert-Gauss and Lower Mammoth reversals recorded in lavas from the Wai'anae volcano, O'ahu, Hawaii, *Journal of Geophysical Research*, *104*, 29,157-129,173.

Herrero-Bervera, E., and J. P. Valet (2003), Persistent anomalous inclinations recorded in the Koolau volcanic series on the island of Oahu (Hawaii, USA) between 1.8 and 2.6 Ma, *Earth And Planetary Science Letters*, *212*, 443-456.

Hoffman, K. (1984), A method for the display and analysis of transitional paleomagnetic data, *Journal of Geophysical Research*, *89*, 6285-6292.

Holt, J. W., et al. (1996), Geomagnetic field inclinations for the past 400 kyr from the 1-km core of the Hawaii Scientific Drilling Project, *Journal Of Geophysical Research-Solid Earth*, *101*, 11655-11663.

Hulot, G., and C. Bouligand (2005), Statistical palaeomagnetic field modeling and symmetry considerations, *Geophysical Journal International*, *161*, 591-602.

Hulot, G., and Y. Gallet (1996), On the interpretation of virtual geomagnetic ple (VGP) scatter curves, *Phys. Earth Planet. Inter.*, *95*, 37-53.

Inokuchi, H., et al. (1992), Clockwise and anticlockwise rotation of Viti Levu, Fiji - in relation to the tectonic development of the North and South Fiji Basin, *Geophysical Journal International*, *110*, 225-237.

Jackson, A., et al. (2000), Four centuries of geomagnetic secular variation from historical records, *Philosophical Transactions - Royal Society. Mathematical, Physical and Engineering Sciences*, *358*, 957-990.

James, A., and D. A. Falvey (1978), Analysis of palaeomagnetic data from Viti Levu, Fiji, *Bull. Aust. Soc. Explor. Geophys.*, *9*, 115-117.

Johnson, C. L., and C. G. Constable (1995), The time-averaged field as recorded by lava flows over the past 5 Myr, *Geophysical Journal International*, *122*, 489-519.

Johnson, C. L., and C. G. Constable (1997), The time-averaged geomagnetic field: Global and regional biases for 0-5 Ma., *Geophysical Journal International*, *131*, 643-666.

Johnson, C. L., and C. G. Constable (1998), Persistently anomalous Pacific geomagnetic fields, *Geophysical Research Letters*, *25*, 1011-1014.

Johnson, C. L., et al. (2005), The Time-Averaged Field Investigation project: A Synthesis, in *American Geophysical Union 2005 Fall Meeting*, edited, Eos, Trans. AGU, San Francisco, CA, United States.

Johnson, C. L., et al. (1998), $^{40}Ar/^{39}Ar$ Ages and paleomagnetism of Sao Miguel lavas, Azores, *Earth and Planetary Science Letters*, *160*, 637 - 649.

Kelly, P., and D. Gubbins (1997), The geomagnetic field over the past 5 million years, *Geophysical Journal International*, *128*, 315-330.

Kono, M., and O. Hiroi (1996), Paleosecular variation of field intensities and dipole moments, *Earth and Planetary Science Letters*, *139*, 251-262.

Korte, M., and C. G. Constable (2005), Continuous geomagnetic field models for the past 7 millennia: 2. CALS7K, *Geochemistry Geophysics Geosystems*, *6*, doi:10.1029/2004GC000801.

Laj, C., et al. (1999), Geomagnetic paleosecular variation at Hawaii around 3 Ma from a sequence of 107 lava flows at Kaena Point (Oahu), *Earth and Planetary Science Letters*, *170*, 365-376.

Laj, C., et al. (2002), Geomagnetic intensity and inclination Variations at Hawaii for the past 98 kyr from core SOH-4 (Big Island): a new study and a comparison with existing contemporary data, *Physics Of The Earth And Planetary Interiors*, *129*, 205-243.

Langereis, C. G., et al. (1997), Magnetostratigraphy and astronomical calibration of the last 1.1 Myr from an eastern Mediterranean piston core and dating of short events in the Brunhes, *Geophysical Journal International*, *129*, 75-94.

Lee, S. (1983), A study of the time-averaged paleomagnetic field for the last 195 million years, Australian National University.

Love, J., and C. G. Constable (2003), Gaussian statistics for paleomagnetic vectors, *Geophysical Journal International*, *152*, 515-565.

Lund, S. P., et al. (1998), Geomagnetic field excursions occurred often during the last million years, *Eos, Transactions, American Geophysical Union*, *79*, 178-179.

Lund, S. P., et al. (2001), Brunhes Chron magnetic field excursions recovered from Leg 172 sediments, *Proceedings of the Ocean Drilling Program, Scientific Results (CD-Rom)*, *172*, 18.

Maillol, J. M., et al. (1997), Paleomagnetism of Plio-Quaternary basalts in the Jalisco block, western Mexico, *Geofisica Internacional*, *36*, 21-35.

Malahoff, A., et al. (1982), Geophysical evidence for post-Miocene rotation of the island of Viti Levu, Fiji, and its relationship to the tectonic development of the North Fiji Basin, *Earth and Planetary Science Letters*, *57*, 398-414.

McElhinny, M. W. (2004), Geocentric Axial Dipole Hypothesis: A Least Squares Perspective, in *Timescales of the Paleomagnetic Field*, edited by J. E. T. Channell, et al.,145, 1-12, American Geophysical Union, Washington, D.C.

McElhinny, M. W., and P. L. McFadden (1997), Palaeosecular variation over the past 5 Myr based on a new generalized database, *Geophysical Journal International*, *131*, 240-252.

McElhinny, M. W., et al. (1996a), The Myth of the Pacific dipole window, *Earth and Planetary Science Letters*, *143*, 13-22.

McElhinny, M. W., et al. (1996b), The Time-averaged paleomagnetic field 0-5 Ma, *J. Geophys. Res., B Solid Earth and Planets*, *101*, 25007-25028.

McFadden, P. L. (1980), The best estimate of Fisher's precision parameter k, *Geophysical Journal Royal Astronomical Society*, *60*, 397-407.

McWilliams, M., et al. (1982), Geomagnetic secular variation from (super 14) C-dated lava flows on Hawaii and the question of the Pacific non-dipole low, *Phil. Trans. Roy. Soc. London, Series A: Mathematical and Physical Sciences*, *306*, 211-222.

Mejia, V., et al. (2002), Paleosecular variation of Brunhes age lava flows from British Columbia, Canada, *Geochemistry, Geophysics, Geosystems*, *3*, doi:10.1029/2002GC000353.

Mejia, V., et al. (2005), Paleosecular variation and time-averaged field recorded in late Pliocene-Holocene lava flows from Mexico, *Geochemistry Geophysics Geosystems*, *6*, doi:10.1029/2004GC000871.

Mejia, V., et al. (2004), Plio-Pleistocene time-averaged field in southern Patagonia recorded in lava flows, *Geochemistry Geophysics Geosystems*, *5*, doi:10.1029/2003GC000633.

Merrill, R. T., et al. (1996), *The Magnetic Field of the Earth: Paleomagnetism, the Core, and the Deep Mantle*, 531 pp., Academic Press, San Diego.

Miki, M., et al. (1998), Geomagnetic paleosecular variation in Easter Island, the southeast Pacific, *Physics of the Earth and Planetary Interiors*, *106*, 93-101.

Nieto-Obergon, J., et al. (1992), Listric faulting and continental rifting in western Mexico, A paleomagnetic and structural study, *Tectonophysics*, *208*, 365-376.

Opdyke, N. D., et al. (2006), The Time averaged field at the Equator: results from Ecuador, *Geochemistry Geophysics Geosystems*, *7*, doi:10.1029/2005GC001221.

Opdyke, N. D., and R. Musgrave (2004), Paleomagnetic results from the newer volcanics of Victoria: Contribution to the Time Averaged Field Initiative, *Geochemistry Geophysics Geosystems*, *5*, doi:10.1029/2003GC000632.

Press, W. H., et al. (1992), *Numerical Recipes in Fortran 77: The Art of Scientific Computing*, 2 ed., 1447 pp., Cambridge University Press, New York.

Quidelleur, X., and V. Courtillot (1996), On low degree spherical harmonic models of paleosecular variation, *Physics of the Earth and Planetary Interiors*, *95*, 55-77.

Quidelleur, X., et al. (1994), Longterm geometry of the geomagnetic field for the last 5 million years; an updated secular variation database from volcanic sequences, *Geophysical Research Letters*, *21*, 1639-1642.

Riley, C. M., et al. (1999), Paleomagnetic constraints on fault motion in the Hilina Fault System, south flank of Kilauea Volcano, Hawaii, *Journal of Volcanology and Geothermal Research*, *94*, 233-249.

Ruiz-Martinez, V. C., et al. (2000), Palaeomagnetism of Late Miocene to Quaternary volcanics from the eastern segment of the Trans-Mexican Volcanic Belt, *Tectonophysics*, *318*, 217-233.

Schneider, D. A., and D. V. Kent (1990), The Time-averaged paleomagnetic field, *Reviews of Geophysics*, *28*, 71-96.

Selkin, P. A., and L. Tauxe (2000), Long-term variations in palaeointensity, *Philosophical Transactions Of The Royal Society Of London Series A-Mathematical Physical And Engineering Sciences*, *358*, 1065-1088.

Shibuya, H., et al. (1995), Paleomagnetism of young New Zealand basalts and longitudinal distribution of paleosecular variation, *Journal of Geomagnetism and Geoelectricity*, *47*, 1011-1022.

Soler-Arechalde, A., and J. Urrutia-Fucugauchi (2000), Paleomagnetism of the Acambay graben, central Trans-Mexican Volcanic Belt, *Tectonophysics*, *318*, 235-248.

Stone, D. B., and P. Layer (2005), Paleosecular variation and GAD studies of 0 - 2 Ma flow sequences from the Aleutian Islands, Alaska, *Geochemistry Geophysics Geosystems*, *7*, doi:10.1029/2005GC001007.

Tarling, D. H. (1967), The Paleomagnetism of some rock samples from Viti Levu, Fiji, *New Zealand Journal of Geology and Geophysics*, *10*, 1235-1247.

Tauxe, L. (1998), *Paleomagnetic Principles and Practice*, 1 ed., 299 pp., Kluwer Academic Publishers, Boston.

Tauxe, L., et al. (2003), Paleomagnetism of the southwestern U.S.A. recorded by 0-5 Ma igneous rocks, *Geochemistry Geophysics Geosystems*, *4*, 8802, doi:8810.1029/2002GC000343.

Tauxe, L., et al. (2004a), Paleomagnetism and $^{40}Ar/^{39}Ar$ ages from volcanics extruded during the Matuyama and Bruhnes chrons near McMurdo Sound, Antarctica, *Geochemistry Geophysics Geosystems*, *5*, doi:10.1029/2003GC000656.

Tauxe, L., and D. V. Kent (2004), A Simplified Statistical Model for the Geomagnetic Field and the Detection of Shallow Bias in Paleomagnetic Inclinations: Was the Ancient Magnetic Field Dipolar? in *Timescales of the Paleomagnetic Field*, edited by J. E. T. Channell, et al.,145, 320, American Geophysical Union, Washington, D.C.

Tauxe, L., et al. (1991), Bootstrap statistics for paleomagnetic data, *Journal of Geophysical Research*, *96*, 11,723-711,740.

Tauxe, L., et al. (2004b), Paleomagnetic results from the Snake River Plain: Contribution to the time-averaged field global database, *Geochemistry Geophysics Geosystems*, *5*, doi:10.1029/2003GC000661.

Tauxe, L., et al. (2000), Paleomagnetism and $^{40}Ar/^{39}Ar$ ages from La Palma in the Canary Islands, *Geochemistry Geophysics Geosystems*, *1*, doi:10.1029/2000GC000063.

Taylor, G. K., et al. (2000), Rapid rotation of Fiji: Paleomagnetic evidence and tectonic implications, *Journal of Geophysical Research*, *105*, 5771-5781.

Teanby, N., et al. (2002), A detailed palaeointensity and inclination record from drill core SOH1 on Hawaii, *Physics Of The Earth And Planetary Interiors*, *131*, 101-140.

Uribe-Cifuentes, R. M., and J. Urrutia-Fucugauchi (1999), Paleomagnetic study of the Valle de Santiago volcanics, Michoacan-Guanajuato volcanic field, Mexico., *Geofisica Internacional*, *38*, 217-230.

Vandamme, D. (1994), A new method to determine paleosecular variation, *Physics of the Earth and Planetary Interiors*, *85*, 131-142.

Yamamoto, Y., et al. (2002), Geomagnetic paleosecular variation for the past 5 Ma in the Society Islands, French Polynesia, *Earth, Planets and Space*, *54*, 797-802.

Chapter 3

Paleomagnetic Field Properties Near the Southern Hemisphere Tangent Cylinder

Abstract

During two recent field seasons we sampled 100 new volcanic sites in the Erebus Volcanic Province (EVP), Antarctica for paleomagnetic analyses including paleointensity and paleodirection measurements. When combined with previous results, the EVP data provide a unique opportunity to examine high latitude magnetic field behavior. It has been proposed that at high latitude the magnetic field may be affected by three-dimensional flow inside the tangent cylinder, whereas lower latitude observations are expressions of columnar flow (and the resulting magnetic field) outside the tangent cylinder. A total of 125 new and previously published sites have high-quality directional data with a non-Fisherian distribution and a mean direction that is indistinguishable from a geocentric axial dipole (GAD). The mean inclination deviates less than 3° from GAD, which falls within 95% confidence limits. Twenty-one normal and reverse polarity sites were selected for new age determinations by the $^{40}Ar/^{39}Ar$ incremental heating method in the geochronology laboratory at New Mexico Tech. For the EVP measurements, the virtual geomagnetic pole (VGP) dispersion for all data (0 – 5 Ma) combined, the normal Brunhes, or the reverse Matuyama chron are statistically indistinguishable from each other regardless of the criteria used to determine a cut-off for transitional data. However,

the EVP dispersion is high (23.7 ± 3.2°) in comparison to dispersion from mid to low-latitudes and is consistent with paleosecular variation (PSV) in Model G but not the more recent statistical PSV model TK03.GAD. IZZI modified Thellier-Thellier experiments provide 40 paleointensity estimates, for which 31 have associated radiometric dates. The mean EVP paleointensity is 29.39 ± 2.35 μT (equivalent to a virtual axial dipole moment of 3.86 ± 0.31 ZAm^2), which is low compared with current intensity (~63 μT) at McMurdo. The high dispersion and low intensity observed here agrees with the global observation of anti-correlation between directional variability and field strength. Comparisons with temporally-varying models of dipole magnitude show that low EVP intensity is most likely a function of bias in temporal sampling.

3.1 Introduction

We examine high latitude paleomagnetic sites in Antarctica to study long-term geomagnetic field behavior near the tangent cylinder, the axisymmetric cylinder tangent to the inner core at the equator that is believed to separate different convective regimes in Earth's outer core (Figure 3.1). Outside the tangent cylinder, columnar convection dominates, while inside, thermal winds are expected to be enhanced by the presence of the magnetic field, generating polar vortices and associated three-dimensional convection. These distinct convection regimes have been inferred from recent magnetic field observations [*Hulot et al.*, 2002; *Olson and Aurnou*, 1999], and are identified in some numerical geodynamo simulations [*Sreenivasan and Jones*, 2005, 2006]. For a detailed discussion of convective flow in the outer core see *Jones*, [2007].

Since the late 16th century, direct magnetic measurements (from observatories, surveys, and satellites) have provided increasingly high-quality constraints on spatial and temporal variations of the geomagnetic field [e.g. UFM, *Bloxham et al.*, 1989; *Bloxham and Jackson*, 1992; GUFM1 *Jackson et al.*, 2000]. Such temporally- and spatially-varying models provide useful constraints on the average field properties over time – the time-averaged field (TAF) – and the variation of field properties over time – secular variation. When the time-varying spherical harmonic model, GUFM1, is downward continued to the core (assuming an insulating mantle), the field is significantly different

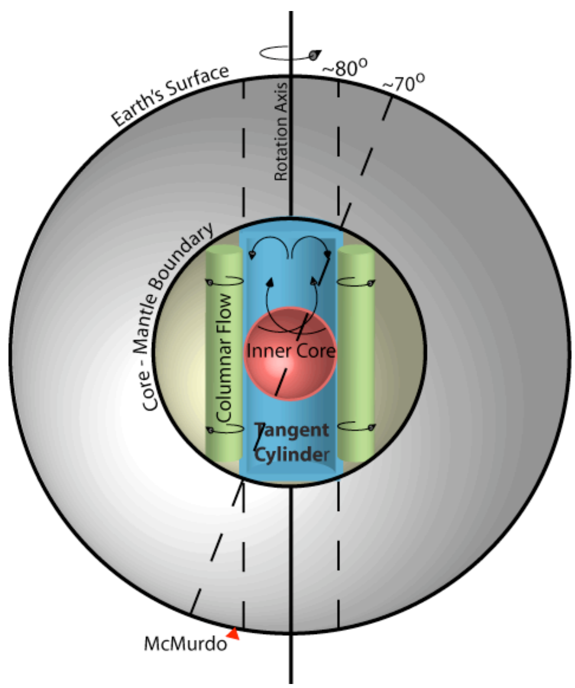

Figure 3.1: Illustration of outer core flow regimes. The tangent cylinder is denoted by the blue cylinder tangential to the red sphere (inner core). The location of study location (McMurdo) is labeled with a red triangle.

from that of a geocentric axial dipole (GAD). This non-GAD structure is inferred to result, in part, from the presence of an inner core, and differing outer core flow within the tangent cylinder. Of particular interest, in GUFM1 a persistent low flux region is observed over the north pole, which is inferred by *Hulot et al.* [2002] and *Olson and Aurnou* [1999] to result from the polar vortex convection regime within the tangent cylinder. In addition, regions of increased flux are seen at high northern and southern latitudes near the tangent cylinder [*Bloxham et al.*, 1989; *Bloxham and Jackson*, 1992; *Jackson et al.*, 2000].

A similar time-varying model of archeomagnetic, sediment, and lava intensities and directions, CALS7K.2, provides analogous constraints on the TAF and paleosecular variation (PSV) for the period from 0 to 7 ka [*Korte and Constable*, 2005]. Longitudinal structure in CALS7K.2 provides further evidence for flux lobes similar, but damped relative to those observed in GUFM1 [*Jackson et al.*, 2000]. This similarity between historical and the 0-7 ka radial field structure suggests a persistence of non-GAD terms resulting from the differing convection regimes on millennial time-scales. Our goal is to determine whether these different convection regimes generate observable differences in properties for the 0-5 Ma paleofield at Earth's surface.

Several data collection efforts have enabled improved temporal and spatial sampling of high-quality paleomagnetic data for the past 5 Myr [see e.g. *Carlut et al.*, 2000; *Herrero-Bervera and Coe*, 1999; *Holt et al.*, 1996; *Johnson et al.*, 1998; *Laj et al.*, 2002; *Miki et al.*, 1998; *Tauxe et al.*, 2000; *Tauxe et al.*, 2003]. One collaborative effort, the TAFI project (Time-Averaged Field Initiative), has resulted in new data archived in a comprehensive data set. The ongoing TAFI project is providing a significant improvement in the number and quality, as well as temporal and spatial sampling of paleomagnetic data. A summary of the TAFI contributions to date is provided in *Johnson et al*. [2008]. As part of the TAFI project, the Erebus Volcanic Province in Antarctica (Figure 3.2) provides an excellent opportunity to improve high-latitude sampling of lava flows suitable for studying the 0-5 Myr TAF and PSV. In particular, this study focuses on Antarctic paleomagnetic directions and intensities measured in a prior study on samples collected in 1965/1966 by [*Mankinen and Cox*, 1988] and re-analyzed by [*Tauxe et al.*, 2004] and those measured from new samples collected in 2003/2004 and 2006/2007 field seasons.

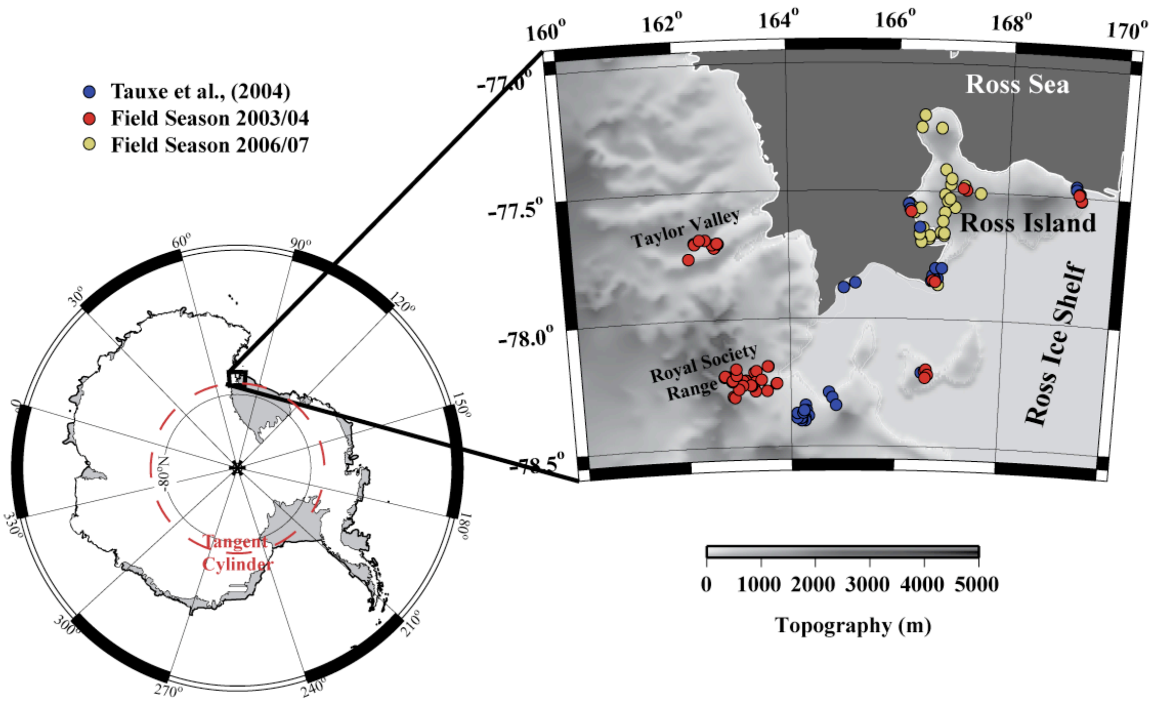

Figure 3.2: Shaded relief map of the southern portion of the Western Ross Embayment projected as conic equal area and illuminated from N/NW. Red (yellow) circles represent data collected in the 2003/04 (2006/2007) field season and presented in this study. Blue circles represent data presented in *Tauxe et al.* [2004]. Small inset is the same projection of the Antarctica continent with the surface expression of the tangent cylinder marked with a red dashed circle (~79°).

We present a brief description of geological setting and sampling techniques. We then discuss paleomagnetic analyses performed on the samples, which yield information about the magnetic field vector at the time of emplacement. We compare the directional and intensity data from other TAFI sites and compilations of similar quality data from around the world to examine TAF and PSV field properties over the past 5 Myr. The paleointensity results from Antarctica indicate that the field intensity is lower when directions lie far from those expected for a dipolar field. Although the paleomagnetic data cannot be used to provide dynamical constraints on features like the polar vortex they will provide useful constraints on statistical models for PSV. In conjunction with similar studies on output from numerical dynamo simulations they may lead to future insight about tangent cylinder field dynamics.

3.2 Study Area

3.2.1 Geologic Setting

The McMurdo Volcanic Group is a late Cenozoic alkali volcanic province found within the western Ross Embayment [*Kyle*, 1990a; 1990b], which includes Sheridan Bluff and Mount Early and excludes the Balleny Islands from *Harrington's* [1958] original designation of the McMurdo Volcanic Group. This group represents the most recent volcanic activity related to the Transantarctic Mountains [*Kyle*, 1981], from the oldest dated lava from Sheridan Bluff (19.8 Ma) to the youngest and continually erupting Mt. Erebus on Ross Island [*Kyle*, 1990a]. Based on volcanic distribution and tectonic setting *Kyle and Cole* [1974] subdivided the McMurdo Volcanic Group into three provinces: Hallett, Melbourne and Erebus. This study focuses on paleomagnetism and geochronology of basalts from the Erebus Volcanic Province (EVP). Specifically, sites were located on Ross Island, Black Island, within Taylor Valley and in the foothills of the Royal Society Ranges.

The 2006-2007 field season sampled locations restricted to Ross Island, which is home to Mt. Erebus the world's southernmost active volcano. Analysis of DVDP (Dry Valley Drilling Project) cores [*Kyle*, 1981] shows that Mt. Erebus started erupting at approximately 1.3 Ma, with the oldest known Mt. Erebus rock having an age of 1.311 Ma [*Esser et al.*, 2004]. Mt. Erebus is still active, and is the only volcano in the Southern Hemisphere with a persistent lava lake. In addition to Mt. Erebus, the 2003-2004 field season samples are from locations in the dry valleys in and around the Royal Society Range. The Royal Society Range and Dry Valleys are in the Transtantarctic Mountains, a 3500 km mountain front that represent the western rift-flank to the West Antarctic Rift System [*Fitzgerald*, 2002]. Uplift and denudation have exposed Precambrian basement rocks with Late Cenozoic alkaline volcanics and intrusions throughout the region. While this region has undergone various forms of tectonic activity since the Paleozoic, there has been little translation or uplift of crustal blocks since the late Miocene [*Cande et al.*, 2000].

3.2.2 Sampling

We sampled 70 sites in the Erebus Volcanic Province during the 2003-2004 field season (Figure 3.2, red circles) and 30 sites during the 2006-2007 field season (Figure 3.2, yellow circles). Sampling was restricted to lava flows and a few thin dikes because these units typically cool rapidly, essentially recording an instantaneous geomagnetic field at the time and location of emplacement. Sites exhibiting evidence of post-emplacement tilting (e.g., slumping or faulting) were not sampled. To minimize the necessity for additional $^{40}Ar/^{39}Ar$ dates, site locations were chosen based on previous geochronology studies by *Wilch* [1991; 1993], who radiometrically dated many lava flows in the EVP. At each field site, a minimum of 10 standard 2.5 cm diameter samples were drilled using a gasoline powered drill with a mixture of water and glycol for the drilling fluid. The samples were oriented using at least two of three methods; magnetic compass, sun compass, and/or a differential GPS (Global Positioning System) orientation technique.

The differential GPS technique was developed at Scripps Institution of Oceanography to facilitate sample orientation at high latitude where weather conditions often preclude the use of a sun compass. This method utilizes two Novotel GPS receivers attached to either end of a one-meter non-magnetic base. The location and azimuth of the horizontal baseline are computed from the difference in signals detected by the two receivers. The orientation of the baseline is transferred to the paleomagnetic samples with a rotatable laser mounted on the base. A prism attached to the sample orientation device is used to reflect the laser beam back onto itself providing accurate orientation of the drill core with respect to the differential GPS baseline (Figure 3.3). The orientations derived by the differential GPS are nearly identical to those obtained by a sun compass, although it typically adds a half hour to the time needed for orienting a site with 10 samples and is rather awkward to transport. Nonetheless, achieving sun-compass accuracy in orientations when direct sunlight is not readily available is a major breakthrough for high-latitude paleomagnetic field studies.

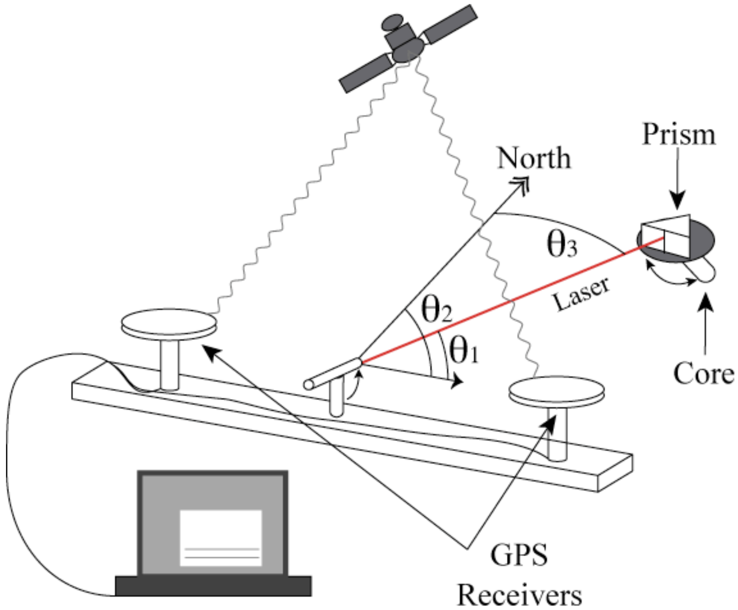

Figure 3.3: Diagram of differential GPS system for orienting paleomagnetic samples in regions with significant cloud cover. Angles θ_1 and θ_3 are measured in the field, while the orientation in relation to North (θ_2) is determined after data reduction of the GPS location and azimuth.

3.2.3 Previous work in the Mt. Erebus Volcanic Province

Mankinen and Cox [1988] completed a paleomagnetic sampling study of 303 fully oriented samples from 39 lava flows from the Erebus Volcanic Province in the vicinity of McMurdo Sound in 1965 and 1966 using a gasoline powered drill for sample collection. Oriented block samples were taken from an additional 11 lava flows. They reported site means based on the natural remanent magnetizations (NRMs). The approximate locations of the sites are shown as blue circles in Figure 3.2. *Tauxe et al.* [2004] remeasured all the NRM directions and subjected at least 5 separately oriented specimens from every site to step-wise alternating field or thermal demagnetization. *Tauxe et al.* [2004] also selected approximately 100 specimens based on the specimen's high median demagnetizing fields for a *Thellier-Thellier* [1959] type experiment. Of the 36 sites that *Tauxe et al.* [2004] observed with reliable directions, 16 sites have both direction and paleointensity estimates. This study also provided new $^{40}Ar/^{39}Ar$ dates for nine sites, ranging from 0.28 to 1.49 Ma. Since *Mankinen and Cox* [1988] focused on Brunhes-aged lava flows, only seven sites are reverse polarity. The new study presented here aims to expand the age distribution and polarity sampling of the Antarctic region and to contribute many more paleointensity estimates.

3.3 Paleomagnetic Analysis

Fundamental paleomagnetic observations are declination (D), inclination (I) and intensity ($|B|$), where

$$D = \tan^{-1}\left(\frac{B_y}{B_x}\right),\; I = \tan^{-1}\left(\frac{B_z}{\left(B_x^2 + B_y^2\right)^{1/2}}\right),\; |B| = \left(B_x^2 + B_y^2 + B_z^2\right)^{1/2}, \tag{3.1}$$

and B_x, B_y, B_z are the vector components of the magnetic field expressed in a local geographic coordinate system at any given location. In sections 3.1 and 3.2 we present the directional and intensity experimental methods and associated results, respectively. In each section we characterize the mean values for the fundamental observations as well as the statistics describing the variation of the paleofield in both time and space.

Although this study sampled sites with ages spanning 0 to 14 Ma, we limit our analyses to data spanning the past 5 Myr for two reasons: first, the number of data available diminishes rapidly with increasing age; second, for ages less than 5 Ma the plate motion corrections needed to obtain accurate paleosite locations are small and reasonably well known. Given the temporal sampling of this study, we present analyses of Brunhes-age normal polarity data, Matuyama-age reverse polarity data, and 0-5 Ma combined normal and reverse polarity data separately. In addition to presenting new 0-5 Ma directional and intensity data, we analyze all available Antarctic data with ages in the 0-5 Myr time interval. All data and subsequent interpretations presented here are available in the MagIC database at http://earthref.org/cgi-bin/magic.cgi?mdt=m000629dt20080226180017.

3.3.1 Paleodirections

We measured NRM directions for all specimens using a 2G cryogenic magnetometer or a Molspin "Minispin" magnetometer if the NRM exceeded 7.5 x 10^{-5} Am^2. At least five specimens per site (750 specimens in total) were magnetically cleaned using either stepwise alternating field (AF) (461 specimens) or thermal demagnetization (289 specimens). Most sites were treated using both techniques using either the Sapphire Instruments SI-4 uniaxial AF demagnetizer or SIO home-built ovens with 2°C accuracy.

For the AF demagnetization experiments, we measured samples at the following applied field magnitudes: 5, 10, 15, 20, 30, 40, 50, 60, 80, 100, 120, 150, and 180 mT. At peak fields of 100 mT and higher, the specimens were subjected to a "triple demagnetization" protocol [*Stephenson*, 1993] whereby specimens were demagnetized along all three axes, measured and then demagnetized along the y-axis, measured and then demagnetized along the z-axis. At every demagnetization field strength, an average of the three measurements was calculated to counteract the effect of (rarely observed) gyroremanent magnetization, an unwanted remanence produced during demagnetization due to preferential anisotropic orientation in the easy axes of magnetization. During the AF demagnetization procedure, specimen orientations alternated from positive to negative axes with each field step. If the difference in directions between field steps was more then 5° a "double demagnetization" protocol [*Tauxe et al.*, 2003; *Tauxe et al.*, 2004] was implemented to detect possible acquisition of anhysteretic remanence.

Thermal demagnetization steps of 50°C were used from 150° - 500°C, steps of 10°C were used from 520° - 560°C, and steps of 5°C were used when necessary until the maximum unblocking temperature was reached. One site with an unusual magnetic remanence spectrum, mc164, required 50°C steps to 620°C and 5°C from 620 to 650°C. Each thermal demagnetization experiment was performed in conjunction with an IZZI modified Thellier-Thellier experiment [*Tauxe and Staudigel*, 2004; *Yu et al.*, 2004] to obtain paleointensity information (see section 3.2).

As with the data analyzed by *Tauxe et al.* [2004], these specimens are very well-behaved. With few exceptions, the magnetization of specimens treated with AF decayed linearly to the origin. Some thermally demagnetized specimens experienced significant alteration, but we attribute this in part to the Thellier-Thellier experimental method, in which the samples are heated repeatedly. Representative AF and thermal demagnetization data are plotted on vector end-point diagrams in Figures 3.4 and 3.5. Principal component analysis [*Kirschvink*, 1980] was used to determine characteristic components. We were unable to determine principal component directions for 3 sites (mc151, mc149, and mc159); these sites were not included in the data compilation. Specimens that yielded aberrant behavior were tested for rotational errors that could have occurred during sample collection, while cutting, or measuring the magnetic direction. If these specimens failed the rotational test or showed evidence of mismarked direction (20 samples total), the results were not included.

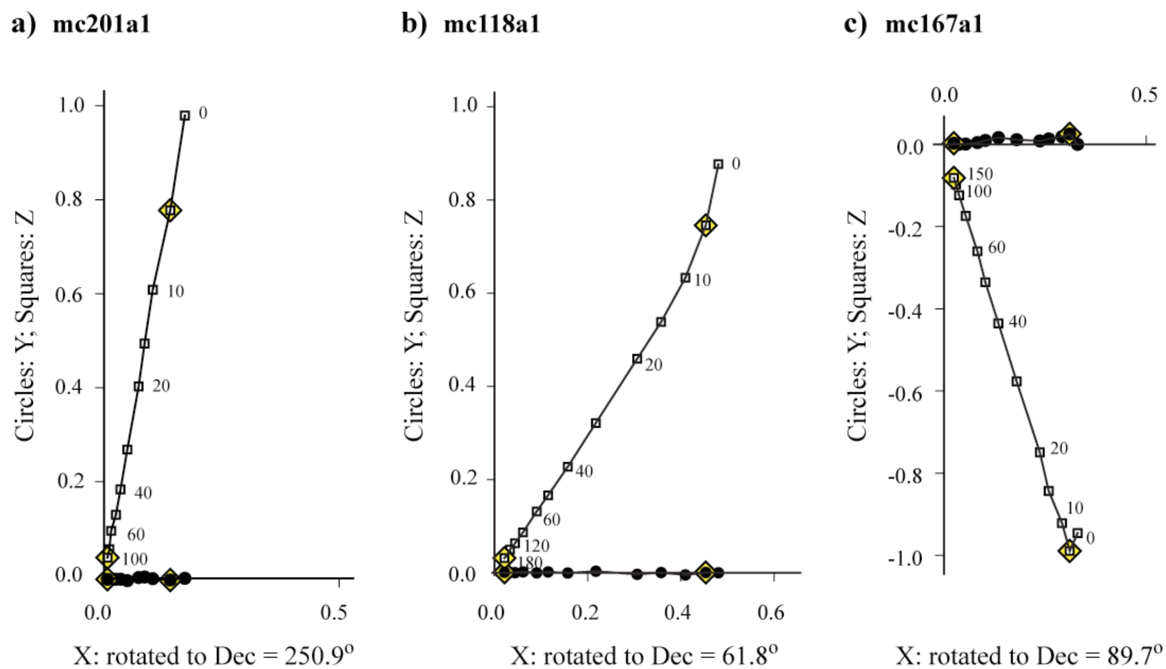

Figure 3.4: Vector-endpoint diagrams of AF (alternating field) demagnetization experiments for representative specimens, **a)** mc201a1, NRM is normalized to 1.84×10^{-5} Am^2, **b)** mc118a1, NRM is normalized to 3.53×10^{-5} Am^2, **c)** mc167a1, NRM is normalized to 6.78×10^{-5} Am^2. Closed (open) circles are the horizontal (vertical) plane projection of the directional vector. The x-direction has been rotated to the NRM declination (labeled for each specimen). The yellow diamonds represent the maximum and minimum demagnetization steps used in the principal component analysis.

Site mean directions are calculated using Fisher statistics [*Fisher*, 1953] of characteristic directions for experiments with at least 4 consecutive demagnetization steps, directions trending to the origin, and a maximum angle of deviation (MAD) less than 5°. All sites have at least 5 samples from which mean summary statistics can be calculated. A summary of site locations and mean directions is presented in Table 3.1 and Figure 3.6a. The within-site scatter about the mean site direction (*D* and *I*) is often described by the 95% confidence cone, α_{95}. This cone is defined as $\alpha_{95} \approx 140 \big/ \sqrt{kN_s}$, where and N_s is the number of samples, and k is the estimate of the Fisherian precision parameter, κ. Our measure of data quality for individual sites is based on k. Guided by results from *Johnson et al.* [2008] we define data selection criteria for further analyses as $n \geq 5$ and $k > 50$. All sites had k values greater than 50 and α_{95} values less than 10°. There are 8 sites (mc106, mc110, mc112, mc113, mc122, mc124, mc130, mc134) that are excluded because they are older than 5 Myr. This yields 89 new sites with high-quality directional data from 0 to 5 Ma. With the inclusion of 36 sites from *Tauxe et al.,* [2004] with ages ranging from 0 to 5 Ma that meet the above criteria, the following analysis incorporates 125 Antarctic sites. The site mean directions for normal and reverse polarity data of all 125 Antarctic sites are shown in Figure 3.6b and tabulated in Table 3.2.

Figure 3.5: Arai plot of NRM remaining vs. pTRM gained during an IZZI-modified T-T paleointensity experiment for representative specimens, **a)** mc217b1, NRM is normalized to 1.06x10^{-4} Am^2, **b)** mc120b1, NRM is normalized to 4.13x10^{-5} Am^2, **c)** mc147k2, NRM is normalized to 3.62x10^{-5} Am^2, and **d)** mc131e1, NRM is normalized to 1.98x10^{-5} Am^2. Open (closed) circles represent the ZI (IZ) steps of the heating sequence (see text). The green line represents the inferred paleointensity and pTRM checks are shown as red triangles. Inset is a vector-endpoint diagram of direction during thermal demagnetization (the zero-field only steps of the T-T experiment) where the x-direction has been rotated to the NRM declination (labeled for each specimen). Closed circles are the horizontal plane and open circles are the vertical plane. The yellow diamonds represent the maximum and minimum demagnetization steps used in the principal component analysis.

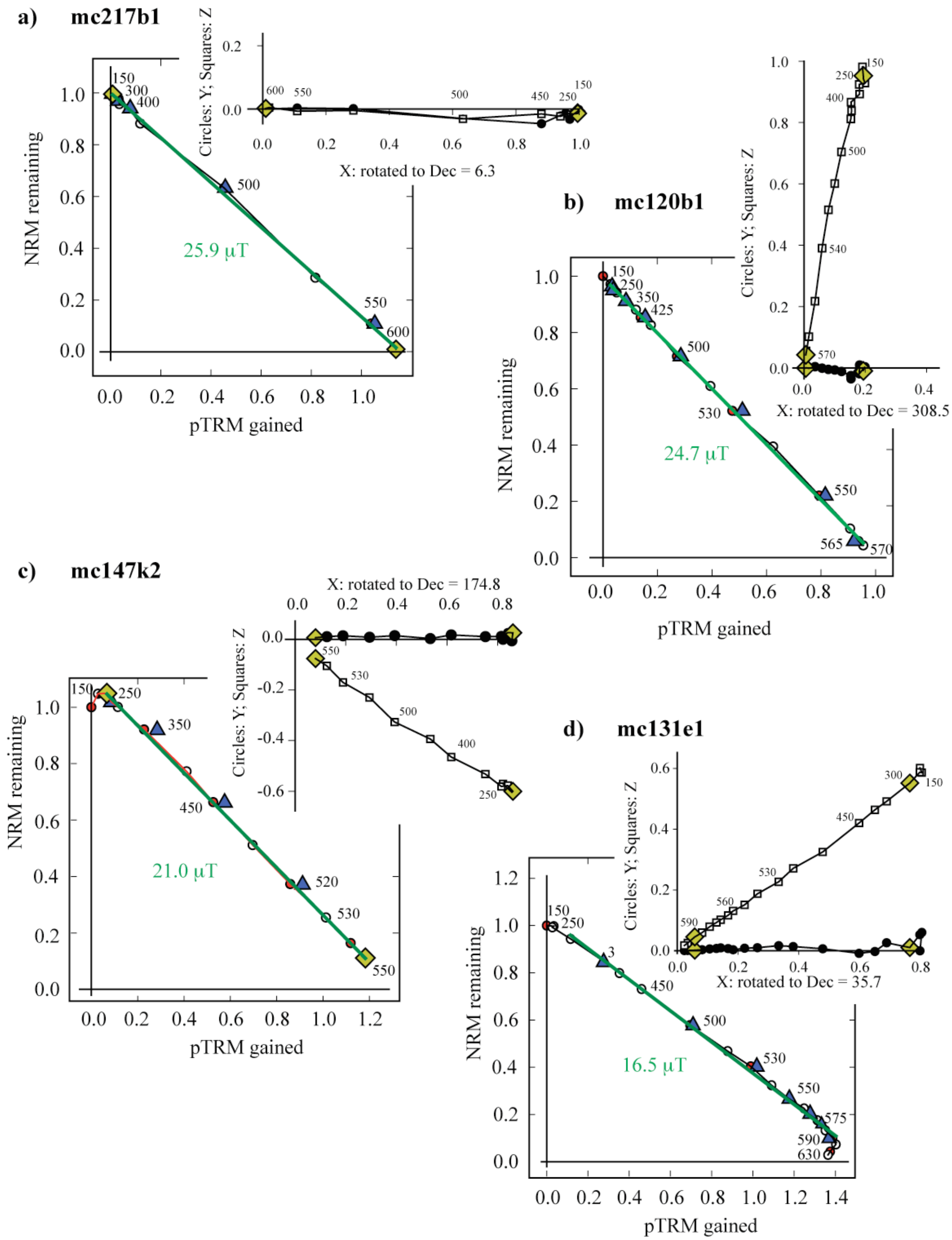
a) mc217b1
NRM remaining
pTRM gained
25.9 μT
Circles: Y; Squares: Z
X: rotated to Dec = 6.3
b) mc120b1
NRM remaining
pTRM gained
24.7 μT
Circles: Y; Squares: Z
X: rotated to Dec = 308.5
c) mc147k2
NRM remaining
pTRM gained
21.0 μT
Circles: Y; Squares: Z
X: rotated to Dec = 174.8
d) mc131e1
NRM remaining
pTRM gained
16.5 μT
Circles: Y; Squares: Z
X: rotated to Dec = 35.7

Table 3.1 Average Directions by Site[a]

Site	Site Lat. (°N)	Site Lon. (°E)	Dec	Inc	N	*k*	α_{95}	VGP Lat.	VGP Lon.	Pol.	Preferred Age (Ma ± 2σ)	Age Reference
mc100	-78.302	162.900	11.8	-75.4	8	318.6	3.2	73.8	182.7	N	0.86 ± 0.23	*This study*
mc101	-78.306	162.928	38.5	-80.6	6	460.8	3.1	78.4	239.0	N	1.07 ± 0.01	*Wilch, 1991*
mc102	-78.235	163.352	150.4	75.7	7	326.5	3.4	-72.3	295.8	R	0.26 ± 0.02	*Wilch, 1991*
mc103	-78.235	163.360	138.2	73.6	6	1460.2	1.8	-67.0	283.3	R	1.42 ± 0.03	*Wilch, 1991*
mc104	-78.238	163.401	72.1	-77.2	7	367.4	3.2	66.5	262.2	N	0.29 ± 0.02	*This study*
mc105	-78.245	163.231	192.1	69.5	8	755.0	2.0	-64.6	0.2	R	0.86 ± 0.07	*Armstrong, 1978*
mc106	-78.210	163.308	19.5	-76.7	5	410.8	3.8	75.3	197.5	N	13.42 ± 0.18	*This study*
mc107	-78.204	163.347	96.0	-84.8	7	1007.6	2.0	73.6	304.3	N	2.57 ± 0.38	*Wilch, 1991*
mc108	-78.247	163.323	69.8	-72.4	5	403.2	3.8	59.8	252.3	N	0.41 ± 0.14	*This study*
mc109	-78.282	163.544	174.6	75.4	6	477.4	3.1	-74.1	334.4	R	1.26 ± 0.04	*Wilch, 1991*
mc110	-78.238	163.443	253.5	79.6	5	218.2	5.2	-69.9	89.6	R	7.94 ± 0.24	*Wilch, 1991*
mc111	-78.224	162.787	47.9	-67.6	7	1243.3	1.7	57.4	223.9	N	1.99 ± 0.04	*This study*
mc112	-78.238	163.441	232.9	75.7	5	220.9	5.2	-68.1	60.0	R	7.63 ± 0.32	*Wilch, 1991*
mc113	-78.226	162.735	266.0	74.7	5	560.7	3.2	-60.0	89.7	R	6.73 ± 0.17	*Wilch, 1991*
mc114	-78.224	162.783	52.4	-69.7	5	614.0	3.1	59.4	230.7	N	1.62 ± 0.28	*Wilch, 1991*
mc115	-78.243	162.958	77.7	68.1	6	357.4	3.5	-47.4	227.7	R	2.46 ± 0.31	*This study*
mc116	-78.222	162.744	274.6	-81.2	5	139.7	6.5	70.0	42.5	N	1.14 ± 0.11	*Wilch, 1991*
mc117	-78.235	162.973	164.5	70.0	6	3152.4	1.2	-65.1	321.0	R	2.28 ± 0.24	*Wilch, 1991*
mc118	-78.241	163.141	58.2	-51.1	6	153.7	5.4	37.4	228.5	N	0.31 ± 0.04	*This study*
mc119	-78.239	162.957	124.8	49.0	6	864.8	2.3	-36.1	281.2	R	1.08 ± 0.22	*Wilch, 1991*
mc120	-78.241	163.092	73.8	-70.6	9	538.1	2.2	56.4	254.1	N	1.76 ± 0.05	*Wilch, 1991*
mc121	-78.235	162.954	117.6	78.4	11	389.0	2.3	-70.3	250.2	R	2.51 ± 0.06	*Wilch, 1991*
mc122	-78.187	163.580	12.2	-72.4	5	177.8	5.8	69.0	182.0	N	12.70 ± 0.09	*This study*

continued

Table 3.1 (continued)

Site	Site Lat. (°N)	Site Lon. (°E)	Dec	Inc	N	*k*	α_{95}	VGP Lat.	VGP Lon.	Pol.	Preferred Age (Ma ± 2σ)	Age Reference
mc123	-78.254	163.729	76.1	-82.1	8	317.2	3.1	73.0	280.9	N	1.93 ± 0.05	*This study*
mc124	-78.186	163.567	13.5	-72.7	6	771.6	2.4	69.4	184.1	N	12.61 ± 0.11	*This study*
mc125	-78.254	163.730	344.1	-67.7	9	93.1	5.4	61.8	142.2	N	4.26 ± 0.18	*Wilch, 1991*
mc126	-78.253	163.737	4.2	-78.0	8	294.6	3.2	78.7	172.1	N		
mc127	-78.254	163.733	326.2	-67.2	8	666.9	2.1	59.1	119.5	N	1.94 ± 0.07	*Wilch, 1991*
mc128	-78.210	166.571	36.9	-80.1	8	395.8	2.8	78.0	238.4	N		
mc129	-78.214	166.577	22.1	-54.5	9	490.9	2.3	45.8	192.8	N		
mc130	-78.210	166.579	150.5	46.1	6	405.9	3.3	-37.5	313.1	R	7.25 ± 0.07	*This Study*
mc131	-78.214	166.573	22.1	-58.2	8	548.6	2.4	49.6	193.5	N		
mc132	-78.206	166.552	1.4	39.1	5	77.4	8.8	-10.3	167.9	R		
mc133	-78.199	166.584	36.3	-85.7	6	235.0	4.4	83.0	300.6	N		
mc134	-78.219	166.607	12.5	-84.3	5	886.4	2.6	87.5	273.8	N	9.02 ± 0.05	*This Study*
mc135	-78.231	166.565	264.1	-77.8	8	215.3	3.8	62.9	46.7	N		
mc136	-78.282	163.329	103.1	15.2	6	357.2	3.6	-10.2	264.6	R	1.99 ± 0.60	*Wilch, 1991*
mc137	-78.261	163.257	71.2	34.2	5	120.4	8.7	-14.7	231.1	R		
mc138	-78.260	163.240	83.1	12.1	5	522.1	4.2	-4.6	245.2	R	1.21 ± 0.18	*Wilch, 1991*
mc139	-78.260	163.080	167.5	79.1	6	1319.1	1.8	-80.1	316.2	R	0.88 ± 0.08	*This study*
mc140	-78.276	163.004	343.7	-79.2	7	654.7	2.4	79.8	128.4	N	2.03 ± 0.09	*This study*
mc141	-77.580	166.246	120.7	84.0	5	353.3	4.1	-78.0	224.9	R	1.31 ± 0.02	*Wilch, 1991*
mc142	-77.851	166.680	312.5	84.6	10	580.2	2.0	-69.1	144.1	R	1.23 ± 0.02	*This study*
mc143	-78.244	162.879	30.7	-49.8	6	198.5	4.9	40.5	198.2	N	2.08 ± 0.65	*This study*
mc144	-77.850	166.688	194.2	79.9	8	197.3	4.0	-81.6	21.2	R		
mc145	-78.240	162.893	28.6	2.7	6	378.0	3.5	9.0	191.9	N	1.90 ± 0.12	*Wilch, 1991*

continued

Table 3.1 (continued)

Site	**Site Lat. (°N)**	**Site Lon. (°E)**	**Dec**	**Inc**	**N**	***k***	α_{95}	**VGP Lat.**	**VGP Lon.**	**Pol.**	**Preferred Age (Ma ± 2σ)**	**Age Reference**
mc146	-78.220	162.963	237.0	62.3	7	120.6	5.5	-49.1	51.0	R	1.37 ± 0.42	*Wilch, 1991*
mc147	-78.196	162.962	220.2	67.4	5	830.9	2.7	-58.5	35.1	R	1.63 ± 0.34	*Wilch, 1991*
mc148	-77.492	167.249	285.0	-78.4	5	198.4	5.4	67.6	61.4	N	0.72 ± 0.66	*Wilch, 1991*
mc150	-77.714	162.637	253.5	84.3	5	125.5	6.9	-75.9	112.1	R	3.57 ± 0.14	*Wilch et al., 1993*
mc152	-77.716	162.645	327.2	-85.3	6	1325.5	1.9	83.3	31.5	N	3.87 ± 0.15	*Wilch et al., 1993*
mc153	-77.760	162.144	315.7	58.8	7	114.7	5.7	-30.3	123.5	R	2.53 ± 0.13	*Wilch et al., 1993*
mc154	-77.719	162.626	297.9	87.1	5	429.1	3.7	-74.2	143.6	R	2.19 ± 0.08	*Wilch et al., 1993*
mc155	-77.699	162.253	226.2	77.7	8	221.3	3.7	-72.7	57.7	R	1.50 ± 0.05	*Wilch et al., 1993*
mc156	-77.705	162.592	161.3	71.1	5	340.9	4.2	-66.9	315.0	R	1.89 ± 0.13	*Wilch et al., 1993*
mc157	-77.703	162.264	270.8	72.0	7	208.4	4.2	-54.8	91.1	R		
mc158	-77.688	162.462	47.9	43.1	5	672.3	3.0	-16.5	207.0	R	3.74 ± 0.25	*Wilch et al., 1993*
mc160	-77.687	162.354	227.9	76.2	10	227.7	3.2	-70.0	55.8	R	3.47 ± 0.05	*Wilch et al., 1993*
mc161	-77.702	162.694	167.9	55.6	7	134.0	5.3	-48.1	328.0	R		
mc162	-77.701	162.690	175.5	58.4	7	267.1	3.8	-51.4	337.1	R	2.56±0.13	*Wilch et al., 1993*
mc163	-77.700	162.680	177.8	52.7	5	912.6	2.5	-45.6	340.1	R		
mc164	-77.514	169.330	200.4	85.8	7	1626.0	1.5	-84.5	137.3	R	1.36 ± 0.01	*This study*
mc165	-77.513	169.332	141.9	81.8	8	174.1	4.2	-80.2	261.0	R	1.45 ± 0.06	*This study*
mc166	-77.849	166.670	224.9	73.8	8	634.1	2.2	-67.0	51.6	R	1.33 ± 0.12	*This study*
mc167	-77.487	169.294	186.8	72.1	8	1698.1	1.3	-69.5	359.9	R		
mc168	-77.488	169.292	187.4	68.2	7	386.4	3.1	-63.7	359.8	R	1.38 ± 0.05	*This study*
mc170	-77.854	166.714	2.7	-87.2	5	7835.9	0.9	83.4	344.4	N	1.03 ± 0.10	*This study*
mc200	-77.550	166.161	296.8	-83.7	5	389.6	3.9	77.0	45.2	N	0.07 ± 0.01	*Esser et al., 2004*
mc201	-77.563	166.220	257.0	-79.6	6	372.8	3.5	64.2	36.6	N	0.09 ± 0.01	*Esser et al., 2004*

continued

Table 3.1 (continued)

Site	Site Lat. (°N)	Site Lon. (°E)	Dec	Inc	N	*k*	α_{95}	VGP Lat.	VGP Lon.	Pol.	Preferred Age (Ma ± 2σ)	Age Reference
mc202	-77.657	166.364	341.0	-47.1	5	3519.1	1.3	39.9	144.4	N	0.54 ± 0.01	*Esser et al., 2004*
mc203	-77.581	166.251	137.0	77.1	5	1785.1	1.8	-72.4	276.0	R		
mc204	-77.640	166.408	99.4	-75.8	5	586.7	3.2	58.8	287.0	N	0.04 ± 0.01	*Esser et al., 2004*
mc205	-77.657	166.725	284.7	-34.6	9	1716.6	1.3	21.7	86.9	N	0.37 ± 0.02	*Esser et al., 2004*
mc206	-77.667	166.780	327.6	-32.0	10	217.6	3.3	27.6	131.5	N		
mc207	-77.679	166.517	46.8	-70.6	5	313.2	4.3	62.0	229.9	N		
mc208	-77.668	166.532	38.1	-66.6	6	315.1	3.9	58.1	216.3	N		
mc209	-77.685	166.368	60.3	-61.6	6	979.8	2.2	47.8	238.1	N		
mc210	-77.691	166.374	50.0	-69.5	5	1627.2	1.9	59.8	232.3	N		
mc211	-77.661	166.340	5.0	-56.0	7	604.2	2.5	48.8	172.4	N		
mc212	-77.565	166.359	43.6	19.2	5	1207.4	2.2	-0.8	209.2	R	2.6 ± 0.3	*Fleck et al., 1972*
mc213	-77.223	166.429	180.6	70.7	5	323.6	4.3	-67.8	347.3	R		
mc214	-77.224	166.429	177.5	77.4	10	2549.0	1.0	-78.7	341.2	R		
mc215	-77.477	166.895	342.5	-79.0	8	611.8	2.2	80.0	128.0	N	0.34 ± 0.02	*Esser et al., 2004*
mc216	-77.424	166.811	346.4	-45.3	7	141.0	5.1	39.0	151.1	N	0.51 ± 0.02	*Esser et al., 2004*
mc217	-77.509	167.441	286.8	-71.3	10	134.3	4.2	57.5	75.2	N	0.16 ± 0.01	*Esser et al., 2004*
mc218	-77.562	166.978	1.1	-82.0	8	86.4	6.0	86.7	172.2	N	0.03 ± 0.01	*Esser et al., 2004*
mc219	-77.848	166.675	226.9	75.2	9	862.2	1.8	-68.7	56.4	R		
mc220	-77.457	166.910	21.9	-82.9	10	516.1	2.1	84.8	251.7	N	0.53 ± 0.04	*Esser et al., 2004*
mc221	-77.516	166.798	275.2	-82.8	5	420.0	3.7	72.1	39.2	N	0.12 ± 0.01	*Esser et al., 2004*
mc222	-77.539	166.848	191.0	-52.5	5	252.0	4.8	20.8	356.7	N	0.11 ± 0.01	*Esser et al., 2004*
mc223	-77.658	166.786	73.2	-85.6	10	327.9	2.7	77.1	305.9	N	0.38 ± 0.03	*Esser et al., 2004*
mc224	-77.530	166.884	190.2	-61.6	5	927.2	2.5	30.5	355.6	N	0.03 ± 0.01	*Esser et al., 2004*

continued

Table 3.1 (continued)

Site	Site Lat. (°N)	Site Lon. (°E)	Dec	Inc	N	*k*	α_{95}	VGP Lat.	VGP Lon.	Pol.	Preferred Age (Ma ± 2σ)	Age Reference
mc225	-77.581	166.802	114.3	-74.6	9	952.3	1.7	54.4	297.8	N	0.06 ± 0.01	*Esser et al., 2004*
mc226	-77.614	166.766	17.9	-51.8	5	2216.5	1.6	44.1	187.9	N	0.24 ± 0.02	*Esser et al., 2004*
mc227	-77.271	166.733	220.3	60.3	5	2807.9	1.4	-50.3	36.3	R	4.5 ± 0.6	*Armstrong, 1978*
mc228	-77.267	166.377	217.5	63.9	10	276.7	2.9	-55.0	34.3	R		
mc229	-77.483	167.154	100.1	73.0	8	346.0	3.0	-58.5	246.6	R	1.07 ± 0.18	*Esser et al., 2004*
mc01	-77.85	166.64	255.6	77.5	8	170	4.3	-66.2	90.1	R	1.18 ± 0.01	*Tauxe et al., 2004*
mc02	-77.85	166.69	324.5	-81.2	6	390.3	3.4	79.9	88	N	0.33 ± 0.02	*Tauxe et al., 2004*
mc03	-77.84	166.76	350.4	-82.2	6	560.2	2.8	86.1	126.2	N	0.35 ± 0.01	*Tauxe et al., 2004*
mc04	-77.84	166.7	328.1	-86.1	5	196.9	5.5	83.1	23.2	N	0.34 ± 0.01	*Tauxe et al., 2004*
mc06	-77.83	166.67	13.6	-78.8	5	254.4	4.8	79.8	196	N		
mc07	-77.8	166.72	156.9	-69.1	5	555.9	3.2	41.2	328.3	N		
mc08	-77.8	166.83	38.5	-78.3	8	429.5	2.7	75.1	234.6	N	0.65 ± 0.05	*Tauxe et al., 2004*
mc09	-77.55	166.2	258	-82.7	8	220.1	3.7	69.2	29.3	N	0.07 ± 0.02	*Tauxe et al., 2004*
mc10	-77.57	166.23	335.3	-78.6	8	184.5	4.1	78.2	116.5	N		
mc11	-77.57	166.23	327	-77.1	8	620.4	2.2	74.4	108.9	N		
mc13	-77.64	166.41	117	-71.6	8	122.5	5	49.4	297.1	N	0.06 ± 0.01	*Tauxe et al., 2004*
mc14	-77.46	169.23	0.6	-80.8	8	439.8	2.6	84.6	171.2	N		
mc15	-77.47	169.23	169.5	84.1	9	637.8	2	-87.6	233	R	1.33 ± 0.02	*Tauxe et al., 2004*
mc19	-77.86	165.23	146.3	-80.5	7	150.9	4.9	60.6	324.2	N		
mc20	-77.88	165.02	138.7	-77.3	7	243.7	3.9	55.7	316.2	N	0.77 ± 0.032	*Tauxe et al., 2004*
mc21	-78.21	166.49	329.7	79.3	8	309.1	3.2	-58.6	146.5	R		
mc26	-78.21	166.57	9.3	-57.4	8	134.5	4.8	49.6	177.9	N		
mc28	-78.29	164.73	92	-82.1	6	187.9	4.9	70.3	292.2	N	0.06 ± 0.01	*Tauxe et al., 2004*

continued

Table 3.1 (continued)

Site	**Site Lat. (°N)**	**Site Lon. (°E)**	**Dec**	**Inc**	**N**	***k***	**α_{95}**	**VGP Lat.**	**VGP Lon.**	**Pol.**	**Preferred Age (Ma ± 2σ)**	**Age Reference**
mc29	-78.31	164.8	9.5	-76.6	8	109.4	5.3	75.9	181.8	N	0.18 ± 0.08	*Tauxe et al., 2004*
mc30	-78.34	164.87	242.1	68.1	8	134.2	4.8	-55.3	61.7	R		
mc31	-78.34	164.28	298.1	-86.1	5	599.9	3.1	79.5	25.1	N		
mc32	-78.36	164.3	265.2	-74.6	7	341.8	3.3	58.2	50.1	N		
mc33	-78.38	164.34	9.6	-75.5	8	343.9	3	74	180.5	N		
mc34	-78.39	164.27	280.2	-81.8	7	321.3	3.4	72	46.2	N		
mc35	-78.39	164.23	293.9	-84.2	8	280.5	3.3	77.5	41.2	N	0.12 ± 0.02	*Tauxe et al., 2004*
mc36	-78.39	164.27	344.8	-82.8	7	158.5	4.8	85.8	103.8	N	0.12 ± 0.02	*Tauxe et al., 2004*
mc37	-78.4	164.27	211.3	81.9	8	323	3.1	-81.6	60.2	R	4.47 ± 0.04	*Tauxe et al., 2004*
mc38	-78.4	164.21	296.6	-78	7	224.6	4	69.5	72	N		
mc39	-78.39	164.21	264.4	-85.9	8	179.4	4.2	75.2	17.8	N	0.08 ± 0.01	*Tauxe et al., 2004*
mc40	-78.39	164.2	192.8	-83.1	7	138.6	5.1	64.9	351.3	N		
mc41	-78.39	164.12	270.8	-78.2	6	114.3	6.3	64.8	49	N	0.28 ± 0.02	*Tauxe et al., 2004*
mc43	-78.37	164.24	281.9	-89.1	6	153.7	5.4	78.6	353.2	N		
mc44	-78.36	164.26	324.2	-73.9	8	153.1	4.5	68.4	111.5	N		
mc48	-78.24	163.36	75.3	-55.7	6	219.6	4.5	38.4	247.5	N		
mc49	-78.24	163.36	156.7	75	6	145.4	5.6	-72.1	306	R	1.14 ± 0.02	*Tauxe et al., 2004*
mc50	-78.25	163.22	191.4	71.4	8	468.6	2.6	-67.5	360	R	1.9 ± 0.1	*Tauxe et al., 2004*

[a] Dec and Inc are mean site declination and inclination, respectively. N is the combined number of best-fit lines and planes of all the specimens used in statistical calculations. *k* is an estimate of the *Fisher* [1953] precision parameter, α_{95} is the *Fisher* [1953] circle of 95% confidence. VGP Lat and Lon are the virtual geomagnetic poles calculated for each site. Pol. is the designated polarity determined by VGP latitude less than (Reverse, R) or greater than zero (Normal, N). Preferred age is the $^{40}Ar/^{39}Ar$ radiometric plateau age in Ma with 2σ error.

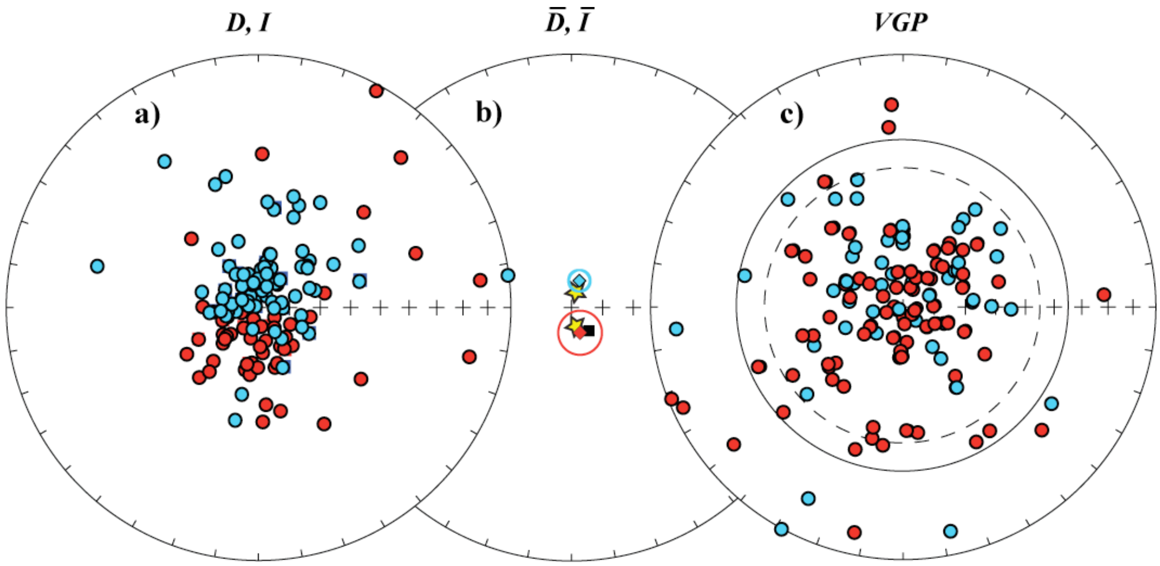

Figure 3.6: Equal area projection of **a)** *D* and *I* for all sites with interpretable directions where normal (blue) and reverse (red) directions are defined by positive and negative Virtual Geomagnetic Pole (VGP) latitude, respectively. **b)** Mean normal (blue) and reverse (red) direction with Fisher 95% confidence cones for sites with $n \geq 5$ and $k > 50$. The yellow stars are the directions as predicted from GAD. The black square is the field direction today at McMurdo Station. **c)** VGP directions for sites with $n \geq 5$ and $k > 50$ with the solid circle at 36° representing the VGP latitude (λ_{VGP}) cut-off calculated using the *Vandamme* [1994] criterion (see text) and the dashed line is the $\lambda_{VGP} = 45°$.

Table 3.2 Mean Directions

	N	$\bar{D}$ (°)	$\bar{I}$ (°)
Grand Mean	125	43.1	-75.5
Normal	76	10.6	-80.9
Reverse	49	156.0	81.4

N is the number sites, $\bar{D}$ is the mean declination, $\bar{I}$ is the mean inclination, Normal and Reverse are defined by positive and negative VGP latitude, respectively.

The virtual geomagnetic pole (VGP) is the pole position of the equivalent geocentric dipole that would give rise to the observed magnetic field direction at any given place. Transitional data are often defined as measurements with absolute value of VGP latitude (λ_{VGP}) less than 45°, and are often excluded from estimates of PSV and the TAF. However, an arbitrary VGP latitude cut-off may bias the interpretation of PSV and TAF properties. For this reason, we present results with 1) no λ_{VGP} cut-off, 2) a cut-off of $|\lambda_{VGP}| < 45°$, and 3) an iteratively defined λ_{VGP} (36º for this data set) that is empirically derived from dispersion, as proposed by *Vandamme* [1994]. VGP directions are shown in Figure 3.6c, with corresponding λ_{VGP} cut-offs.

Inclination anomaly (ΔI) is a summary statistic of average direction often used to describe the TAF, and is defined as:

$$\Delta I = I_{obs} - I_{GAD} \tag{3.2}$$

where I_{obs} is the observed site inclination and I_{GAD} is the prediction of the geocentric axial dipole field. PSV is often represented by S_B, the root mean square angular deviation of VGPs about the geographic axis,

$$S_B = \sqrt{\frac{1}{N-1}\sum_{i=1}^{N}\left(\Delta_i^2 - \frac{S_{w_i}^2}{N_{s_i}}\right)} \tag{3.3}$$

where Δ_i represents the angular deviation of the pole for the i^{th} site from the geographic North Pole, N is the number of sites, and S_B represents the geomagnetic signal remaining after correcting for the within-site VGP dispersion S_{w_i} ($81°/\sqrt{k}$), determined from N_{s_i} samples. Here, k has been converted to an approximation for the precision parameter for VGPs using the transformation provided by *Creer* [1962]. A summary of dispersion and inclination anomaly as a function of λ_{VGP} cut-off can be found in Table 3.3 where the 95% confidence limits are calculated using a bootstrap technique.

Table 3.3 Results of Summary Statistics

		0-5 Ma	**Brunhes**	**Matuyama**
No Cutoff	***N***	125	34	41
	$\overline{\Delta I}$ (°)	$2.4_{-0.3}^{5.2}$	$-1.2_{-6.1}^{4.4}$	$5.4_{1.2}^{9.4}$
	S_B (°)	$34.5_{30.2}^{38.5}$	$32.5_{25.1}^{38.8}$	$34.7_{26.7}^{42.7}$
$\lvert \lambda_{VGP} \rvert < 45°$	***N***	105	27	35
	$\overline{\Delta I}$ (°)	$2.8_{0.9}^{4.7}$	$-3.1_{-5.2}^{-0.9}$	$3.8_{0.7}^{6.3}$
	S_B (°)	$23.7_{20.4}^{26.9}$	$21.4_{17.3}^{25.2}$	$23.7_{20.4}^{26.9}$
Vandamme Cutoff	***N***	112	31	36
	$\overline{\Delta I}$ (°)	$3.7_{1.7}^{5.9}$	$0.9_{-2.8}^{5.8}$	$4.5_{1.1}^{7.4}$
	S_B (°)	$26.6_{24.2}^{29.2}$	$27.0_{21.6}^{32.1}$	$24.8_{20.9}^{28.8}$

$\overline{\Delta I}$ is average inclination anomaly, S_B is angular dispersion. Both statistics are presented in degrees. $|\lambda_{VGP}| > 45°$ indicates statistic was calculated with sites having an absolute VGP latitude greater than 45°. *Vandamme Cutoff* indicates statistic was calculated using only sites with that passed the *Vandamme* (1994) criterion $|\lambda_{VGP}| > 36°$ (see text).

3.3.2 Paleointensity

Our study applies the IZZI variant of the Thellier-Thellier paleointensity experiment [*Thellier and Thellier*, 1959] to estimate intensity for 289 specimens. The experiments were performed in the paleomagnetic laboratory at Scripps Institution of Oceanography in custom-built ovens (as described above). In this experiment, the specimens were heated to a given temperature step and allowed to cool in a zero field (the zero-field step). Next, the specimens were heated to the same temperature and cooled in a field applied along the specimen's cylindrical axis (in-field step). The "zero-field/in-field” method (ZI) of progressively replacing NRM with pTRM allows calculation of the NRM remaining and the pTRM gained after each temperature step through vector subtraction (after *Coe et al.* [1978]). The IZZI method alternates the order of zero-field and in-field measurements (IZ vs. ZI) at each temperature step in order to monitor inequalities in blocking and unblocking temperature (the temperature below which material can retain a remanent magnetization despite changes in applied field). This adaptation makes the IZZI method uniquely devised to monitor multi-domain behavior, a non-uniform magnetization state, (see *Yu et al.*, [2004]) within the rock and replaces the need for the more time consuming pTRM-tail checks [*Riisager and Riisager*, 2001].

Each paleointensity experiment consisted of a series of at least 11 IZ-ZI heating steps in a field of either 25 μT (2003/2004 field season) or 30 μT (2006/2007). After processing the data from the 2003/2004 field season, it was apparent that the sites have an average closer to 30 μT than 25 μT, and therefore the lab applied field was changed accordingly. pTRM checks were performed every other heating step, yielding a minimum of 5 checks per specimen. The samples were heated until at least 95% of the NRM was demagnetized.

We perform initial quality control by visually inspecting both the Arai and vector-endpoint diagrams, disregarding data for which no component is obviously linear. The remaining specimens that have relatively linear components of magnetization are interpreted for paleointensity using the following rules in order of priority:

1) The component must be linear for a minimum of 4 temperature steps.
2) No data are used at temperature steps higher than a failed pTRM check.

3) The temperature range of the interpreted component must be related to the ChRM (characteristic remanent magnetization) of the specimen.
4) Temperature steps are not interpreted beyond a temperature step where the pTRM gained is lower than at a previous lower temperature step, as this is an indication of alteration.

With the initial quality control complete, we further refine the interpretation of these data with the following guidelines to ensure that the fundamental assumptions of the paleointensity experiment are not violated. We define the following statistics to evaluate data quality (for further detail, see [*Ben-Yosef et al.*, 2008; *Tauxe and Staudigel*, 2004]):

$\boldsymbol{\beta}$, the scatter statistic, is the standard error of the slope, divided by the absolute value of the best fit slope [*Coe et al*., 1978]. This accounts for uncertainty in pTRM and NRM data.

DANG, the "Deviation of the ANGle" is the angle between the interpreted component and the origin, as measured from the Vector-endpoint diagram [*Pick and Tauxe*, 1993].

MAD, the "Maximum Angle of Deviation", is the angular uncertainty of the best-fit line [*Kirschvink*, 1980].

$\mathbf{f_{vds}}$, the ratio between the y intercept of the interpreted component on the Arai plot and the total NRM of the experiment [*Tauxe and Staudigel*, 2004].

DRATS, the "Difference RATio Sum", is the sum of differences between the original pTRM and the pTRM checks at each given temperature step normalized by the pTRM of the maximum temperature step in the interpreted component [*Tauxe and Staudigel*, 2004].

Z is a statistic that assesses the "zig-zag" behavior seen in some IZZI experiments [e.g. *Yu et al.*, 2004] by testing for common mean slopes or directions [using the F-test; see *Ben-Yosef et al.*, 2008] between the IZ and ZI steps of the interpreted component on the Arai plot or vector-endpoint diagram, respectively.

The cut-off values for each specimen-level criterion used for subsequent analysis as described above are defined in Table 3.4. There is no single agreed upon set of criteria that define a high-quality Thellier-Thellier experiment because every data set has different mineralogy, degrees of magnetic contamination, and experimental methodologies. The list of criteria described in Table 3.4 were chosen to maximize the number of sites having repeatable measurements. Note, the evaluation of *Tauxe et al.* [2004] used different criteria from those presented here. By including the raw data from *Tauxe et al.* [2004] in this study, we evaluate all specimen and site-level paleointensity analyses with consistent criteria for all Antarctica paleointensity results. 53% (or 177) of the 333 specimens interpreted after visual inspection passed the specimen-level criteria described in Table 3.4. Many of the 177 specimens are well behaved, with statistics far better than the cut-off levels, examples of which are shown in Figure 3.5.

Table 3.4 Specimen Level Cutoff Criteria

Statistic	Cutoff
f_{vds}	> 0.2
MAD	< 9.0°
β	< 0.09
DANG	< 13.0
Z	< 3.0
DRATS	< 17.0

As seen in *Ben-Yosef et al.* [2008] the most dramatic improvement in consistency of paleointensity results for each site occurs as a result of setting an appropriate cut-off for DRATS, the alteration check statistic. Consequently, the cut-off value for DRATS (DRATS < 17.0) rejects more specimen intensities than other specimen-level criterion choice (e.g. Z < 3, or DANG < 13). For thoroughness, we present several examples of problematic and borderline data in Figure 3.7 to demonstrate how the criteria selectively retain or reject particular behaviors that plague paleointensity studies and have characteristic signatures in Arai plot and vector-endpoint diagrams. For example, the specimen mc113a2 (Figure 3.7a) is rejected due to high DRATS (17.3), while mc113j1 is included with a slightly lower DRATS (13.2). Clearly, the pTRM checks are better for specimen mc113j1 than for mc113a2. Specimen mc225b1 is included but exhibits moderate DANG (5.7) and high MAD (7.1). Specimen mc128b1 is an example where only a portion of the Arai plot is interpreted due to failure of pTRM checks at high temperature steps. A summary of site-level results is presented in Table 3.5.

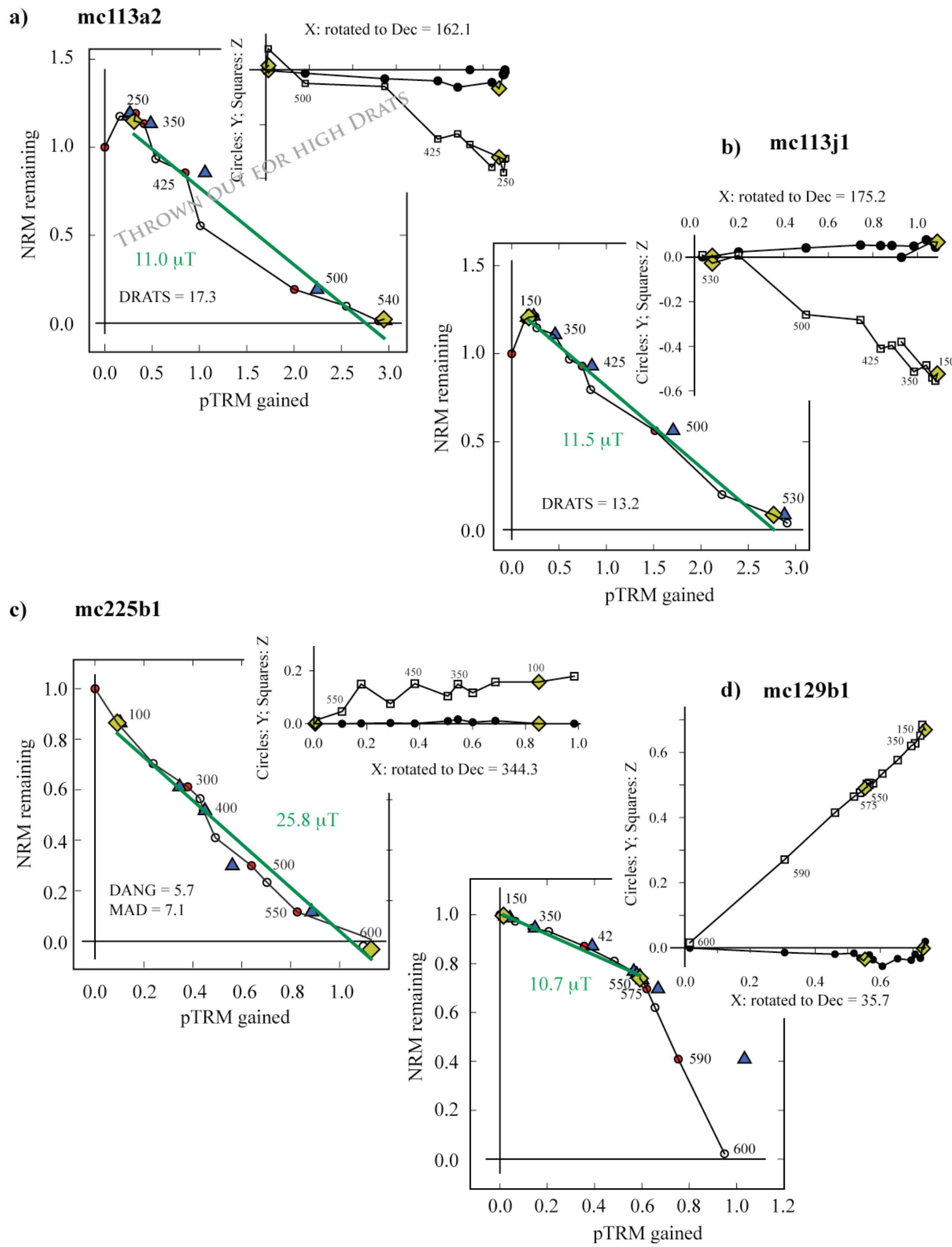

Figure 3.7: Same as Figure 3.5 for specimens **a)** mc113a2 **b)** mc113j1 **c)** mc225b1 and **d)** mc129b1 where NRM has been normalized to 3.99×10^{-5} Am^2, 3.71×10^{-5} Am^2, 3.87×10^{-6} Am^2, 3.96×10^{-5} Am^2, respectively. These specimens represent examples of marginally-acceptable paleointensity results. The specimen-level criterion(a) that the sample nearly fails are labels in each subplot. Specimen mc113a2 is removed from any analysis for failing the DRATS criterion (see text), while mc113j1, mc225b1 and mc129b1 are included.

Table 3.5 Site Paleointensity Summary

Site	N_B	B (μT)	σ_B	$d\sigma_B$	VADM (ZAm^2)	σ_{VADM}
mc105	4	31.03	1.24	4.00	40.68	1.62
mc109	3	34.80	1.16	3.30	45.62	1.51
mc111	2	23.68	0.30	1.30	31.05	0.39
mc113	2	11.82	0.46	3.90	15.5	0.60
mc115	2	24.60	0.43	1.80	32.25	0.57
mc116	1	38.53	0.00	--	50.52	--
mc117	4	26.41	0.73	2.80	34.63	0.95
mc119	5	40.32	1.28	3.20	52.87	1.68
mc120	5	24.32	0.72	3.00	31.89	0.95
mc121	4	21.54	7.65	35.50	28.24	10.03
mc123	4	29.25	1.52	5.20	38.35	1.99
mc125	1	25.92	0.00	--	33.98	--
mc127	2	38.49	1.52	4.00	50.46	1.99
mc128	3	34.09	2.57	7.50	44.7	3.37
mc129	4	10.64	0.16	1.50	13.95	0.20
mc131	5	16.71	0.71	4.30	21.91	0.93
mc132	6	3.32	0.10	3.10	4.35	0.13
mc133	2	47.97	0.66	1.40	62.9	0.87
mc139	1	19.76	0.00	--	25.91	--
mc140	2	19.45	0.42	2.10	25.5	0.55
mc142	3	15.44	4.60	29.80	20.27	6.04
mc144	5	11.72	3.74	31.90	15.38	4.90
mc145	4	6.64	0.43	6.50	8.71	0.57
mc146	2	17.21	0.71	4.10	22.57	0.93
mc147	4	22.77	2.54	11.10	29.86	3.33
mc148	2	46.97	5.20	11.10	61.71	6.83
mc155	3	26.98	6.84	25.40	35.43	8.98
mc160	2	21.80	1.29	5.90	28.63	1.70
mc161	1	5.80	0.00	--	7.62	--
mc164	3	81.29	0.06	0.10	106.8	0.08
mc165	2	20.05	1.56	7.80	26.34	2.05
mc166	2	20.22	0.14	0.70	26.54	0.19
mc167	2	42.80	0.12	0.30	56.23	0.16
mc205	3	52.79	5.79	11.00	69.33	7.60
mc211	1	75.20	0.00	--	98.76	--
mc214	5	44.07	3.66	8.30	57.95	4.81

continued

Table 3.5 (continued)

Site	N_B	B (μT)	σ_B	$d\sigma_B$	VADM (ZAm^2)	σ_{VADM}
mc217	5	30.45	4.46	14.60	40.01	5.85
mc218	5	34.30	2.48	7.20	45.06	3.26
mc219	1	33.58	0.00	--	44.08	--
mc220	3	54.32	1.19	2.20	71.38	1.56
mc222	1	12.67	0.00	--	16.64	--
mc223	3	22.60	1.90	8.40	29.68	2.50
mc225	2	25.91	0.08	0.30	34.03	0.10
mc226	1	20.95	0.00	--	27.52	--
mc01	2	19.99	0.18	0.90	26.24	0.24
mc08	3	43.36	1.51	3.50	56.92	1.98
mc09	2	23.65	1.11	4.70	31.07	1.46
mc10	1	40.21	0.00	--	52.82	--
mc11	1	23.43	0.00	--	30.78	--
mc13	2	28.39	4.46	15.70	37.28	5.85
mc14	2	55.28	21.76	39.40	72.64	28.59
mc15	4	26.66	3.65	13.70	35.03	4.80
mc19	1	25.18	0.00	--	33.05	--
mc21	4	43.28	6.74	15.60	56.75	8.83
mc26	4	11.97	0.63	5.30	15.7	0.83
mc28	1	27.55	0.00	--	36.12	--
mc30	3	39.28	0.55	1.40	51.49	0.72
mc32	3	35.88	7.90	22.00	47.03	10.35
mc34	1	23.05	0.00	--	30.21	--
mc35	2	24.86	0.83	3.30	32.58	1.08
mc36	4	24.59	3.65	14.80	32.23	4.78
mc37	4	59.43	9.30	15.70	77.89	12.19
mc38	1	46.31	0.00	--	60.69	--
mc39	2	22.55	4.81	21.30	29.55	6.30
mc40	1	39.36	0.00	--	51.59	--
mc44	1	38.66	0.00	--	50.67	--

N_B is the number of specimens meeting the minimum specimen-level criteria and used to calculate site mean intensity. B (μT) is the average field strength per site. σ_B is standard deviation of the specimens used to calculate the site average intensity (B). $d\sigma_B$ is the standard deviation of the specimen intensities as a percent fraction of the mean intensity. VADM (ZAm^2) is the virtual axial dipole moment where Z = 10^{21}. σ_{VADM} is the standard deviation of the specimens used to calculate the average VADM.

In addition to the specimen-level statistics, we evaluate site-level statistics to ensure that outliers do not adversely effect our final paleointensity estimation. The most fundamental site-level statistic is the number of specimens evaluated per site, N_B. We require within-site reproducibility, which means $N_B \geq 2$. There is a tradeoff between increasing the N_B cut-off and decreased number of sites available for analysis. The second site-level statistic is the standard deviation of the specimen intensities as a percent fraction of the mean intensity, which we define as $d\sigma_B = 100 \times \sigma_B / \bar{B}$. By implementing a $d\sigma_B$ cut-off, we institute further tradeoff between site reproducibility and site quantity. We explore a range of values for both of these statistics to determine the optimal pair of statistic cut-offs as well as the stability of the resultant intensity for all sites (Table 3.6). The resultant mean paleointensities are statistically indistinguishable for all pairs of cut-off criteria. Therefore, we choose $N_B \geq 2$ and $d\sigma_B \leq 15.0$ to maximize the number of sites (and ages) interpreted in this study, providing a mean paleointensity of 29.39 ± 2.35 μT. The equivalent virtual axial dipole moment (VADM) is 3.86 ± 0.31 ZAm^2. In fact, even if no specimen- or site-level criteria are used, the average intensity (29.1 ± 1.1 μT) for all 333 interpreted specimens is statistically indistinguishable from all mean values in Table 3.6. Consequently, we are confident that the mean paleointensity and corresponding standard deviation are robustly determined.

Table 3.6 Average Paleointensity Results

Criteria	Age	N_{sites}	$\overline{B}$ (μT)	STD Error
$N_B \geq 2$, $d\sigma_B \leq 20$	No cutoff	43	30.38	2.32
$N_B \geq 3$, $d\sigma_B \leq 20$	No cutoff	26	32.64	3.30
$N_B \geq 2$, $d\sigma_B \leq 15$	**No cutoff**	**40**	**29.39**	**2.35**
$N_B \geq 3$, $d\sigma_B \leq 15$	No cutoff	24	31.08	3.48
$N_B \geq 2$, $d\sigma_B \leq 10$	No cutoff	34	28.57	2.62
$N_B \geq 3$, $d\sigma_B \leq 10$	No cutoff	19	30.99	4.21
All specimens	No cutoff	333	29.09	1.07
$N_B \geq 2$, $d\sigma_B \leq 15$	0 -5 Ma	30	30.43	2.62
$N_B \geq 2$, $d\sigma_B \leq 15$	0 - 0.78 Ma	11	34.89	3.69
$N_B \geq 2$, $d\sigma_B \leq 15$	0.78 - 2.58 Ma	19	27.84	3.46

Criteria define the set of site-level cut-offs used to determine an acceptable site result. Age is the range of ages used to calculate the average location paleointensity, $\overline{B}$. N_{sites} is the number of sites used to calculate, $\overline{B}$. STD error is the standard deviation of the mean location paleointensity.

3.4 $^{40}Ar/^{39}Ar$ Results

We selected 21 normal and reverse polarity sites from the 2003/2004 field season for new age determinations by the $^{40}Ar/^{39}Ar$ incremental heating method in the geochronology laboratory at New Mexico Tech. Fresh groundmass concentrates weighing 50 – 100 mg were prepared by crushing and sieving optimally chosen samples and then washing the fractions in diluted HCl. Standard magnetic separation techniques and hand-picking were employed to remove phenocryst phases including olivine, pyroxene, and calcic plagioclase. Splits from each sample were loaded into machined aluminum discs and irradiated in one batch (NM-207) for 6 hours in the D-3 position at the Nuclear Science Center, College Station, TX. They were then allowed to cool for 3 months. Samples were degassed using a double vacuum resistance furnace with molybdenum crucible and crucible liner with a heating duration of 10 minutes. Reactive gas species were removed using 2 SAES GP-50 getters operated at ~450°C and 1 getter at 20°C prior to isotope separation in the Mass Analyzer Products Limited (MAP) 215-50 noble gas mass spectrometer. J-factors were determined to a precision of ± 0.1% by CO_2 laser-fusion of 6 single crystals from each of 6 radial positions around the irradiation tray. Correction factors for interfering nuclear reactions were determined using K-glass and CaF_2. Ages are calculated using the decay constants and isotopic abundances from *Steiger and Jäger* [1977] and are calculated relative to FC-2 Fish Canyon Tuff sanidine interlaboratory standard (28.02 Ma, *Renne et al*. [1998]). Reported plateau ages for step-heated samples are weighed by the inverse variance for the steps which met plateau criteria (3 or more contiguous steps comprising more than 50% of ^{39}Ar released which agreed to within $\pm 2\sigma$). Imprecise, low-radiogenic-yield initial and final steps were excluded from age plateaus. MSWD (mean square weighted deviate) values are calculated for each weighted mean, and errors are determined using the method of *Taylor* [1982]. If the MSWD value is greater than 1, the error is multiplied by the square root of the MSWD. Details of the analytical methods and the analytical data are available in the EarthRef Digital Archive (ERDA).

All samples, with the exception of mc100 and mc143 yielded fairly flat age spectra having well-defined, relatively precise ($\pm 2\sigma$ < 0.2 Ma) plateau ages that agree within error with isochron intercept ages. All isochrons have $^{40}Ar/^{36}Ar$ intercepts within error of the atmospheric value (295.5) indicating no significant excess ^{40}Ar is present in the dated groundmass concentrates. Examples of selected age spectra and correlation diagrams are shown in Figure 3.8. A summary of age information is provided in Table 3.7 which displays $^{40}Ar/^{39}Ar$ ages ranging from 0.29 ± 0.02 Ma to 13.42 ± 0.18 Ma, with all errors given as $\pm 2\sigma$.

3.5. Discussion

The data set presented here provides a unique opportunity to examine paleointensity and paleodirection at high latitude. The complete dataset analyzed includes directional (93 sites) and intensity (40 sites) results from this new study and results from *Tauxe et al.* [2004] from the same volcanic province. The intensity results from the previous study were reanalyzed to maintain consistency in specimen-level quality. All sites from this combined data set have $k > 50$ and $n \geq 5$, criteria suggested by *Johnson et al.* [2008] as requirements for high-quality directional data. 82 sites from this combined data set have associated radiometric $^{40}Ar/^{39}Ar$ dates ranging from 0.026 Ma to 13.422 Ma, 8 sites of which are older than 5 Ma. This data set represents a substantial number of high-quality directions with a non-Fisherian distribution and a mean direction that is indistinguishable from GAD (Figure 3.6b). The good temporal distribution of these high-quality data enable us to compare behavior between the Brunhes and Matuyama polarity chrons, as there are an unusually large number of samples with ages between 0.78 and 2.58 Ma.

The inclination anomalies, presented here, provide important high-latitude constraints on the TAF. The observation of negligible 0-5 Ma inclination anomaly (< 3°,

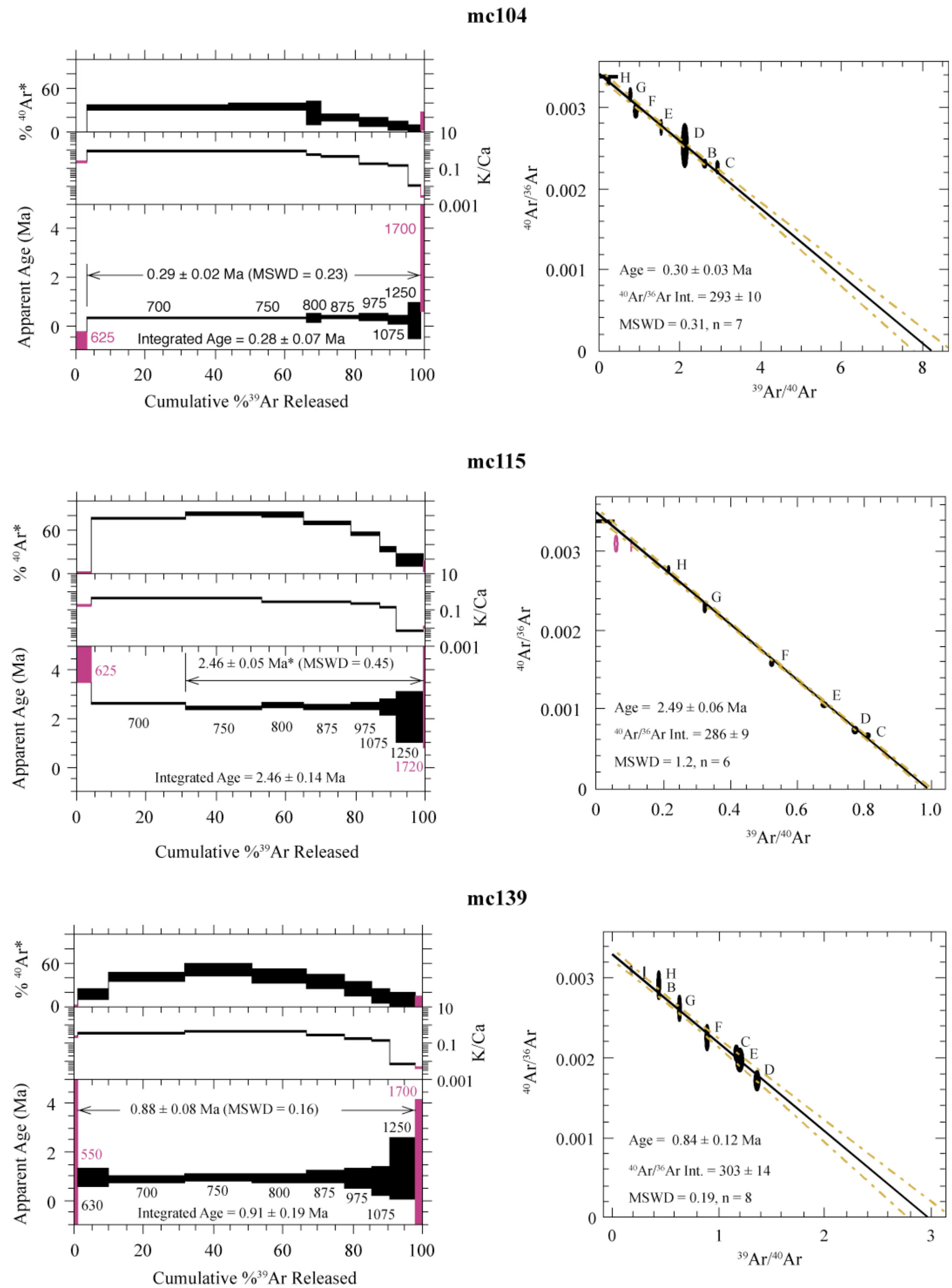

Figure 3.8: Examples of $^{40}Ar/^{39}Ar$ spectra from selected samples. Data from incremental heating experiments are plotted as apparent age at each temperature step vs. cumulative fraction of ^{39}Ar released. The black arrow indicated the steps used in the calculation of the weighted mean plateau age. All errors reported are 2σ with the error in J.

Table 3.7 Summary of $^{40}Ar/^{39}Ar$ Results

Sample	Lab #	Irrad	material	Preferred Age analysis	n	%^{39}Ar	MSWD	K/Ca ± 2σ	Age ± 2σ, Ma	Comments
mc100	57090-01	NM-207G	GMC	Plateau	5	67.1	0.8	0.1 ± 0.0	0.86 ± 0.23	poor precision
mc104	57100-01	NM-207J	GMC	Plateau	7	95.6	0.2	0.6 ± 0.6	0.29 ± 0.02	
mc106	57097-02	NM-207H	GMC	Plateau	7	84.7	0.8	0.2 ± 0.0	13.42 ± 0.18	
mc108	57092-01	NM-207H	GMC	Plateau	5	73.5	1.4	0.2 ± 0.2	0.41 ± 0.14	
mc111	57095-01	NM-207H	GMC	Plateau	4	75.8	0.8	0.3 ± 0.2	1.99 ± 0.04	
mc115	57094-01	NM-207H	GMC	Plateau	6	68.1	0.5	0.3 ± 0.3	2.46 ± 0.31	
mc118	57089-01	NM-207G	GMC	Plateau	7	93.7	1.7	0.6 ± 0.4	0.31 ± 0.04	
mc122	57085-01	NM-207F	GMC	Plateau	5	68.0	1.4	0.5 ± 0.3	12.70 ± 0.09	
mc123	57099-01	NM-207J	GMC	Plateau	6	87.0	1.3	0.4 ± 0.3	1.93 ± 0.05	
mc124	57084-01	NM-207F	GMC	Plateau	7	92.0	1.8	0.3 ± 0.3	12.61 ± 0.11	
mc130	57086-01	NM-207G	GMC	Plateau	5	58.5	0.8	0.3 ± 0.2	7.25 ± 0.07	
mc134	57093-01	NM-207H	GMC	Plateau	5	84.5	1.5	0.3 ± 0.1	9.02 ± 0.05	
mc139	57081-01	NM-207F	GMC	Plateau	8	97.0	0.2	0.3 ± 0.3	0.88 ± 0.08	
mc140	57083-02	NM-207F	GMC	Plateau	4	69.7	0.5	0.3 ± 0.1	2.03 ± 0.09	
mc142	57080-01	NM-207F	GMC	Plateau	5	79.7	2.0	6.8 ± 3.9	1.23 ± 0.02	
mc143	57082-01	NM-207F	GMC	Plateau	8	75.9	1.0	0.0 ± 0.0	2.08 ± 0.65	very poor precision
mc164	57087-02	NM-207G	GMC	Plateau	6	76.8	1.0	15.3 ± 19.2	1.36 ± 0.01	
mc165	57088-01	NM-207G	GMC	Plateau	7	84.8	0.7	0.4 ± 0.4	1.45 ± 0.06	
mc166	57096-02	NM-207H	GMC	Plateau	7	93.0	2.7	0.7 ± 0.5	1.33 ± 0.12	
mc168	57091-01	NM-207G	GMC	Plateau	6	85.3	1.7	0.5 ± 0.3	1.38 ± 0.05	
mc170	57098-02	NM-207J	GMC	Plateau	6	74.1	0.8	0.3 ± 0.1	1.03 ± 0.10	

Notes:
GMC is Groundmass Concentrate
Ages are calculated relative to FC-2 Fish Canyon Tuff sanidine interlaboratory standard (28.02 Ma, [*Renne et al.*, 1998]).
Analyses were performed at New Mexico Geochronology Research Laboratory using an MAP 215-50 mass spectrometer on line with automated all-metal extraction system.
All errors are reported at ±2σ.
Details of irradiation, analytical procedures, calculation methods, and analytical data are in Data Repositiory.

Table 3.2) at this location is not unexpected since previous observational and modeling studies predict the largest inclination anomaly at equatorial latitudes [see review in *Johnson and McFadden*, 2007]. We also analyze the Brunhes and Matuyama chrons separately; these show a small mean negative inclination anomaly during the Brunhes, and a larger amplitude positive mean inclination anomaly during the Matuyama. This is consistent with the conclusions of *Johnson et al.* [2008] that inclination anomalies are small and negative for the Brunhes, and in the southern hemisphere, are larger and positive in the Matuyama.

We also investigate VGP dispersion to characterize PSV behavior. As presented by *McElhinny et al.* [1996] many studies have observed polarity chron dependence of dispersion, where the Matuyama (as compared to the Brunhes) is often associated with higher than average dispersion. In this study we find no evidence for differences in dispersion for the Brunhes and Matuyama polarity chrons. For the EVP study, regardless of the VGP cut-off applied (none, Vandamme, or $|\lambda_{VGP}| < 45°$) the dispersion for all data (0 – 5 Ma), the normal Brunhes, or the reverse Matuyama chron are statistically indistinguishable from each other. However, the implementation of a λ_{VGP} cut-off does result in lower estimates of dispersion (e.g., for the 0-5 Ma combined polarity data the dispersion is ~24° vs. ~35°). This is due to the classification of either 8% or 15% of the data as transitional for the Vandamme and 45° λ_{VGP} cut-offs, respectively. The mean dispersion calculated with the Vandamme λ_{VGP} cut-off is slightly higher (26.6 ± 2.5°) than, but statistically indistinguishable from that calculated using the $|\lambda_{VGP}| < 45°$ cut-off (23.7 ± 3.2°), because of the removal of fewer low VGP-latitude data.

While not polarity chron dependent for this region, the dispersion results presented here do support the observation of a latitudinal variation in dispersion in the southern hemisphere. This is apparent when the Antarctic results are compared with those from other high-quality directional datasets [*Johnson et al.*, 2008] (Figure 3.9). The high dispersion is not a function of poor data quality, since this data set passes all the criteria set out by *Johnson et al.* [2008] for directional results. We compare the new high-latitude dispersion results with predictions from two PSV models - Model G [*McFadden et al.*, 1988], and a statistical model, TK03, [*Tauxe and Kent*, 2004]. Statistical PSV models, such as TK03, allow the prediction of geomagnetic field vectors at any location, by modeling the time-varying geomagnetic field as a "Giant Gaussian Process" in which the spherical harmonic coefficients are assumed to be temporally

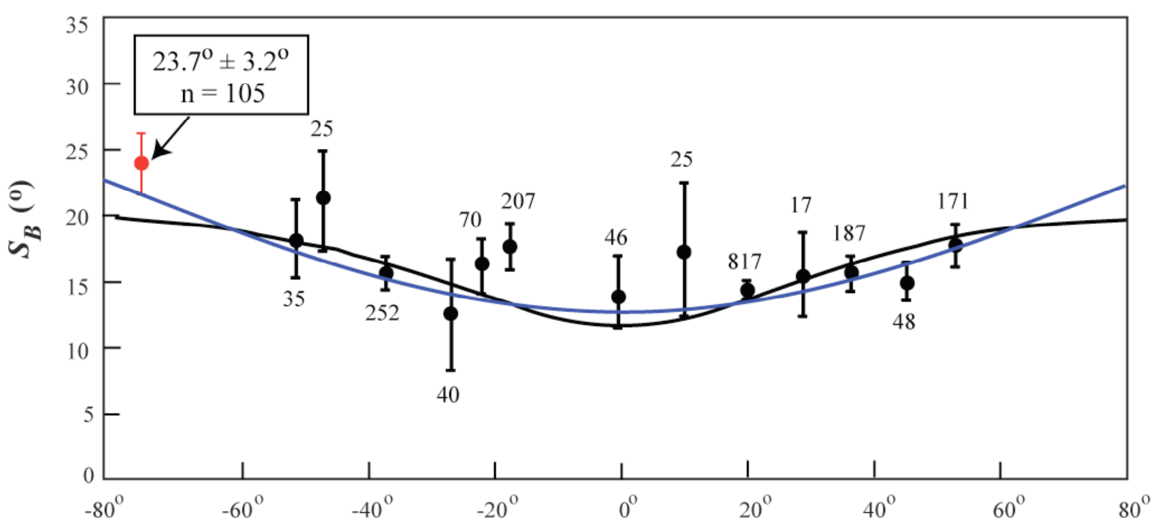

Figure 3.9: VGP dispersion (S_B) as a function of latitude. The mean dispersion for the Erebus Volcanic Province shown as a red circle, all other data from *Johnson et al.* [2008] shown as black circles. Errors bars are 2σ. All data have $k > 50$, Age < 5 Myr, and $|\lambda_{VGP}| < 45°$. Model G [*McFadden et al.*, 1988] shown in blue and model, TK03 [*Tauxe and Kent*, 2004] shown in black.

independent random variables with Gaussian distributions [see *Johnson and McFadden*, 2007 for a review]. The high dispersion at -78° is underestimated by the PSV model TK03, but predicted by the Model G. Clearly PSV models that predict flat [e.g. CP88, *Constable and Parker*, 1988] dispersion with latitude do not explain the southern hemisphere observations.

A common assumption is that the time-averaged geomagnetic field can be approximated by a dipole. The intensity of an axial-dipole field varies with latitude according to the following equation:

$$B = g_1^0 \left(1 + 3\cos^2\theta\right)^{1/2}, \tag{3.4}$$

where g_1^0 is the axial dipole term in the spherical harmonic expansion and θ is colatitude. Consequently, the intensity at either pole should be twice that of the equatorial value. Today's field (represented by IGRF2005) has a latitudinal dependence (black line in Figure 3.10) that is strikingly similar to that of a dipole (blue line, Figure 3.10) with a g_1^0 term equal to 30 μT. The statistical PSV model, TK03 shows a similar pattern of increase in intensity near the poles. However, when paleointensities from the 0-5 Ma time period are plotted versus latitude, evidence for a dominantly dipole field is not obvious. Figure 3.10 shows site-averaged paleointensity estimates (1158 grey crosses) derived from the Pint06 database [*Tauxe and Yamazaki*, 2007]. For consistency, all data from Pint06 included in Figure 3.10 pass the same site-level criteria as outlined in section 3.3.2. Southern hemisphere data are combined with the Northern hemisphere to minimize the influence of latitudinal gaps. To reduce the effects of regional variations, the site-level estimates are averaged in 15° latitude bins (black diamonds) with 95%

confidence levels calculated using a bootstrap technique. For comparison, all McMurdo Volcanic Province paleointensities are plotted on Figure 10 as red crosses, and the associated mean is plotted as a red diamond with corresponding 95% confidence level of the means.

The 0-5 Ma mean paleointensity for McMurdo (red diamond) is well determined and is low (29.39 ± 2.35 μT) relative to current intensity (~63 μT). Outliers do not heavily bias the mean as the median lies within the 95% confidence intervals from the mean. The intensities for both the Brunhes (34.89 ± 3.69 μT) and Matuyama (27.84 ± 3.46 μT) magnetic chrons are low, but statistically indistinguishable from each other and from the 0-5 Ma mean. The relatively high dispersion and low intensity observed here agrees with the global observation of anti-correlation between dispersion and intensity [e.g. *Bogue and Coe*, 1984; *Love*, 2000].

We consider several possible hypotheses for the lack of high 0-5 Ma high-latitude intensities and specifically for those presented here. First, we investigate possible bias introduced by an uneven temporal sampling of a dipole field with varying intensity. Following *Ziegler et al.* [2008] we model the g_1^0 term as a time-varying function and sample the theoretical dipole intensity at known times and latitudes associated with both the Pint06 dataset and McMurdo volcanic province data. The time-varying g_1^0 function is modeled as random series with power spectra as defined by *Ziegler et al.* [2008], who fit a simple functional form to approximate the empirical power spectrum of the 0 - 160 Ma paleointensity data set as modeled by *Constable and Johnson* [2005]. The functional

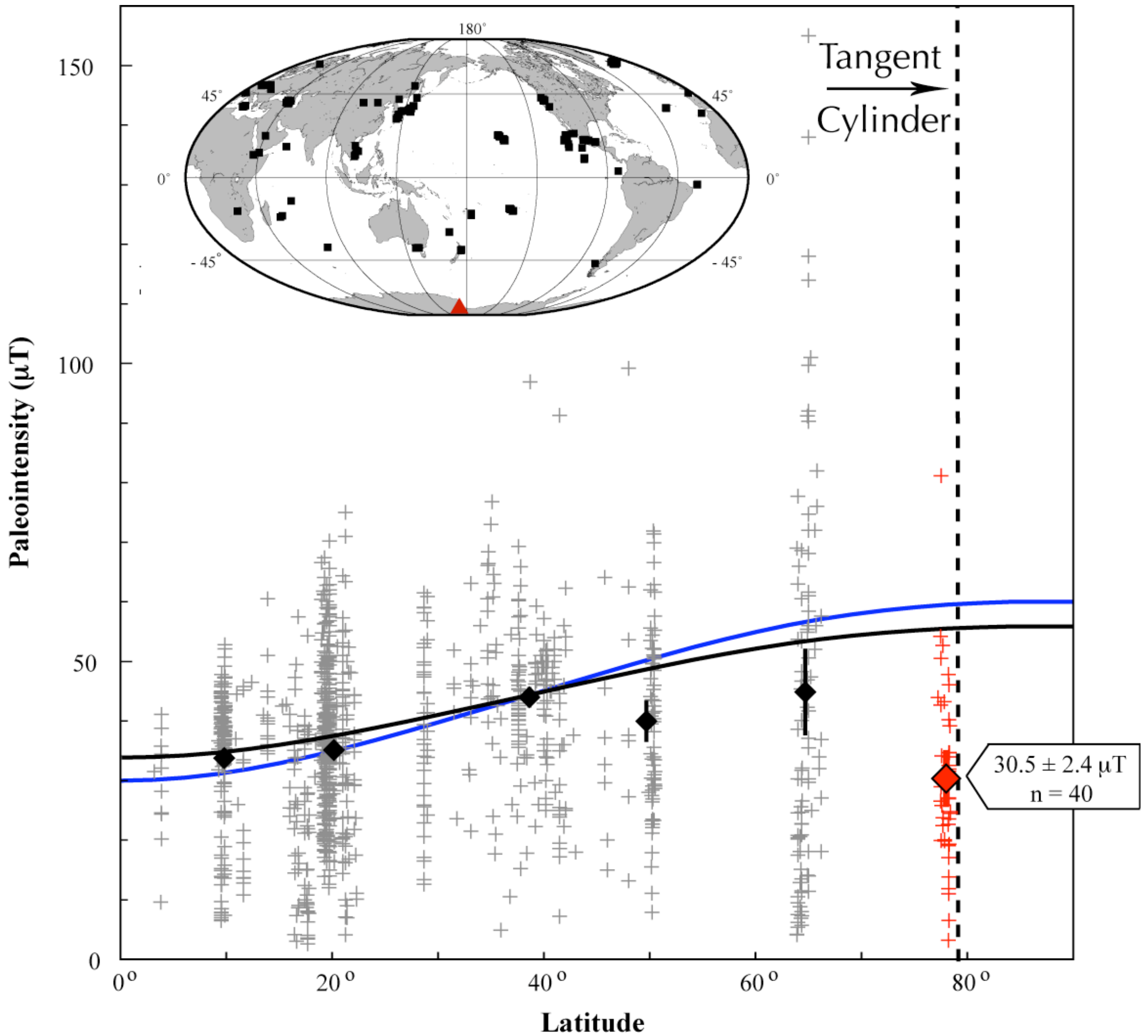

Figure 3.10: Paleointensity vs. latitude of the Pint06 database (grey crosses) [*Tauxe and Yamazaki*, 2007] and paleointensity estimates from this study (red crosses) for data with ages less than 5 Ma, $d\sigma_B \leq 15$ μT, and $N_{site} \geq 2$. Mean paleointensity results (black diamonds) are calculated for 15º latitude bins and errors are shown as 2σ. The black line is the longitudinal-averaged intensity for today's field. The vertical dashed line is the surface expression of the edge of the tangent cylinder. The locations of the paleointensity results are shown in the inset with the Antarctica data set as a red triangle. Southern hemisphere data have been flipped to the Northern hemisphere. The black line represents the mean intensity for today's field as defined by the 2005 IGRF model coefficients, while the blue line represents the intensity associated with a geocentric axial dipole with a dipole term of 30 μT.

form and empirical power spectrum are constant to a corner frequency of 10^{-5} yr^{-1} and decay according a power law thereafter.

We test a set of 100 stochastic time-varying functions computed with distinct randomizing seeds. We set the minimum and maximum values of the g_0^1 term to 5 and 60 μT, respectively. We then determine the average intensity for 15° bins as done above. While many of the resultant average intensities increased with latitude, many do not, of which one example is shown in Figure 3.11. Approximately two out of three resultant intensity-latitude distributions were dampened/flattened to some degree. Nearly half of the modeled average intensity-latitude distributions had lower intensity at high latitude than mid latitude. In Figure 3.11 the minimum and maximum values of the g_1^0 term were 10 and 40 μT, providing a relatively flat intensity-latitude distribution. We do not attempt to optimize for a preferred model because there are an infinite number of possible theoretical solutions that could used random, sinusoidal, cosinusoidal, Gaussian, or uniform time varying functions for the g_1^0 term in the 0 – 5 Ma period. Instead we have merely demonstrated that a flat intensity with respect to latitude may result from non-uniform temporal sampling of a time varying field. As with the 0 - 1 Myr time interval (*Ziegler et al.,* 2008), the current 0-5 Myr data compilation appears to have insufficient temporal sampling to robustly characterize the 0 – 5 Myr dipolar intensity.

Next, we test whether spatial bias due to non-uniform sampling of the global magnetic field, can produce similarly flat intensity with respect to latitude. We simulate paleointensities using the PSV model TK03 at the same locations as Pint06 and our Antarctica sites. We simulate 100 points per site and find little effect due to spatial biasing. When the results are averaged in 15° bins, the averages show an increase in intensity with latitude. The results from this and the previous tests indicate that inadequate spatial sampling is less significant than inadequate temporal sampling in the paleointensity database.

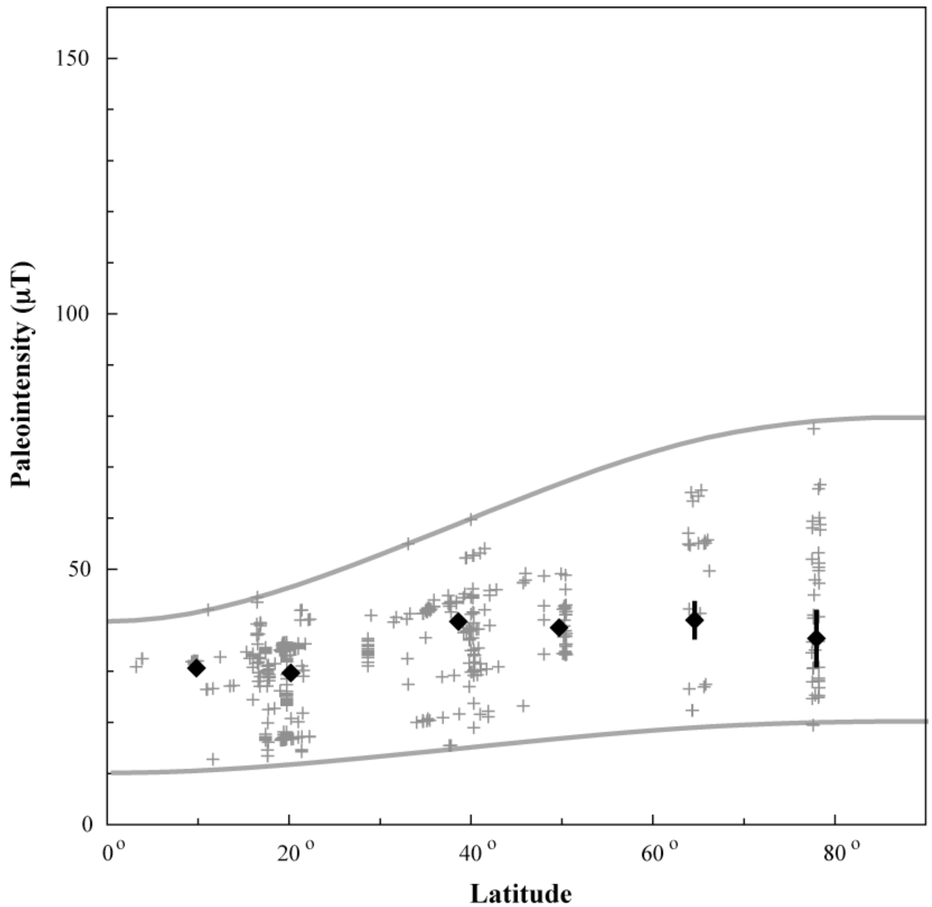

Figure 3.11: Paleointensity vs. latitude for a theoretical dipole that was allowed to vary between 10 and 40 μT and was sampled at equivalent times as the Pint06 database site ages. Mean paleointensity (black diamonds) was calculated for every 15° latitude bin. Grey lines are dipole fields with mean values of 10 (lower) and 40 (upper) μT.

The lower than expected mean field in Antarctica may not be due strictly to temporal sampling bias. It may be a result of geodynamical differences in the outer core.

Therefore we examine high-latitude predictions from some magnetohydrodymamic models by *Glatzmaier et al.* [1999] and *Sreenivasan and Jones* [2006] that include both convective regimes (internal and external to the tangent cylinder) with paleomagnetic results from Antarctica and discuss possible constraints the high-latitude paleointensity results place on the models. Three-dimensional geodynamical models of the convective core are self-consistent computer simulations of the simultaneous solution to the nonlinear equations of magnetohydrodynamics (equations describing thermodynamics, velocity and magnetic field generation).

Glatzmaier et al. [1999] produce eight simulations (Models A-H) based on different, time-independent patterns of radial heat flux imposed at the core-mantle boundary (CMB) that span 300,000 years. The magnetic field predicted in these models is predominantly dipolar in structure with a time-dependent westward drift of the non-dipolar component. Model E is the only model that exhibits increased in dispersion with latitude, as observed in this study. While Model G correctly simulates a decrease in intensity during both excursions and reversals, it does not correctly predict either dispersion or intensity as observed here. Model H predicts that an Earth-like CMB heat flux boundary condition will produce a not only uniform dispersion with latitude, but also a low absolute value of intensity which is roughly dipolar with latitude. However, none of the *Glatzmaier et al.* [1999] models predict both the increased dispersion with latitude and the absolute values of dispersion observed in the global record. Model E exhibits increased dispersion with latitude but the model remains dipolar with normal polarity for the duration of its lifetime. With respect to high-latitude observations, none of the *Glatzmaier et al.* [1999] models predict lower field intensity at high latitude at Earth's surface. Conversely, the *Sreenivasan and Jones* [2006] model predicts regions of lower field intensity at the core-mantle boundary within the tangent cylinder due to transient core convective upwellings. But this model currently lacks equivalent magnetic field predictions at the Earth's surface from which direct comparisons between the magnetohydrodynamic model and paleointensity data can be made; and it is likely that the upward continuation to Earth's surface of the field produced by this model will not exhibit measurable intensity lows at the poles. Therefore, the low paleointensity observed in this data set could merely represent a transient regional feature, and may not represent the typical time-averaged field structure at high latitudes. Unfortunately, the comparison presented here cannot be substantiated because the aforementioned models.

Further investigations of spatio-temporal properties of geodynamo models exhibiting polar vortices are necessary to realistically compare paleomagnetic data with the model outputs. Both the high dispersion and low intensity seen at this locale may indicate some unusual behavior at the pole due to tangent cylinder convective changes. However, we cannot differentiate among the possible causes until we have both a more uniformly sampled data set and the geodynamical models can provide paleomagnetic observables for million year timescales.

3.6 Conclusions

The analyses of new volcanic sites in the Erebus Volcanic Province (EVP), Antarctica from two recent field seasons and previous results from *Tauxe et al.* [2004] provide evidence for high dispersion and low intensity at high latitude (-78°). These studies provide 125 new sites with high-quality directional data ($n \geq 5$ and $k > 50$) and ages ranging from 0 to 5 Ma. The directions have a non-Fisherian distribution and a mean direction that is indistinguishable from GAD. The directions also yield a small inclination anomaly (~3°) for this location, which is not unexpected, as the dipole components of the magnetic field will dominate at high latitude.

New $^{40}Ar/^{39}Ar$ ages were determined for twenty-four new reverse & normal polarity sites. With these new radiometric dates and existing dates from *Esser et al.* [2004] and *Wilch* [1991, *et al.* 1993] most of the sites investigated here (82) were radiometrically dated, so Brunhes and Matuyama chrons may be compared. For the McMurdo volcanic province study, regardless of the λ_{VGP} cut-off applied (none, Vandamme, or $|\lambda_{VGP}| < 45°$) the dispersion for all data (0 – 5 Ma), the normal Brunhes, or the reverse Matuyama chron are statistically indistinguishable from each other. However, the dispersion for the Erebus Volcanic Province is high (23.7 ± 3.2°) in comparison to dispersion from mid to low-latitudes, which is not a function of poor data quality as proposed by *Johnson et al.* [2008]. Interestingly, Model G fits the EVP dispersion within the 95% confidence intervals, while the PSV model, TK03, underestimates the measured dispersion.

IZZI and Coe modified Thellier-Thellier experiments provided 40 paleointensity estimates, for which 75% have associated radiometric dates. The mean EVP paleointensity is 29.39 ± 2.35 μT and is low relative to current intensity (~63 μT) at McMurdo. The intensities for both the Brunhes (34.89 ± 3.69 μT) and Matuyama (27.84 ± 3.46 μT) magnetic chrons are also low, and statistically indistinguishable from each other and the 0-5 Ma mean. The observed high dispersion and low intensity are predicted by the global anti-correlation between dispersion and intensity [e.g. *Bogue and Coe*, 1984; *Love*, 2000]. When latitudinal averages for global paleointensity estimates for the past 5 Myr are plotted there is no sign of the expected increase with latitude due to a dipole field. One plausible explanation for this is temporal sampling bias in a (dipolar) field with time varying magnitude. While these paleomagnetic data cannot provide direct dynamical constraints on features like polar vortices inside the tangent cylinder, they will provide useful constraints on statistical models for PSV. In conjunction with theoretical studies of numerical dynamo simulations, future studies may lead to greater insight about tangent cylinder field dynamics.

3.7 Acknowledgements

We thank Julie Bowles, Jasper Konter, and Elise Sbarbori for their hard work in the field to collect these samples. We thank Jason Steindorf for his contributions in sample preparation and processing. We also thank Frank Vernon, Mert Ingraham, and Mark Zumberge for their collaboration efforts in developing the GPS orientation method. This research was supported by NSF grants 0538392 and 0229403.

This chapter has been submitted for publication uder the following citation, Lawrence, K. P., L. Tauxe, H. Staudigel, C. G. Constable, W. McIntosh, M. Heizer, C. L. Johnson (2008), Paleomagnetic field properties near the southern hemisphere tangent cylinder, *Geophysics, Geochemistry and Geosystems*.

3.8 References

Armstrong, R. L. (1978), K-Ar dating: Late Cenozoic McMurdo Volcanic Group and dry valley glacial history, Victoria Land, Antarctica, *J. of Geol. and Geophys*, *21*(6), 685-698.

Ben-Yosef, E., et al. (2008), Application of copper slag in archeointensity research, *J. Geophys. Res.*, submitted.

Bloxham, J., et al. (1989), Geomagnetic secular variation, *Philos. Trans. R. Soc. London, Ser. A*, *329*(1606), 417.

Bloxham, J., and A. Jackson (1992), Time-Dependent Mapping Of The Magnetic-Field At The Core-Mantle Boundary, *J. Geophys. Res.*, *97*(B13), 19537-19563.

Bogue, S., and R. S. Coe (1984), Transitional paleointensities from Kauai, Hawaii, and geomagnetic reversal models, *J. Geophys. Res.*, *89*(12), 10,341-310,354.

Cande, S. C., et al. (2000), Cenozoic motion between East and West Antarctica, *Nature*, *404*, 145-150.

Carlut, J., et al. (2000), Paleomagnetic directions and K/Ar dating of 0 to 1 Ma lava flows from La Guadeloupe Island (French West Indias): Implications for time-averaged field models, *J. Geophys. Res.*, *105*(B1), 835-849.

Coe, R. S., et al. (1978), Geomagnetic paleointensities from radiocarbon-dated lava flows on Hawaii and the question of the Pacific nondipole low, *J. Geophys. Res.*, *83*, 1740-1756.

Constable, C. G., and R. L. Parker (1988), Statistics of the geomagnetic secular variation for the past 5 m.y., *J. Geophys. Res.*, *93*, 11569-11581.

Constable, C. G., and C. L. Johnson (2005), A paleomagnetic power spectrum, *Phys. Earth Planet. Inter.*, *153*(1-3), 61-73.

Creer, K. M. (1962), The dispersion of the geomagnetic field due to secular variation and its determination from remote times from paleomagnetic data, *J. Geophys. Res.*, *67*, 3461-3476.

Esser, R. P., et al. (2004), $^{40}Ar/^{39}Ar$ dating of the eruptive history of Mount Erebus, Antarctica: Volcano evolution, *Bull. Volcanol.*, *66*, 671-686.

Fisher, R. A. (1953), Dispersion on a sphere, *Proc. R. Soc. London, Ser. A*, *217*, 295-305.

Fitzgerald, P. (2002), Tectonics and landscape evolution of the Antarctic plate since the break-up of Gondwana, with an emphasis on the West Antarctic Rift System and the Transantarctic Mountains, *Bull. R. Soc. N. Z.*, *35*, 453-469.

Fleck, R. J., et al. (1972), K-Ar dates of the McMurdo volcanics and their relation to the glacial history of Wright Valley, *Antarctic Journal of the U.S.*, *7*, 244-246.

Glatzmaier, G. A., et al. (1999), The role of the Earth's mantle in controlling the frequency of geomagnetic reversals, *Nature*, *401*, 885-890.

Harrington, H. J. (1958), Nomenclature of rock units in the Ross Sea region, Antarctica, *Nature*, *182*(4631), 290.

Herrero-Bervera, E., and R. S. Coe (1999), Transitional field behavior during the Gilbert-Gauss and Lower Mammoth reversals recorded in lavas from the Wai'anae volcano, O'ahu, Hawaii, *J. Geophys. Res.*, *104*(B12), 29,157-129,173.

Holt, J. W., et al. (1996), Geomagnetic field inclinations for the past 400 kyr from the 1-km core of the Hawaii Scientific Drilling Project, *J. Geophys. Res.*, *101*(B5), 11655-11663.

Hulot, G., et al. (2002), Small-scale structure of the geodynamo inferred from Oersted and Magsat satellite data, *Nature*, *416*(6881), 620-623.

Jackson, A., et al. (2000), Four centuries of geomagnetic secular variation from historical records, *Philos. Trans. R. Soc. London, Ser. A*, *358*(1768), 957-990.

Johnson, C. L., et al. (1998), $^{40}Ar/^{39}Ar$ Ages and paleomagnetism of Sao Miguel lavas, Azores, *Earth Planet. Sci. Lett.*, *160*, 637 - 649.

Johnson, C. L., and P. L. McFadden (2007), The Time-averaged field and paleosecular variation, in *Treatise on Geophysics, Geomagnetism Volume*, edited by M. Kono, pp. 417-453, Elsevier.

Johnson, C. L., et al. (2008), Recent investigations of the 0-5 Ma geomagnetic field recorded by lava flows, *Geochem. Geophys. Geosyst.*, *9*, Q04030, doi:04010.01029/02007GC001719.

Jones, C. A. (2007), Thermal and compositional convection in the outer core, in *Treatise on Geophysics, Core Dynamics*, edited by P. Olson, pp. 131-185, Elsevier.

Kirschvink, J. L. (1980), The least-squares line and plane and the analysis of paleomagnetic data, *Geophys. J. R. Astron. Soc.*, *62*, 699-718.

Korte, M., and C. G. Constable (2005), Continuous geomagnetic field models for the past 7 millennia: 2. CALS7K, *Geochem. Geophys. Geosyst.*, *6*(Q02H16), doi:10.1029/2004GC000801.

Kyle, P. R., and J. W. Cole (1974), Structural control of volcanism in the McMurdo Volcanic Group, Antarctica, *Bull. Volcanol.*, *38*(1), 16-25.

Kyle, P. R. (1981), Glacial history of the McMurdo Sound area as indicated by the distribution and nature of McMurdo Volcanic Group rocks., in *Dry Valley Drilling Program*, edited by L. D. McGinnis, American Geophysical Union, Washington DC.

Kyle, P. R. (1990a), Erebus Volcanic Province: Summary, in *Volcanoes of the Antarctic Plate and Southern Oceans*, edited by W. LaMasurier and J. Thomson, pp. 81-88, American Geophysical Union, Washington DC.

Kyle, P. R. (1990b), McMurdo Volcanic Group-Western Ross Embayment: Introduction, in *Volcanoes of the Antarctic Plate and Southern Oceans*, edited by W. LaMasurier and J. Thomson, pp. 18-25, American Geophysical Union, Washington DC.

Laj, C., et al. (2002), Geomagnetic intensity and inclination variations at Hawaii for the past 98 kyr from core SOH-4 (Big Island): A New study and a comparison with existing contemporary data, *Phys. Earth Planet. Inter.*, *129*, 205-243.

Love, J. J. (2000), On the anisotropy of secular variation deduced from paleomagnetic volcanic data, *J. Geophys. Res.*, *105*, 5799-5816.

Mankinen, E. A., and A. Cox (1988), Paleomagnetic investigation of some volcanic rocks from the McMurdo volcanic province, Antarctica, *J. Geophys. Res.*, *93*, 11599-11612.

McElhinny, M. W., et al. (1996), The Time-averaged paleomagnetic field 0-5 Ma, *J. Geophys. Res.*, *101*(11), 25007-25028.

McFadden, P. L., et al. (1988), Dipole/quadrupole family modeling of paleosecular variation, *J. Geophys. Res.*, *93*, 11853-11588.

Miki, M., et al. (1998), Geomagnetic paleosecular variation in Easter Island, the southeast Pacific, *Phys. Earth Planet. Inter.*, *106*, 93-101.

Olson, P., and J. Aurnou (1999), A polar vortex in the Earth's core, *Nature*, *402*(6758), 170-173.

Pick, T., and L. Tauxe (1993), Holocene Paleointensities: Thellier experiments on submarine basaltic glass from the east Pacific Rise, *J. Geophys. Res.*, *98*(B10), 17949-17964.

Renne, P. R., et al. (1998), Intercalibration of standards, absolute ages and uncertainties in $^{40}Ar/^{39}Ar$ dating, *Chemical Geology*, *145*(1-2), 117-152.

Riisager, P., and J. Riisager (2001), Detecting multidomain magnetic grains in the Thellier palaeointensity experiments, *Phys. Earth Planet. Inter.*, *125*(1-4), 111-117.

Sreenivasan, B., and C. A. Jones (2005), Structure and dynamics of the polar vortex in the Earth's core, *Geophys. Res. Lett.*, *32*, doi:10.1029/2005GL023841.

Sreenivasan, B., and C. A. Jones (2006), Azimuthal winds, convection and dynamo action in the polar regions of planetary cores, *Geophys. Astrophys. Fluid Dyn.*, *100*(4-5), 319-339.

Steiger, R. H., and E. Jäger (1977), Subcommission on geochronology: Convention on the use of decay constants in geo- and cosmochronology, *Earth Planet. Sci. Lett.*, *36*, 359-362.

Stephenson, A. (1993), 3-Axis static alternating-field demagnetization of rocks and the identification of natural remanent magnetization, gyroremanent magnetization, and anisotropy, *J. Geophys. Res.*, *98*(B1), 373-381.

Tauxe, L., et al. (2000), Paleomagnetism and ^{40}Ar/^{39}Ar ages from La Palma in the Canary Islands, *Geochem. Geophys. Geosyst.*, *1*, 23 pp.

Tauxe, L., et al. (2003), Paleomagnetism of the southwestern U.S.A. recorded by 0-5 Ma igneous rocks, *Geochem. Geophys. Geosyst.*, *4*(4), 8802, doi:8810.1029/2002GC000343.

Tauxe, L., et al. (2004), Paleomagnetism and ^{40}Ar/^{39}Ar ages from volcanics extruded during the Matuyama and Brunhes chrons near McMurdo Sound, Antarctica, *Geochem. Geophys. Geosyst.*, *5*(6), doi:10.1029/2003GC000656.

Tauxe, L., and D. V. Kent (2004), A Simplified Statistical Model for the Geomagnetic Field and the Detection of Shallow Bias in Paleomagnetic Inclinations: Was the Ancient Magnetic Field Dipolar? in *Timescales of the Paleomagnetic Field*, edited by J. E. T. Channell, et al., p. 320, American Geophysical Union, Washington, D.C.

Tauxe, L. T., and H. Staudigel (2004), Strength of the geomagnetic field in the Cretaceous Normal Superchron: New data from submarine basaltic glass of the Troodos Ophiolite, *Geochem. Geophys. Geosyst.*, *5*(Q02H06), doi:10.1029/2003GC000635.

Tauxe, L. T., and T. Yamazaki (2007), Paleointensities, in *Treatise on Geophysics, Geomagnetism Volume*, edited by M. Kono, pp. 509-563, Elsevier.

Taylor, J. R. (1982), *An Introduction to Error Analysis: The Study of Uncertainties in Physical Measurements*, 270 pp., University Science Books, Mill Valley.

Thellier, E., and O. Thellier (1959), Sur l'intensité du champ magnétique terrestre dans le passé historique et géologique, *Ann. Geophys.*, *15*, 285-378.

Vandamme, D. (1994), A new method to determine paleosecular variation, *Phys. Earth Planet. Inter.*, *85*, 131-142.

Wilch, T. I. (1991), The surficial geology and geochronology of middle Taylor Valley Antarctica: Implications for Plio-Pleistocene Antarctic glacial history, University of Maine, Orono, Maine.

Wilch, T. I., et al. (1993), Minimal Pliocene-Pleistocene uplift of the dry valleys sector of the Transantarctic Mountains: A key parameter in ice-sheet reconstructions, *Geology*, *21*, 841-844.

Yu, Y. J., et al. (2004), Toward an optimal geomagnetic field intensity determination technique, *Geochem. Geophys. Geosyst.*, *5*(2), doi:10.1029/2003GC000630.

Ziegler, L. B., et al. (2008), Testing the robustness and limitations of 0 - 1 Ma absolute paleointensity data, *Phys. Earth Planet. Inter.*, submitted.

Chapter 4

Lunar Paleointensity Measurements: Implications for Lunar Magnetic Evolution

Abstract

We analyze published and new paleointensity data from Apollo samples to reexamine the hypothesis of an early (3.9 to 3.6 Ga) lunar dynamo. Our new paleointensity experiments on four samples use modern absolute and relative measurement techniques, with ages ranging from 3.3 to 4.3 Ga, bracketing the putative period of an ancient lunar field. Samples 60015 (anorthosite) and 76535 (troctolite) failed during absolute paleointensity experiments. Samples 72215 and 62235 (impact breccias) recorded a complicated, multi-component magnetic history that includes a low temperature (< 500^{o}C) component associated with a high intensity (~90 μT) and a high temperature (> 500^{o}C) component associated with a low intensity (~2 μT). Similar multi-component behavior has been observed in several published absolute intensity experiments on lunar samples. Additional material from 72215 and 62235 was subjected to a relative paleointensity experiment (a saturation isothermal remanent magnetization, or sIRM, experiment); neither sample provided unambiguous evidence for a thermal origin of the recorded remanent magnetization. We test several magnetization scenarios in an attempt to explain the complex magnetization recorded in lunar samples. Specifically, an overprint from exposure to a small magnetic field (an isothermal

remanent magnetization) results in multi-component behavior (similar to absolute paleointensity results) from which we could not recover the correct magnitude of the original thermal remanent magnetization. In light of these new experiments and a thorough reevaluation of existing paleointensity measurements, we conclude that although some samples with ages of 3.6 Ga to 3.9 Ga are strongly magnetized, and sometimes exhibit stable directional behavior, it has not been demonstrated that these observations indicate a primary thermal remanence. Particularly problematic in the interpretation of lunar sample magnetizations are the effects of shock. As relative paleointensity measurements for lunar samples are calibrated using absolute paleointensities, the lack of acceptable absolute paleointensity measurements renders the interpretation of relative paleointensity measurements unreliable. Consequently, current paleointensity measurements do not support the existence of a 3.9-3.6 Ga lunar dynamo with 100 μT surface fields, a result that is in better agreement with satellite measurements of crustal magnetism and that presents fewer challenges for thermal evolution and dynamo models.

4.1 Introduction

Evidence of an internally generated magnetic field is a crucial constraint for understanding the thermal and dynamical evolution of any planetary body. Although the Moon currently does not possess a core-generated magnetic field [*Russell, et al.*, 1974; *Sonett, et al.*, 1967], Apollo surface magnetometer and sub-satellite measurements indicated spatially heterogeneous magnetic anomalies, of amplitudes up to 300 nT, interpreted as remanent crustal magnetization [e.g. *Fuller and Cisowski*, 1987; *Hood, et* *al.*, 1981; *Lin, et al.*, 1988]. More recently, analyses of Lunar Prospector Electron Reflectometer experiment [*Halekas, et al.*, 2003; *Halekas, et al.*, 2001; *Mitchell, et al.*, 2008] and Lunar Prospector Magnetometer experiment [e.g. *Hood, et al.*, 2001; *Richmond and Hood*, 2008] data have confirmed crustal anomalies, with the largest magnitude signals located antipodal to major impact basins [e.g. *Lin, et al.*, 1988; *Mitchell, et al.*, 2008]. Remanent magnetizations in lunar samples, returned during the Apollo missions, provide an opportunity to deduce information about past magnetic field environments. Because no lunar samples, to date, have been unambiguously oriented, paleomagnetic studies focused on paleointensity rather than direction and field geometry.

Paleointensity investigations of nearly seventy lunar samples from 1970 to 1987 using multiple absolute and relative paleointensity measurement techniques, led to the suggestion that the Moon once generated a magnetic field [e.g., *Collinson*, 1993; *Fuller*, 1998; *Pearce, et al.*, 1972; *Runcorn, et al.*, 1971] despite the small size of the lunar core [*Hood, et al.*, 1999; *Wieczorek, et al.*, 2006]. Based on these measurements, Cisowski et al. [1983] and others [*Collinson*, 1985; *Runcorn*, 1994, 1996] proposed that from approximately 3.9 to 3.6 Ga, the strength of the lunar surface field was comparable to Earth's present day surface field. Although the high-field paleointensities are often assumed to result from a core dynamo, other mechanisms such as magnetization in a transient field generated by a basin-forming impact may be responsible [e.g. *Crawford and Schultz*, 1993, 1999; *Hood and Artemieva*, 2007; *Hood and Huang*, 1991]. Even if the magnetization originated due to a core dynamo field, it is not possible to differentiate between different driving mechanisms, for example, tidal dissipation [*Williams, et al.*, 2001] or rapid and transient core cooling [*Stegman, et al.*, 2003].

The distribution of lunar paleointensities over time, as summarized by Cisowski et al. [1983], has dictated the predominant view of lunar magnetism. In particular, the thermal implications of an inferred early lunar dynamo have propagated throughout lunar literature [*Collinson*, 1985; *Runcorn*, 1994, 1996; *Schubert, et al.*, 2001; *Stegman, et al.*, 2003]. However, interpretation of the existing paleointensity between 3.6 and 3.9 Ga (Figure 4.1a) the scatter in measurements during this period is almost two orders of magnitude among different samples, and can be up to an order of magnitude within the same sample. Second, many current lab protocols critical to interpreting an estimated paleointensity as reflecting a primary thermal remanence (i.e., an intrinsic lunar field), were not available at the time the existing data were measured. Third, there is considerable uncertainty in the age that should be assigned to the acquisition of magnetic remanence. Because of the heterogeneous nature of most lunar samples, different radiometric systems record different events within the same sample, and which, if any, of the measured ages is associated with a putative thermal remanent magnetization is unclear. Furthermore, the preferred approach for estimating paleointensity (an absolute measurement – see section 2 below) involves heating the sample and so a radiometric age must be acquired from a different subsample of the same lunar rock.

In light of significant technical advances made in paleomagnetic techniques and understanding over the past few decades, the interpretation of lunar paleointensity deserves re-examination. This study examines existing lunar paleointensity measurements and contributes new measurements to assess the commonly accepted interpretation of lunar paleointensity data: that of a 3.9 – 3.6 Ga dynamo. We begin with a brief introduction to paleomagnetic terminology and methodology. We then use objective selection criteria to show that only four absolute intensity measurements from over 30 previously published studies can be considered "reliable". Furthermore, we demonstrate that it is not possible to assess whether any of the published data reflect a primary thermal remanence. We present new paleointensity measurements on four lunar samples (3.3 to 4.2 Ga) using both absolute and relative techniques. The results are complicated, with multiple magnetic components recorded in lunar samples that can be easily overlooked or misinterpreted with older techniques. We then test several magnetization scenarios in an attempt to explain these complex magnetizations. The non-unique interpretation of the new multi-component results, combined with contamination during sample return [*Strangway, et al.*, 1973], and the poorly understood effects of shock, suggest that less sophisticated absolute techniques and relative techniques (e.g., sIRM) incapable of distinguishing between single- and multi-component records, cannot be reliably interpreted. Consequently, current lunar paleointensity data cannot be interpreted as evidence for a primary thermal remanence acquired in a lunar dynamo field.

4.2 Paleomagnetic Methods

4.2.1 Background

The original orientation of lunar samples is unknown; therefore lunar paleomagnetic studies focus primarily on magnetic sample properties (e.g. mineralogy, and magnetic domain state [e.g. *Nagata, et al.*, 1972, 1974; *Wasilewski*, 1974]), magnitude of magnetization (e.g. natural remanent magnetization, NRM, and paleointensity [e.g. *Banerjee and Mellema*, 1974; *Collinson, et al.*, 1973; e.g. *Pearce, et al.*, 1973]), and the possible origin of observed magnetizations (e.g. solar wind [*Banerjee and Mellema*, 1976] or lunar dynamo [e.g. *Cisowski, et al.*, 1982; e.g. *Pearce, et al.*, 1972]). Most samples have also been dated with one or more radiometric systems, however the interpretation of these dates is complicated by subsequent shock events. Paleomagnetic studies of lunar samples (summarized by Fuller and Cisowski [1987] and Collinson [1993]) include measurements of Curie temperature (the temperature below which a mineral exhibits long range magnetic order), magnetic susceptibility (the proportionality constant relating an induced magnetization to the inducing field), magnetic anisotropy (variation in magnetization as a function of crystal axis), and coercivity (resistance of a sample to align with an applied magnetic field). From these studies, it is concluded that metallic iron (Fe^0) is the dominant magnetic phase in lunar samples. Since metallic iron is a non-oxidized phase, care must be taken during magnetic experimentation in Earth's atmosphere to ensure that the metallic iron does not oxidize, thereby altering the magnetic carrier. Alloys of metallic iron with nickel (kamacite) and/or cobalt, also contribute experimental complications as they can respectively lower or raise the Curie point of a sample by tens of degrees relative to pure metallic iron (770°C).

The natural remanent magnetization (NRM) of a sample is the vector sum of all the different possible components of magnetization acquired over its history. Thermal remanent magnetization (TRM) is a type of NRM that arises from magnetic material cooling through the Curie temperature in the presence of a magnetic field. An original TRM is of particular interest because for igneous rocks it records the magnetic conditions at the time of emplacement. Demonstrating a primary TRM origin for the remanence of any sample is difficult. However, high stability to temperature and alternating field demagnetization combined with the decay of the remanence to the origin of a vector endpoint diagram are necessary requirements for an ancient original TRM.

Estimates of paleointensity fall into two categories: absolute and relative. Absolute techniques rely on replacing the natural remanent magnetization (NRM) by a laboratory-imparted thermal remanence (TRM). Theory then allows the calculation of absolute paleointensity. Relative methods rely on normalization by some non-thermal remanence, and an empirically-derived scaling factor must be used to derive an absolute intensity. In the following two sections we provide a cursory description of each approach (see Tauxe and Yamazaki [2007] for a more detailed summary of paleointensity theory and methods).

4.2.2 Absolute Paleointensity

In some cases, it is possible to estimate the absolute intensity of an original magnetic field in which a sample was magnetized. Thellier [1938] proposed that the intensity of the original field could be determined by assuming a linear relationship between an applied field, B, and a magnetization, M, for each sample: $B = \alpha M$. Assuming the proportionality constant does not change over the range of applied fields a sample is exposed to, ancient fields (B_{anc}) and laboratory-controlled fields (B_{lab}) can be linearly related to the NRM (M_{anc}) and the laboratory-imparted TRM (M_{lab}) through the following relationship,

$$B_{anc} = \frac{M_{anc}}{M_{lab}} B_{lab} \,. \tag{4.1}$$

Equation 1.1 requires that the acquired magnetization of the rock (both in the lab and when originally emplaced) must be reproducible. Two necessary prerequisites for such a reproducible experiment are 1) the presence of uniformly magnetized (single domain) grains in which a remanence acquired at a particular temperature is also completely removed by zero field cooling from the same temperature, and 2) the lack of alteration, which may change the capacity to acquire a remanence, during the paleointensity experiment. Unfortunately, alteration often happens as a result of heating and changes the magnetization properties of a sample such that this relationship is different in the lab than at the time of initial magnetization. Therefore, a good paleointensity procedure should identify the alteration if, and when, it happens. The most commonly employed method today is the double heating Koenigsberger-Thellier-Thellier [*Thellier and Thellier*, 1959] technique (referred to as KTT in lunar literature and just Thellier-Thellier or T-T in terrestrial studies), during which the sample is heated in a stepwise manner, progressively replacing the original NRM with a laboratory-controlled partial TRM (pTRM). Thus, the stability of the proportionality (M_{anc}/M_{lab}) can be determined, at least prior to the onset of any alteration.

An important modification to the double heating paleointensity method is the pTRM check, which involves reheating the sample at lower temperatures to check that the remanent magnetization measured at a previous heating step is reproducible. This check therefore monitors changes in the sample's ability to acquire TRM due to alteration. Because it is a modern development, the pTRM check method has not previously been performed successfully for lunar samples.

Our study uses the IZZI variant of the KTT paleointensity experiment [*Tauxe and Staudigel*, 2004; *Yu, et al.*, 2004] to perform an intensity experiment on four lunar samples. In this experiment, the subsamples are heated to a given temperature step and allowed to cool in a zero field (zero-field step). Next, the specimens are heated to the same temperature and cooled in a field applied along the specimen's cylindrical axis (in-field step). The "zero-field/in-field" method (ZI) of progressively replacing NRM with pTRM allows calculation of the NRM remaining and the pTRM gained after each temperature step through vector subtraction, and is often attributed to Coe et al. [1978]. The IZZI method alternates the order of zero-field and in-field measurements (IZ vs. ZI) at each temperature step in order to monitor inequalities in blocking and unblocking temperature (the temperature below which material can retain a remanent magnetization despite changes in applied field). This adaptation makes the IZZI method uniquely devised to monitor multi-domain behavior, a non-uniform magnetization state, within the rock and replaces the need for the more time consuming pTRM-tail checks (Riisager and Riisager [2001]).

The methodology outlined above provides a means of evaluating two necessary requirements (remanence carried by single domain grains and the lack of alteration) for a successful absolute paleointensity experiment. Results from a Thellier-Thellier experiment are traditionally displayed on an Arai plot of NRM remaining versus pTRM gained. An Arai plot representing ideal primary remanence (no secondary overprint), single domain behavior, and no alteration would have a straight line from which the paleofield could be calculated (Equation 4.1).

4.2.3 Relative Paleointensity

To avoid problems incurred through heating of the rock, relative methods have been developed which normalize the NRM by a room temperature magnetic parameter proportional to the magnitude of NRM. The most common relative method used on lunar samples is the sIRM method [*Cisowski, et al.*, 1977; *Fuller*, 1974], which normalizes the NRM with a saturation isothermal remanence (sIRM, sometimes written IRMs). Relative methods also require an empirically-derived scaling factor (assuming linearity), *f*, to estimate the absolute field intensity. The absolute field strength is then calculated as *f* * sIRM/NRM. The sIRM is measured after exposing a sample to a (typically 0.6 - 3T) magnetic field at room temperature; such a field will saturate the magnetization of the sample. The sIRM method assumes (often inappropriately) that 1) the NRM is a single component remanence, 2) the NRM is an original TRM, 3) the magnetic grains are single-domain and isotropic in shape (thereby adhering to Néel theory), 4) the coercivity spectra (strength of magnetization as a function of alternating field strength) of the NRM is similar to that of the IRM. Due to the limitations of these assumptions any relative estimate of paleointensity is at best accurate to within an order of magnitude.

While there have been modifications to the sIRM method [e.g., *Gattacceca and Rochette*, 2004], none are capable of determining that all assumptions (1-4 above) have been satisfied. The most common adaptation to lunar samples was proposed by Cisowski et al. [1983], and uses a slightly demagnetized value of NRM normalized by a sIRM demagnetized to the same arbitrary AF strength (20 mT) in an attempt to remove unwanted secondary components of magnetization. While it is possible that secondary components are removed, this sIRM adaptation does not verify that the primary component is correctly isolated, nor can it confirm that the primary component is a TRM.

Despite the possibility that relative-to-absolute scaling factors may be dependent upon grain size and mineralogy, several studies have attempted to calculate a single scaling factor for all lunar samples. The approach assumes a linear scaling of relative to absolute intensity that is also independent of field strength. Cisowski et al. [1983] compared absolute paleointensity measurements for 14 lunar samples to corresponding relative measurements to estimate a mineralogy-independent lunar scaling factor ($f = 0.47$ μT), although the data indicate considerable scatter (see Figure 3 of Cisowski et al. [1983]). Kletetschka et al. [2003] proposed another mineralogy-independent scaling factor ($f = 0.3$ μT) based on a combination of synthetic minerals, terrestrial basalts, and the same 14 lunar samples. However, in experiments on five lunar samples Fuller & Cisowski [1987] showed that the scaling of TRM to sIRM varied by a factor of 3 for different rock types and, for four samples, also depended on field strength. More recently, Yu [2006] finds that the scaling factor is dependent on grain size and asserts that mineralogy-dependence has not been sufficiently tested. Consequently, the reliability of either previously proposed single scaling factor for lunar materials is uncertain.

4.2.4 Paleomagnetic Direction

Most studies seek to investigate the original, or primary NRM. However, many mechanisms, including impact related demagnetization/remagnetization [*Halekas, et al.*, 2002], thermal events [e.g. *Collinson*, 1985], or viscous remanent magnetization [*Collinson, et al.*, 1973; *Sugiura and Strangway*, 1980] , can overprint or erase the original magnetization. These secondary components of NRM add vectorially to the primary component to produce the total NRM. If the coercivity spectra of these secondary components do not overlap with the primary remanence, they can often be linearly removed through partial demagnetization procedures (thermal or alternating magnetic field). Only through examination of progressive changes in both the direction and magnitude of NRM with increasing demagnetization steps (temperature or field strength) can it be determined that the coercivity spectra do not overlap. In addition, an original primary remanence should also correspond to the highest stability magnetization component. For a paleointensity experiment, this means that the temperature range used to estimate the paleofield should correspond to a magnetization component that trends toward the origin of a vector endpoint diagram. This is demonstrated by the demagnetization vector having a maximum angle of deviation (MAD) value less than the angle the vector makes with the origin (dANG). Modern paleointensity studies include analyses of both the direction and magnitude of NRM, which is accomplished through a display known as the vector-endpoint diagram (see Butler [1992] and Tauxe [1998] for discussions of paleomagnetic methods and analyses). Prior to this study, no lunar paleomagnetic experiment used vector-endpoint diagrams to show that the full NRM vector decays linearly to zero, and therefore can be interpreted as the primary (presumably thermal) magnetization recorded by the sample.

Of particular importance, it is possible to add an isothermal remanent magnetization (IRM) through short-term exposure to magnetizing fields (> 1 mT or approximately 10 times the Earth's field) at constant temperatures. Strangway et al. [1973] showed that an IRM was acquired in a lunar sample during the return trip to Earth in the Apollo capsule. Therefore, it is imperative to use a method that can distinguish between primary NRMs and potentially damaging overprints such as the spacecraft IRM.

4.3 Evaluation of Existing Paleointensity Data

4.3.1 Previous Paleointensity and Age Compilation

Cisowski et al. [1983] present two distinct compilations of lunar paleointensity. One compilation comprises paleointensities measured using several different paleointensity methods (Figure 2 of their paper, and recreated here in Figure 4.1a); most of these data are absolute paleointensity measurements. The other compilation comprises measurements made using a single technique: the relative paleointensity sIRM technique (their Figure 7). The sIRM compilation was further assessed by Fuller & Cisowski [1987], and is the one most often reproduced in the lunar literature [e.g. *Wieczorek, et al.*, 2006]. Here we assess both these previous compilations; however, our primary interest is in the absolute paleointensity data because of the theoretical [*Dunlop and Ozdemir*, 1997] - rather than empirical - underpinning for such paleofield estimates. In addition, absolute paleointensity estimates have been used to establish the scaling factor (Cisowski et al. 1983) needed to convert sIRM relative paleointensities into an absolute paleofield value (see section 2.3). Clearly, then, the reliability of the absolute paleointensity data set is of critical importance, since these play a role in the interpretation of all lunar paleointensity results.

4.3.2 Criteria for Acceptable Absolute Paleointensity Data

The paleointensity data shown in Figure 4.1a are a recreation of the published absolute paleointensity vs. age figure of Cisowski et al. [1983; Figure 2 in their paper]. Due to multiple measurement techniques and within-sample heterogeneity there is a great deal of uncertainty in both the age and proposed paleofield for nearly every sample. The quality criteria applied to the existing database were quite inclusive, allowing the inclusion of both relative and absolute paleointensity measurements.

In this reevaluation, it is paramount to restrict interpretation of paleointensity data to measurements that represent primary TRM. There are several ways in which intensity experiments may fail to accurately identify a primary TRM; 1) alteration due to grain growth or destruction, 2) magnetic grain interaction at different temperatures, 3) weak and/or unstable remanence, 4) non-reproducibility of paleointensity measurements. Selkin and Tauxe [2000] identify a set of six criteria that define an acceptable and reliable terrestrial Thellier-Thellier paleointensity measurement. Importantly, there are no published lunar results that pass all of these modern criteria, because the necessary current experimental diagnostics had not been developed (or were not commonly used) when these measurements were made. We define a set of criteria to emulate the stringent terrestrial criteria, but that is more appropriate for the information available for lunar samples.

Figure 4.1: Paleointensity versus age for lunar samples **a)** reproduced from Cisowski et al. (1983) where samples measured using Thellier-Thellier (closed circle), Shaw (open circle) and ARM (x) techniques are labeled with associated sample number. The uncertainties in intensity represent the range in intensity estimates on a given sample as a result of multiple measurement techniques. Ages are determined using a variety of isotope systems and uncertainties represent uncertainty in the best estimate of age. Note the condensed timescale in the age axis at 3 Ga and the y-axis is logarithmic. **b)** Paleointensity versus age for lunar samples measured using reliable absolute paleointensity measurements (see supplemental Table A4.1). The ages are determined using a variety of isotope systems (see text and supplemental Table A4.1 for a detailed description). Uncertainty in radiometric age is shown as solid line for each sample while dashed lines represent the range of ages inferred from collection site location (i.e., no radiometric date available). Uncertainties in paleointensity represent ranges in multiple methods as well as individual sample uncertainties.

a)

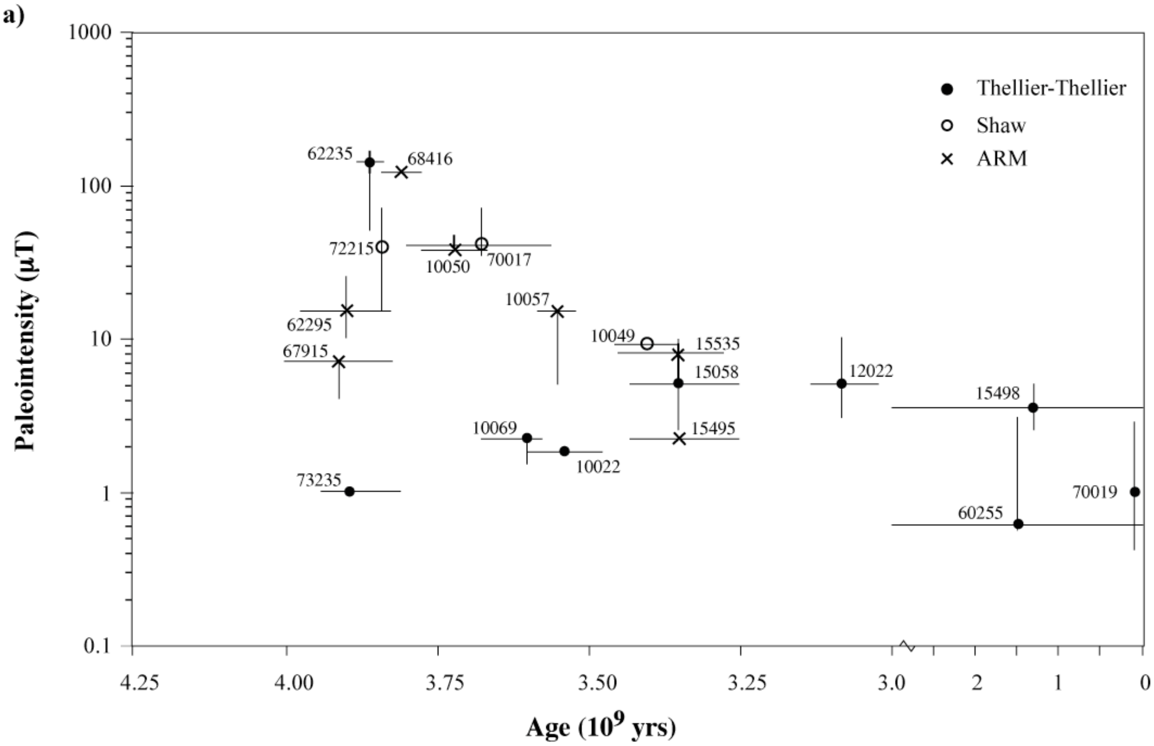
Thellier-Thellier
Shaw
ARM
Paleointensity (μT)
Age (10^9 yrs)
1000
100
10
1
0.1
4.25
4.00
3.75
3.50
3.25
3.0
2
1
0
62235
68416
72215
10050
70017
62295
10057
10049
15535
67915
15058
12022
15498
10069
15495
10022
73235
70019
60255

b)

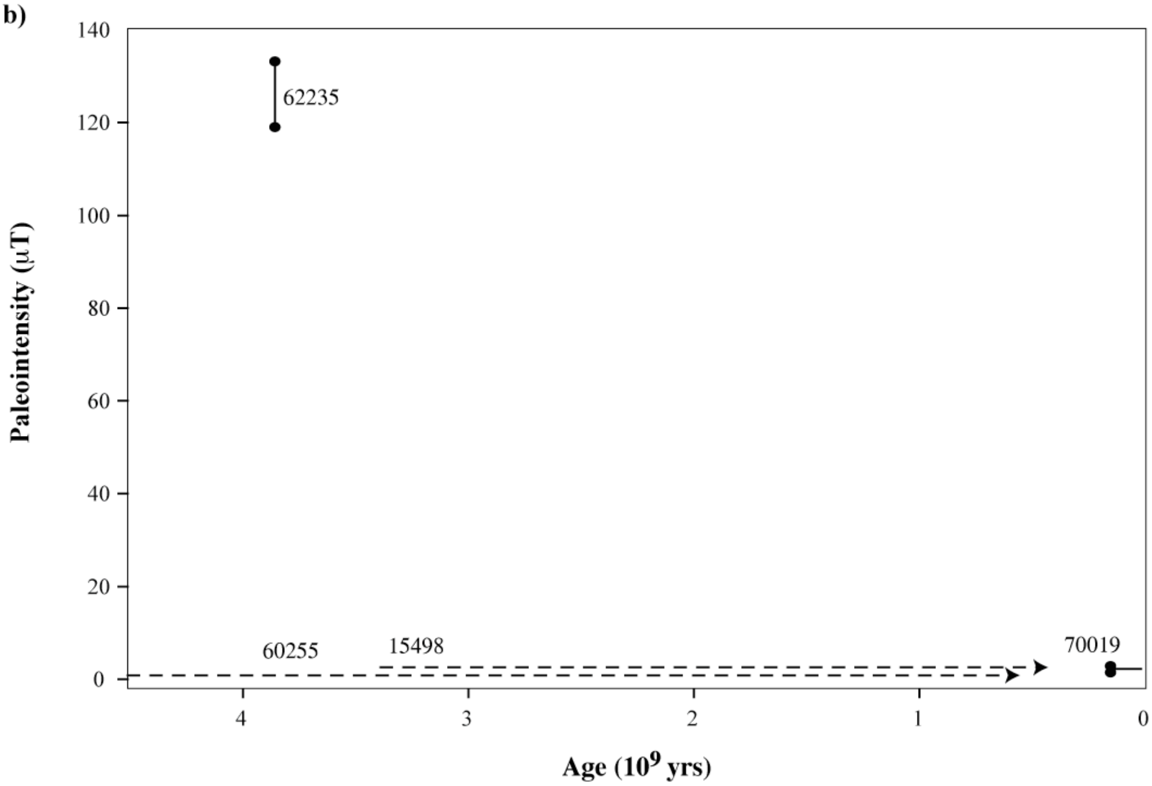
Paleointensity (μT)
Age (10^9 yrs)
140
120
100
80
60
40
20
0
4
3
2
1
0
62235
60255
15498
70019

1. **Absolute Methods** – Only methods like the Thellier-Thellier- and Shaw-type methods will be considered for the compilation of absolute paleointensity. Although they were included as absolute measurements by Cisowski et al. [1983] we exclude ARM techniques as published by Stephenson and Collinson [1974] and Banerjee and Mellema [1974]. ARM is in fact a relative method and uses a poorly-calibrated scaling parameter [*Banerjee and Mellema*, 1976; *Gattacceca and Rochette*, 2004]. Banerjee and Mellema [1976] argue that it provides estimates of absolute paleointensity with no better than 50% accuracy, which could be due to the chaotic AF (alternating field) demagnetization of kamacite (a prevalent lunar mineral) [*Gattacceca and Rochette*, 2004].
2. **Published Reliability** - In many cases, the authors who publish a paleointensity estimate for a particular sample will provide additional arguments and evidence as to why the estimate is unreliable (e.g. sample 75035 [*Sugiura, et al.*, 1978]). A paleointensity estimate is excluded from this study if the publishing authors refute their own estimate for reasons including: evidence of alteration during the experiment, the natural remanent magnetization is (or likely is) not a thermal remanent magnetization, evidence of contamination during sample division (e.g. saw marks), or noted inadequate implementation of technique.
3. **Within-Sample Reproducibility (I)** – If the Thellier-Thellier or Shaw method is used, a minimum of four consecutive points must be used to

calculate the best-fit line from which paleointensity will be estimated (modification of criteria 3 from Selkin and Tauxe [2000]).

4. **Within-Sample Reproducibility (II)** - If a single NRM/pTRM ratio is used, at least three measurements on different pieces of the same sample must agree within 25% of one another. This is an adaptation of criteria 3 applied to a technique that only heats a sample once and then calculates the paleointensity from a total TRM and measured NRM. We consider this method with the stated criteria in an effort to consider the largest data set possible.

5. **Documentation** - A measurement is discarded if it is published without raw data or figures since the quality of the data is then impossible to evaluate. We note that if a sample fails this criterion it also fails one or more other criteria.

These criteria limit the number of acceptable data to four measurements (one less than a similar re-evaluation by Sugiura and Strangway [1983]). For each of the four acceptable samples, we attempted to determine the best age estimate. The reliability of these age estimates is highly variable, ranging from completely unconstrained (15498 and 60255), a U-Pb concordia diagram (70019), to a well-defined ^{40}Ar-^{39}Ar age plateau (62235). All ages reported in this study have been recalculated (when necessary) using standard radiometric decay constants proposed by Steiger and Jäger [1977]. Figure 4.1b shows reliable absolute paleointensity measurements versus age without a compressed timescale or logarithmic paleointensity scale as seen in Figure 4.1a. Supplemental Table A1 contains a complete reference list and summary of our evaluation of measurement reliability. For some samples in Figure 4.1a, we were unable to find published paleointensities (and sometimes ages) that reflect the choice of error bars in the figure.

Regrettably, after a thorough search of the literature, we were unable to resolve the cause of such differences.

4.3.3 Acceptable Absolute Paleointensity Measurements

Here, we provide a brief synopsis of the paleointensity measurements for the four acceptable samples shown in Figure 4.1b. Sample 62235 (impact melt breccia) had two successful KTT experiments that yielded reliable intensities of 120μT [*Collinson, et al.*, 1973] and 132μT [*Sugiura and Strangway*, 1983] for temperatures between 0 and ~500°C. Neither used pTRM checks during the relevant temperature steps, nor reported vector endpoint diagrams to verify primary remanence. The sample has a well-defined ^{40}Ar-^{39}Ar plateau age of 3.872 ± 0.032 Ga [*Norman, et al.*, 2006].

Sugiura and Strangway [1980] performed four paleointensity experiments (ARM, KTT, Shaw, sIRM) on sample 60255 (impact melt breccia) and discuss the reliability of each method. After comparing results of various experiments on a single sample, they conclude that the ARM, Shaw and sIRM measurements are significantly affected by a strong viscous remanent magnetization component. Although the KTT experiment met the criteria set by this study, the results are considered questionable because of the high scatter in the data, so a paleointensity estimate from this sample of 0.5 μT (temperature steps 500°C to 795°C) is included with caution. In addition to the tenuous paleointensity result the age estimate for this sample is ill constrained. The possible age range provided in Figure 4.1b (dashed line) is merely representative of other Apollo 16 rocks, as no radiometric dates have been published for sample 60255. Nagata et al. [1973] and

Sugiura & Strangway [1980] quote a preferred age of 3.9 Ga; we were unable to uncover the reason for Cisowski et al.'s [1983] age of 0 – 3 Ga (their Figure 2, our Figure 4.1a).

A single KTT experiment was performed on sample 15498 (a glass-coated breccia) [*Gose, et al.*, 1973], including a single successful pTRM check at 300°C, which yielded a well-behaved intensity of 2.2 μT for temperatures between 550 and 650°C. We note that the published figure by Gose et al. [1973] illustrates an unreported, but much higher intensity associated with temperature steps from 300 to 500°C. Like sample 60255 there are no published data to verify primary remanence, and the poorly defined age is merely representative of other Apollo 15 results. As with 60255, it is unclear why Cisowski et al. [1983] excluded ages older than 3 Ga as possible ages of this sample.

Sugiura et al. [1979] performed successful KTT experiments on two glassy portions of sample 70019 (a soil breccia). The authors speculated failure in laboratory procedure which possibly resulted in sample alteration above 500°C but do not have pTRM checks to verify this conclusion. However, if alteration did not occur, then the sample exhibits a multi-component NRM that implies lower intensity associated with high temperature steps above 500°C. The authors report paleointensities of 1.2 and 2.5 μT for each subsample, which are associated with low temperature steps (140 to 470°C). However, it is impossible to determine whether this paleointensity represents primary remanence as no directional data is provided. The best age estimate (~175 Ma) of this sample is determined from a single U-Pb concordia diagram for measurements on a similar glassy portion of sample 70019 [*Nunes*, 1975].

4.3.4 Criteria for Acceptable Relative Paleointensity Data

Due to the paucity of acceptable absolute lunar paleointensity measurements, and the abundance of published relative measurements, we provide a cursory reevaluation of the relative measurements here. The abundance of relative measurements directly results from 1) the ease of relative techniques, and 2) the ability to measure paleointensity at room temperature, thereby reducing the risk of alteration during heating. The relative paleointensity compilation of Fuller and Cisowski [1987] has a paleointensity vs. age distribution similar to the absolute compilation presented by Cisowski et al. [1983]. While uncertainties in both age and intensity are large, only samples with ages between approximately 3.6 and 3.9 Ga were reported to have relatively high intensities (20-100 μT). There is also a lack of data prior to 4 Ga and between 3 and 1.5 Ga. As noted above, relative measurements (including sIRM) are potentially problematic, and require stringent criteria in order to verify that samples are acceptable.

According to Gattacceca and Rochette [2004], relative measurements must pass the following criteria to be considered reliable in a modern experiment. First, any sIRM measurement must be able to differentiate between secondary overprint (IRM), partial demagnetizations (viscous decay, and zero-field shock or heating), and original thermal remanences. Second, as with any reliable paleointensity technique the measurable component of magnetization must decay toward the origin. The sIRM measurements provided by Cisowski et al. [1983], and Fuller and Cisowski [1987] fail both of these criteria because their method cannot differentiate between the components of a multi-component NRM, and there is no published record of directional decay through vector-endpoint diagrams. While there have been more recent measurements by Garrick-Bethel and Weiss [2007], they use the original sIRM method proposed by Cisowski et al. [1983] and do not provide vector endpoint diagrams of directional data, therefore failing the same criteria. Consequently, there are no verifiably acceptable relative paleointensity measurements with which we can create a modern compilation. Hence, we present 2 new sIRM measurements on lunar specimens as a comparison to new absolute as well as previous sIRM and absolute paleointensity measurements. Through directional analysis of these new measurements we assess the assumption of primary remanence necessary for a successful sIRM measurement.

4.3.5 Summary and Reinterpretation of Paleointensity vs. Age

Most striking in a comparison of Figures 4.1a and 4.1b is the absence of reliable data (both in age and absolute paleointensity) resulting from a reexamination of the literature. In the new compilation there is only one reliable lunar sample with a corresponding paleointensity greater than 2.1 μT. The updated compilation also reflects changes in estimated ages relative to those in Cisowski et al. (1983) for 2 of the samples retained. Samples 60255 and 15498 have no age information, and can only be loosely associated with ages of nearby sites.

Our results have implications for the interpretations of lunar magnetic evolution posited by Cisowski et al. [1983]. Despite the great deal of scatter in both age and intensity measurements for samples from 3.9 to 3.6 Ga of Figure 4.1a, Cisowski et al. [1983] inferred the presence of an internal lunar dynamo strong enough to produce surface strengths upwards of 100 μT. Based on the assessment presented here, it is clear that the data are insufficient to determine if there was in fact a time interval with an associated high magnetic field intensity, much less the presence or duration of an internal lunar dynamo. Furthermore, if there was a high-field era in lunar history, it is impossible to identify initiation and/or cessation of this era due to the lack of reliable paleointensity data.

4.4 New Lunar Paleointensity Measurements

Although the lunar paleointensity studies performed in the 1970's provided influential interpretations of lunar magnetism, the results of our compilation make it apparent that new data that clearly demonstrate a primary thermal remanence are needed. New laboratory studies can provide an opportunity to investigate lunar paleointensity with more accuracy and sensitivity simply due to 30 years of improved instrumentation. We present paleointensity experiments for four samples obtained from the Johnson Space Center lunar sample return collection, intended to both bracket (4.3 and 3.3 Ga samples) and fall within the age range of the putative dynamo (3.9 and 3.7 Ga samples). In addition two of our samples are ones for which high paleofield values were previously reported. Unfortunately, experimental requirements of measuring paleointensity will destroy all natural magnetic information of a specimen. It is therefore impossible to perform additional magnetic experiments (e.g. hysteresis), on a sample that was previously used in a paleointensity experiment. Although measuring rock magnetic information on a separate piece of the same lunar sample is possible, within sample heterogeneity means that the measured properties of one specimen can be different from those giving rise to the observed paleointensity behavior of a different specimen. Due to these restrictions and limited lunar material available to us for this initial study we focus on the reliability of previously measured and new absolute paleointensity data. The following section contains a brief description of the samples, experimental details, results for absolute and relative paleointensity experiments, and previous magnetic, paleointensity, and age work done on each of the four samples.

4.4.1 Sample Descriptions and Previous Work

4.4.1.1 Sample 72215

Sample 72215 is a clast-rich impact melt breccia (see Ryder et al. [1975] for a detailed mineral and petrographic analysis) from Apollo 17. There are no existing double heating paleointensity experiments on this sample. Banerjee and Mellema [1976] performed an unsuccessful Shaw paleointensity experiment on 3 specimens, while Banerjee and Swits [1975] performed an ARM experiment on another specimens. The best age estimate of this sample is an Ar-Ar measurement of 3.83 ± 0.03 Ga [*Schaeffer, et al.*, 1982]. We note here that we were unable to determine the decay constant used from the published documentation, but we assume it follows the values outlined by Steiger and Jäger [1977] due to the 1982 publication date. We performed a KTT experiment on specimen 72215.262 and a sIRM experiment on 72215.259. To be consistent with paleomagnetic literature, henceforth we will refer to the smaller pieces of a lunar sample as specimens.

4.4.1.2 Sample 62235

Sample 62235 is an impact melt breccia (see Crawford and Hollister [1974] for a detailed mineral and petrographic analysis) from Apollo 16. Sugiura and Strangway [1983] performed the most recent paleointensity analysis using the Coe-modified

Thellier-Thellier method. To reduce alteration during their experiment, specimens were prepared for heating with a two-stage vacuum method proposed by Taylor [1979]. Alteration of the sample was monitored by measuring the coercivity of a separate sample that underwent the same heating steps. Modern pTRM checks were not performed in this experiment. As documented above, the best age estimate is 3.876 ± 0.032 Ga (Norman et al., 2006). We performed a KTT experiment on specimen 62235.120 and a sIRM experiment on 62235.118.

4.4.1.3 Sample 60015

Sample 60015 is a cataclastic ferroan anorthosite from Apollo 16 (see Ryder and Norman [1980] and its updated online edition http://curator.jsc.nasa.gov/lunar/compendium.cfm for a detailed review of mineral, chemical and petrological studies). There are no existing absolute paleointensity measurements for this sample. However, Stephenson and Collinson [1974] report a single ARM measurement. The best age estimate of this sample is provided by Schaeffer and Husain [1974] as an Ar-Ar plateau age of 3.34 ± 0.04 Ga. This has been recalculated for decay new constants [*Steiger and Jäger,* 1977]. We performed a KTT experiment on specimen 60015.67.

4.4.1.4 Sample 76535

Sample 76535 is a coarse-grained troctolite from Apollo 17 (see Dymek et al. [1975] for a detailed petrographic description). Textual evidence indicates a slow cooling history and the sample shows little evidence of shock [*Gooley, et al.*, 1974]. This lunar sample has been dated using a variety of isotopic systems, the most recent and most through analysis is provided by Premo and Tatsumoto [1992] who conclude that the U-Pb date of 4.236 ± 0.015 Ga is most appropriate. No previous paleointensity measurements or magnetic investigations have been made on this sample. We performed a KTT experiment on specimen 76535.136.

4.4.2 IZZI Experimental Method

IZZI-modified KTT paleointensity experiments on four lunar specimens were conducted in 50°C temperature steps until 500°C followed by smaller temperature increments until > 95% of the NRM was lost. Demagnetization and field acquisition in a 15 μT field were performed with custom-built ovens at the Scripps Paleomagnetic Laboratory. Samples were stored continuously in a magnetically shielded room (ambient field < 250 nT) for ~ three months prior to the experiment. In an effort to reduce oxidation and subsequent alteration during the experiment, sample preparation included wrapping each specimen in quartz fiber paper (to prevent sample rotation during the lengthy experiment) and sealing the specimen in an evacuated quartz tube (~10^{-4} Torr). Prior to sealing the lunar samples, we verified that the process of sealing the quartz tubes did not contaminate the samples. This preliminary experiment involved giving a test sample of terrestrial submarine basaltic glass a known TRM, sealing it within the test tube, and successfully recovering the intensity (carried by grains with blocking temperatures > 100ºC) imparted to the sample prior to the sealing process. We verified that the evacuation technique was effective by demonstrating that copper wool samples encased in the evacuated chambers did not oxidize when heated. All remanence measurements were made using a 2G Enterprises three-axis through-bore cryogenic magnetometer.

Figures 4.2 – 4.5 display Arai plots, equal area, vector-endpoint, and demagnetization diagrams for lunar specimens 72215.262, 62235.120, 60015.67, and 76535.17, respectively. The temperature steps, intensity, and direction for each step of the IZZI-modified KTT paleointensity experiments can be found in Supplemental Tables A4.2-A4.5.

4.4.3 KTT Results

4.4.3.1 Specimen 72215.262

Lunar specimen 72215.262 shows several interesting, and potentially important, results. Two distinct regions of behavior can be seen in the Arai plot (Figure 2a) above and below 520 - 540°C. These regions will be referred to as slope A (temperatures below 520 - 540°C) and slope B (above 520 - 540°C). The green triangles represent the pTRM checks performed during the experiment. A failed pTRM check will not fall on or near it's associated temperature step (open or closed circle). This specimen passes its pTRM checks, implying no alteration has occurred. The remanent intensity associated with slope B is 1.8 μT, while slope A is associated with an intensity of 103.7 μT. Figure 4.2b also supports a change in sample behavior (possibly a change in the magnetic remanence carrier) at 540°C, at which point the specimen begins to acquire partial remanence in the lab. Interestingly, the specimen loses most of its NRM prior to the temperature where it begins to acquire a measureable pTRM.

A vector endpoint diagram of direction is shown in Figure 4.2c. The directional data define two directions. The first direction, associated with temperature steps 0°C – 520°C, is well behaved (linear on vector-endpoint diagram) but does not trend toward the

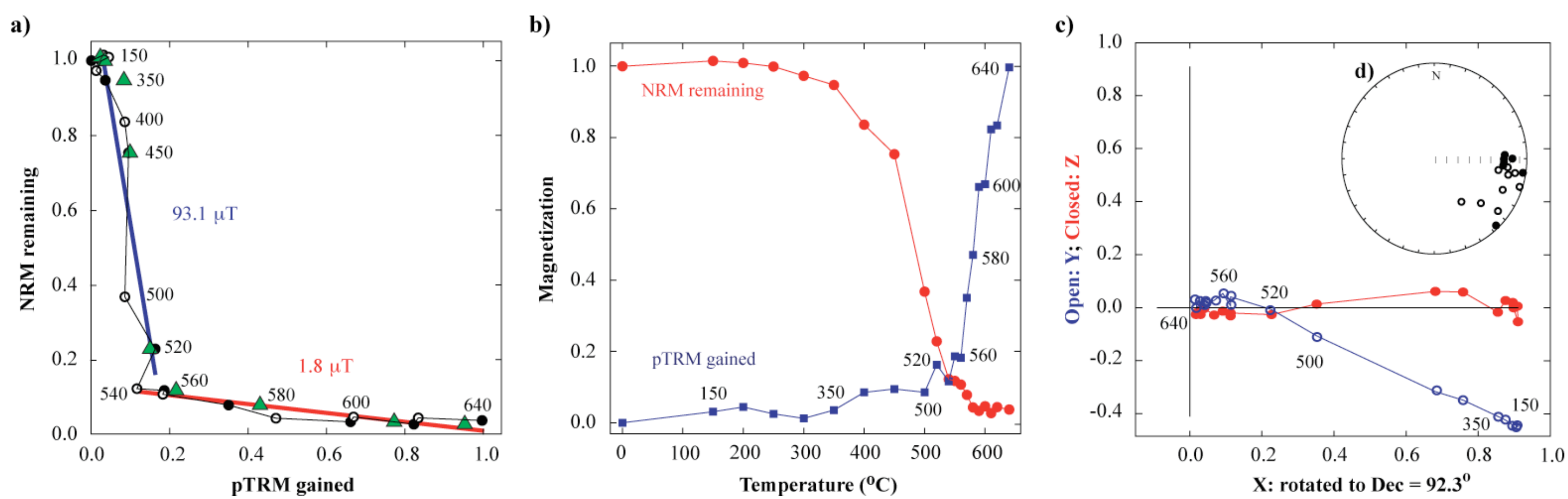

Figure 4.2: Paleomagnetic analysis of lunar specimen 72215.262 where the NRM is normalized to a magnetic moment of 3.65e-08 Am^2. Demagnetization steps are labeled in ^{o}C. **a)** Arai plot of NRM remaining vs. pTRM gained during an IZZI-modified T-T paleointensity experiment. Open (closed) circles represent the ZI (IZ) steps of the heating sequence (see text). The red (blue) line represents the inferred paleointensity associated with the high- (low-) temperature steps. pTRM checks (green triangles) are performed at 200, 250, 350, 450, 520, 550, 570, 590, 610, and 640°C. **b)** Demagnetization curve with the NRM remaining displayed as red circles and pTRM gained as blue squares. **c)** Vector-endpoint diagram of direction during thermal demagnetization (the zero-field only steps of the T-T experiment) where the x-direction has been rotated to the NRM declination, 92.3^{o}, closed circles are the horizontal plane and open circles are the vertical plane. **d)** Equal area plot of the direction at each demagnetization step where closed (open) circles represent projections onto the upper (lower) hemisphere.

origin. The second direction, associated with temperature steps 540°C - 640°C, is well behaved and approaches the origin, a requirement for a primary remanence. The stability of each direction is less clear in the equal area plot of Figure 4.2d.

4.4.3.2 Specimen 62235.120

As with the previous specimen, 62235.120 displays two distinct regions of behavior (Figure 4.3a) above (slope B) and below (slope A) 500°C. It is likely that this specimen failed a pTRM check at 450°C, since the pTRM check performed does not fall on or near its associated temperature step (filled circle). In addition this specimen exhibits a distinct zigzag shape produced by the alternating red (IZ-step) and white (ZI-step) dots below 500°C, which likely represents multi-domain behavior, and implies that an intensity value derived from these points is unreliable. If interpreted as reliable despite non-reciprocal behavior of magnetization (elucidated by the zigzag pattern in the Arai plot), slope A yields a paleointensity estimate of 92.9 μT. Slope B exhibits a linear trend (red line), with little zigzag behavior, and passes pTRM checks. The remanent intensity associated with slope B is 2.9 μT. However, the failed pTRM check at 450°C, suggests that alteration has occurred, and caution is needed in interpretation of the Arai plot at higher temperatures. The remanence acquisition of 62235 is similar to 72215 since the specimen loses most of its NRM below the same approximate temperature (520 ± 20°C) at which it gains the majority of its experimentally induced remanence (Figure 4.3b). Again, the change in remanence occurs at the same temperature where the slope changes on the Arai plot.

A vector endpoint diagram of direction is shown in Figure 4.3c. The directional data define two directions. The first direction, defined by temperature steps 0°C – 500°C, is well behaved (linear on vector-endpoint diagram) and approaches the origin. The second direction, defined by temperature steps 500°C - 570°C, is erratic and it is difficult to determine a clear associated direction. The stability of the first direction is seen in the equal area plot of Figure 4.3d.

4.4.3.3 Specimen 60015.67

The original IZZI-modified Thellier-Thellier experiment specimen 60015.67 failed. The specimen readily demagnetized at low temperature and quickly became too weak to measure. The directions associated with the measured demagnetization steps are unstable and do not yield a coherent component of magnetization. The results from this experiment are displayed in Figure 4.4.

4.4.3.4 Specimen 76535.17

The paleointensity experiment for specimen 76535.17 was unsuccessful. The specimen fails nearly all of the pTRM checks performed (Figure 5a), including those at lower temperature steps. From temperature steps 0 to 540°C the specimen steadily demagnetizes to 20% of its original NRM. The directions associated with temperature steps 0 to 540°C are very stable and uni-directional (Figure 4.5c,d). The paleointensity experiment on specimen 76535.17 was terminated after temperature step 770°C since nearly all pTRM checks failed and the specimen was no longer losing NRM or gaining pTRM in a regular fashion (Figure 4.5b).

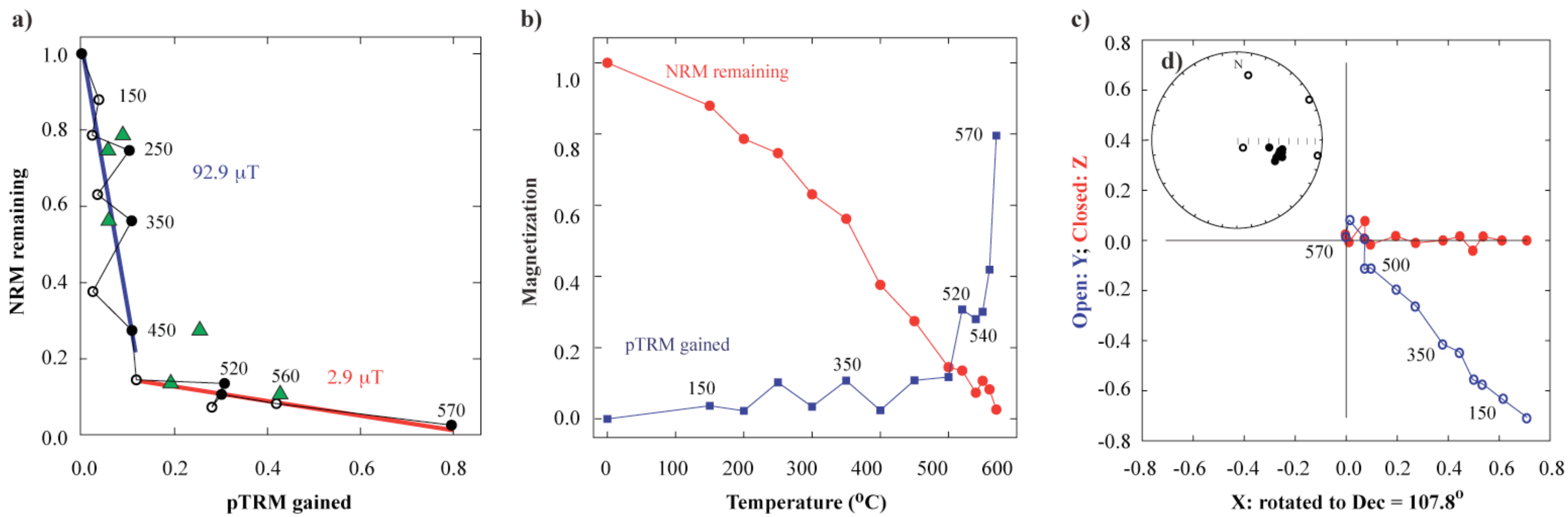

Figure 4.3: Same as Figure 2 for lunar specimen 62235.120 where the NRM is normalized to 4.00e-08 Am^2 and the x-direction has been rotated to the NRM declination, 107.8°.

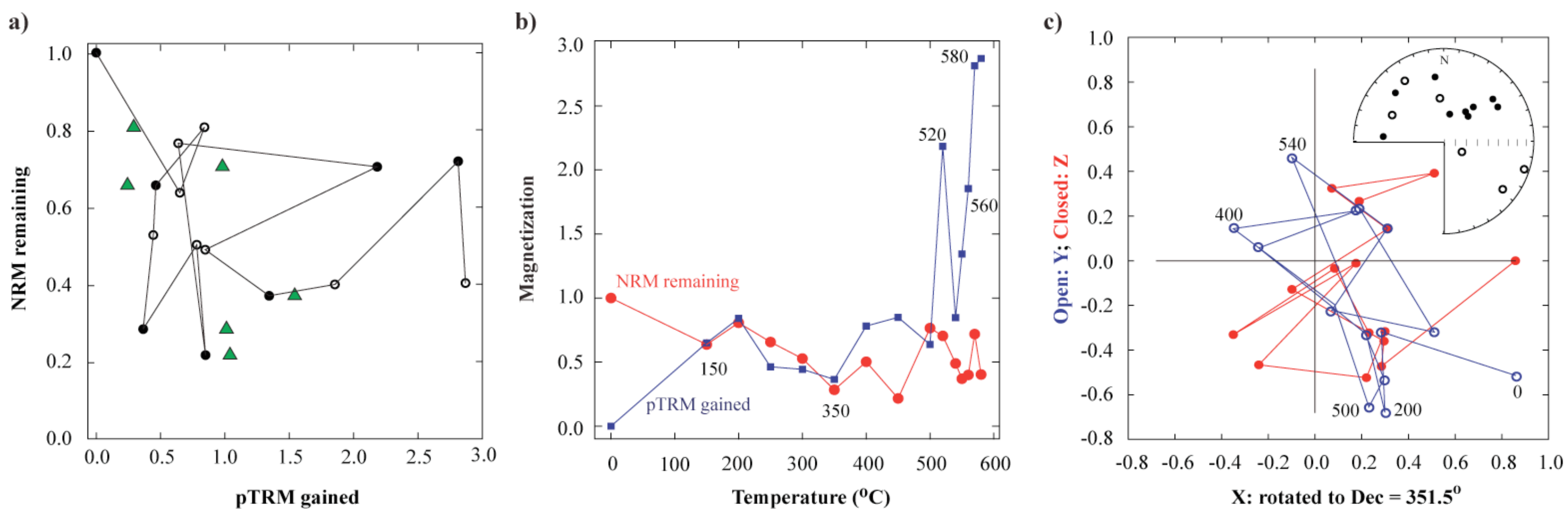

Figure 4.4: Same as Figure 4.2 for lunar specimen 60015.67 where the NRM is normalized to 1.54e-10 Am^2 and the x-direction has been rotated to the NRM declination, 351.5°

Interestingly, the pattern of NRM remaining versus pTRM gained is similar to the results from a paleointensity experiment done on sample 62235 by Pearce et al. [1976]. The failure at low temperature (~300°C) is most likely due to magnetic interactions of troilite and metallic iron [*Pearce, et al.*, 1976], whereas the failure at higher temperature (>600°C) is likely due to reduction of ilmenite to iron and rutile [*Pearce, et al.*, 1976].

4.4.4 sIRM Experimental Method

Results from an SIRM experiment on two lunar specimens (72215.259 and 62235.118) are also presented. The NRM of each specimen was demagnetized using a Sapphire Instruments SI-4 alternating field demagnetizer using a triple demagnetization scheme [*Stephenson*, 1993] whereby specimens are demagnetized along all three axes, measured and then demagnetized along the y-axis, measured and then demagnetized along the z-axis. At every demagnetization field strength, an average of the three measurements is calculated to counteract the effect of gyroremanent magnetization (GRM). GRM is an unwanted remanence produced during demagnetization due to anisotropy in the orientation of the easy axes of magnetization. Specimens were demagnetized in steps of 3 mT until 80% of the NRM was demagnetized, followed by coarser steps until the magnetization was no longer stable. Exposing the demagnetized specimens to a 1 T field using an ASC Pulse Magnetizer induced saturation remanence. The sIRM was demagnetized with the same protocol applied to the corresponding NRM. The individual measurements of direction and intensity for each level of demagnetization are reported in Supplemental Tables A6-A9.

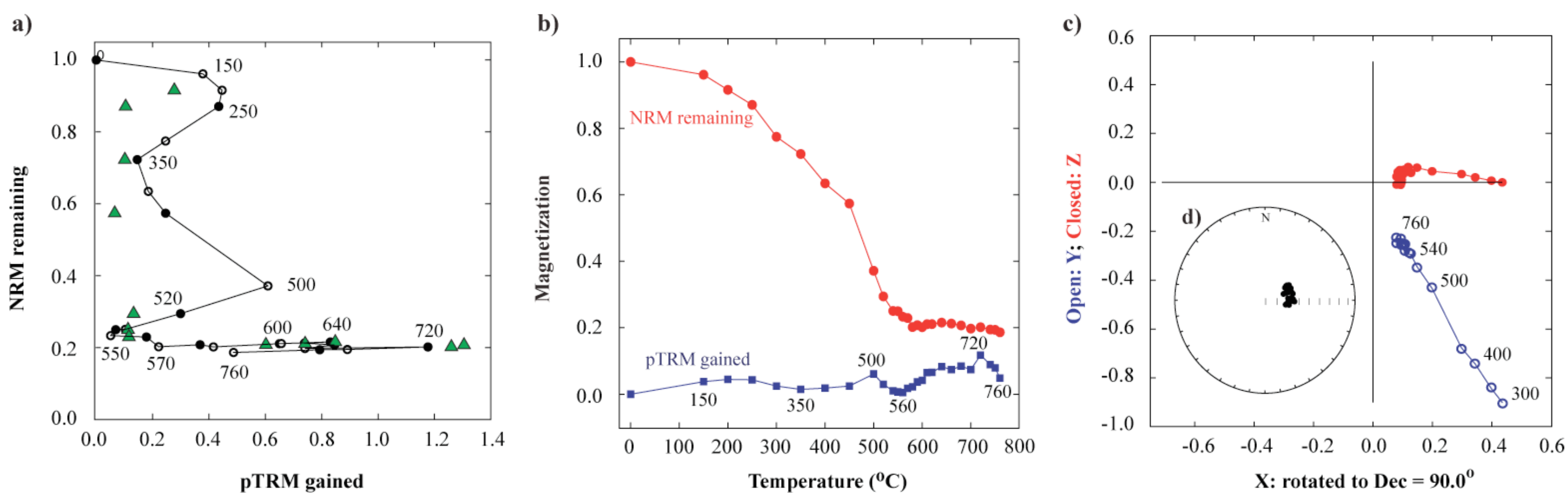

Figure 4.5: Same as Figure 4.2 for specimen 76535.17 where the NRM is normalized to 2.57e-08 Am^2 and the x-direction has been rotated to the NRM declination, 90.0^o.

4.4.5 sIRM Results

4.4.5.1 Specimen 72215.259

The NRM coercivity spectrum for specimen 72215.259 is very soft and is completely demagnetized by 21 mT (Figure 6a). A soft component of magnetization is suggestive of an IRM. This interpretation is supported by the fact that all that is necessary to recreate the originally measured NRM is a 3 mT IRM (dashed line in Figure 6a). The direction of NRM as shown in Figure 6b also displays an unstable NRM. The specimen begins to exhibit GRM behavior after 15 mT at which point the average NRM and direction of the three demagnetized axes markedly vary (this may be a subtle change in Figure 6 because multiple measurements have been averaged, see the raw data in Supplemental Table A6 for complete results). The NRM/sIRM ratio (i.e., at 0 mT demagnetization level) for specimen 72215.259 is 0.023. The method proposed by Cisowski et al. [1983] involves the estimation of the NRM/sIRM ratio at 20 mT, but is inappropriate here since the specimen has been completely demagnetized by 20 mT.

4.4.5.2 Specimen 62235.118

The NRM coercivity spectrum of specimen 62235.118, as shown in Figure 7a is well behaved and directionally stable until ~65 mT. GRM behavior is observed after 40 mT. Qualitatively the NRM curve looks similar to an IRM curve. The NRM/sIRM ratio (at 0 mT) for specimen 62235.118 is 0.018 while applying the partial demagnetized method proposed by Cisowski et al. [1983] yields a NRM(20mT)/sIRM(20mT) ratio of 0.019.

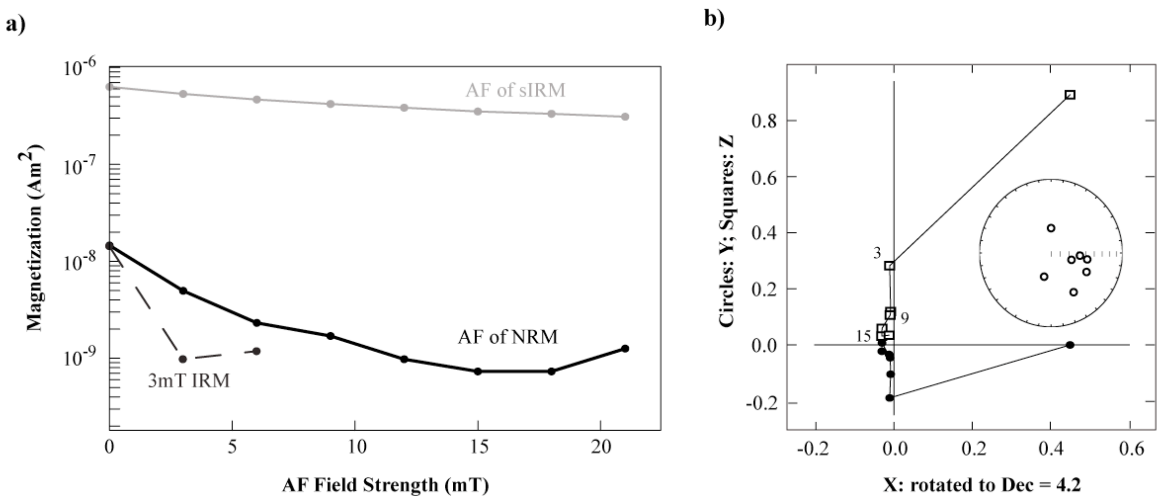

Figure 4.6: a) Alternating field (AF) demagnetization of sample 72215.259 using steps of 3mT following the GRM protocol outlined by Stephenson (1993). The average of the measurements for each demagnetization step of the NRM (sIRM) are shown in black (grey). The sample was also subjected a 3 mT IRM and demagnetized (shown as a dashed line). **b)** Vector endpoint diagram of demagnetized direction of NRM with the X direction rotated to 4.2^{o}. Inset is an equal area plot of the direction each demagnetization step of the NRM.

4.5 Possible Magnetization Scenarios

The apparent multi-component nature (slopes A and B for samples 72215 and 62235) of the new absolute paleointensity results (section 3) is more difficult to interpret than single-component, well-behaved Thellier-Thellier measurements. Here we consider several scenarios in which one, both or neither component of the Thellier-Thellier analysis is an accurate representation of a field(s) present during a portion of the sample's history. Although it is possible that either or both slopes are erroneous measurements due to experimentation error, alteration, or nonlinear magnetization, our experiments show no conclusive evidence for any of these cases. Therefore we examine the possibility that both slopes represent one or more records of magnetic events.

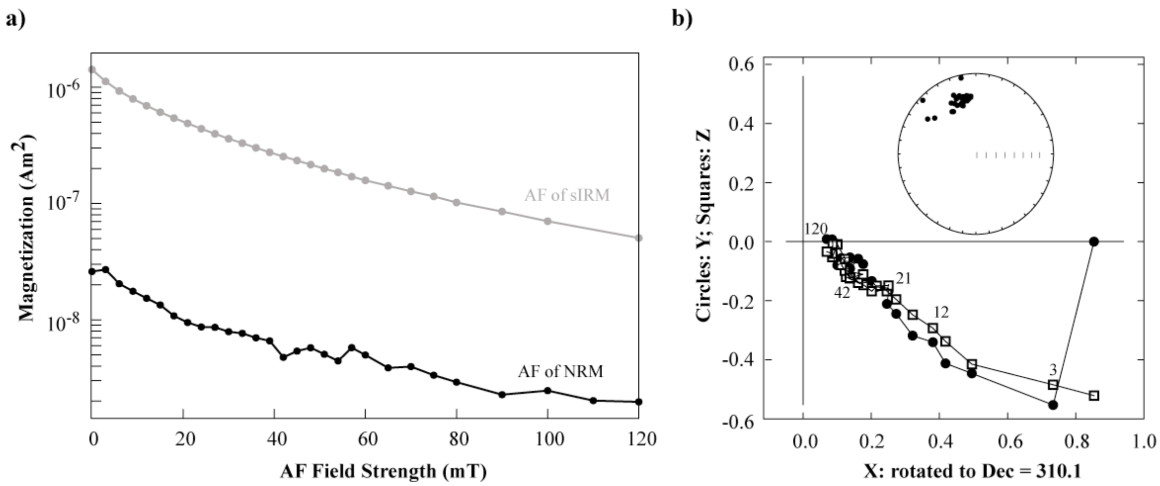

Figure 4.7: Same as Figure 6 for sample 62235.118 where the direction of NRM is rotated to 310.1°

First, we hypothesize that samples 72215 and 62235 could each contain two distinct populations of magnetic carriers with different magnetization proportionality constants and blocking temperature spectra, which could result in two slopes produced simultaneously during a single magnetization event. We test this case (Case 1) through thermal acquisition and controlled KTT experiments. Second, it may be possible for multiple magnetizing events due to different mechanisms (TRM, IRM, etc) to cause slopes A and B even with a single population of magnetic carriers. In this scenario (Case 2), we attempt to differentiate between the various possible mechanisms through KTT experiments with known TRM origins and subsequent exposure to controlled secondary IRM overprint in the lab.

4.5.1 Case 1: Single Magnetization Event

A paleofield interpretation of any component of the Arai plot requires that we validate an assumption of the Thellier-Thellier experiment – that of linear acquisition of magnetization with applied field (section 4.2.2). After completion of the initial IZZI-modified KTT experiment, specimens from samples 62235 and 72215 were repeatedly heated to temperatures above which the specimens were completely demagnetized and cooled in the presence of magnetic fields of increasing strength. The results of this test verify that both specimens linearly acquire magnetization in fields ranging from 5 to 70 μT. It is likely that even in fields up to 100 μT, our specimens will not violate the linearity assumption of the Thellier-Thellier experiment.

The most direct way to test whether the two-component character of the KTT experimental result originates from a single magnetization event is to repeat the experiment with a known TRM. We heated 3 of the 4 specimens demagnetized in the original KTT experiment (72215.262, 62235.120, 60015.67) to 640°C and cooled them in a 5 μT field. We repeated the KTT experiment, the results of which are shown in Figure 8. The linear Arai plots of all three specimens strongly indicate that if a sample cooled in the presence of a 5 μT field the sample would respond in a linear way, inconsistent with the hypothesis of two carriers. Since the samples behave in a linear fashion for fields ranging from 5 to 70 μT, the same conclusion can be made for high fields. These two independent experiments strongly indicate that scenario 1 (the sample has two different carriers from which a single magnetization event is expressed by 2 slopes in the IZZI experiment) is improbable. Although the result in Figure 8 indicates that specimen 62235.120 can still faithfully record an applied field, the type and extent of alteration is unknown (we noted previously that it probably altered in the original KTT experiment) and so we do not conduct further experiments on this specimen.

Interestingly, sample 60015, which did not have a measurable remanence during the original KTT experiment, may be capable of recording a field as low as 5 μT. Assuming that the specimen did not alter in the original KTT experiment, the results of the controlled TRM experiment (Figure 8c) indicate that after cooling in the presence of a 5 μT field, it was possible to faithfully recover the strength of the magnetizing field present. Combining the results in Figure 8c and Figure 4 we infer that the sample was never exposed to a core-field of lunar origin, at or after its Ar-Ar age of ~3.3 Ga.

4.5.2 Case 2: Secondary IRM Overprint

We next test the effect of a secondary IRM on the record of a hypothetical original thermal remanence in a Thellier-Thellier experiment. This experiment is motivated by results presented by Strangway et al. [1973] concerning the magnetic environment the samples were exposed to during the return trip to Earth. After sending a demagnetized Apollo 12 sample on a round trip with Apollo 16, Strangway et al. [1973] concluded that the Apollo samples must have been exposed to an IRM on the order of 3 – 5 mT, while aboard the Apollo Command Module.

During our controlled TRM+IRM experiment specimen 72215.259 was heated to and cooled in a 5 μT field, thereby imparting a TRM of known magnitude. The specimen was then exposed to an IRM in an arbitrary direction and with strength necessary to recreate the original NRM. The magnitude of a secondary IRM necessary to recreate the original NRM is 4.5 mT, which is within the range specified by Strangway et al. [1973]. The high-temperature slope does not accurately reflect TRM of 5 μT given to the specimen at the outset of the experiment. Most importantly, the specimen

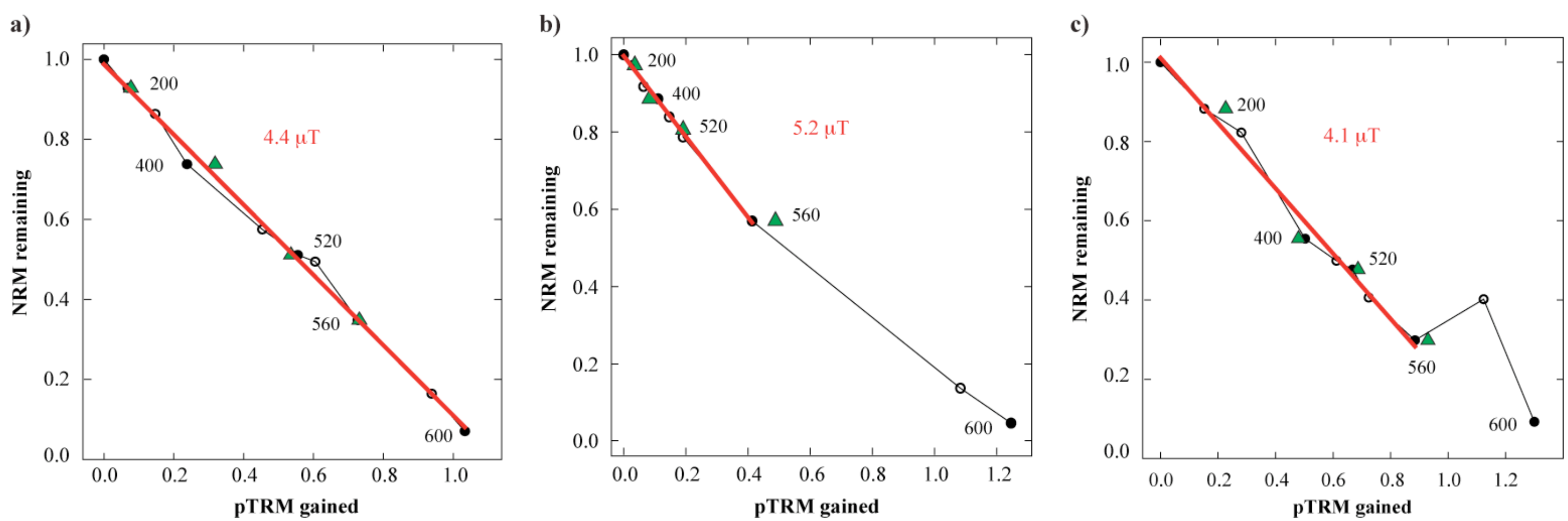

Figure 4.8: Results from a Thellier-Thellier experiment performed after samples **a)** 72215.262 **b)** 62235.120 **c)** 60015.67 were completely demagnetized and subsequently cooled in a 5 µT field. Results presented as Arai plots using notation conventions defined for Figures 4.2 – 4.5. Red lines represent the best estimate of intensity recorded by each sample.

does not fail pTRM checks implying that no alteration has occurred. Therefore, our failure to recover the TRM is a result of the IRM overprint.

This controlled IRM overprint experiment is not the only experiment that indicates an IRM as a major component of the original NRM. The sIRM experiment performed on specimen 72215.259 in this study also indicates an IRM origin for the NRM. The coercivity spectrum of specimen 72215.259 is very soft, having been completely demagnetized by 20 mT (Figure 6), suggesting a non-thermal origin for the remanence. In addition to the demagnetization characteristics, the observed NRM was reproducible with a 3 mT IRM.

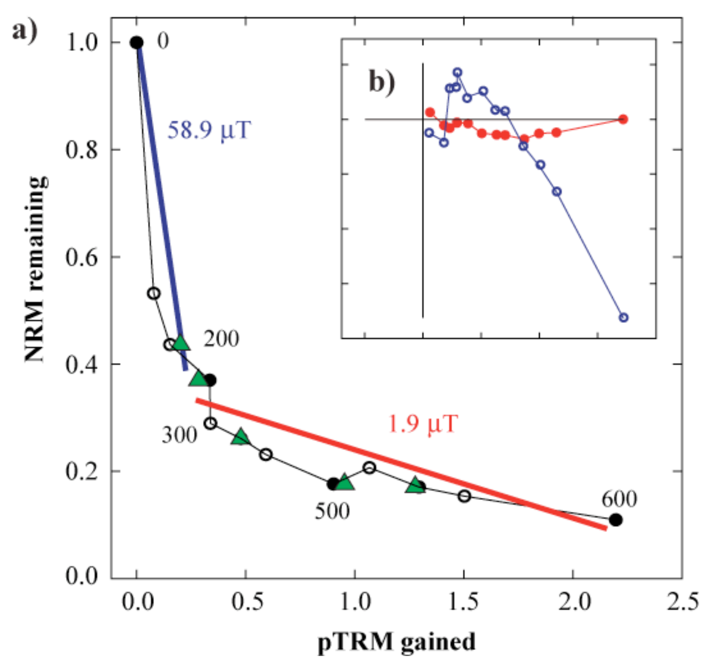

Figure 9. Results from a Thellier-Thellier experiment performed on sample 72215.262 after being completely demagnetized, cooled in a 5 μT field and then exposed to a 4.5 mT magnetic field. **a)** Results presented in an Arai plot using notation conventions defined for Figures 2 - 5. The red and blue lines represent the best estimate of intensity for two portions of the Arai plot. Intensity is normalized to 3.09e-8 Am^2. **b)** Vector-endpoint diagram of direction associated with each demagnetized step. Red dots (blue circles) represent the x-z (x-y) plane.

From this controlled experiment it is apparent that the overprint of even a small IRM (much less than saturation IRM) will adversely affect the blocking temperature spectrum of a specimen, leaving it impossible to accurately recover the intensity of the original TRM. This result has a profound impact on the interpretation of lunar paleointensity. It calls into question the validity of previous KTT results as well as the interpretation of relative intensity methods such as sIRM, because of the use of KTT data in establishing the relative-to-absolute scaling factor.

4.6 Discussion

4.6.1 Interpretation of Paleointensity Experiments

4.6.1.1 Previous Studies

The re-evaluation of the published lunar paleointensity data in light of improved measurement techniques shows that paleointensities recorded by lunar samples are not as unambiguously determined as previously thought. We have shown that only four absolute paleointensity measurements meet a set of objective selection criteria (Figure 1b); these criteria require (a) documentation of original data, (b) no evidence of alteration, and (c) some measure of within-sample reproducibility. Of the four samples, only one has a reported high intensity (62235). Additionally, there are no relative paleointensity data for which the published experimental results currently allow the NRM to be unambiguously interpreted as a primary TRM. Specifically for sIRM measurements, the technique of choice for lunar samples, vector-endpoint diagrams are not routinely displayed with earlier analyses of Apollo samples. In addition, the use of the ratio of NRM to sIRM at an AF demagnetization level of 20 mT to determine a relative paleointensity need not reflect any one of the multiple components of magnetization present in the sample.

Our new paleointensity experiments on sample 62235 produce Arai plots with two distinct slopes. Careful examination of the published literature shows that other studies have also observed this behavior, with a change in the slope of NRM lost versus pTRM gained, at or above 500°C [*Gose, et al.*, 1973; *Sugiura and Strangway*, 1980, 1983; *Sugiura, et al.*, 1979]. This indicates multiple components of magnetization and previous studies analyzed the results in different ways: some interpreting the high-temperature component, and others interpreting the low-temperature component. The low temperature steps yield paleointensity estimates consistent with previously-proposed high field values for the moon, whereas paleointensities derived from the high temperature steps are an order of magnitude lower and consistent with previously-published low field values. For example, Gose et al. [1973] determine low intensity for temperature steps above 500°C of sample 15498 whereas interpretation of their temperature steps below ~500°C would yield a much higher intensity. Given this multi-component behavior, it is essential to demonstrate which component (if either) is associated with an original thermal remanence.

<u>4.6.1.2 New Experiments</u>

The controlled TRM experiments (section 4.5.1) indicate that three of our samples are capable of accurately recording a primary thermal remanence in applied magnetic fields that span the range of proposed low and high lunar fields. Our new experiments show that three modern laboratory protocols, unavailable or not routinely used in the 1970s, are critical to the interpretation of absolute paleointensity data: these are the simultaneous measurement of paleodirection during the Thellier-Thellier experiments (also essential for relative paleointensity methods), the use of pTRM checks (to detect alteration), and the IZZI approach (to detect non-reciprocal blocking and unblocking behavior).

Of the new measurements, samples 62235 and 72215 show multi-component Arai plots with associated intensities of ~90 μT (low temperature) and ~2 μT (high temperature), which are equivalent to the high intensity assertion from Sugiura and Strangway [1983] for sample 62235 and the low intensity assertion of Gose et al. [1973] for sample 15498. Because of our detailed laboratory procedures, we are able to investigate whether either component is clearly a primary thermal remanence. We summarize the implications of both our absolute and relative paleointensity experiments on these samples below.

Specimen 62235.120 has well-behaved directions (low scatter) that linearly decay toward the origin at temperature steps lower than 500°C (Figure 3c). Yet, the measurements of NRM remaining versus pTRM gained (Arai plot in Figure 3a) exhibit a strong zigzag characteristic, often indicative of multi-domain magnetic carriers, which are unreliable recorders of magnetic field. It is the use of the IZZI method that allows the detection of this non-reciprocal magnetization/demagnetization behavior; without it the low temperature portion of the Arai plot would appear linear and well-behaved, resulting in a confident interpretation of a high paleofield value. The use of pTRM checks indicates that the specimen altered at 450°C, likely leaving the high temperature component of the specimen uninterpretable.

The sIRM results for specimen 62235.118 are also complicated. There is an overprint of unknown origin that is removed by 6 mT (Figure 7). The specimen directions are then relatively stable until ~21 mT, but the direction does not linearly decay to the origin. This is clearly seen by the dashed lines extending the trend of demagnetization steps 6 to 21 mT in Figure 10. In addition, the maximum angle of deviation (MAD = 5.2°) of the best-fit direction for this component is less than the angular difference the component makes with the origin (dANG = 5.6°). The failure of the best-fit directions to decay to the origin indicates that it is not a primary remanence, and that the sIRM measurement does not accurately record the field intensity at the time of sample formation. In summary, any postulate of a high-field era based solely on sample 62235 cannot be substantiated by comparison with previous sIRM results on the same sample, because these earlier studies neglected to prove primary remanence of the observed remanent magnetization.

The results from specimen 72215.262 also do not support a high field interpretation. The KTT results do not exhibit the same zigzag nature at low temperature as specimen 62235.120. However, the direction associated with these low-temperature steps does not decay linearly to the origin (MAD = 7.2, which is less dANG = 7.7). The high-temperature steps are associated with a lower intensity by a factor of 50 (1.8 as compared to 93.1 μT) and a direction that trends to origin (Figure 2c) but is relatively unstable (Figure 2d). In addition, the sIRM results from specimen 72215.259 strongly suggest an IRM origin of remanence since the NRM is completely demagnetized by 20 mT.

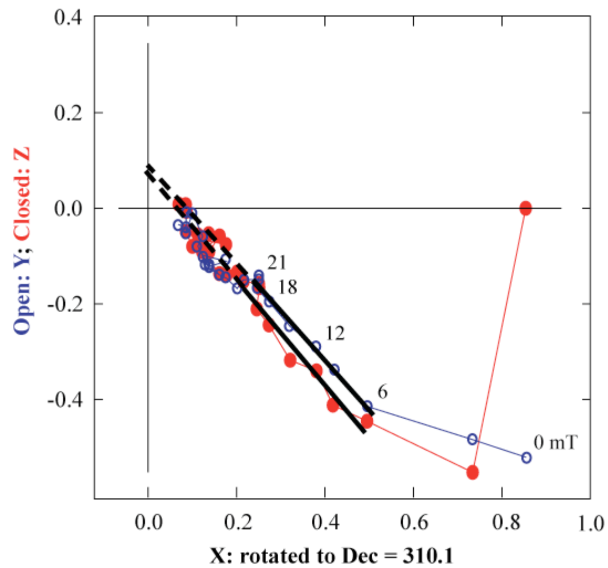

Figure 10. Vector-endpoint diagram of direction during alternating field demagnetization of sample 62235.118 where the NRM is normalized to 2.60e-8 Am^2 and x-direction has been rotated 310.1°. Closed circles are the horizontal plane and open squares are the vertical plane. Black lines represent the best-fit direction calculated using principal component analysis between 6 mT and 21 mT demagnetizations steps. Dashed lines linearly extrapolate the calculated trend.

4.6.2 Possible Sources for Multiple Components of Magnetization

<u>4.6.2.1 IRM</u>

Meaningful paleofield interpretation of paleointensity experiments requires that the paleointensity estimate be associated with a primary TRM. The primary TRM can only be identified for a component if the direction linearly decays to the origin and the specimen is free from alteration during the experiment. As these criteria cannot be assessed for previously published paleointensity results, and as any high field values for our new data are not clearly primary in origin, we have attempted to understand what might give rise to apparent high paleointensities. Given that lunar samples returned in Apollo capsules were exposed to a small, but potentially damaging magnetic field [*Strangway, et al.*, 1973], and given that perhaps the most reliable interpretation of our own Thellier-Thellier experiments is the low paleofield value recorded by 72215.262 we conducted an experiment to investigate the effect of a primary TRM (a possible lunar paleofield) with a secondary IRM overprint (spacecraft contamination). The results from this experiment (Section 4.2) indicate that such a magnetization scenario can give rise to paleointensity results that qualitatively resemble those obtained for lunar samples, with Arai plots exhibiting a break in slope. The field in which the sample acquired a TRM was unrecoverable during the experiment, suggesting that it is possible that neither component (slope A or B) accurately represents the strength of a magnetic field in existence when lunar materials cooled through the Curie temperature. It has yet to be explored whether the adverse effects of an IRM overprint can be removed through AF demagnetization to yield a successful Thellier-Thellier experiment.

It is readily apparent from the data presented in this study that multi-component NRM behavior must be assessed and documented in order to accurately interpret the magnetizations of lunar samples. Therefore, sIRM methods that fail to identify and correctly characterize multiple components of an NRM are inadequate to measure remanent magnetic fields in lunar samples, and should not be used to infer a high field era in early lunar evolution. Gattacceca and Rochette [2004], note that even after the removal of secondary (overprint) components via alternating field demagnetization the sIRM method cannot accurately determine the paleomagnetic field because it does not account for instances where residual fractions of NRM and IRM differ after the highest demagnetization step, and at the demagnetization step used to establish a relative paleointensity (typically, 20 mT).

The estimated absolute paleointensity for any sIRM measurement is subject to a poorly constrained scaling factor (*f*), which is dependent on parameters such as field strength, magnetic mineralogy, grain size, and grain shape. Earlier [*Fuller and Cisowski*, 1987] and recent work [*Gattacceca and Rochette*, 2004; *Kletetschka, et al.*, 2004; *Kletetschka, et al.*, 2006; *Yu*, 2006] reach differing conclusions on the importance of these parameters; theory indicates that all should play a role. Relative paleointensities have been measured for different types of lunar rocks that have different mineralogy, grain shape, and size, and may have formed during different magnetic fields. If *f* depends on magnetic carrier (type, grain size, anisotropy) and/or field strength then the use of a constant scaling factor is inappropriate, and importantly, might affect the resulting temporal structure of the relative paleointensity data set. Furthermore, as a result of our re-evaluation of published absolute paleointensity data, the uncertainty in even an average single empirical lunar scaling factor [e.g. *Cisowski, et al.*, 1983; *Kletetschka, et al.*, 2004] is large because only 4 of the 14 samples used to calculate the scaling factor are considered acceptable. From this discussion we deem it inappropriate to provide estimates of absolute paleointensity for our sIRM measurements because of the ill-constrained lunar scaling factor, and the questionable association of the new sIRM measurements with primary TRMs. Authors who have recently applied the sIRM method [e.g., *Garrick-Bethel and Weiss*, 2007; *Gattacceca and Rochette*, 2004; *Yu*, 2006] acknowledge its shortcomings of limited precision for estimating the paleofield, in some cases providing no better than an order of magnitude estimate.

4.6.2.2 Impacts & Shock

Clearly impacts, and therefore shock, have played a significant role in the formation of the lunar surface. All samples that have paleointensity measurements passing the reliability criteria set forth in this study have been extensively modified by shock-related events. For example, sample 15498 is a shock-lithified sample that was most likely heated in a high-field ejecta blanket [*Christie, et al.*, 1973; *Gose, et al.*, 1972]. Cisowski et al. [1976; 1973; 1975] conducted a suite of experiments in the presence of a magnetic field (Earth's field) that demonstrate the possible adverse effects of low to moderate shock on the magnetic remanence for lunar materials. Cisowski et al. [1975] argue that SRM (shock remanent magnetization) is the likely source of NRM in certain regolith breccias and that shock may modify the primary remanence of many other samples.

Of particular interest is sample 62235, which has yielded a component of magnetization with an apparently high paleointensity in previous studies and our new results. A recent re-examination of previous work on 62235 by Fuller and Halekas [2008] suggests that the data are consistent with a small high-temperature TRM, accompanied by a strong SRM acquired in a later event. Our new data support this interpretation and clearly indicate that further examination of the role of shock on lunar samples is needed. In particular, Fuller and Halekas [2008] note that shock may be affecting the magnetic signature of lunar samples, even for samples where there are no strong petrological effects evident.

Analyses of lunar crustal magnetic fields indicate that impact processes govern the distribution of surface fields [e.g. *Halekas, et al.*, 2001; *Hood, et al.*, 2003; *Lin, et al.*, 1988; *Richmond, et al.*, 2005]. Lunar Prospector Electromagnetic Reflectometer [e.g. *Mitchell, et al.*, 2008] and Magnetometer [e.g. *Richmond and Hood*, 2008] studies show that 1) the majority of the moon's surface has weak (< 3 nT) surface fields, 2) impact basins have weaker magnetic anomalies than surrounding crust [*Halekas, et al.*, 2003; *Halekas, et al.*, 2002], and 3) the strongest magnetic anomalies are antipodal to 4 large impact basins (Imbrium, Orientale, Crisium and Serenitatis) [e.g. *Lin, et al.*, 1988]. The strong magnetic crustal fields antipodal to large impact basins have motivated the hypothesis that crustal magnetization is a result of hypervelocity impacts causing plasma clouds to compress and amplify pre-existing ambient magnetic fields (whether internal dynamo or inter-planetary magnetic field in origin) near the antipode of an impact site [e.g. *Crawford and Schultz*, 1991; e.g. *Crawford and Schultz*, 1999; *Hood and Artemieva*, 2007; *Hood and Huang*, 1991; *Snkra, et al.*, 1979]. SRM may be acquired by pre-existing basement materials and/or ejecta at the antipode due to magnetization of due to increased pressure (2-10 GPa) from focused 1) seismic energy or 2) secondary impacts at the antipode from primary impact ejecta. Several studies [*Hood and Artemieva*, 2007; *Hood and Huang*, 1991] argue that the field amplification effects at the antipode are sufficiently large that the properties of the pre-existing ambient magnetic field are negligibly important, eliminating the need for a strong pre-existing field to produce magnetic anomalies at impact antipodes. In fact, the lack of even weak magnetic anomalies within the Imbrium basin [*Halekas, et al.*, 2003; *Halekas, et al.*, 2002] supports the hypothesis that a strong ambient field did not exist during its formation (3.75-3.87 Ga [*Stoffler and Ryder*, 2001]).

4.6.3 An Uneasy Case for an Early Dynamo

Our new paleointensity data and our reevaluation of published results indicate that inferred high paleointensities do not reflect magnetization of samples in a 3.9 – 3.6 Ga lunar dynamo-driven field. This inference is consistent with the general absence of strong magnetic anomalies associated with both the edges of Imbrium-aged basins and the mare basalts that formed in the 3.9 - 3.6 Gyr time period. In addition, the strong surface fields present problems for dynamo models, as originally pointed out by Hood et al. [1979]. The 100 μT surface fields previously proposed for the 3.9 - 3.6 Ga interval, require core surface fields that are at least 100 times this value (assuming a dipolar surface field geometry), and a core Elsasser number that is difficult to reconcile with current understanding of dynamo-generated fields. Finally, an early dynamo driven by heat flow through the core-mantle boundary (Stegman et al., 2003) places severe constraints on the early thermo-chemical evolution of the Moon, that are relaxed in the absence of a high field era.

SRM, not TRM, provides the most straightforward explanation for both observed lunar crustal anomalies and the paleointensity data. Unfortunately, both previous and modern paleomagnetic methods cannot differentiate between SRM and TRM, complicating lunar paleomagnetic interpretations, and clearly further work is needed to understand the role shock has played in the magnetization of lunar samples.

The existence of a lunar dynamo prior to 3.9 Ga is an open question. It is possible that the high temperature, low intensity component observed in some lunar samples may reflect magnetization in an earlier, weak (few micro-Tesla) field [*Fuller and Halekas*, 2008]; however this has not yet been unequivocally demonstrated. Additionally the inferred paleointensities are low enough that magnetization in the ambient interplanetary magnetic field is plausible, negating the need for an intrinsic lunar field. Some support for a Nectarian or pre-Nectarian weak lunar surface field is provided by the distribution of crustal magnetic fields, particular those inside major basins (Mitchell et al., 2008), however the distribution and interpretation of these crustal fields is complex.

4.7 Conclusions

In summary, lunar paleointensity measurements to date do not support the previously-proposed interpretation: that of a 3.9 – 3.6 Ga lunar dynamo. Compilation and analyses of lunar paleointensities are hindered by 1) the limited number of measurable samples, 2) the variety and quality of previous paleointensity experiments, and 3) the ambiguous interpretation of complex paleointensity results. There is not a single lunar paleointensity result (in this study or in the published literature) that passes the criteria of a successful and robust paleointensity experiment (relative or absolute) as applied to terrestrial samples [*Gattacceca and Rochette*, 2004; *Selkin and Tauxe*, 2000]. Of the four samples measured here, one (76535) experiment failed due to alteration, another (60015) did not record a measurable paleointensity, the paleointensity of a third sample (72215) is most likely due to shock or IRM contamination during sample return rather than thermal remanent magnetization, and the complicated results of the fourth

(62235) cannot be unambiguously interpreted as a thermal remanent magnetization. More importantly, there is no conclusive evidence that any measured paleointensities are original thermal remanent magnetizations for lunar samples, regardless of the measurement method used. Hence, all future lunar paleointensity studies need to demonstrate primary remanent magnetization through directional data prior to interpreting paleointensity as recording magnetization acquired in a lunar dynamo field. The absence of reliable absolute paleointensity measurements is particularly problematic as it renders relative paleointensity measurements unreliable, since they are scaled using absolute measurements. A re-evaluation of previous results and the new data presented here do not negate the existence of an early lunar dynamo; they merely demonstrate a lack of evidence for one. While a dynamo may have existed early in the Moon's history, the absence of dynamo-driven strong (~100 μT) surface fields during the 3.9 - 3.6 Ga period is more compatible with other surface and satellite magnetic field observations, presents fewer difficulties for lunar thermal evolution models and is easier to reconcile with current understanding of dynamo processes.

4.8 Acknowledgments

We thank the reviewers, Mike Fuller and anonymous, for insightful feedback and constructive suggestions. We would like to thank Rob Van der Voo, Mark Jellinek, and Jesse Lawrence for discussions, which improved the manuscript. We also thank Bruce Deck for aid in experimental set-up and execution. The work was supported under NASA Planetary Geology and Geophysics Grant NNG05GK34G.

This chapter is a reformatted version of Lawrence, K.P.; Johnson, C.L.; Tauxe, L.; Gee, J.S. (2008), Lunar paleointensity measurements: Implications for lunar magnetic evolution, *Physics of the Earth and Planetary Interiors,* in press.

4.9 References

Banerjee, S. K., and J. P. Mellema (1974), A new method for the determination of paleointensity from the A.R.M. properties of rocks, *Earth Planet. Sci. Lett.*, *23*, 177-184.

Banerjee, S. K., and J. P. Mellema (1976), A solar origin for the large lunar magnetic field 4.0 x 10^9 yr ago? *Proceedings of the Lunar Science Conference 7th*, 3259-3270.

Banerjee, S. K., and G. Swits (1975), Natural remanent magnetization studies of a layered breccia boulder from the lunar highland region, *The Moon*, *14*, 473-481.

Butler, R. F. (1992), *Paleomagnetism: Magnetic Domains to Geologic Terranes*, 336 pp., Blackwell Scientific, Boston.

Christie, J. M., D. T. Griggs, A. H. Heuer, G. L. Nord Jr., S. V. Radcliffe, J. S. Lally, and R. M. Fisher (1973), Electron petrography of Apollo 14 and 15 breccias and shock-produced analogs, *Proceedings of the Lunar and Planetary Science Conference*, *4*.

Cisowski, S. M., D. W. Collinson, S. K. Runcorn, and A. A. Stephenson (1983), A review of lunar paleointensity data and implications for the origin of lunar magnetism, *J. Geophys. Res.*, *88*, A691-A704.

Cisowski, S. M., D. W. Collinson, A. Stephenson, and S. K. Runcorn (1982), A new look at lunar paleomagnetic data: Evidence for a well-defined lunar "magnetic Epoch" 3.65 - 3.85 GY B.P., *Lunar and Planetary Science XIII*, *Abstract*, 107-108.

Cisowski, S. M., J. R. Dunn, M. Fuller, Y. Wu, M. F. Rose, and P. Wasilewski (1976), Magnetic effects of shock and their implications for lunar magnetism (II), *Proceedings of the Lunar and Planetary Science Conference, 7th*, 3299-3320.

Cisowski, S. M., M. Fuller, M. F. Rose, and P. Wasilewski (1973), Magnetic effects of experimental shocking of lunar soil, *Proceedings of the Lunar and Planetary Science Conference*, *4*, 3003.

Cisowski, S. M., M. Fuller, Y. Wu, M. F. Rose, and P. Wasilewski (1975), Magnetic effects of shock and their implications for magnetism of lunar samples, *Proceedings of the Lunar and Planetary Science Conference, 6th*, 3123-3141.

Cisowski, S. M., C. Hale, and M. Fuller (1977), On the intensity of ancient lunar fields, *Proceedings of the Lunar Science Conference 8th*, 725-750.

Coe, R. S., S. C. Grommé, and E. A. Mankinen (1978), Geomagnetic paleointensities from radiocarbon dated lava flows on Hawaii and the question of the Pacific nondipole low, *J. Geophys. Res.*, *83*, 1740-1756.

Collinson, D. W. (1985), Primary and secondary magnetizations in lunar rocks - Implications for the ancient magnetic field of the Moon, *Earth Moon and Planets*, *33*, 31-58.

Collinson, D. W. (1993), Magnetism of the Moon - A Lunar core dynamo or impact magnetization, *Surv. Geophys.*, *14*, 89-118.

Collinson, D. W., A. Stephenson, and S. K. Runcorn (1973), Magnetic properties of Apollo 15 and 16 rocks, *Proceedings of the Fourth Lunar Science Conference*, *3*, 2963-2976.

Crawford, D. A., and L. S. Hollister (1974), KREEP Basalt: A possible partial melt from the lunar interior, *Proceedings of the Fifth Lunar Science Conference (Supplement 5, Geochimica et Cosmochimica Acta)*, *1*, 399-419.

Crawford, D. A., and P. H. Schultz (1991), Laboratory investigations of impact-generated plasma, *J. Geophys. Res.*, *96*, 18807-18817.

Crawford, D. A., and P. H. Schultz (1993), The production and evolution of impact-generated magnetic fields, *International Journal of Impact Engineering*, *14*, 205-216.

Crawford, D. A., and P. H. Schultz (1999), Electromagnetic properties of impact-generated plasma, vapor and debris, *International Journal of Impact Engineering*, *23*, 169-180.

Dunlop, D. J., and O. Ozdemir (1997), *Rock Magnetism: Fundamentals and Frontiers*, 573 pp., Cambridge University Press.

Dymek, R. F., A. L. Albee, and A. A. Chodos (1975), Comparative petrology of lunar cumulate rocks of possible primary origin: Dunite 72415, troctolite 76535, norite 78235, and anorthosite 62237, *Proceedings of the Lunar and Planetary Science Conference, 6th*, *1*, 301-341.

Fuller, M. (1974), Lunar magnetism, *Reviews of Geophysics and Space Physics*, *12*, 23-70.

Fuller, M. (1998), Lunar magnetism; a retrospective view of the Apollo sample magnetic studies, *Physics and Chemistry of the Earth*, *23*, 725-735.

Fuller, M., and S. M. Cisowski (1987), Lunar paleomagnetism, in *Geomagnetism*, edited by J. A. Jacobs, pp. 307-456, Academic Press, San Diego, CA.

Fuller, M., and J. Halekas (2008), The role of impact related shock in lunar magnetism, *Lunar and Planetary Science XXXIX*, Abstract #1430.

Garrick-Bethel, I., and B. P. Weiss (2007), Early lunar magnetism, *Lunar and Planetary Science XXXVI*, Abstract #2405.

Gattacceca, J., and P. Rochette (2004), Toward a robust normalized magnetic paleointensity method applied to meteorites, *Earth Planet. Sci. Lett.*, *227*, 377-393.

Gooley, R., R. Brett, J. Warner, and J. R. Smyth (1974), A lunar rock of deep crustal origin: Sample 76535, *Geochimica et Cosmochimica Acta*, *38*, 1329-1339.

Gose, W. A., G. W. Pearce, D. W. Strangway, and E. E. Larson (1972), On the applicability of lunar breccias for paleomagnetic interpretations, *Earth, Moon, and Planets*, *5*, 106.

Gose, W. A., D. W. Strangway, and G. W. Pearce (1973), A Determination of the intensity of the ancient lunar magnetic field, *The Moon*, *7*, 196-201.

Halekas, J., R. P. Lin, and D. L. Mitchell (2003), Magnetic fields of lunar multi-ring impact basins, *Meteoritics and Planetary Science*, *38*, 565-578.

Halekas, J. S., D. L. Mitchell, R. P. Lin, S. Frey, L. L. Hood, M. H. Acuna, and A. B. Binder (2001), Mapping of crustal magnetic anomalies on the lunar near side by the Lunar Prospector electron reflectometer, *J. Geophys. Res.*, *106*, 27841-27852.

Halekas, J. S., D. L. Mitchell, R. P. Lin, L. L. Hood, M. H. Acuna, and A. B. Binder (2002), Demagnetization signatures of lunar impact craters, *Geophys. Res. Lett.*, *29*.

Hood, L. L., and N. A. Artemieva (2007), Antipodal effects of lunar basin-forming impacts: Initial 3D simulations and comparisons with observations, *Icarus*, *in press*, doi:10.1016/j.icarus.2007.1008.1023.

Hood, L. L., P. J. Coleman, C. T. Russell, and D. E. Wilhelms (1979), Lunar magnetic anomalies detected by the Apollo subsatellite magnetometers, *Phys. Earth Planet. Int.*, *20*, 53-57.

Hood, L. L., and Z. Huang (1991), Formation of magnetic anomalies antipodal to lunar impact basins: Two-dimensional model calculations, *J. Geophys. Res.*, *96*, 9837-9846.

Hood, L. L., D. L. Mitchell, R. P. Lin, H. Acuna, and A. B. Binder (1999), Initial measurements of the lunar induced magnetic dipole moment using Lunar Prospector magnetometer data, *Geophys. Res. Lett.*, *26*, doi:10.1029/1999GL900487.

Hood, L. L., N. C. Richmond, E. Pierazzo, and P. Rochette (2003), Distribution of crustal magnetic fields on Mars: Shock effects of basin-forming impacts, *Geophys. Res. Lett.*, *30*, doi:10.1029/2002GL016657.

Hood, L. L., C. T. Russell, and P. J. Coleman (1981), Contour maps of the lunar remanent magnetic fields, *J. Geophys. Res.*, *86*, 1055-1069.

Hood, L. L., A. Zakharian, J. Halekas, D. L. Mitchell, R. P. Lin, M. H. Acuna, and A. B. Binder (2001), Initial mapping and interpretation of lunar crustal magnetic anomalies using Lunar Prospector magnetometer data, *J. Geophys. Res.*, *106*, 27825-27839.

Kletetschka, G., H. Acuna, T. Kohout, P. Wasilewski, and J. E. P. Connerney (2004), An empirical scaling law for acquisition of thermoremanent magnetization, *Earth Planet. Sci. Lett.*, *226*, 521-528.

Kletetschka, G., M. Fuller, T. Kohout, P. Wasilewski, E. Herrero-Bervera, N. F. Ness, and H. Acuna (2006), TRM in low magnetic fields: a minimum field that can be recorded by large multi-domain grains, *Phys. Earth Planet. Int.*, *154*, 290-298.

Kletetschka, G., T. Kohout, and P. J. Wasilewski (2003), Magnetic remanence in the Murchison meteorite, *Meteoritics & Planetary Science*, *38*, 399-405.

Lin, R. P., K. A. Anderson, and L. L. Hood (1988), Lunar surface magnetic field concentrations antipodal to young impact basins, *Icarus*, *74*, 529-541.

Mitchell, D. L., J. Halekas, R. P. Lin, S. Frey, L. L. Hood, H. Acuna, and A. B. Binder (2008), Global mapping of lunar crustal magnetic fields by Lunar Prospector, *Icarus*, *194*, 401-409.

Nagata, T., R. M. Fisher, and F. C. Schwerer (1972), Lunar rock magnetism, *Earth, Moon, and Planets*, *4*, 160-186.

Nagata, T., R. M. Fisher, and F. C. Schwerer (1974), Some characteristic magnetic properties of lunar materials, *The Moon*, *9*, 63-77.

Nagata, T., R. M. Fisher, F. C. Schwerer, M. Fuller, and J. R. Dunn (1973), Magnetic properties and natural remanent magnetization of Apollo 15 and 16 lunar materials, *Proceedings of the Fourth Lunar Science Conference*, *3*, 3019-3043.

Norman, M. D., R. A. Duncan, and J. J. Huard (2006), Identifying impact events within the lunar cataclysm from ^{40}Ar-^{39}Ar ages and compositions of Apollo 16 impact melt rocks, *Geochemica et Cosmochimica Acta*, *70*, 6032-6049.

Nunes, P. D. (1975), Pb loss from Apollo 17 glassy samples and Apollo 16 revisited, *Proceedings of the Lunar and Planetary Science Conference, 6th*, 1491-1499.

Pearce, G. W., W. A. Gose, and D. W. Strangway (1973), Magnetic studies on Apollo 15 and 16 lunar samples, *Proceedings of the Fourth Lunar Science Conference*, *3*, 3045-3076.

Pearce, G. W., G. S. Hoye, D. W. Strangway, B. M. Walker, and L. A. Taylor (1976), Some complexities in the determination of lunar paleointensities, *Proceedings of the Lunar Science Conference 7th*, 3271-3297.

Pearce, G. W., D. W. Strangway, and W. A. Gose (1972), Remanent magnetization of the lunar surface, *Proceedings of the Third Lunar Science Conference*, *3*, 2449-2464.

Premo, W. R., and M. Tatsumoto (1992), U-Th-Pb, Rb-Sr, and Sm-Nd isotopic systematics of lunar troctolite cumulate 76535: Implications on the age and origin of this early lunar, deep-seated cumulate, *Proceedings of the Lunar and Planetary Science Conference, 22nd*, 381-397.

Richmond, N. C., and L. L. Hood (2008), A preliminary global map of the vector lunar crustal magnetic field based on Lunar Prospector magnetometer data, *J. Geophys. Res.*, *in press*, doi:10.1029/2007JE002888.

Richmond, N. C., L. L. Hood, D. L. Mitchell, R. P. Lin, H. Acuna, and A. B. Binder (2005), Correlations between magnetic anomalies and surface geology antipodal to lunar impact basins, *J. Geophys. Res.*, *110*.

Riisager, P., and J. Riisager (2001), Detecting multidomain magnetic grains in the Thellier palaeointensity experiments, *Phys. Earth Planet. Int.*, *125*, 111-117.

Runcorn, S. K. (1994), The early magnetic-field and primeval satellite of the Moon: Clues to planetary formation, *Philos. Trans. R. Soc. London, Ser. A*, *349*, 181-196.

Runcorn, S. K. (1996), The formation of the lunar core, *Geochimica et Cosmochimica Acta*, *60*, 1205-1208.

Runcorn, S. K., D. W. Collinson, W. O'Reilly, A. Stephenson, M. H. Battey, A. J. Manson, and P. W. Readman (1971), Magnetic properties of Apollo 12 lunar samples, *Proceedings of the Royal Society of London Series A-Mathematical and Physical Sciences*, *325*, 157-174.

Russell, C. T., P. J. Coleman, B. R. Lichtenstein, and G. Schubert (1974), The permanent and induced magnetic dipole moment of the moon, *Proceedings of the Fifth Lunar Science Conference*, *3*, 2747-2760.

Ryder, G., and M. D. Norman (1980), Catalog of Apollo 16 rocks, *Curator's Office Publication #52*, *3*, JSC #16904.

Ryder, G., D. B. Stoeser, U. B. Marvin, J. F. Bower, and J. A. Wood (1975), Boulder 1, Station 2, Apollo 17: Petrology and petrogenesis, *The Moon*, *14*, 327 - 357.

Schaeffer, O. A., and L. Husain (1974), Chronology of lunar basin formation, *Proceedings of the Fifth Lunar Science Conference*, *2*, 1541-1555.

Schaeffer, O. A., R. Warasila, and T. C. Labotka (1982), Ages of Serenitatis breccias, *Lunar and Planetary Science XIII*, *Abstract*, 685-686.

Schubert, G., D. L. Turcotte, and P. Olson (2001), *Mantle Convection in the Earth and Planets*, 956 pp., Cambridge University Press.

Selkin, P. A., and L. Tauxe (2000), Long-term variations in paleointensity, *Philos. Trans. R. Soc. London, Ser. A*, *358*, 1065-1088.

Snkra, L. J., G. Martelli, G. Newton, S. M. Cisowski, M. Fuller, and R. B. Schaal (1979), Magnetic field and shock effects and remanent magnetism in a hyper-velocity impact environment, *Earth Planet. Sci. Lett.*, *42*, 127-137.

Sonett, C. P., D. S. Colburn, R. G. Currie, and J. D. Mihalov (1967), The geomagnetic tail, topology, reconnection and interaction with the Moon, in *Physics of the Magnetosphere*, edited by R. L. Carovillano, et al., pp. 461-484, Dordrecht, Reidel.

Stegman, D. R., M. J. Jellinek, S. A. Zatman, J. R. Baumgardner, and M. A. Richards (2003), An early lunar core dynamo driven be thermochemical mantle convection, *Nature*, *421*, 143-145.

Steiger, R. H., and E. Jäger (1977), Subcommission on geochronology: Convention on the use of decay constants in geo- and cosmochronology, *Earth Planet. Sci. Lett.*, *36*, 359-362.

Stephenson, A. (1993), 3-Axis static alternating-field demagnetization of rocks and the identification of natural remanent magnetization, gyroremanent magnetization, and anisotropy, *J. Geophys. Res.*, *98*, 373-381.

Stephenson, A., and D. W. Collinson (1974), Lunar magnetic field palaeointensities determined by an anhysteretic remanent magnetization method, *Earth Planet. Sci. Lett.*, *23*, 220-228.

Stoffler, D., and G. Ryder (2001), Stratigraphy and isotope ages of lunar geological units: Chronological standard for the inner solar system, *Space Science Reviews*, *96*, 9-54.

Strangway, D. W., W. A. Gose, G. W. Pearce, and J. G. Carnes (1973), Magnetism and the history of the Moon, in *Magnetism and Magnetic Minerals - 1972*, edited by C. D. Graham Jr. and J. J. Rhyne, pp. 1178-1196, American Institute of Physics, New York.

Sugiura, N., and D. W. Strangway (1980), Comparison of magnetic paleointensity methods using a lunar sample, *Proceedings of the Lunar and Planetary Science Conference, 11th*, 1801-1813.

Sugiura, N., and D. W. Strangway (1983), Magnetic paleointensity determination on lunar sample 62235, *Proceedings of the Thirteenth Lunar and Planetary Science Conference, Part 2, Journal of Geophysical Research*, *88*, A684-A690.

Sugiura, N., D. W. Strangway, and G. W. Pearce (1978), Heating experiments and paleointensity determinations, *Proceedings of the Lunar and Planetary Science Conference, 9th*, *3*, 3151-3163.

Sugiura, N., Y. M. Wu, D. W. Strangway, G. W. Pearce, and L. A. Taylor (1979), A new magnetic paleointensity value for a "young lunar glass", *Proceedings of the Lunar and Planetary Science Conference, 10th*, 2189-2197.

Tauxe, L. (1998), *Paleomagnetic Principles and Practice*, 299 pp., Kluwer Academic Publishers, Dordrecht.

Tauxe, L. T., and H. Staudigel (2004), Strength of the geomagnetic field in the Cretaceous Normal Superchron: New data from submarine basaltic glass of the Troodos Ophiolite, *Geochem. Geophys. Geosyst.*, *5*, doi:10.1029/2003GC000635.

Tauxe, L. T., and T. Yamazaki (2007), Paleointensities, in *Treatise on Geophysics, Geomagnetism Volume*, edited by M. Kono, pp. 509-563, Elsevier.

Taylor, L. A. (1979), Paleointensity determinations at elevated temperatures: Sample preparation technique, *Proceedings of the Lunar and Planetary Science Conference, 10th*, 2183-2187.

Thellier, E. (1938), Sur l'aimantation des terres cuites et ses applications géophysique, *Ann. Inst. Phys.*, *16*, 157-302.

Thellier, E., and O. Thellier (1959), Sur l'intensité du champ magnétique terrestre dans le passé historique et géologique, *Ann. Geophys.*, *15*, 285-378.

Wasilewski, P. (1974), Possible magnetic effects due to fine particle metal and intergrown phases in lunar samples, *The Moon*, *11*, 301-311.

Wieczorek, M. A., B. L. Jolliff, A. Khan, M. E. Pritchard, B. P. Weiss, J. G. Williams, L. L. Hood, K. Righter, C. R. Neal, C. K. Shearer, I. S. McCallum, S. Tompkins, B. R. Hawke, C. Peterson, J. J. Gillis, and B. Bussey (2006), The constitution and structure of the lunar interior, in *New Views of the Moon*, edited, p. 221, Mineralogical Soc America, Chantilly.

Williams, J. G., D. H. Boggs, C. F. Yoder, J. T. Ratcliff, and J. O. Dickey (2001), Lunar rotational dissipation in solid body and molten core, *J. Geophys. Res.*, *106*, 27933-27968.

Yu, Y. J. (2006), How accurately can NRM/SIRM determine the ancient planetary magnetic field intensity? *Earth Planet. Sci. Lett.*, *250*, 27-37.

Yu, Y. J., L. T. Tauxe, and A. Genevey (2004), Toward an optimal geomagnetic field intensity determination technique, *Geochem. Geophys. Geosyst.*, *5*, doi:10.1029/2003GC000630.

Appendix A: Supplemental Data Tables

Supplemental Table 4.A.1 Paleointensity of Lunar Samples

Sample	Method☾	Pint (μT)	Reliability†	Reference
10017	Shaw	71	fails 2	Hoffman et al.(1979)
	Shaw	14	fails 2,3	Sugiura et al. (1978)
	ARM	70	fails 1	Stephenson et al. (1977)
	ARM	93	fails 1	Hoffman et al. (1979)
	KTT	--	fails 2	Hoffman et al. (1979)
10022	Single pTRM Ratio	1.75	fails 2,4	Helsley (1971)
10049	Shaw	7	fails 2,5	Fuller et al. (1979)
10050	ARM	38	fails 1	Stephenson and Collinson (1974)
10057	ARM	14	fails 1,2	Stephenson and Collinson (1974)
10069	Single pTRM Ratio	21.5	fails 2,4	Helsey (1970)
	Single pTRM Ratio	5	fails 2,4	Helsey (1970)
	KTT	--	fails 2,3	Chowdary et al. (1987)
	ARM	--	fails 1,2,3	Chowdary et al. (1987)
10072	ARM	50	fails 1,5	Chowdary et al. (1987)
	ARM	60	fails 1,5	Chowdary et al. (1987)
12002	KTT	4.5	fails 2	Hesley (1971)
12018	KTT	--	fails 2,3	Chowdary et al. (1987)
12022	Unknown	4.8	fails 3,4,5	Helsley (1971)
	KTT	--	fails 2,3	Chowdary et al. (1987)
15058	ARM	4.9	fails 1	Banerjee and Mellema (1974)
15495	ARM	2.2	fails 1	Banerjee and Mellema (1974)
15498	KTT	2.2	Considered Reliable	Gose et al. (1973)
	Van Zijl	27	fails 2,3	Hale et al. (1978)
15535	ARM	7.6	fails 1	Banerjee and Mellema (1974)
15597	KTT	--	fails 2,3	Chowdary et al. (1987)
60015	ARM	33	fails 1	Stephenson and Collinson (1974)
60018	KTT	--	fails 2,3	Sugiura et al. (1978)
	KTT	--	fails 2,3	Sugirua and Strangway (1983b)
60255	KTT	0.5	Considered Reliable	Sugirua and Strangway (1980)
	ARM	2.8	fails 1,2	Sugirua and Strangway (1980)
	Shaw	3.2	fails 2	Sugirua and Strangway (1980)
	sIRM	6.0	fails 1	Sugirua and Strangway (1980)
60315	Single pTRM Ratio	40	fails 2,4	Brecher et al. (1973)
	Single pTRM Ratio	180	fails 2,4	Brecher et al. (1973)
	KTT	> 100	fails 2,3	Sugirua and Strangway (1983b)
62235	KTT	132	Considered Reliable	Sugirua and Strangway (1983)
	KTT	120	Considered Reliable	Collinson et al. (1973)
	KTT	--	fails 2,3	Pearce et al. (1976)

continued

Supplemental Table 4.A.1 (continued)

Sample	Method[☾]	Pint (μT)	Reliability[†]	Reference
	ARM	140	fails 1	Stephenson and Collinson (1974)
62295	Single pTRM Ratio	8.2	fails 2,4	Brecher et al. (1973)
	Single pTRM Ratio	50	fails 2,4	Brecher et al. (1973)
68415	KTT	5	fails 3	Stephenson and Collinson (1974)
68416	ARM	120	fails 1	Pearce et al. (1976)
70017	Single pTRM Ratio	14	fails 2,4	Brecher et al. (1974)
	Single pTRM Ratio	51	fails 2,4	Brecher et al. (1974)
	KTT	30-70	fails 2,3	Stephenson et al. (1974)
	ARM	30	fails 1,5	Stephenson et al. (1974)
70019	KTT	2.5	Considered Reliable	Sugiura et al. (1979)
	KTT	1.2	Considered Reliable	Sugiura et al. (1979)
70215	KTT	2	fails 2	Stephenson et al. (1974)
	KTT	7.5	fails 2	Stephenson et al. (1974)
	ARM	6	fails 1	Stephenson et al. (1974)
71055	Single pTRM Ratio	43	fails 4	Brecher et al. (1974)
	Single pTRM Ratio	127	fails 4	Brecher et al. (1974)
72215	Shaw	55	fails 3	Banerjee and Mellema (1976)
	Shaw	41	fails 3	Banerjee and Mellema (1976)
	Shaw	28	fails 3	Banerjee and Mellema (1976)
	ARM	62	fails 1,5	Banerjee and Swits (1975)
72255	ARM	35	fails 1,5	Banerjee and Swits (1975)
72275	ARM	19	fails 1	Banerjee and Swits (1975)
	Single pTRM Ratio	16	fails 4,5	Brecher et al. (1974)
73235	Single pTRM Ratio	1.1	fails 4,5	Watson et al. (1974)
74275	Single pTRM Ratio	3.3	fails 4	Brecher et al. (1974)
	Single pTRM Ratio	13.3	fails 4	Brecher et al. (1974)
75035	KTT	14	fails 2	Sugiura et al. (1978)
	ARM	56	fails 1	Stephenson et al. (1974)
77017	Single pTRM Ratio	81	fails 4	Brecher et al. (1974)
	Single pTRM Ratio	57	fails 4	Brecher et al. (1974)
77135	Single pTRM Ratio	16	fails 4	Brecher et al. (1974)
	Single pTRM Ratio	1.5	fails 4	Brecher et al. (1974)
	Microwave KTT	7	fails 2, 3	Hale et al. (1978)

[☾]Method = Paleointensity measurement technique used
[†]Reliability = The acceptability criteria that the sample did not pass (for details see text)

Supplemental Table 4.A.2 Thellier-Thellier Experimental Data of Specimen 72215.262

Temp (°C)[€]	**CSD (°)**[†]	**Int (Am^2)**	**Dec (°)**	**Inc (°)**
0.0	0.4	3.65E-08	92.3	26.1
150.1	0.4	3.69E-08	93.7	25.8
150.0	0.4	3.70E-08	95.6	26.1
200.1	0.4	3.68E-08	94.6	25.2
200.0	0.4	3.68E-08	91.9	25.8
250.0	0.4	3.65E-08	91	26.3
200.2	0.4	3.61E-08	90	25.5
250.1	0.4	3.60E-08	89.7	25.8
300.1	0.4	3.56E-08	90.5	25.1
300.0	0.4	3.55E-08	90.5	25.8
350.0	0.4	3.46E-08	93.4	25.6
250.2	0.4	3.45E-08	91.3	24.8
350.1	0.4	3.40E-08	92.2	24
400.1	0.4	3.15E-08	93.5	22.9
400.0	0.4	3.05E-08	87.8	24.6
450.0	0.4	2.75E-08	87.1	24.8
350.2	0.4	2.62E-08	93.1	22.7
450.1	0.4	2.54E-08	92.1	20.9
500.1	0.4	1.63E-08	93.5	14
500.0	0.4	1.34E-08	90	16.7
520.0	0.4	8.33E-09	98.7	1.6
450.2	0.5	8.63E-09	103.3	-22.4
520.1	0.5	7.61E-09	108.1	-41
540.1	0.5	7.45E-09	104.1	-50
540.0	0.5	4.46E-09	102.1	-19.8
550.0	0.4	4.28E-09	107.3	-3.8
520.2	0.4	6.84E-09	99.7	-56.5
550.1	0.4	7.84E-09	95.6	-63.1
560.1	0.4	9.00E-09	118.9	-71.4
560.0	0.5	3.91E-09	100.1	-30.3
570.0	0.5	2.85E-09	114.1	-21.1
550.2	0.4	9.27E-09	119.3	-74
570.1	0.4	1.40E-08	109.6	-81.4
580.1	0.4	1.79E-08	110.4	-82.6
580.0	0.5	1.57E-09	96	-21.4
590.0	0.8	1.22E-09	128.7	-12.7
570.2	0.4	1.60E-08	113.8	-84.5
590.1	0.4	2.45E-08	123.4	-86
600.1	0.4	2.54E-08	101.7	-86.9
600.0	0.9	1.69E-09	132.4	-32.5
610.0	0.7	9.85E-10	136.4	3.7
590.2	0.4	2.82E-08	102.5	-87.2
610.1	0.4	3.00E-08	101.8	-87.5
620.1	0.4	3.16E-08	88.5	-87
610.2	0.3	3.51E-08	92.5	-88.1
640.1	0.4	3.67E-08	143.4	-87.9

[€]Temperature in degrees Celsius where .0 is the zero-field step, .1 is the in-field step and .2 is in-field pTRM check
[†]Circular standard deviation

Supplemental Table 4.A.3 Thellier-Thellier Experimental Data of Specimen 62235.120

Temp (°C)[ℭ]	CSD (°)[†]	Int (Am^2)	Dec (°)	Inc (°)
0.0	0.3	4.00E-08	107.8	44.9
150.1	0.3	3.44E-08	104.8	46
150.0	0.3	3.52E-08	107.8	46
200.1	0.3	3.11E-08	108.2	46.4
200.0	0.3	3.14E-08	106.1	46.9
250.0	0.3	2.98E-08	112.5	48.1
200.2	0.3	2.81E-08	105.4	44.5
250.1	0.3	2.73E-08	104.4	44.9
300.1	0.3	2.40E-08	106.1	43.5
300.0	0.3	2.52E-08	105.7	45
350.0	0.3	2.25E-08	107.8	47.5
250.2	0.3	2.06E-08	105.5	44.6
350.1	0.3	1.82E-08	106.3	48.2
400.1	0.3	1.51E-08	105.7	41.7
400.0	0.3	1.51E-08	109.9	43.7
450.0	0.3	1.10E-08	102.7	44.8
350.2	0.3	1.07E-08	110.5	34.1
450.1	0.4	8.74E-09	105.4	23.1
500.1	0.8	2.50E-09	137.9	-0.5
500.0	0.5	5.81E-09	117.5	48.5
520.0	0.5	5.42E-09	101.6	58.5
450.2	0.7	5.44E-09	134.9	-78.6
520.1	0.5	8.25E-09	103.9	-68.2
540.1	0.4	1.14E-08	122.9	-81.8
540.0	0.9	2.94E-09	100.3	-3
550.0	0.8	4.28E-09	61.3	-3.9
520.2	0.4	8.43E-09	77	-67.9
550.1	0.3	1.29E-08	69.9	-73.1
560.1	0.3	2.00E-08	69.8	-82.4
560.0	0.9	3.32E-09	138.8	-81.2
570.0	1.2	1.06E-09	9.6	-25.1
550.2	0.4	1.75E-08	82.7	-81.9
570.1	0.3	3.23E-08	346.1	-88.8

[ℭ]Temperature in degrees Celsius where .0 is the zero-field step, .1 is the in-field step and .2 is in-field pTRM check

[†]Circular standard deviation

Supplemental Table 4.A.4 Thellier-Thellier Experimental Data of Specimen 60015.67

Temp (°C)[ℂ]	CSD (°)[†]	Int (Am^2)	Dec (°)	Inc (°)
0.0	**0.8**	**1.54E-10**	**351.5**	**30.9**
150.1	3.7	3.22E-11	326.4	1.5
150.0	1.3	1.02E-10	49.3	31.2
150.0	1.4	9.46E-11	51.7	28.6
200.1	2	8.41E-11	61.9	-14.1
200.0	1.5	1.25E-10	38.1	57.3
250.0	1.5	1.01E-10	58.7	30.1
200.2	2	9.08E-11	65.5	4.5
250.1	10.4	4.85E-11	62.4	-10
300.1	2.8	9.94E-11	79.8	-40.6
300.0	1.7	8.14E-11	108.8	-6.2
350.0	2.9	4.38E-11	355.1	-51.7
250.2	3.1	5.32E-11	272	-60
350.1	2	8.67E-11	305.6	-83.5
400.1	1	1.54E-10	103.8	-64
400.0	2.7	7.75E-11	128.1	-16.6
450.0	11.2	3.34E-11	13.9	65.2
350.2	1.7	1.28E-10	242.2	-42.7
450.1	1.5	1.15E-10	279.3	-23
500.1	1.3	1.08E-10	11.6	14.2
500.0	1.4	1.18E-10	45.9	58.8
520.0	2.1	1.09E-10	42.1	48.6
450.2	2	9.58E-11	121.7	-26.5
520.1	0.5	2.61E-10	341.2	-70
540.1	1.2	2.02E-10	111.9	-86.3
540.0	2.5	7.56E-11	119.1	-70.7
550.0	2.4	5.71E-11	326.9	-23.1
520.2	1	1.57E-10	108.4	-81.8
550.1	0.7	2.10E-10	149.7	-77
560.1	0.5	2.61E-10	240.3	-71.6
560.0	1.4	6.17E-11	274	33.8
570.0	1.6	1.11E-10	314	26.4
550.2	0.9	1.75E-10	347.3	-83.4
570.1	0.4	3.57E-10	140.5	-78.7
580.1	0.3	4.78E-10	255	-87.7
580.0	3	6.22E-11	296.9	-35.9

[ℂ]Temperature in degrees Celsius where .0 is the zero-field step, .1 is the in-field step and .2 is in-field pTRM check
[†]Circular standard deviation

Supplemental Table 4.A.5 Thellier-Thellier Experimental Data of Specimen 76535.17

Temp (°C)[¢]	CSD (°)[†]	Int (Am^2)	Dec (°)	Inc (°)
0.0	0.3	2.57E-08	334.6	45.9
150.1	0.3	2.48E-08	338.3	45.5
150.0	0.3	2.47E-08	335.1	45.5
200.1	0.3	2.37E-08	337.9	45.3
200.0	0.3	2.35E-08	334	45.3
250.0	0.3	2.24E-08	335.5	44.9
200.2	0.3	2.23E-08	333	44.6
250.1	0.3	2.19E-08	332	44.1
300.1	0.3	2.02E-08	93.6	64.1
300.0	0.3	1.99E-08	90	64.2
350.0	0.3	1.86E-08	89	64.7
250.2	0.3	1.85E-08	90.9	64.7
350.1	0.3	1.82E-08	90.1	64.8
400.1	0.3	1.67E-08	88.6	64.7
400.0	0.3	1.63E-08	86.6	65.1
450.0	0.2	1.47E-08	83.5	66.1
350.2	0.3	1.46E-08	85.6	66
450.1	0.3	1.42E-08	85.7	65.5
500.1	0.4	1.11E-08	81	65.2
500.0	0.3	9.54E-09	77.2	64.8
520.0	0.3	7.56E-09	67.9	65.1
450.2	0.3	7.48E-09	66.1	64.3
520.1	0.3	6.80E-09	68.6	66
540.1	0.7	6.50E-09	67.7	66.2
540.0	0.4	6.44E-09	73.1	65.6
550.0	0.3	6.42E-09	62.1	65.4
520.2	0.6	6.41E-09	69.4	65.8
550.1	0.8	6.35E-09	61.1	64
560.1	0.7	6.06E-09	63.9	67.6
560.0	0.3	5.99E-09	66.5	68
570.0	0.4	5.89E-09	63.6	66.7
550.2	0.7	5.61E-09	62.1	67.2
570.1	0.6	5.44E-09	65.4	66.4
580.1	0.6	4.73E-09	63.6	63
580.0	0.3	5.19E-09	60.9	66.6
590.0	0.3	5.34E-09	61.2	67.5
570.2	0.4	5.06E-09	63	66.6
590.1	0.7	4.50E-09	65.3	62.7
600.1	0.9	4.21E-09	64.7	63.4
600.0	0.3	5.18E-09	63	68.8
610.0	0.5	5.42E-09	72.7	67.5
590.2	1.2	4.03E-09	75.8	59.2
610.1	0.9	4.01E-09	65.4	57
620.1	0.9	4.01E-09	68.8	55.6
610.2	0.9	3.88E-09	62.3	56.3
640.1	1.1	3.72E-09	61.4	53.9
660.1	0.9	3.96E-09	66.9	51.2
660.0	0.6	5.46E-09	67.6	65.6
680.0	0.3	5.32E-09	83.9	68.7
640.2	1.3	3.64E-09	66.3	52.5

continued

Supplemental Table 4.A.5 (continued)

Temp (°C)[ℂ]	CSD (°)[†]	Int (Am^2)	Dec (°)	Inc (°)
680.1	0.7	3.53E-09	68.1	54.1
700.1	1.6	3.50E-09	68.4	55
700.0	0.4	5.07E-09	72.7	69.4
720.0	0.5	5.18E-09	73.4	71.4
680.2	1	2.65E-09	73.4	36.9
720.1	1	2.74E-09	76.6	44
740.1	0.7	3.11E-09	72	53.2
740.0	0.3	5.00E-09	96.1	68.1
750.0	0.3	4.98E-09	90.4	67.5
720.2	0.8	2.49E-09	76	34.3
750.1	1	3.14E-09	95.2	55
760.1	0.4	3.60E-09	89.6	65.9
760.0	0.4	4.79E-09	96.4	70.5
770.0	0.3	4.69E-09	92	69.1

[ℂ]Temperature in degrees Celsius where .0 is the zero-field step, .1 is the in-field step and .2 is in-field pTRM check
[†]Circular standard deviation

Supplemental Table 4.A.6 AF Demagnetization of the NRM of Specimen 72215.259

AF (mT)[ℂ]	CSD (°)[†]	Int (Am^2)	Dec (°)	Inc (°)
0	0.4	1.46E-08	4.2	-63.2
3	0.5	5.27E-09	97.2	-57.7
3	0.5	4.90E-09	99.5	-57.1
3	0.6	4.76E-09	96.2	-53.5
6	0.8	2.30E-09	100.6	-43.3
6	0.7	2.15E-09	93.2	-53.9
6	0.7	2.53E-09	101.8	-49.1
9	0.8	1.71E-09	107	-69.9
9	1	1.74E-09	95.8	-64.1
9	0.9	1.67E-09	117.3	-64.1
12	1.2	7.83E-10	213.5	-57.5
12	0.9	9.94E-10	187	-61.6
12	0.7	1.17E-09	194	-63.7
15	1.9	5.07E-10	180.6	-20.7
15	1.1	9.06E-10	123.1	-39.7
15	1.4	9.23E-10	152.3	-43.6
18	1.2	7.28E-10	111.8	-38.2
18	1.7	7.71E-10	100.5	-21.4
18	0.9	8.77E-10	148.5	-64
21	0.8	1.02E-09	103.4	-60.1
21	0.9	1.79E-09	105.3	-1.8
21	1	1.31E-09	93.6	-21.8

[ℂ]Strength of alternating field
[†]Circular standard deviation

Supplemental Table 4.A.7 AF Demagnetization of Specimen 72215.259 Post Saturation

AF (mT) ᶜ	CSD (°)†	Int (Am^2)	Dec (°)	Inc (°)
0	0.4	6.32E-07	359	0.5
3	0.3	5.34E-07	1	0.3
6	0.4	4.68E-07	1.3	0
9	0.4	4.21E-07	0.7	-0.3
12	0.4	3.85E-07	1.1	0.1
15	0.3	3.52E-07	1.2	-0.3
18	0.3	3.33E-07	1.1	-0.8
21	0.4	3.11E-07	2.1	0.1

ᶜStrength of alternating field
†Circular standard deviation

Supplemental Table 4.A.8 AF Demagnetization of the NRM of Specimen 62235.118

AF (mT) ᶜ	CSD (°)†	Int (Am^2)	Dec (°)	Inc (°)
0	0.8	2.60E-08	310.1	31.4
3	0.7	2.71E-08	348.2	28
3	0.8	2.69E-08	347.1	27.8
3	0.8	2.71E-08	346.1	27.5
6	0.8	2.02E-08	350	31.9
6	0.7	2.05E-08	354.4	32.1
6	0.8	2.04E-08	351.8	31.6
9	0.8	1.78E-08	353	29.5
9	0.8	1.77E-08	355.5	30.5
9	0.8	1.74E-08	355.6	29.7
12	0.8	1.56E-08	351.6	29.4
12	0.8	1.53E-08	354.2	32.1
12	0.8	1.51E-08	350	27.8
15	0.8	1.39E-08	357.9	27.9
15	0.8	1.35E-08	352	29.8
15	0.8	1.29E-08	354.4	28.4
18	0.9	1.08E-08	352.8	29.4
18	0.9	1.09E-08	350.9	28.7
18	0.9	1.07E-08	351.9	26.3
21	0.9	9.49E-09	352.5	28.3
21	0.9	9.48E-09	348.6	27.1
21	0.9	9.47E-09	350.9	26.8
24	0.9	8.50E-09	344	25.8
24	0.9	8.73E-09	342.2	28.1
24	0.9	8.82E-09	344.6	22.8
27	0.9	8.33E-09	343.4	25.4
27	0.9	8.80E-09	344.9	25.7
27	0.9	8.74E-09	338.6	29
30	0.9	8.10E-09	348.5	30.8
30	1	7.70E-09	342.9	29.1
30	0.9	7.92E-09	344.9	28.5
33	0.9	8.15E-09	343	35.4
33	0.9	7.44E-09	341.1	36

continued

Supplemental Table 4.A.8 (continued)

AF (mT) ᶜ	CSD (°)†	Int (Am^2)	Dec (°)	Inc (°)
33	0.9	7.37E-09	346.7	32.9
36	0.9	7.47E-09	350.3	35.1
36	0.9	6.92E-09	348.8	33
36	0.9	6.64E-09	345.7	30.6
39	0.9	6.52E-09	350	36
39	0.9	6.63E-09	348.8	32.9
39	0.9	6.63E-09	352.2	31.2
42	1.1	4.16E-09	353	26.1
42	1.1	4.96E-09	341.1	29.1
42	0.9	5.32E-09	346.7	43.7
45	1	5.86E-09	344.6	38.2
45	1.1	5.30E-09	340.4	33
45	1	5.03E-09	346.2	39.8
48	0.9	5.75E-09	328.6	43.2
48	1	5.68E-09	328.3	37.5
48	0.9	5.84E-09	332.4	36.6
51	1	5.66E-09	348.9	33
51	1	4.89E-09	340	43.6
51	1.1	4.68E-09	343.9	37.9
54	1.1	4.56E-09	344.7	37.7
54	1.1	4.47E-09	331.4	32
54	1.2	4.30E-09	339.5	35.7
57	1	5.85E-09	329.3	23.1
57	1	6.15E-09	333.4	31.8
57	1	5.38E-09	338.4	35.2
60	1.2	4.49E-09	329	29.9
60	1	5.80E-09	330.4	43.2
60	1	4.77E-09	335.1	44.9
65	1.2	4.27E-09	337.3	30
65	1.2	3.53E-09	328.5	42.3
65	1.3	3.89E-09	341.2	25.6
70	1.2	3.71E-09	348.7	17.1
70	1.2	4.43E-09	339.6	18.9
70	1.2	3.93E-09	326.6	31.6
75	1.1	3.57E-09	345.9	3
75	1.5	2.62E-09	354.9	15
75	1.3	3.93E-09	347.1	-2.1
80	1.2	3.82E-09	0.2	19.6
80	1.3	3.10E-09	334.9	32.2
80	1.6	2.31E-09	308.8	30.1
90	1.5	2.71E-09	315.8	-18.8
90	1.7	2.07E-09	285.4	2
90	1.1	2.95E-09	335.4	28.6
100	1.8	2.21E-09	306.7	22.2
100	1.4	2.59E-09	267.6	35.9
100	1.3	3.29E-09	327.4	13.9
110	1.2	3.34E-09	318.1	35.8
110	1.6	2.57E-09	301.8	17.6
110	1.8	2.16E-09	313.1	47.2
110	1.5	2.62E-09	296.2	12.7

continued

Supplemental Table 4.A.8 (continued)

AF (mT) ☾	**CSD (°)**†	**Int (Am^2)**	**Dec (°)**	**Inc (°)**
62235.118	110	2.1	1.74E-09	309.3
62235.118	110	3.6	9.36E-10	238
62235.118	120	1.7	2.34E-09	336.5
62235.118	120	2.3	1.41E-09	283.6
62235.118	120	2	1.83E-09	254.4
62235.118	120	1.4	3.45E-09	304.5
62235.118	120	1.4	2.99E-09	266.4
62235.118	120	2.1	1.69E-09	283.1

☾Strength of alternating field
†Circular standard deviation

Supplemental Table 4.A.9 AF Demagnetization of Specimen 62235.118 Post Saturation

AF (mT) ☾	**CSD (°)**†	**Int (Am^2)**	**Dec (°)**	**Inc (°)**
0	0.2	1.42E-06	359.4	1.9
3	0.2	1.13E-06	0.8	0.5
3	0.2	1.12E-06	1.8	0.4
3	0.2	1.12E-06	0.7	-0.4
6	0.2	9.31E-07	1.3	1.6
6	0.1	9.27E-07	0.3	0.8
6	0.1	9.24E-07	1.5	0.7
9	0.2	7.99E-07	2.7	0.2
9	0.2	7.92E-07	1.3	0.9
9	0.1	7.89E-07	1.6	0.9
12	0.2	6.96E-07	1.4	1.5
12	0.2	6.93E-07	1.6	1.7
12	0.2	6.88E-07	3.8	0.2
15	0.2	6.12E-07	1.5	-0.6
15	0.2	6.08E-07	1.8	-0.4
15	0.2	6.06E-07	1.6	-0.9
18	0.2	5.46E-07	3.2	-0.2
18	0.2	5.41E-07	3.9	-0.6
18	0.2	5.38E-07	1.6	0.2
21	0.1	4.90E-07	1.4	-0.1
21	0.2	4.88E-07	2.5	-0.5
21	0.2	4.85E-07	1.7	-0.6
24	0.2	4.42E-07	1.8	-0.1
24	0.1	4.39E-07	2.7	-0.1
24	0.2	4.37E-07	3	-1
27	0.2	4.00E-07	1.5	-0.1
27	0.2	3.96E-07	1.3	-0.9
27	0.2	3.95E-07	1.8	-0.7
30	0.2	3.65E-07	2.4	-0.3
30	0.3	3.59E-07	2.9	0
30	0.2	3.57E-07	2.1	0.4
33	0.2	3.33E-07	2.2	-0.6
33	0.2	3.30E-07	2	-0.6
33	0.2	3.29E-07	2.1	-1.3
36	0.3	3.03E-07	3.1	0.2

continued

Supplemental Table 4.A.9 (continued)

AF (mT) [ℭ]	**CSD (°)** [†]	**Int (Am^2)**	**Dec (°)**	**Inc (°)**
36	0.2	3.01E-07	3.8	-0.4
36	0.2	2.97E-07	2	-0.4
39	0.2	2.78E-07	2.3	-0.9
39	0.2	2.74E-07	2.2	-0.3
39	0.2	2.73E-07	2.7	-0.3
42	0.2	2.55E-07	1.9	1.7
42	0.2	2.54E-07	2.3	0.7
42	0.2	2.50E-07	2.9	-0.2
45	0.2	2.36E-07	3.5	-2.4
45	0.3	2.34E-07	2.1	-0.6
45	0.2	2.33E-07	4.1	-0.2
48	0.2	2.18E-07	2	-0.7
48	0.1	2.17E-07	2.8	-0.8
48	0.3	2.13E-07	2.3	-0.7
51	0.3	2.01E-07	3.6	-0.2
51	0.2	1.99E-07	2.4	-0.4
51	0.3	1.99E-07	2.9	-0.2
54	0.3	1.85E-07	4.7	-1.2
57	0.3	1.71E-07	2.9	-0.4
57	0.4	1.70E-07	3.7	-1.2
57	0.4	1.70E-07	4.9	-0.4
60	0.3	1.60E-07	4	-1.3
60	0.3	1.58E-07	3.7	-1.4
60	0.3	1.56E-07	3.4	-1.3
65	0.3	1.45E-07	2.7	-1.4
65	0.4	1.41E-07	3.8	-1.5
65	0.4	1.41E-07	3.4	-1.9
70	0.4	1.29E-07	3.4	-1.1
70	0.3	1.27E-07	4.5	-1.6
70	0.4	1.25E-07	5	-1.1
75	0.4	1.17E-07	5	-1.4
75	0.4	1.14E-07	3.3	-1.1
75	0.4	1.13E-07	3.8	-0.7
80	0.5	1.04E-07	5.7	-2.5
80	0.5	1.02E-07	4.8	-1.4
80	0.5	9.97E-08	5.7	-1.4
90	0.4	8.70E-08	5.3	-1.9
90	0.4	8.48E-08	4.1	-1.1
90	0.5	8.39E-08	4.5	-1.6
100	0.5	7.26E-08	6.4	-1.7
100	0.8	7.03E-08	3.1	-1.6
100	0.7	6.84E-08	4.2	-2.3
120	0.7	5.21E-08	5.5	-3.3
120	0.7	4.90E-08	4.7	-3.1
120	0.8	5.06E-08	5.8	-3

[ℭ] Strength of alternating field
[†] Circular standard deviation

Chapter 5

Microwave Paleointensity Experiments on Lunar Specimens

5.1 Introduction

As seen in Chapter 4, the provocative, but as yet unsubstantiated suggestion that the Moon produced an internally generated dynamo is drawn from many inferences from disparate data fraught with complications. The strongest support for an internally generated dynamo is generally drawn from inferred high paleointensities of lunar samples returned during the Apollo missions [*Cisowski, et al.*, 1983; *Fuller and Cisowski*, 1987; *Wieczorek, et al.*, 2006]. Absolute paleointensity measurements, especially Koenigsberger-Thellier-Thellier (KTT) [*Thellier and Thellier*, 1959], are preferable to relative measurements because the method is based on a linear relationship between the ancient magnetic field and a known applied field for single-domain grains [*Dunlop and Ozdemir*, 1997]. The primary difficulties in absolute paleointensity experiments are alteration (particularly for lunar specimens [*Pearce, et al.*, 1976]) and the time required per measurement (~1 month). In this chapter, I investigate the application of the absolute microwave paleointensity technique [*Walton, et al.*, 1996] for use with magnetic lunar specimens.

The T-T microwave experimental method [*Hill, et al.*, 2006; *Shaw, et al.*, 1996], utilizes high frequency microwaves (14 GHz) to excite magnetized grains rather than thermally heating the entire specimen. The heating steps of the thermal experiment are replaced by increasing increments of applied microwave energy.

Hale et al. [1978] attempted a microwave KTT experiment on five lunar specimens. The experimental system employed for these experiments included a modified commercial microwave oven (Sharpe model 6500) capable of producing up to 650 Watts of power at 2.45 GHz. In an attempt to minimize alteration, the magnetic and atmospheric conditions were controlled inside the sample chamber. *Hale et al.* [1978] concluded that microwave paleointensity experiments on lunar specimens are theoretically possible, but that with their experimental setup the heat generated by microwave energy decay within the specimen matrix was an intractable problem. The experiments successfully reproduced accurate intensity estimates for synthetic samples with known magnetic histories, but failed to produce interpretable results with the lunar specimens.

With the failure to generate robust magnetic history interpretations, *Hale et al.* [1978] suggested several improvements. First, a microwave source that could impart greater energy into the sample is needed (the experimental configuration at Liverpool, described in section 5.2, does this successfully). Second, a lunar sample with a stronger NRM should be tried (in section 5.2 I describe measurements attempted on lunar samples with a range of NRM values).

Numerous studies have successfully utilized the microwave technique for ceramics [*Shaw, et al.*, 1996], lavas [*Hill and Shaw*, 1999; *Hill, et al.*, 2006], and Martian meteorites [*Shaw, et al.*, 2001]. *Shaw et al.* [2001] performed adapted, single-heating-step KTT experiments [*Hill and Shaw*, 1999; *Kono and Ueno*, 1977] on two

Martian meteorites, with significant scatter in the results. This scatter was attributed to the weak magnetization of the samples compared to the sensitivity of the SQUID magnetometer. According to *Shaw et al.* [2001], the results displayed a "curved character" rather than ideal linear behavior, typically associated with a single component of magnetization. This curved character was interpreted as two components of magnetization where the low power portion resulted from shock or thermal contamination. The high power portion was interpreted as a putative Martian field of 3-5 μT.

The principle drawback of the adapted KTT method of *Shaw et al.* [2001] is that it cannot monitor for alteration *in situ*. Therefore, in this study, I employ the IZZI double-heating technique (described in Chapters 3 and 4), in the following experiments. Also, in light of the previous difficulties in working with lunar specimens, I test the IZZI microwave method on terrestrial specimens with proven thermally derived paleointensity results.

The IZZI modified microwave Thellier-Thellier technique is appealing for application to lunar specimens for several reasons. First, it does not require large specimens, which is well suited for the limited availability of lunar samples. Second, under ideal conditions, the microwave method does not cause thermal alteration of the bulk specimen. Third, the method is directly comparable to standard thermal absolute paleointensity techniques. Here, I investigate the feasibility of modern microwave intensity measurements for lunar specimens.

5.2 Theory and Experimental Set-up

All microwave paleointensity experiments presented here were performed at the Liverpool University Paleomagnetics Laboratory using the IZZI variant [*Tauxe and Staudigel*, 2004; *Yu, et al.*, 2004] of the KTT paleointensity experiment. This technique is analogous to the thermal IZZI KTT experiments presented in Chapters 3 and 4. The KTT method uses a double heating technique during which the specimen is heated in a stepwise manner, progressively replacing the original natural remanent magnetization (NRM) with a laboratory-controlled partial TRM (pTRM). The ratio of NRM remaining to pTRM gained yields an estimate of ancient field strength. Successful experiments should include procedures to verify that 1) the intensity is a primary remanence, 2) no alteration occurs during the experiment, and 3) the specimen is magnetized in a linear fashion. The particular stepwise pattern of the IZZI variant is uniquely devised to evaluate all three criteria (see Chapters 3 and 4).

The microwave technique is equivalent to the thermal technique, but uses high frequency microwaves (~14.4 GHz) to (de)remagnetize magnetic grains rather than thermal energy (heat) [*Walton, et al.*, 1993; *Walton, et al.*, 1992; *Walton, et al.*, 1996]. Microwave energy directly excites the magnetic spin system of a mineral such that the magnetic carriers may realign with an applied field direction. Because the entire specimen is not heated, the microwave technique reduces the likelihood of thermo-chemical alteration [e.g. *Gratton, et al.*, 2005; *Thomas, et al.*, 2004; e.g. *Walton, et al.*, 1996]. At the atomic level microwave photons generate precession of atomic dipole moments (spin waves, or magnons) in magnetic grains. This precession allows magnetic grains to realign their net dipole moments in the direction of the ambient field [*Böhnel, et al.*, 2003]. The application of microwave photons is equivalent to the use of thermal phonons (lattice vibrations) in traditional heating methods [e.g. *Hill, et al.*, 2002; *Hill and Shaw*, 1999; *Hill, et al.*, 2006; *Shaw, et al.*, 1996]. The microwave technique reduces the chance of thermal alteration by avoiding excitation of thermal phonons, which are the primary source of magneto-mineralogical or magneto-physical alteration [*Böhnel, et al.*, 2003]. While reliant on microwave photons rather than thermal phonons, the spin waves generated in the microwave technique decay and consequently generate phonons in the magnetic grains [*Hale, et al.*, 1978; *Walton*, 2004]. This exchange between microwave photons and thermal phonons can propagate through the matrix, causing bulk specimen heating. The temperature increase associated with the microwave technique is usually less than 200°C [*Hill and Shaw*, 2000; *Walton*, 2004], although not always. Experimentation has shown that the use of short microwave exposures (3–6 s) greatly reduces the probability of thermal alteration [*Hill and Shaw*, 1999; *Walton*, 2002, 2004].

The orientations of magnetic grains only realign appropriately if the specimen absorbs the correct amount of microwave energy. For this reason, the specimen is placed in an adjustable cylindrical resonance cavity that is tuned to the frequency of the nominal microwave source (14.4 GHz). By optimizing the resonance within the cavity, the system transfers more energy to the magnetic grains of a specimen than the source would provide alone. Unfortunately, the resonance characteristics of the cavity change when a specimen is placed within it. Therefore, the microwave source is also tuned from the nominal frequency of 14.4 GHz to optimize the resonance for each sample. The resonance characteristics of the cavity are more easily controlled with smaller specimen sizes. In addition, smaller specimens require less microwave power to (de)remagnetize the intrinsically fewer number of magnetic grains. For this reason, I use drilled cylindrical specimens that are 3mm long by 5mm diameter from terrestrial samples. Due to limited supplies of lunar samples I use uncut but unevenly shaped specimens on the order of 3 to 5 mm in width and 3-8 mm in length.

The microwave paleointensity experiments are performed using an automated SQUID magnetometer system with an integrated tuned microwave cavity [*Shaw, et al.*, 1984; *Shaw, et al.*, 1996]. A schematic and picture of the experimental apparatus are shown in Figure 5.1. The microwave source is a Klystron amplifier operating at 14.4 GHz with a maximum power output of 80 watts. During microwave application, the system is kept in resonance by adjusting the frequency via an automated computer program. The resonant cavity is housed in a mu-metal shield, which reduces the ambient field to less than 0.05 μT within the cavity. Three-axis field coils placed around the resonant cavity are used to produce a constant applied field of up to 75 μT inside the shielded cavity. The experimental configuration allows for the field to be applied in any direction. During this study I apply a 25 μT and 15 μT field along the +z direction for the terrestrial and lunar specimens, respectively.

Following each microwave exposure, the remanent direction and intensity of the specimen are measured in a Tristan Technologies small-bore SQUID magnetometer. The microwave paleointensity experiments presented in this chapter use the IZZI KTT protocol for direct comparison with thermal IZZI KTT experiments presented in Chapter 4. Ideally, each specimen is exposed to increasingly strong power (2 to 80 Watts) for 3-6 seconds until the specimen is 95% demagnetized or the remaining magnetization is too small to measure (the noise floor of the instrument is ~5 x 10^{-10} Am^2). It is difficult to impart a prescribed dose of microwave energy to a specimen because the absorbed energy is not only dependent upon the power and duration, but also the resonance characteristics of the apparatus, which change with each specimen, and can change if alteration occurs. Therefore, I calculate the cumulative absorbed energy *in situ* from the difference between the applied and reflected energies during each microwave step [*Hill and Shaw*, 2007]. If the reflected (or absorbed) energy significantly changes between steps of the experiment, alteration is suspected.

There are limitations to this experimental set-up; in particular, the magnetic material in the lunar specimens is small relative to similarly sized terrestrial specimens, making experimental limits on specimen size more critical. The small amount of magnetic material also makes an experiment difficult to complete. As the sample is demagnetized the NRM remaining approaches the measurement limit of the magnetometer. In some cases it is impossible to measure the specimen after 75% of the original NRM is removed. This limitation may also be a result of moderately high ambient field contamination within the microwave cavity. In addition, the specimens are not regularly shaped which can cause the specimen to move within or fall from the specimen holder. Since glue causes problems, the system is now modified with a vacuum to hold the specimens in a vertical position (personal communication, John Shaw, 2007). However, unless the specimen has a perfectly uniform side it is somewhat precariously hung from the hollow specimen holder. In most experiments the specimen remains stable, but on occasion the specimen rotates or in extreme cases falls from the holder, making the specimen direction impossible to interpret.

5.3 Microwave Test Experiments with Known Specimens

In this section I compare microwave experiments of terrestrial specimens from Antarctica: mc105d2, mc120d1 and mc131b2. These were previously measured using thermal Thellier-Thellier experiments performed at Scripps Paleomagnetics Laboratory. The results from these original experiments are in Chapter 3. These test experiments with the microwave KTT method serve multiple purposes. First, they provide an opportunity to learn and practice the microwave experimental procedures. Second, the microwave method is relatively new, and using previously well characterized specimens, these tests verify the reliability of this method. The three specimens chosen for the test experiments are selected primarily for two reasons; 1) there is abundant material from these sites, such that one specimen from each site could be used to practice the microwave experimental procedures, and 2) these specimens are known to behave well during thermal experiments.

The terrestrial specimens were prepared for measurement with the microwave a)

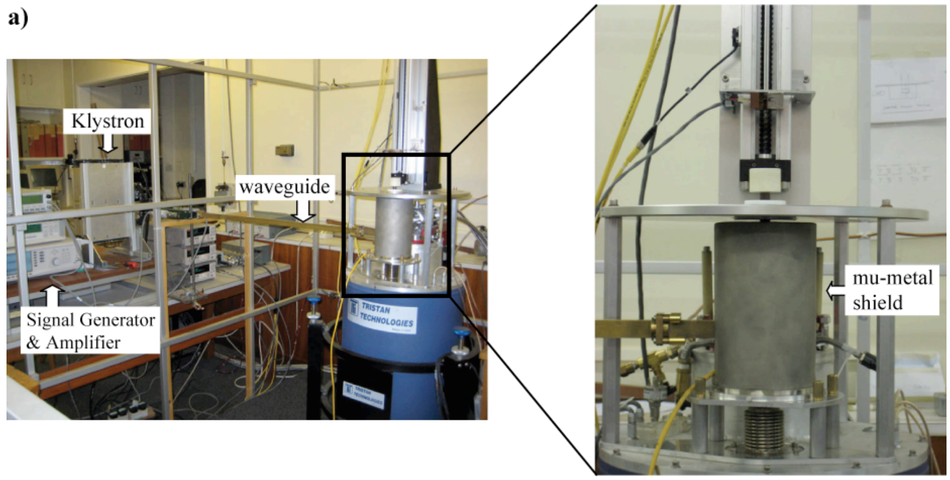

b)

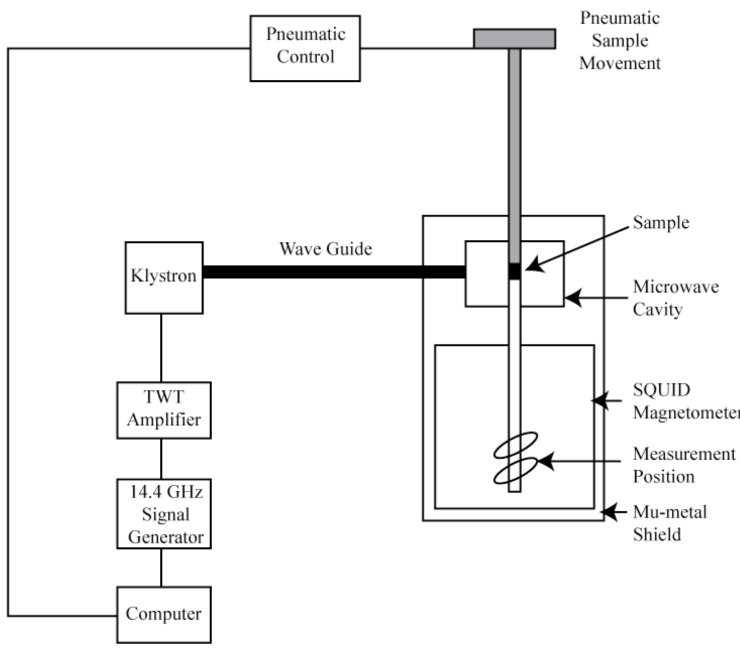

Figure 5.1: a) Image of experimental set-up for the inline microwave demagnetizer and SQUID magnetometer at the Liverpool Paleomagnetics Laboratory. **b)** Schematic diagram [after *Shaw et al.,* 1996] of apparatus shown in a) where the microwave source is a Klystron amplifier with a maximum power output of 80 Watts operating at 14.4 GHz. The 3-axis coil system around the microwave cavity has not been drawn on the diagram for clarity. The microwave power exposure, frequency tuning, field application and measurement of specimen magnetization are performed automatically with the pneumatic control system.

experimental method by drilling cylinders 3 mm in length and 5 mm in diameter from the ~2.54 cm diameter specimens typical for use in thermal KTT experiments. A single specimen typical for a thermal experiment can yield many sub-specimens for a microwave experiment. For each of the terrestrial specimens examined here, I scrutinize two sub-specimens, denoted by appending the specimen name with ".1" or ".2". Unfortunately, a method for accurately orienting the 3x5 mm cylinder specimens during the microwave experiment does not presently exist. Consequently, the direction measurements are limited to sample orientation, not geographic orientation. Note the lack of geographic orientation does not adversely effect the paleointensity interpretation.

Specimen mc105d2 was the first terrestrial specimen measured. Figure 5.2 displays the results of this experiment. In an attempt to proceed cautiously in light of an unknown blocking power spectrum (the microwave equivalent to blocking temperature spectrum), I started with small increments of applied power (5-20 watt-seconds; note here that I use watt-sec instead of Joules to remind the reader that either time or power may be changed to achieve the same energy output) so as to not excessively demagnetize the sub-specimen in any one step. Sub-specimen mc105d2.1 passes pTRM checks but exhibits a slight zig-zag component in the Arai plot. The paleointensity interpretation for this sub-specimen is 28 μT and the directions indicate a single primary remanence. The second experiment, performed on mc105d2.2, is shown in Figure 5.2b, having larger demagnetization steps (25 watt-seconds). This specimen has a paleointensity interpretation of 27.0 μT, passing all pTRM checks.

Sub-specimen mc105d2.2 does not exhibit the same zig-zag behavior as mc105d2.1. The zig-zag behavior seen for mc105d2.1 is most likely due to imprecision of applied power that is comparable to the small applied power steps used for this particular experiment. The relatively high (as compared to the Scripps experimental apparatus) background field in the microwave cavity may also contribute to the inaccurate zero-field steps. Therefore, the zig-zag behavior observed here likely represents limitations on the resolution of the microwave experimental instruments. For this reason, all further experiments presented in this chapter use applied power increments of 9 watt-seconds or greater. For comparison, the thermal KTT experiment yields a site-level average paleointensity of 30.6 ± 1.2, which agrees within two standard deviations of the microwave results.

Two sub-specimens were drilled from specimen mc131b2 as before, to examine the stability and reproducibility of the microwave KTT experimental procedure and apparatus. For both sub-specimens, microwave power steps of 25 watt-seconds were applied. Both sub-specimens of mc131b2 exhibit linear decay to the origin and a linear Arai plot yielding a paleointensity of 17.6 μT for mc131b1.1 and 17.0 μT for mc131b2.2 (Figure 5.3). This agrees well with the thermal KTT experiment (Chapter 3), where the mean site intensity is 16.5 ± 0.8. Sub-specimen mc131b2.1 passed pTRM checks. However, the experiment ended at 80% demagnetization rather than 95% because the test was working remarkably well. The second sub-specimen passed pTRM checks until an applied power of 175 watt-seconds, at which point the direction and the slope of the Arai plot changes. The interpretable portion (power steps < 175 watt-seconds) provides a stable and consistent primary remanence interpretation.

Specimen mc120d1 was prepared in the same manner as both previous specimens. For sub-specimen mc120d1.2, the experiment ended prematurely when it failed a pTRM check, exhibited decreased absorbed power, and required a change in tuning frequency. Upon visually inspection, a melt bubble was clearly evident, so the experiment was stopped. Prior to the power step of 175 watt-seconds, the experiment was well behaved in both direction and intensity, yielding a reliable intensity estimate of 24.3 μT. With the limited laboratory time available, sub-specimen mc120d1.1 was not completely demagnetized (85% of the NRM was removed), but yielded stable single-component primary remanence with an intensity estimate of 23.1 μT (Figure 5.4). These intensity estimates agree well with thermal KTT measurement (Chapter 3) for site mc120 (24.55 ± 0.44 μT).

Based on these six successful test experiments, it is clear that the microwave method is capable of producing consistent and reliable measurements of paleointensity that are comparable to those from the standard thermal KTT experiment, as performed at the Scripps Paleomagnetic Laboratory. However, there are experimental difficulties one should be aware of when performing this experiment. Clearly, some specimens do alter during the microwave experiment; the alteration is evidenced from the failed pTRM checks, inconsistent absorbed power results, and in extreme cases visible alteration. The observed melt bubble on sub-specimen mc120d1.2 indicates that the

Figure 5.2: Arai plot of NRM remaining vs. pTRM gained during an IZZI-modified KTT paleointensity experiment for sub-specimens, **a)** mc105d2.1, NRM is normalized to 2.95 x10^{-4} Am^2/kg, and **b)** mc105d2.2, NRM is normalized to 2.49 x10^{-4} Am^2/kg. Open (closed) circles represent the ZI (IZ) steps of the energy sequence. The red line represents the inferred paleointensity and pTRM checks are shown as green triangles. Inset is a vector-endpoint diagram of direction during thermal demagnetization (the zero-field only steps of the KTT experiment) where the x-direction has been rotated to the NRM declination (labeled for each specimen). Closed (open) circles are the horizontal (vertical) plane. On the right, NRM remaining (blue circles) and pTRM gained (red squares) are plotted as functions of energy applied in Watt-seconds.

a) mc105d2.1

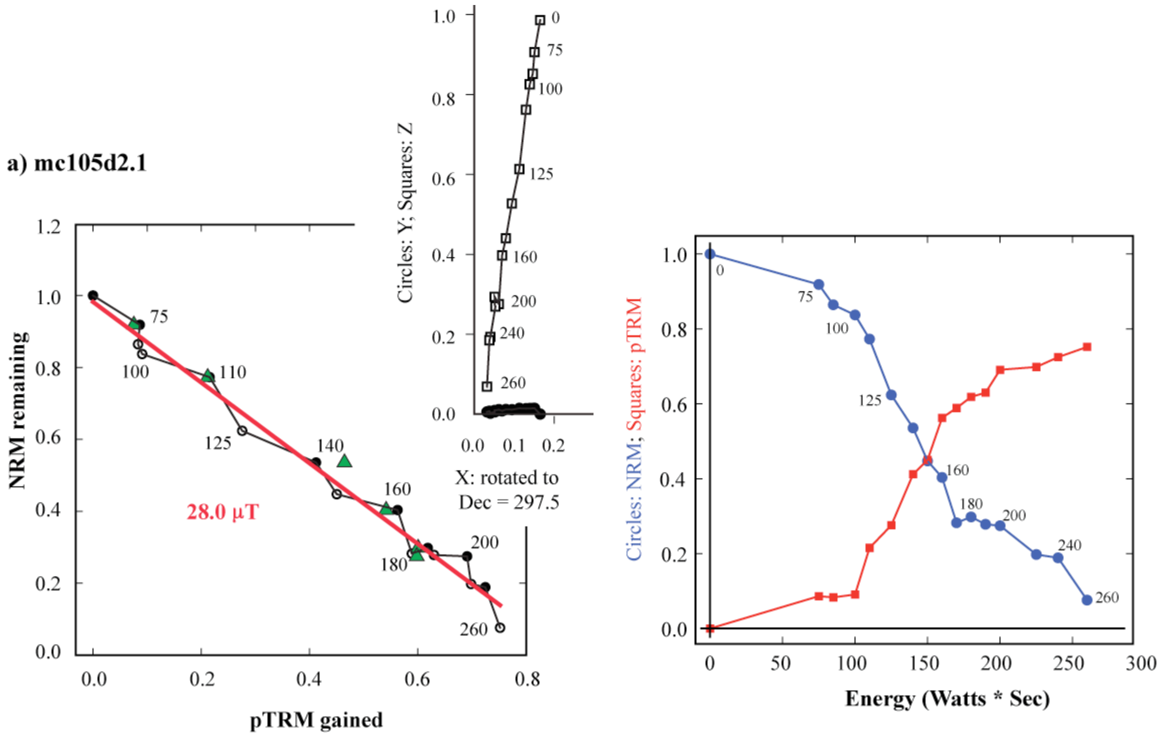

b) mc105d2.2

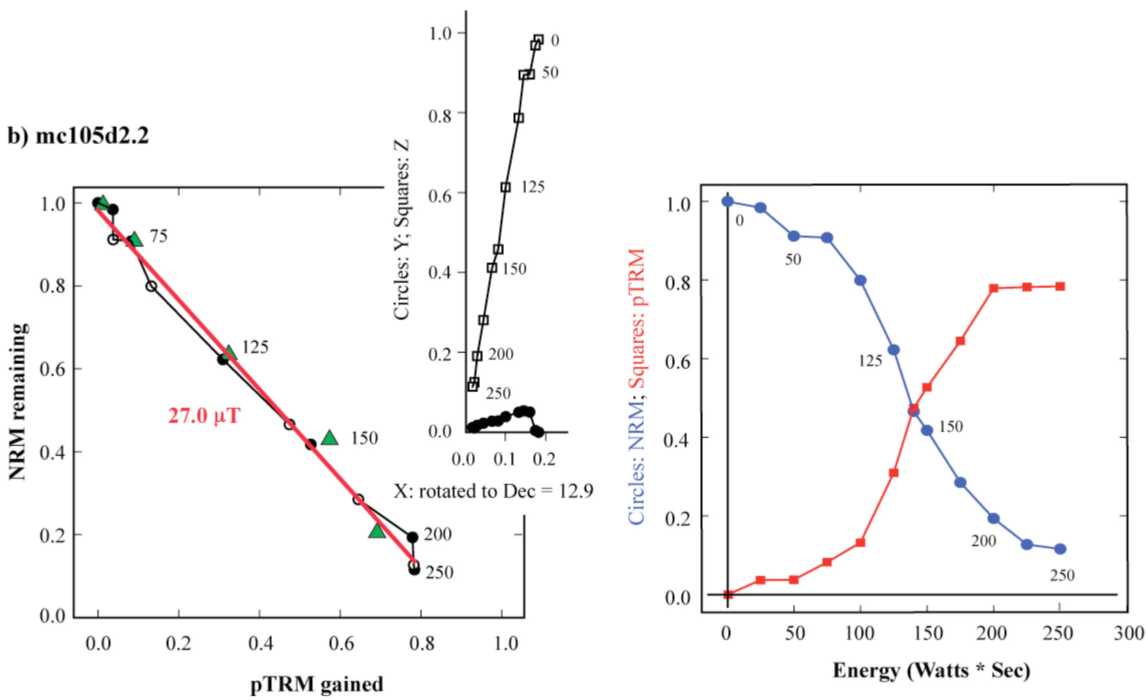

specimen underwent an extreme, localized, temperature increase. In addition, inconsistent power absorption as a result of specimen characteristics generates imprecise demagnetization steps. This may limit the sensitivity, particularly for low intensity

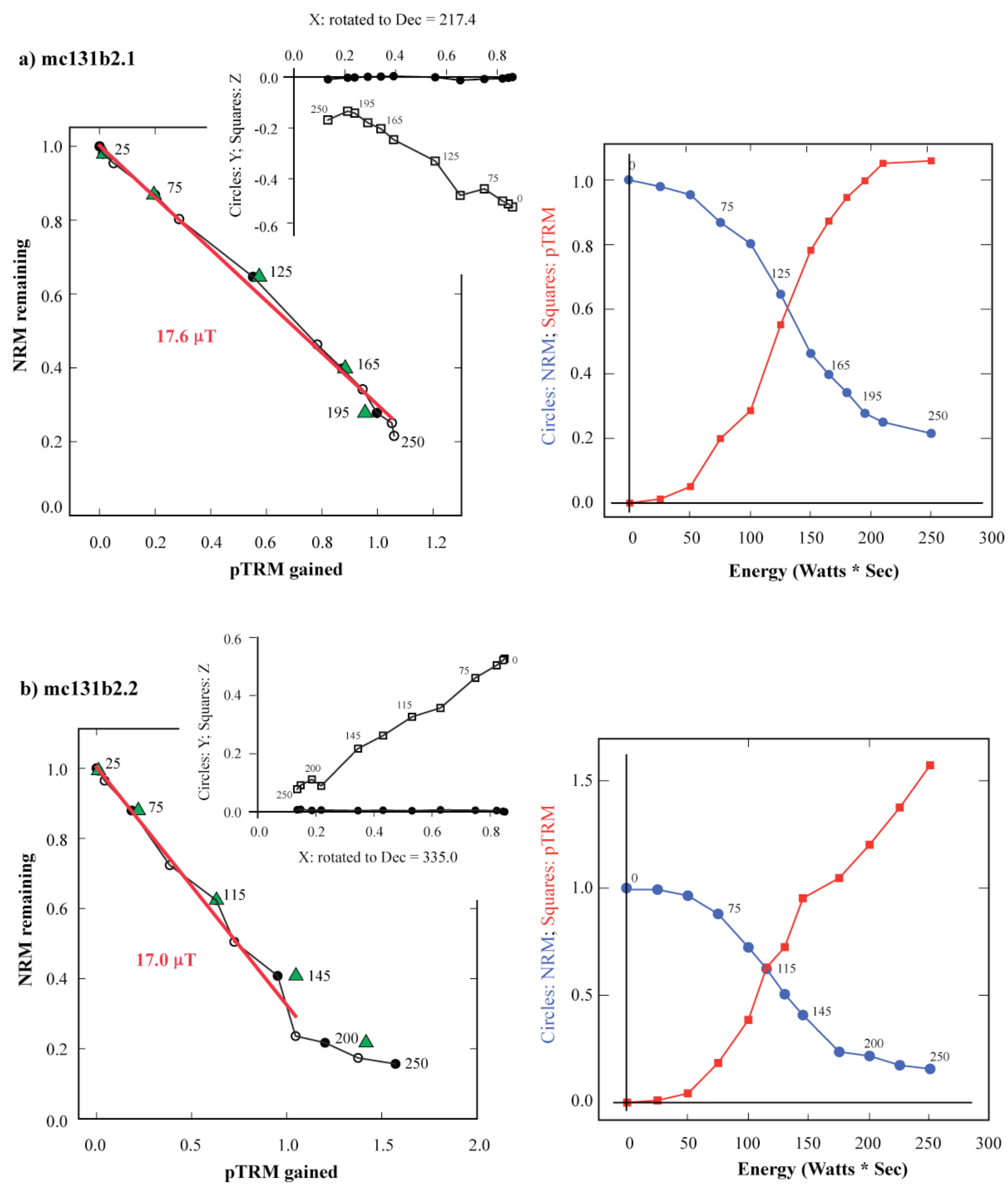

Figure 5.3: Same as Figure 5.2 for sub-specimens, **a)** mc131b2.1, NRM is normalized to 1.98 x10^{-4} Am^2/kg, and **b)** mc1131b2.2, NRM is normalized to 1.41 x10^{-4} Am^2/kg.

Specimens. Also, the very large residual field in the "zero field" demagnetization step leads to a failure to fully demagnetize the NRM and represents a practical limit to the method.

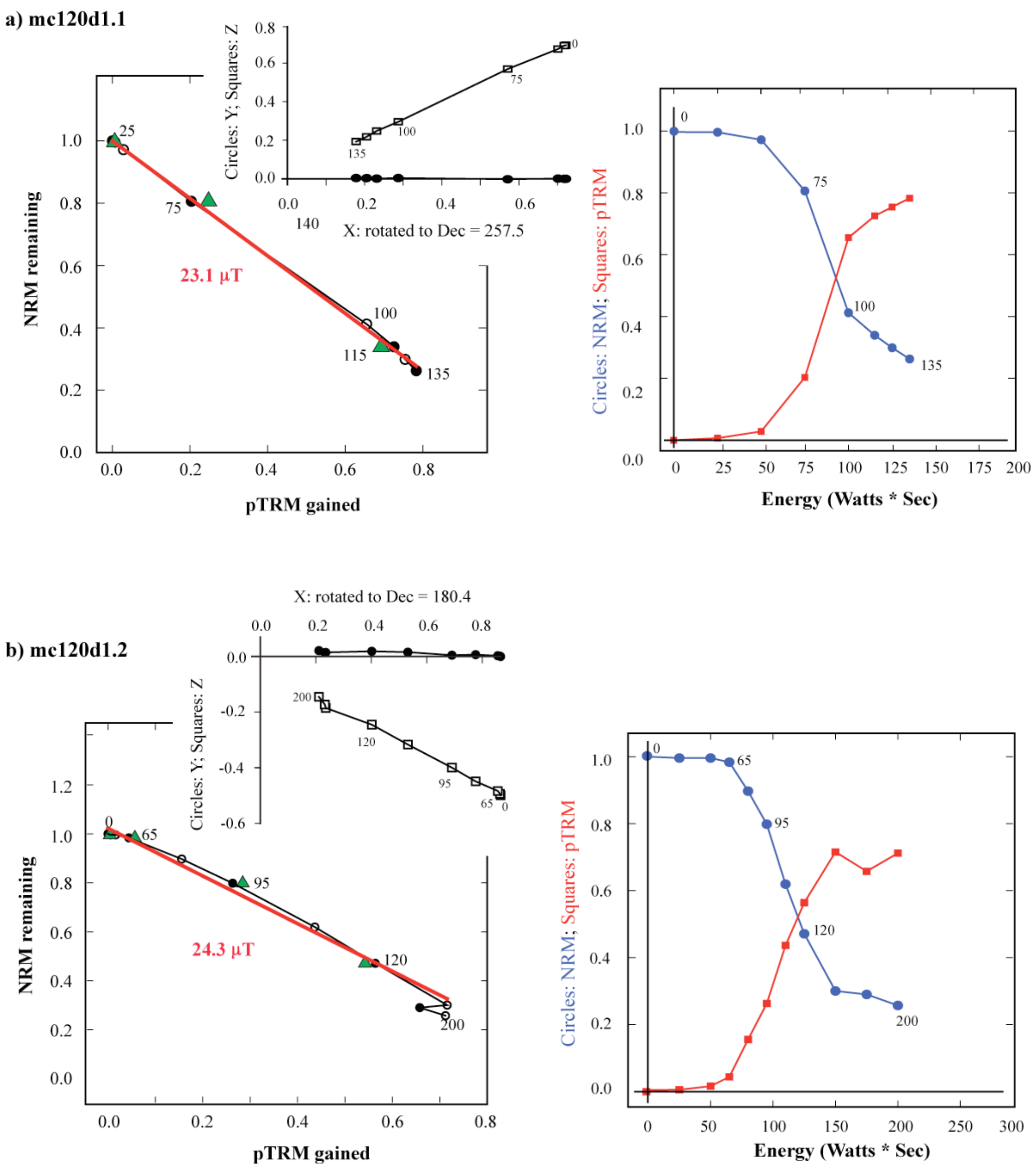

Figure 5.4: Same as Figure 5.2 for sub-specimens, **a)** mc120d1.1, NRM is normalized to 4.95 x10^{-4} Am^2/kg, and **b)** mc120d1.2, NRM is normalized to 4.86x10^{-4} Am^2/kg.

5.4 Results from Lunar Specimens

Here I discuss microwave paleointensity experiments on specimens from three lunar samples (60015, 62235, 73235). The power, time, direction and intensity for each experiment can be found in Supplemental Tables 5.A.1 - 5.A.3. Descriptions of samples 60015 and 62235 are given in Chapter 4; a brief description of sample 73235 is given below. Before proceeding, it should be noted that the lunar microwave experiments differ from their terrestrial counterparts in the following ways. First, unlike the terrestrial samples (section 5.3), the lunar samples are not drilled to provide multiple uniformly shaped cylinders. Two specimens (60015.37 and 73235.19) were not small enough to fit in the microwave apparatus and were cut with a diamond saw prior to measurement. Second, the lunar NRMs are often an order of magnitude smaller than the terrestrial NRMs presented in the previous section. Third, the magnetic carrier in lunar specimens is likely metallic iron (versus magnetite, titanomagnetite, or hematite), and therefore has a different blocking spectrum than the terrestrial specimens.

Specimen 73235.19 is a clast-rich impact melt breccia with an $^{40}Ar/^{39}Ar$ whole-rock plateau age of 3.90 ± 0.08 [*Turner and Cadogan*, 1975]. This is the first reported KTT experiment for this specimen. Unfortunately, the experiment did not produce an interpretable paleointensity as it failed all pTRM checks during the experiment (Figure 5.5). Using an applied field of 15 μT, the specimen did not gain a significant pTRM. This specimen gained very little pTRM relative to the NRM remaining, so the failed pTRM checks may result from limitations in measurement sensitivity for such low magnetizations. This experiment ended before the specimen completely demagnetized due to limited magnetometer sensitivity. Yet, before the experiment ended, the direction of magnetization was stable and may have trended to the origin since the low-energy magnetization component has a maximum angle of deviation (MAD = 4.9°) greater than the angle the component makes with the origin (dANG = 3.6°). See Chapter 3 for detailed descriptions of these quality criteria.

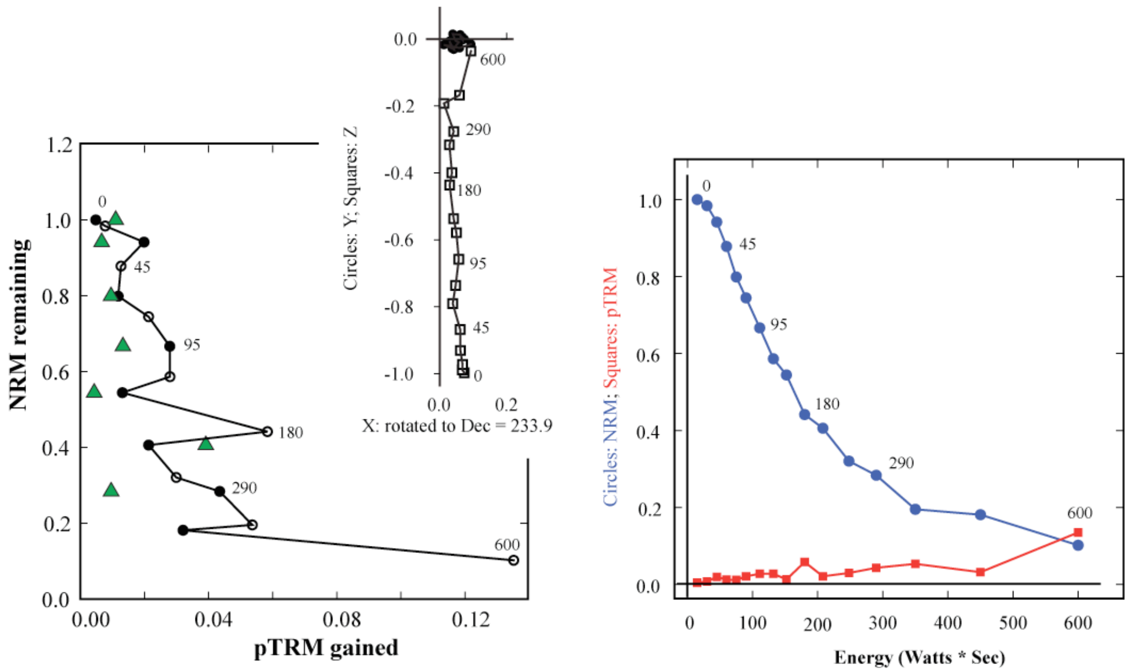

Figure 5.5: Same as Figure 5.2 for lunar specimen 73235.19 where NRM is normalized to 1.06×10^{-5} Am^2/kg.

The microwave experiment for sub-specimen 62235.119 (impact breccia) was completed (less than 2% of the original NRM remains) without experimental problems (the specimen did not rotate or fall from the specimen holder). Similar to the thermal KTT results, specimen 62235.119 recorded high paleointensity (~1 mT) at low-energy steps (6 – 105 Watt-secs), failed pTRM checks at mid-energy steps (105 and 135 Watt-secs), and then had a low paleointensity interpretation correlating with high-energy steps

(120 to 270 Watt-secs). The results are shown in Figure 5.6 with arrows elucidating the failed pTRM checks. Near the end of the experiment alteration was observed as a deviation in energy absorption (144 Watt-secs), failed pTRM checks, and through visual verification. The high-intensity (low-energy) component does not decay to the origin (MAD = 4.2°, dANG = 11.9°), indicating a non-primary remanence. Similar to the microwave KTT experiment on specimen 73235.19, specimen 62235.119 did not gain a measurable pTRM prior to failed pTRM checks. After inferred alteration the specimen rapidly gained pTRM.

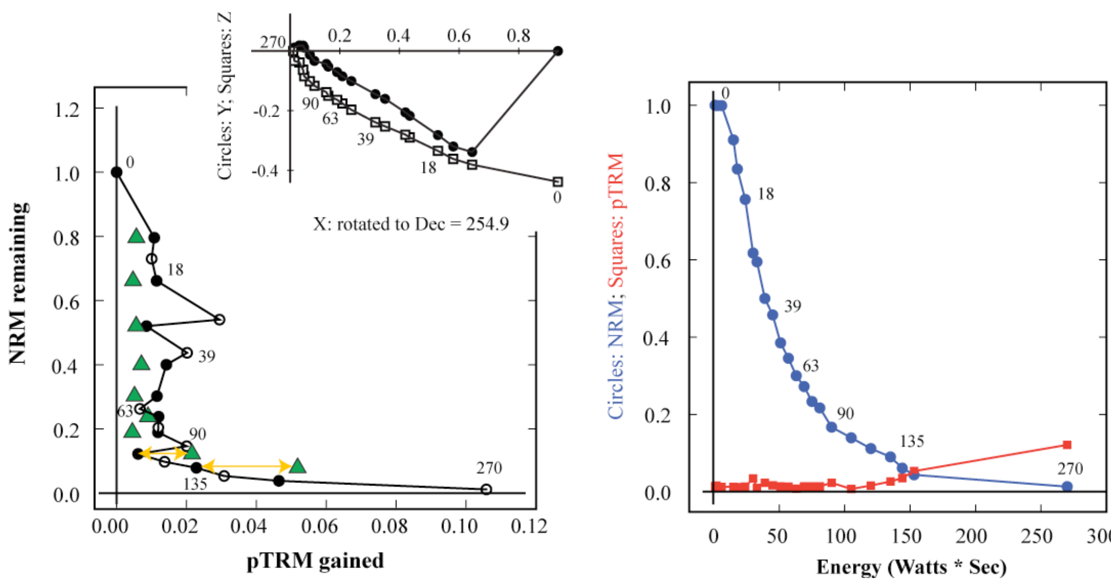

Figure 5.6: Same as Figure 5.2 for lunar specimen 62235.119 where NRM is normalized to 1.06 x 10^{-4} Am^2/kg. Yellow arrows indicated failed pTRM checks.

I performed a microwave KTT experiment on a glassy portion of specimen 60015.37 (separated with a diamond saw blade). Note this specimen is mineralogically different from the anorthosite specimen, 60015.67, used in the thermal KTT experiment

(Chapter 4). Unlike the other microwave paleointensity experiments for lunar specimens, specimen 60015.37 gained a measurable pTRM (~20% of the NRM) before the experiment ended prematurely due to experimental complications, in which the specimen physically moved between energy steps. While this experiment yields no evidence of two magnetization components, the incomplete (60% demagnetization) nature of the experiment cannot verify a single component of magnetization (Figure 5.7). The direction is stable, but does not trend to the origin (MAD = 3.1°, dANG = 6.4°), so the corresponding low-energy intensity interpretation of 45.3 μT may be associated with an overprint.

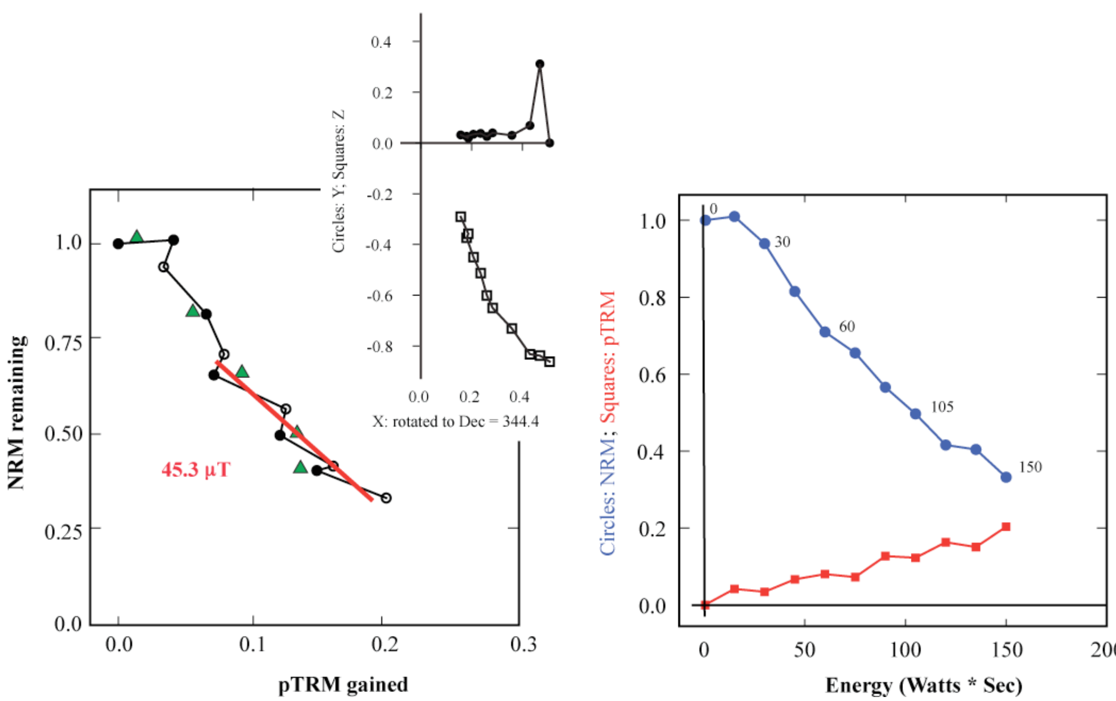

Figure 5.7: Same as Figure 5.2 for lunar specimen 60015.67 where NRM is normalized to 7.07 x 10^{-6} Am^2/kg.

5.5 Discussion

The goal of the microwave experiments was to assess the applicability of the microwave paleointensity measurement method for use with lunar specimens. The microwave Thellier-Thellier technique is appealing for application to lunar specimens because it does not require large specimens, and ideally does not cause thermal alteration. Here I present several advantages and disadvantages of the microwave method, and the trade-offs that I observe.

As with all paleointensity methods, there is no single perfect methodology guaranteed to work for every specimen. One disadvantage of the current microwave experimental arrangement is the reliance on cylindrical specimens with particular dimensions. The cylindrical shape allows the flat end of the specimen to be held securely to a specimen holder by a vacuum and provide more steady resonance within the microwave cavity. Abundant terrestrial magnetic specimens may be cut into ideally shaped sub-specimens, but the limited supply of generally smaller lunar specimens precludes waste caused by cutting less ideally shaped specimens. Furthermore, the small specimen size limits the total specimen magnetization, which is exacerbated by the generally low concentration of magnetic carriers often present in lunar specimens. This makes intensity measurements difficult with the less sensitive magnetometer (~ 1 order of magnitude less sensitive than the magnetometer used for the thermal KTT experiments) currently being employed for the microwave technique. With adaptations to the existing magnetometer to increase its sensitivity, this method could be made more applicable to lunar specimens.

The applicability of the microwave technique to terrestrial specimens continues to be explored in studies by *Hill and Shaw* [1999; 2000; 2007], *Hill et al.* [2002], *Brown et al.* [2006], *Shaw et al*. [1996] and *Böhnel et al.* [2003]. For the experiments performed in this study, the paleointensities measured with the microwave technique are noisier (larger scatter in Arai plots) than experiments on sister specimens measured with the equivalent thermal method. The preferred method for microwave studies [e.g. *Hill and Shaw*, 2007] uses an applied field with a perpendicular configuration [*Kono and Ueno*, 1977], which only requires a single microwave exposure at each energy step and results in less dispersion in the Arai plot. The single applied energy method eliminates the need for higher precision of applied power but does not provide a method to check for alteration during the experiment. The overall quality of results as a function of experimental method (perpendicular vs. double-heating KTT) have been shown to be statistically indistinguishable (personal communication with Maxwell Brown, 2007.)

Despite several detracting features, the microwave paleointensity measurement technique is still a viable method worth pursuing. The microwave technique provides complementary results with which the thermal KTT results may be compared. Agreement between results from two methods using inherently different physical processes can demonstrate a robustness of the results independent of measurement biases. On the other hand, disagreement between results from two methods could highlight experimental error, abnormal magnetic behavior or failure to meet one or more of the underlying assumptions behind either method. The microwave KTT method is much faster than a traditional thermal KTT technique for small numbers of specimens, which is generally the case for lunar material. The microwave technique is also useful for lunar specimens because is may be less likely to thermally alter a specimen than the thermal KTT technique. However, some specimens obviously undergo deleterious heating, as demonstrated by melt bubbles for sub-specimens 62235.119 (a lunar specimen) and mc102d1.2 (a terrestrial specimen).

The microwave KTT experiment on lunar specimen 62235.119 in particular suggests that alteration may play a big role in the dual-component Arai plots seen in previous thermal KTT results (Chapter 4). For example, specimen 62235.119 likely altered at or after energy step 105 watt-secs, which divides the apparent high and low intensity components of magnetization (Figure 5.4). Additional alteration at 144 watt-secs is inferred from a distinct change in the observed absorbed power spectrum at this energy step and the visual observation of a melt bubble (Figure 5.8) after the experiment. Furthermore, specimen 62235.119 did not gain significant pTRM until the 144 watt-secs energy, after which the pTRM increased from < 2% of the NRM to 10% of the NRM. This specimen is the only specimen in the microwave experiments that showed a sharp transition between two components, but it is also one of the only specimens measured to full demagnetization (> 95% of NRM removed). The origin of the dual-component magnetization remains unclear from results of both the microwave and thermal paleointensity experiments. The sharp transition between components could be related to an IRM overprint, alteration during experimentation, or the expression of shock from impact. Further investigations of this specimen as well as other specimens are needed to determine the significance of the two components seen in paleointensity results.

Figure 5.8: Image of lunar specimen 62235.119 after exposure to microwave energy equivalent to 144 watt-secs. The dark circle in the center of the specimen is a glassy and most likely a melt bubble produced during decay of spin waves generating heat through lattice vibrations within the bulk specimen.

The outer glass coating of 60015 exhibited inconclusive results with a non-primary magnetic remanence having apparent ancient field strength of 43.5 μT. However, investigations of this specimen had many experimental problems. This apparent high intensity is not corroborated by the results from the thermal KTT experiment on specimen 60015.37 (Chapter 4). If the age (~3.3 Ga) and inferred paleointensity (43.5 μT) of 60015.67 were to be interpreted as a primary thermal remanence obtained in a lunar field, it would be difficult to reconcile with either the putative strong field era between 3.9 and 3.6 Ga [*Cisowski, et al.*, 1983; *Runcorn*, 1994, 1996] or existing thermal models that generate a lunar dynamo [*Stegman, et al.*, 2003; *Stevenson*, 2003]. It is likely that the remanence seen in this specimen is an IRM, shock, or even contamination while in the Earth's field. It would be beneficial to repeat this experiment using both the microwave and thermal KTT analysis on sister specimens of the glassy portion of 60015 to yield a complete and interpretable experiment.

The following suggestions may improve future lunar microwave paleointensity experiments. Only specimens with large NRM relative to their size should be selected to ensure measurability throughout the demagnetization process. Small, uniformly shaped samples will provide a more consistent resonance within the microwave cavity. Ideally, these specimens should have at least one flat side to ensure a proper vacuum seal to the specimen holder. Specimens that have experienced extensive shock, such as impact breccias, should be avoided. However, glasses (even impact glasses) may be useful for microwave experiments because they are known to provide well-behaved paleointensity results in thermal KTT experiments [*Pick and Tauxe*, 1993; *Tauxe and Staudigel*, 2004]. The microwave results from sample 60015 corroborate this hypothesis, but lunar glasses need to be examined further before a definitive conclusion may be drawn. With multiple sister specimens, both microwave and thermal IZZI KTT experiments can be performed with redundancy to verify the reliability of all results. With adjustments to the experimental configuration and the magnetometer employed in the microwave experiment, it could be possible to increase the measurement sensitivity and reduce the ambient field in the microwave cavity.

5.6 Conclusions

The microwave technique has been demonstrated to provide similar paleointensity results to both the Kono perpendicular applied field [*Hill and Shaw*, 2007] and the Coe-modified KTT [*Böhnel, et al.*, 2003] thermal methods. This study demonstrates that the microwave technique provides similar results to the IZZI modified KTT experimental method, as performed at Scripps Paleomagnetics Laboratory. Additionally, this chapter shows that the microwave technique has promise for future measurements of lunar paleointensity because it reduces the likelihood of thermal alteration of the bulk specimen, relative to traditional double heating methods. However, the marginal success of this study is integrally linked to several primary factors; 1) the number of specimens available, 2) the available variety of specimen mineralogies, and 3) limitations in experimental configuration. In the future, these factors may be addressed by appropriate sample selection and adaptations to the existing experimental apparatus.

Clearly the preliminary microwave paleointensity results presented in this chapter are insufficient to draw significant conclusions about the early lunar magnetic environment. Of the three lunar specimens examined, only 62235 yielded a complete experiment, demonstrating a non-primary remanence associated with a high paleointensity (similar results to the thermal KTT results in Chapter 4). The experiment on 60015 was incomplete, but also indicated a non-primary remanence. 73235 failed to yield an interpretable result.

While the results of this study were inconclusive, the main purpose of this study was to evaluate the applicability of the microwave paleointensity method for lunar specimens. To first order, where complete microwave experiments were possible, the resultant microwave paleointensity results are similar in character to those of the thermal paleointensity results presented in Chapter 4. The fundamental conclusion of Chapter 4, that no lunar paleointensity measurements have definitively observed a primary TRM, is supported by these preliminary microwave intensity results. The microwave measurements also underscore the importance of demonstrating primary remanence.

5.7 Acknowledgments

We would like to thank the members of the Liverpool Paleomagnetics Laboratory for the generous use of their laboratory facilities and their helpful discussions, which made this chapter possible.

5.8 References

Brown, M. C., J. Shaw, and A. T. Goguitchaichvili (2006), Microwave palaeointensity from the R3-N3 geomagnetic field reversal, *Geophys. J. Int.*, *167*, 54-69.

Böhnel, H., A. J. Biggin, D. Walton, J. Shaw, and J. Share (2003), Microwave palaeointensities from a recent Mexican lava flow, baked sediments and reheated pottery, *Earth Planet. Sci. Lett.*, *214*, 221-236.

Cisowski, S. M., D. W. Collinson, S. K. Runcorn, and A. A. Stephenson (1983), A review of lunar paleointensity data and implications for the origin of lunar magnetism, *J. Geophys. Res.*, *88*, A691-A704.

Dunlop, D. J., and O. Ozdemir (1997), *Rock Magnetism: Fundamentals and Frontiers*, 573 pp., Cambridge University Press.

Fuller, M., and S. M. Cisowski (1987), Lunar paleomagnetism, in *Geomagnetism*, edited by J. A. Jacobs, pp. 307-456, Academic Press, San Diego, CA.

Gratton, M. N., J. Shaw, and E. Herrero-Bervera (2005), An absolute palaeointensity record from SOH1 lava core, Hawaii using the microwave technique, *Phys. Earth Planet. Int.*, *148*, 193-214.

Hale, C. J., M. Fuller, and R. C. Bailey (1978), On the application of microwave heating to lunar paleointensity determination, *Proceedings of the Lunar and Planetary Science Conference, 9th*, 3165-3179.

Hill, M. J., M. N. Gratton, and J. Shaw (2002), A comparison of thermal and microwave palaeomagnetic techniques using lava containing laboratory induced remanence, *Geophys. J. Int.*, *151*, 157-163.

Hill, M. J., and J. Shaw (1999), Palaeointensity results for historic lavas from Mt Etna using microwave demagnetization/remagnetization in a modified Thellier-type experiment, *Geophys. J. Int.*, *139*, 583-590.

Hill, M. J., and J. Shaw (2000), Magnetic field intensity of the 1960 Kileauea lava flow, Hawaii, using the micorwave palaeointensity technique, *Geophys. J. Int.*, *142*, 487-504.

Hill, M. J., and J. Shaw (2007), The use of the 'Kono perpendicular applied field method' in microwave palaeointensity experiments, *Earth Planets Space*, *59*, 711-716.

Hill, M. J., J. Shaw, and E. Herrero-Bervera (2006), Determining palaintensity from the Gilbert-Gauss Reversal recorded in the Pu'u Heleakala lava section, Wai'anae Volcano, Oahu, Hawaii, *Earth Planet. Sci. Lett.*, *245*, 29-38.

Kono, M., and N. Ueno (1977), Paleointensity determination by a modified Thellier method, *Phys. Earth Planet. Int.*, *13*, 305-314.

Pearce, G. W., G. S. Hoye, D. W. Strangway, B. M. Walker, and L. A. Taylor (1976), Some complexities in the determination of lunar paleointensities, *Proceedings of the Lunar Science Conference 7th*, 3271-3297.

Pick, T., and L. Tauxe (1993), Holocene Paleointensities: Thellier experiments on submarine basaltic glass from the east Pacific Rise, *J. Geophys. Res.*, *98*, 17949-17964.

Runcorn, S. K. (1994), The early magnetic-field and primeval satellite of the Moon: Clues to planetary formation, *Philos. Trans. R. Soc. London, Ser. A*, *349*, 181-196.

Runcorn, S. K. (1996), The formation of the lunar core, *Geochimica et Cosmochimica Acta*, *60*, 1205-1208.

Shaw, J., M. J. Hill, and S. J. Openshaw (2001), Investigating the ancient Martian magnetic field using microwaves, *Earth Planet. Sci. Lett.*, *190*, 103-109.

Shaw, J., J. Share, and J. Rogers (1984), An automated superconducting magnetometer and demagnetizing system, *Geophys. J. R. Astron. Soc.*, *78*, 209-217.

Shaw, J., D. Walton, S. Yang, T. C. Rolph, and J. Share (1996), Microwave archaeointensities from Peruvian ceramics, *Geophys. J. Int.*, *124*, 241-244.

Stegman, D. R., M. J. Jellinek, S. A. Zatman, J. R. Baumgardner, and M. A. Richards (2003), An early lunar core dynamo driven be thermochemical mantle convection, *Nature*, *421*, 143-145.

Stevenson, D. J. (2003), Planetary magnetic fields, *Earth Planet. Sci. Lett.*, *208*, 1-11.

Tauxe, L. T., and H. Staudigel (2004), Strength of the geomagnetic field in the Cretaceous Normal Superchron: New data from submarine basaltic glass of the Troodos Ophiolite, *Geochem. Geophys. Geosyst.*, *5*, doi:10.1029/2003GC000635.

Thellier, E., and O. Thellier (1959), Sur l'intensité du champ magnétique terrestre dans le passé historique et géologique, *Ann. Geophys.*, *15*, 285-378.

Thomas, D. N., M. J. Hill, and A. S. Garcia (2004), Comparison of the Thellier and microwave palaeointensity techniques: Results from a Tertiary basaltic intrusion from the Sydney Basin, New South Wales, *Earth Planet. Sci. Lett.*, *229*, 15-29.

Turner, G., and P. H. Cadogan (1975), The history of lunar bombardment inferred from ^{40}Ar - ^{39}Ar dating of highland rocks, *Proceedings of the Lunar and Planetary Science Conference, 6th*, 1509-1538.

Walton, D. (2002), Conditions for ferromagnetic resonance in nanoparticles and microwave magnetization, *Geophys. Res. Lett.*, *29*, doi:10.1029/2002GL016049.

Walton, D. (2004), Avoiding mineral alteration during microwave magnetization, *Geophys. Res. Lett.*, *31*, doi:10.1029/2003GL019011.

Walton, D., J. Share, T. C. Rolph, and J. Shaw (1993), Microwave magnetization, *Geophys. Res. Lett.*, *20*, 109-111.

Walton, D., J. Shaw, J. Share, and J. Hakes (1992), Microwave demagnetization, *Journal of Applied Physics*, *71*, 1549-1551.

Walton, D., S. Snape, T. C. Rolph, J. Shaw, and J. Share (1996), Application of ferrimagnetic resonance heating to palaeointensity determinations, *Phys. Earth Planet. Int.*, *94*, 183-186.

Wieczorek, M. A., B. L. Jolliff, A. Khan, M. E. Pritchard, B. P. Weiss, J. G. Williams, L. L. Hood, K. Righter, C. R. Neal, C. K. Shearer, I. S. McCallum, S. Tompkins, B. R. Hawke, C. Peterson, J. J. Gillis, and B. Bussey (2006), The constitution and structure of the lunar interior, in *New Views of the Moon*, edited, p. 221, Mineralogical Soc America, Chantilly.

Yu, Y. J., L. T. Tauxe, and A. Genevey (2004), Toward an optimal geomagnetic field intensity determination technique, *Geochem. Geophys. Geosyst.*, *5*, doi:10.1029/2003GC000630.

Appendix 5.A: Supplemental Data Tables

Supplemental Table 5.A.1: Data for Specimen 62235.119

Name	Field	Power (Watts)	Time (Sec)	Intensity ($\mu Am^2/Kg$)	Dec	Inc	Power Absorbed (Watt-Secs)
62235.119	NRM	0	0	107	278.2	27.9	0
62235.119	Z	1	1	106	278.6	28.1	0.57
62235.119	A	1	1	106	279.5	28	0.62
62235.119	A	1	2	106	280.3	28	1.5
62235.119	Z	1	2	106	281.3	28	1.55
62235.119	Z	1	3	106	281.6	28	2.38
62235.119	A	1	1	106	281.9	28	0.57
62235.119	A	1	3	106	282.4	28	2.32
62235.119	A	2	3	106	282.8	28	4.72
62235.119	Z	2	3	106	283.6	28	4.81
62235.119	Z	5	3	96.3	283.9	28.6	12.24
62235.119	A	1	3	96.1	284.4	28.7	2.32
62235.119	A	5	3	95.4	284.5	28.8	12.01
62235.119	A	6	3	89.1	284.5	29.8	14.44
62235.119	Z	6	3	88.3	285.2	29.7	14.53
62235.119	Z	8	3	80	284.5	30.4	18.69
62235.119	A	5	3	79.6	284.1	30.6	11.7
62235.119	A	8	3	78.8	284.3	30.7	18.4
62235.119	A	10	3	69	283.5	32.2	23.45
62235.119	Z	10	3	65.4	283.3	32.4	23.89
62235.119	Z	11	3	62.9	282.9	32.6	26.14
62235.119	A	8	3	62.9	283.5	32.7	18.67
62235.119	A	11	3	62.2	283.2	33.2	25.63
62235.119	A	13	3	55.3	282	34.9	30.75
62235.119	Z	13	3	52.9	281.6	35.3	30.64
62235.119	Z	15	3	48.4	281.7	36.7	35.42
62235.119	A	11	3	48.1	280.8	36.7	26.03
62235.119	A	15	3	46.8	281.3	37.2	35.52
62235.119	A	17	3	42.2	281.1	39	39.72
62235.119	Z	17	3	40.8	280.9	39.4	38.79
62235.119	Z	19	3	36.5	281	40.7	44.48
62235.119	A	15	3	36.6	280.2	41.9	36.14
62235.119	A	19	3	35.5	280.1	42	45.22
62235.119	A	21	3	32.4	281.1	42.8	48.75
62235.119	Z	21	3	31.7	280.7	42	49.49
62235.119	Z	23	3	28.8	279	43.4	53.02
62235.119	A	19	3	28.7	279.3	44.6	45.07
62235.119	A	23	3	27.9	279.3	45.7	51.79
62235.119	A	25	3	26.1	276	47.6	59.87
62235.119	Z	25	3	24.7	277.1	47.3	56.95
62235.119	Z	27	3	22.9	274.4	46.9	63.46
62235.119	A	23	3	22.8	274	49.6	53.31
62235.119	A	27	3	22.4	277.4	49.7	62.65
62235.119	A	30	3	19.9	271.6	53.1	71.57

continued

Supplemental Table 5.A.1 (contiuned)

Name	Field	Power (Watts)	Time (Sec)	Intensity ($\mu Am^2/Kg$)	Dec	Inc	Power Absorbed (Watt-Secs)
62235.119	Z	30	3	17.7	277	52.9	71.71
62235.119	Z	35	3	14.7	265.6	56.4	83.54
62235.119	A	27	3	14.7	265.4	58.5	64.93
62235.119	A	35	3	14.9	269.1	58.5	83.28
62235.119	A	40	3	12.5	255.5	59	90.09
62235.119	Z	40	3	11.8	241.6	60.1	95.79
62235.119	Z	45	3	9.5	232.3	53	106.38
62235.119	A	35	3	12	236.4	56.7	82.37
62235.119	A	45	3	10.9	211.5	60.8	111.57
62235.119	A	48	3	9.9	224.6	56.1	114.75
62235.119	Z	48	3	6.4	224.2	46.3	116.57
62235.119	Z	51	3	4.6	216.1	60.6	126.05
62235.119	A	45	3	10.4	260	74.4	107.94
62235.119	A	51	3	9.8	245.2	76.9	134.03
62235.119	A	54	5	12.9	273.5	81.5	202.69
62235.119	Z	54	5	1.4	279.8	-1.4	218.27

Field A is applied field, Z is zero field, **Power** is the power in Watts of the microwave generator which is applied for **Time** in seconds (secs), **Intensity** is the measured strength of the magnetic vector at each demagnetization step, **Dec** is declination, **Inc** is inclination, **Power Absorbed** is the calculated energy absorbed by the sample in Watt-secs

Supplemental Table 5.A.2: Data for Specimen 73235.19

Name	Field	Power (Watts)	Time (Sec)	Intensity ($\mu Am^2/Kg$)	Dec	Inc	Power Absorbed (Watt-Secs)
73235.19	NRM	0	0	10.7	233.9	85.8	0
73235.19	Z	5	3	10.6	229	86.1	8.65
73235.19	A	5	3	10.6	225.2	86.2	8.28
73235.19	A	10	3	10.5	230.6	86.1	16.04
73235.19	Z	10	3	10.4	236.1	86	17.12
73235.19	Z	15	3	10.0	228	86.2	25.55
73235.19	A	5	3	10.0	232.1	85.6	8.42
73235.19	A	15	3	9.9	210.6	86.5	25.25
73235.19	A	20	3	9.4	221.8	85.7	33.09
73235.19	Z	20	3	9.3	221.8	85.9	33
73235.19	Z	25	3	8.5	212.7	87	41.45
73235.19	A	15	3	8.5	213.3	87	25.56
73235.19	A	25	3	8.5	216.7	86.2	42.14
73235.19	A	30	3	7.9	215.2	86.4	49.84
73235.19	Z	30	3	7.9	240.6	86.3	49.7
73235.19	Z	37	3	7.1	243.5	85	61.69
73235.19	A	25	3	7.1	241.5	85.8	43.6
73235.19	A	37	3	6.9	222.8	86	60.95
73235.19	A	33	4	6.5	251.6	85	75.5
73235.19	Z	33	4	6.2	254.1	84.8	75.51
73235.19	Z	38	4	5.8	270.7	84.5	86.03
73235.19	A	37	3	5.8	261.5	83.5	61.24
73235.19	A	38	4	5.7	265.5	83.4	84.37
73235.19	A	45	4	5.3	262	83.3	100.09
73235.19	Z	45	4	4.7	262.8	85.6	100.16
73235.19	Z	52	4	4.3	271.3	83.5	113.42
73235.19	A	38	4	4.3	267.5	83.7	85.73
73235.19	A	52	4	4.1	270	83.6	117.32
73235.19	A	62	4	3.7	255.9	83.7	136.07
73235.19	Z	62	4	3.4	246.5	84.7	136.51
73235.19	Z	58	5	3.0	270.3	79.4	161.96
73235.19	A	52	4	3.4	288.2	81.2	110.63
73235.19	A	58	5	3.3	308.7	80.8	165.25
73235.19	A	70	5	2.5	240.6	76.7	196.72
73235.19	Z	70	5	2.1	288.4	83.8	203.25
73235.19	Z	75	6	1.9	258.3	68.9	262.97
73235.19	A	58	5	1.9	262.1	71.4	163.43
73235.19	A	75	6	1.7	265.5	77.3	259.84
73235.19	A	75	8	2.0	258.7	63.6	362.22
73235.19	Z	75	8	1.1	243.3	20.9	370.67

Field A is applied field, Z is zero field, **Power** is the power in Watts of the microwave generator which is applied for **Time** in seconds (secs), **Intensity** is the measured strength of the magnetic vector at each demagnetization step, **Dec** is declination, **Inc** is inclination, **Power Absorbed** is the calculated energy absorbed by the sample in Watt-secs

Supplemental Table 5.A.3: Data for Specimen 60015.67

Name	Field	Power (Watts)	Time (Sec)	Intensity ($\mu Am^2/Kg$)	Dec	Inc	Power Absorbed (Watt-Secs)
60015.67	NRM	0	0	14.30	344.4	59.5	0
60015.67	Z	5	3	14.50	310.8	56.1	11.05
60015.67	A	5	3	14.50	315	55.8	11.38
60015.67	A	10	3	13.80	332.4	62.7	22.83
60015.67	Z	10	3	13.50	335.3	62.4	22.22
60015.67	Z	15	3	11.70	339.6	63.8	33.53
60015.67	A	5	3	11.80	338	63.9	10.75
60015.67	A	15	5	11.50	336.6	68.3	58.01
60015.67	A	20	3	11.20	337.2	68.7	43.13
60015.67	Z	20	3	10.20	336.4	66.3	45.05
60015.67	Z	25	3	9.39	338.8	66.5	54.01
60015.67	A	15	3	10.20	337.3	67.9	33.55
60015.67	A	25	3	10.30	336.4	68.8	55.13
60015.67	A	30	3	9.78	336.4	69.8	65.01
60015.67	Z	30	3	8.11	335.3	65.1	64.16
60015.67	Z	35	3	7.12	335	65	74.03
60015.67	A	25	3	8.37	334.7	68.7	55.89
60015.67	A	35	3	8.69	334.5	70.8	73.17
60015.67	A	40	3	8.14	336.9	71	85.42
60015.67	Z	40	3	5.96	336.1	64	81.22
60015.67	Z	45	3	5.79	338.4	62.3	85.59
60015.67	A	35	3	7.58	338.6	69	73.82
60015.67	A	45	3	7.70	334	70.8	85.83
60015.67	A	50	3	7.46	333	71.8	98.19
60015.67	Z	50	3	4.76	333	61.2	97.65
60015.67	A	45	3	6.57	334.3	69.5	91.75

Field A is applied field, Z is zero field, **Power** is the power in Watts of the microwave generator which is applied for **Time** in seconds (secs), **Intensity** is the measured strength of the magnetic vector at each demagnetization step, **Dec** is declination, **Inc** is inclination, **Power Absorbed** is the calculated energy absorbed by the sample in Watt-secs